Characterization and quantification of glacial sediment transport in two small valley glaciers

Centre for Glaciology

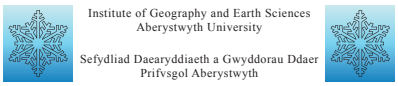

Canolfan Rhewlifeg

Samuel Roberson

Institute of Geography and Earth Sciences

Aberystwyth University

A thesis submitted for the degree of

Philosophiæ Doctor (PhD)

October 2009

Declaration

This work has not previously been accepted in substance for any degree and is not being concurrently submitted in candidature for any degree.

Signed  (candidate)

Date 20.01.2010

STATEMENT 1

This work is the result of my own investigations, except where otherwise stated. Where correction services have been used, the extent and nature of the correction is clearly marked in a footnote(s).

Other sources are acknowledged (e.g. by footnotes giving explicit references). A bibliography is appended.

Signed  (candidate)

Date 20.01.2010

STATEMENT 2

I hereby give consent for my work, if accepted, to be available for photocopying and for inter-library loan, and for the title and summary to be made available to outside organisations.

Signed  (candidate)

Date 20.01.2010

Abstract

This study investigates sediment transport processes and sediment-landform development at two small valley glaciers of contrasting basal thermal-regime. A range of innovative techniques are applied to characterize and quantify glacier structure, glacially transported sediment facies and sediment-landform assemblages at Glacier de Tsanfleuron, Switzerland, and Midre Lovénbreen, Svalbard. Sediment transport at Glacier de Tsanfleuron is dominated by a rockfall-derived supraglacial debris stripe and abrasion-derived subglacial debris planes. Modeled sediment transport rates are equivalent to a glacier-wide erosion rate of 0.5 mm a^{-1}. Subglacially transported sediment ablates to form a complex network of debris stripes, the texture and morphology of which are consistent with sediment supply from palaeokarst sinkholes. These sinkholes dominate the limestone plateau on which the glacier is situated and also restrict glaciofluvial sediment transport by rerouting much of the glacier's meltwater though the karst system. This results in a landsystem that is atypical of valley glaciers in the Alps. Sediment transport at Midre Lovénbreen is strongly influenced by glacier structure, identified at the glacier surface and in digital optical televiewing borehole logs. Glacier structure is successfully reconstructed in three-dimensions, revealing several visually distinctive englacial ice properties and deformation structures. Basally derived englacial sediment layers are found to be intercalated with primary stratification, elevated into near-vertical planes around a gently upglacier dipping central fold axis by large-scale lateral folding. Sediment analysis also allows supraglacial longitudinal debris ridges to be sub-classified into two types, with a new (Type II) form experiencing secondary deformation by small-scale flow parallel recumbent folding in association with vertical displacements across arcuate shear planes near the glacier terminus. Non-structurally controlled sediment transport at Midre Lovénbreen is dominated by low-intensity deformation of subglacial till, and is also characterized by the formation of supraglacial debris cones and proglacial flutes. Flutes at Midre Lovénbreen are interpreted to form beneath warm-based ice by the squeezing of partially fluidized till into cavities where freeze-on occurs due to a 'heat-pump' effect across subglacial boulders. The results of this investigation demonstrate that, while basal-thermal regime may exert a strong influence on glacial sediment-transport processes that operate at the small-scale, bedrock physiography ultimately defines glacier morphometry and resulting large-scale flow structures. Additionally, although some of the sediment-landform types identified in this study are exclusive to a particular set of basal-thermal conditions, the composition and morphology of these sediment-landform assemblages are such that they are unlikely to be preserved in the geological record.

Acknowledgements

First and foremost I would like to thank Bryn Hubbard for providing the large majority of the support for this project in the form of: the initial motivation; sound advice; informative discussions, and a healthy, flexible work ethic. In addition, I owe thanks to Neil Glasser, Poul Christoffersen, Mike Hambrey, Alun Hubbard, Duncan Quincey and Pete Bunting, who have all provided advice and instruction on various topics.

I would also like to thank all those who have provided the invaluable logistical support for fieldwork. Glacier 3000 at Glacier de Tsanfleuron, Switzerland. In Ny-Ålesund: Bjørn Valle, Nick Cox, Simon Henniman and Jack Kohler. Thanks to Robertson Geologging Ltd. for provision of a customized televiewer. Thanks to all those who helped on fieldwork: Hayley Coulson, Bryn Hubbard, Femke Davids, Ali Banwell, Richard Morris, Rich Farnell, Lise Fivez, Johannes Teuchies. The instruction of the Swiss Ski School and Outward Bound is much appreciated in helping fieldwork take place on and in the snow in sometimes very 'foul' conditions. Thanks to Dave Kelly for helping design, make and modify pieces of field equipment. Thanks to Alun Hubbard, Dave Chandler, Dave Hildes and Dan Clewey for providing model code and helping me to decipher it.

Many thanks go to Eva Sahlin for being available for useful discussions, idle gossip, drinking coffee and eating cake.

This work has been funded by NERC grant NER/S/A/2006/14079, whose support I gratefully acknowledge.

Contents

CONTENTS

List of Figures

LIST OF FIGURES

List of Tables

LIST OF TABLES

Chapter 1

Introduction

> I felt the keenest delight when I first read of the action of icebergs in transporting boulders, and I gloried in the process of geology

(Darwin, 1887)

1.1 Rationale

It is well known that glaciers erode their beds and transfer sediment from their interior toward their margin (Hallet et al., 1996; Alley et al., 1997; Hambrey et al., 1999). Glaciers commonly form networks of distinct erosional landforms and depositional sediment-landform assemblages; these can be studied geologically and geomorphologically. Results from such studies can, for instance, be used to evaluate the consequences of glaciological processes over time and reconstruct histories of glacier advances and retreat. Although studies of sediment transport by glaciers go back to Darwin's (1842) interpretation of moraines in North Wales, the nature of sediment entrainment and delivery remain a subject of considerable debate (Clarke, 2005). This ongoing debate can be partly attributed to the inaccessibility of glacial environments, and partly the comparatively under-developed field of sedimentological research. In contrast to the fields of engineering and geotechnology, which have benefitted from both technological developments and improvements in statistical analyses, sedimentology and in particular the study of glacigenic sediments, still relies on qualitative or semi-quantitaive techniques to derive much of its data. Observations of sediment facies transported beneath and within ice masses, nonetheless, have provided a number of key insights.

Following observations beneath Breiðamerkürjokull in Iceland, Boulton and Hindmarsh (1987) proposed (a weakly non-linear) viscous rheology for subglacial till and suggested that

sediment transfer is defined mainly by pervasive deformation within the till layer. Large volumes of sediment deposited by glaciers, e.g. in glaciated terrains and along high-latitude continental shelves, are easily reconciled with interpreted sediment transfer by viscous flow within subglacial till layers (Alley, 1989; Alley, 1991). However, entirely different material behaviour is reported from studies of till at the bottom of boreholes and in laboratory experiments. In both cases till is observed to deform as a (highly non-linear) Coulomb-plastic material (Kamb, 1991; Fischer and Clarke, 1994; Iverson et al., 1998; Tulaczyk et al., 2000; Truffer et al., 2001). Although, there is a developing consensus that the correct flow law for subglacial sediment is plastic (Clarke, 2005), this rheology does not easily explain the large sediment fluxes evident from the palaeoglaciological records because non-linearity prevents pervasive deformation (Kamb, 1991; Tulaczyk et al., 1998). Hence, if this consensus is correct, sediment transport must be dominated by englacial material entrained from the bed by structural deformation and/or basal ice accretion. The widespread presence of debris-rich basal ice layers in glaciers (Lawson, 1979; Hubbard and Sharp, 1995a; Knight, 1997; Waller, 2001; Cook et al., 2007) suggests that englacial transport of sediment is significant, but net fluxes within glacierized catchments have so far not been quantitatively assessed.

Fundamental to this project will be the testing of the following three hypotheses:

i. The distribution and composition of proglacial sediments are attributable to the transport of englacial sediment by entrainment processes and ice flow vectors, or a combination of these two processes,

ii. The volumes of sediment entrained by small valley glaciers and transported by ice flow are fundamentally different in Arctic and Alpine glaciers, yet the two processes control englacial and basal sediment transfer in both environments,

iii. There is a thermally controlled relationship between ice rheology and sediment transfer in Arctic and Alpine environments.

This thesis will be primarily concerned with the testing of these hypotheses. Empirical, conceptual and numerical investigations of the relationships between sediment transfer and ice mass properties, and the determination of how they operate at a catchment scale. The sampling of different types of ice facies and sediment-landform assemblages will enable the validity of conceptual models to be evaluated and built upon. The analysis of ice facies characteristics and the sediments associated with them will serve to elucidate the relationship between different ice facies, sediment transport mechanisms and the formation of proglacial sediment-landform assemblages. Ice facies sampling will also be used to quantify

the volumes of sediment being transported by the glacier, which will be used to provide a first-order approximation of sediment discharge rates.

This project is important because the global distribution of ice masses is responding sensitively to climate change. Glaciers in Arctic and Alpine land systems are particularly affected by global warming. Alpine glaciers are in worldwide recession because snow accumulation cannot compensate for the increase in summer melting. A similar tendency is observed in the Arctic, a region that warms faster than the global mean because recession of reflective ice masses leads to increased absorption of solar energy by exposure of darker land and ocean surfaces. To date, most attention in the climate-glacier debate has been focused on glacier mass balance and global sea level rise. Comparatively unknown empirically, is how the transport of sediment by ice masses are affected by changes in dynamic responses to changes in climate.

1.2 Aims

The fundamental aim of this project is to investigate the roles of ice deformation and subglacial thermal regimes upon sediment transfer by cold- and warm-based glaciers. The project will make a significant contribution to the cryospheric sciences by quantifying the physical relationships between glaciological processes and Arctic and Alpine land-system evolution. Specific outputs from this project will include new field data sets from Midre Lovénbreen in the high-Arctic archipelago of Svalbard and Glacier de Tsanfleuron in Switzerland. These data sets will be used to calibrate and validate conceptual models as well as computer models integrating sediment transfer and ice mass behaviour. More specifically, the aims of this project are to:

i. Develop a new suite of precise automated methods to quantifying particle morphology and apply these to particles sampled from ice facies and sediment-landform assemblages at both Alpine and Arctic valley glacier landsystems,

ii. Map glacier surface and subsurface structure and examine the influence of structure on sediment transport processes at both Alpine and Arctic valley glaciers,

iii. Calculate glacial sediment discharge on the basis of the distribution and concentration of sediments transported by the glacier and modeled three-dimensional ice-flow velocities,

iv. Evaluate and contribute to existing conceptual models of glacial sediment transport and glacigenic sediment-landform assemblage development,

v. Evaluate the influence of basal thermal-regime on glacier structure and sediment transport on the basis of these research findings.

1.3 Research areas

This section provides an overview of the research areas that are central to data collection in this study. This thesis focuses on two contrasting field areas: Glacier de Tsanfleuron, Switzerland and Midre Lovénbreen, Svalbard. These glaciers are chosen primarily for their logistical convenience, i.e. ease of access to the glacier surface and frontal zones, and support infrastructure.

1.3.1 Glacier de Tsanfleuron, Switzerland

Glacier de Tsanfleuron is an east-facing largely warm-bedded polythermal glacier situated in the massif des Diablerets-Suisse, on the northern side of the Rhone valley [46°18N to 46°19N, 7°12E to 7°15E], ∼10 km northwest of Sion, Valais canton, Switzerland. The glacier occupies ∼2.8 km^2 of a high plateau, ranging from 2844 m to 2475 m a.s.l., with an equilibrium line at ∼2800 m a.s.l.(Fig. 1.1).

The glacier is underlain by Mesozoic and Tertiary carbonate limestones of the Hauterivian and Urgonian series (Fairchild et al., 1994). The Hauterivian series forms the massif of the Oldenhorn (3123 m a.s.l.) and Sanetschhorn (2923 m a.s.l.), constraining the glacier to the north. At the glacier's southern margin the Urgonian series forms the peaks of Les Diablerets (3003 m a.s.l.) and the Tour St Martin (2908 m a.s.l.). The high plateau on which the glacier terminates is near to a boundary between the massive Urgonian series and thinly bedded Tertiary limestone. The plateau has a well developed karstic drainage system and is believed to comprise the majority of the glacier bed (Grust, 2004). The northeastern tip of the glacier terminus occupies an over-deepened syncline, composed of a thrust fault within the Cretaceous lithologies (Fairchild et al., 1994) (Fig. 1.2).

The glacier has receded ∼1800 m since 1865 (ETHZ, 2008). The extent of the glacier at the end of the Little Ice Age is demarcated by an extensive terminal moraine complex at ∼2440 m a.s.l. (Marie, unpublished, cited in Tison and Lorrain, 1987). Two further suites of terminal moraines at 2350m a.s.l. and 2250 m a.s.l. exist beyond the Little Ice Age moraine. These are best viewed from remotely sensed imagery and have not been investigated to date. Their positions suggest that they may be corollary with the Egesen and Daun advances at ∼11000 a BP and ∼13000 a BP respectively (Paul and Maisch, 2006; Kelly et al., 2004)

Figure 1.1: Photograph of Glacier de Tsanfleuron - taken from the Sanetschhorn looking southwest. Note the Nunatak and supraglacial debris stripe towards the left of the image. Credit: Jürg Alean.

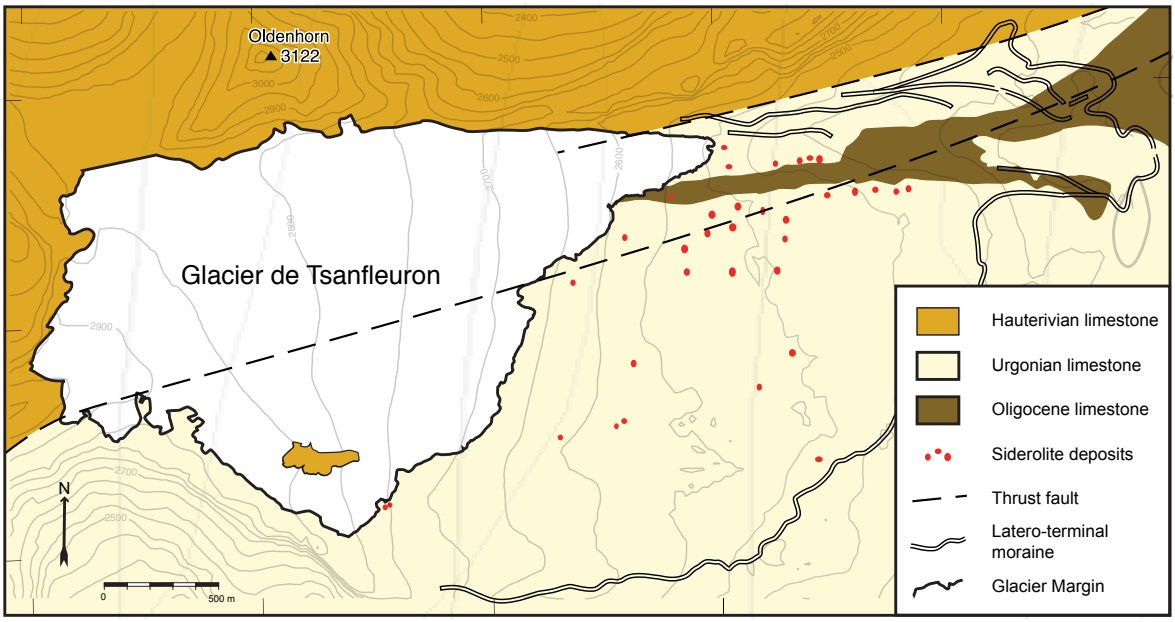

Figure 1.2: Geological map of Glacier de Tsanfleuron - adapted from Fairchild et al. (1994) and Gremaud et al. (2009).

1.3.1.1 Previous research at Glacier de Tsanfleuron

Glacier de Tsanfleuron has been the focus of a number of studies concerning: subglacial hydrology (Masotti, 1991; Fairchild et al., 1994; Grust, 2004), basal ice facies evolution (Hubbard and Sharp, 1993; Hubbard, Tison, Janssens and Spiro, 2000), ice flow dynamics (Hubbard, 2002; Hubbard et al., 2003; Chandler, 2005), ice crystallography (Souchez and Lemmens, 1985; Tison and Hubbard, 2000; Hubbard, Tison, Janssens and Spiro, 2000; Freeman et al., 2005; Murray et al., 2007), energy balance modelling (Essery et al., 2006) and optical borehole televiewing (Hubbard et al., 2008). Studies concerning the glaciers subglacial drainage and flow dynamics are pertinent to a sedimentological study, both having considerable influence on glacial sediment transport. Studies of the glacier's hydrology have revealed that it is unique amongst Alpine glaciers, being one of few entirely underlain by karstic limestone. The karst system has a profound influence on subglacial drainage and flow dynamics (Hubbard and Hubbard, 1998; Chandler, 2005). On the basis of the distribution of cavities in the proglacial zone, Sharp et al. (1989) argued that the subglacial drainage network was composed of a series of linked cavities. Grust (2004) calculated that ~95% of the glacier's meltwater drains subglacially through the karst system; this represents a significant negative energy flux. Cold-based ice has rarely been documented within Alpine glaciers, but has been identified at Glacier de Tsanfleuron by both Murray et al. (2007) and Bailey (2007), and is probably related to the configuration of the drainage system. Similarly, sliding at the bed is limited to the area under the northern ice tongue (Chandler, 2005),

where a locally constrained channelised drainage system is inferred to develop during the ablation season (Grust, 2004).

Comparatively few studies have considered the glacial sediment-landform assemblages deposited by the glacier, with the exception of Marie (Unpublished, cited in Tison and Lorrain, 1987), who dated the large terminal moraine complex using lichenometry to 1855 - 1865. Given the relative sparsity of sediment in the forefield compared to other glaciers in the vicinity, e.g. Glacier de Trient or Bas Glacier d'Arolla, the dearth of sedimentological studies is not unexpected.

1.3.2 Midre Lovénbreen, Svalbard

Midre Lovénbreen [78° 52N to 78° 54N, 11° 57E to 12° 06E] is a ∼4 km^2 polythermal valley glacier located in northwest Spitsbergen (Fig. 1.2). The glacier is composed of four accumulation basins feeding into a narrow tongue, flowing south to north (Fig. 1.3).

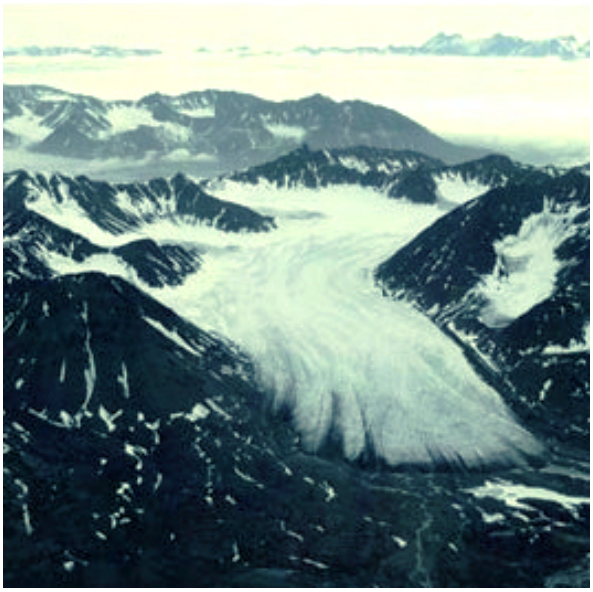

Figure 1.3: Aerial photograph of Midre Lovénbreen - taken from the north during 2005 Lidar survey. Note the large supraglacial debris ridges at the left-hand margin of the glacier (image provided by NEODC).

The glacier ranges from ∼50 to ∼600 m a.s.l, with an equilibrium line altitude at ∼400 m a.s.l. The basin is underlain by continuous permafrost ∼70 to 140 m deep (Liestøl, 1988). Radio echo soundings (Björnsson et al., 1996) have revealed that Midre Lovénbreen is very probably polythermal; a hypothesis which is supported by the annual emergence of turbid pressurised water beyond the terminus (Hodson et al., 2000; Rippin et al., 2003) and formation of proglacial icings (Hagen and Sætrang, 1991). Midre Lovénbreen has been retreating since a Neoglacial maximum ∼1905 (Lefauconnier and Hagen, 1991), marked by

a large terminal thrust-moraine complex ∼1 km from the present day terminus. Between the confines of the terminal moraine complex and the present glacier are a series of complex sediment-landform assemblages, indicative of former flow dynamics and sediment transport processes (Hambrey et al., 2005).

The Brøgger peninsula, where Midre Lovénbreen is located, is composed predominantly of Proterozoic lithologies with some Carboniferous and Permian layers (Fig. 1.4). Midre Lovénbreen is underlain by a series of gently southerly dipping strata, which are exposed from south to north in the following order: the southernmost Lower and Middle Proterozoic Bogegga Formation (mica-schist and quartz-carbonate-schist), the Late Proterozoic Steenfjellet Formation (marble), and the northernmost Upper Proterozoic Nieslenfjellet Formation (phyllite). The Permian Kapp Starostin formation (siliceous shale and chert) forms a series of isolated outcrops to the north of the glacier terminus, but is otherwise overlain by Quaternary moraine deposit, with Holocene fluvial deposits outside the Neoglacial moraine complex.

1.3.2.1 Previous research at Midre Lovénbreen

Research into the relationships between glacier structure and sediment has been conducted at the Midre Lovénbreen by Hambrey et al. (2005). This documented surface structures, mapped englacial structures using ground penetrating radar and used a finite-difference ice-flow model to investigate present and former ice flow and structural dynamics. Additional research into the nature of sediment-landform assemblages at Midre Lovénbreen was undertaken by Bennett et al. (1997). Mass balance surveys of the glacier have also received a great deal of focus, which has involved using an ablation stake network since 1967 (Hagen and Liestøl, 1990), stereo-photogrammetry (Rippin et al., 2003), as well as more recent Lidar GPS surveys (Rees and Arnold, 2007). Lidar has also been applied to investigations of ice surface roughness (Arnold et al., 2006). The configuration of the glacier's hydrology was investigated by Rippin et al. (2003) and Irvine-Fynn et al. (2005a), whose research both concluded that long-term changes in subglacial drainage network were caused by a strongly negative mass balance, but that short-term changes in the network were controlled by early season water pressures and changes in energy-fluxes at the glacier surface. Radar and seismic-based investigations of the glacier's basal conditions and thermal structure have been instrumental in understanding how sediment facies are entrained and then transported at the bed of small-polythermal glaciers (King et al., 2008).

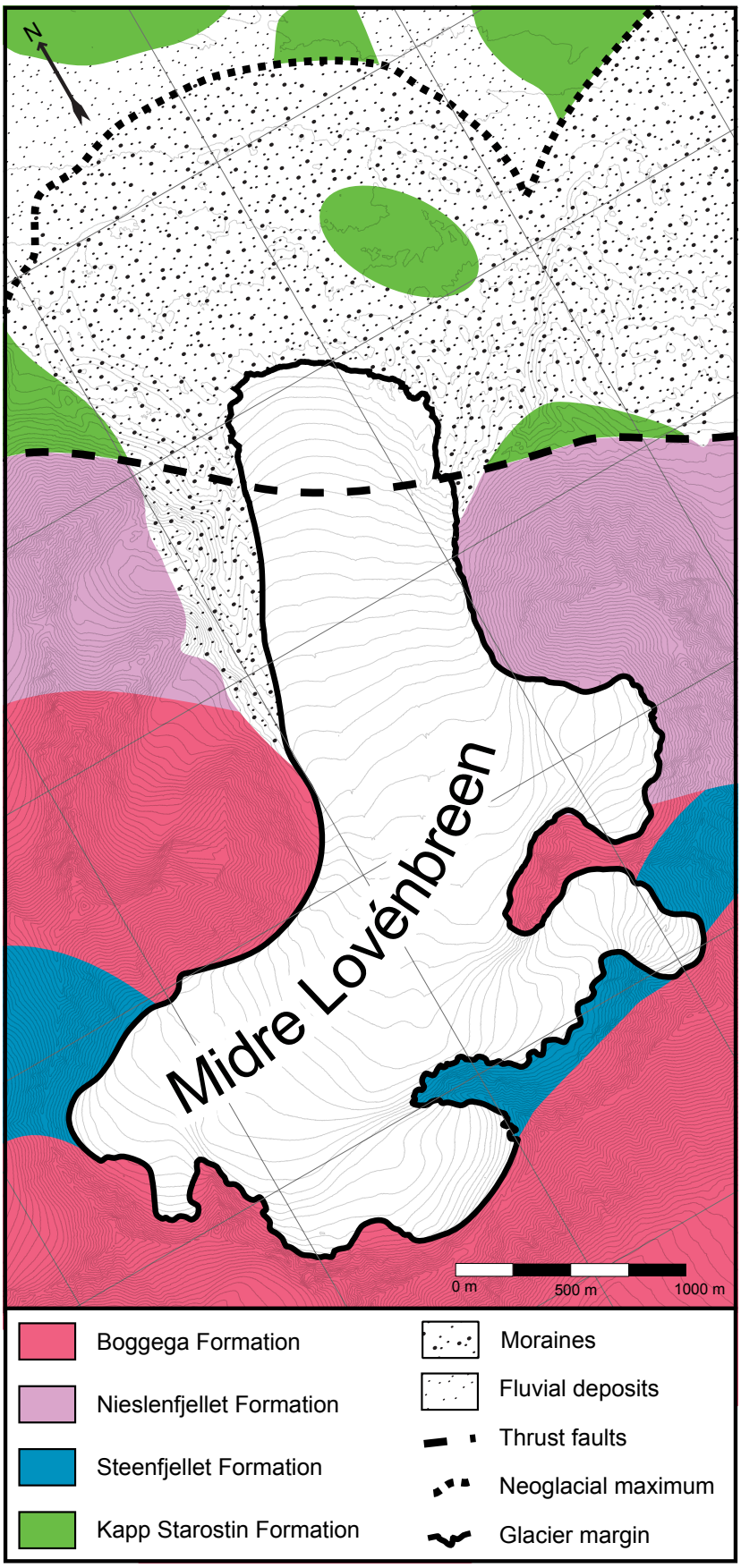

Figure 1.4: Geological map of Midre Lovénbreen - adapted from Norsk Polar Institutt Temakart no. 30 (1990)

1.4 Thesis Outline

This thesis is composed of eight chapters. Chapter 1 describes the field sites and provides the rationale and the aims of the study. Chapter 2 reviews the contemporary literature regarding glacial and glaciofluvial sediment transport . Chapter 3 provides details of techniques applied in the field, laboratory analyses, statistical methods and numerical modelling. Chapter 4 concerns the design, application and testing of techniques for the automation and quantification of particle morphology analysis. The results, interpretation and discussion of empirical data collected during fieldwork are presented thematically: Chapter 5 deals with the structure and sediment dynamics of Glacier de Tsanfleuron and presents the results of a three-dimensional numerical sediment transport model for Glacier de Tsanfleuron. Chapter 6 concerns the three-dimensional structural dynamics of Midre Lovénbreen, and the sedimentology of Midre Lovénbreen is the subject of Chapter 7. Chapter 8 synthesizes the main findings from the previous three chapters, discussing the influence of basal-thermal regime on glacier structure and landform genesis. Chapter 8 also gives a summary of the major research findings of this study and provides suggestions for future research.

Chapter 2

Glacial sediment transport: a review

2.1 Introduction

Sediment discharges in contemporary glaciers remain poorly quantified, which is in part attributable to the relative inaccessibility of the subglacial environment. If Alley et al.'s (1997) assertion that 'Most glacial sediment transport probably occurs subglacially' is correct, this presents both field researchers and modelers alike with a problem of unrepresentative sampling. Sediment transported in the comparatively accessible supraglacial zone have been documented to the same extent as sediment transported in the comparatively inaccessible subglacial zone. This relative lack of knowledge is reflected in the way that mechanisms of glacial erosion and transport have been well parameterized *a priori* (Fig. 2.1), but which have not been validated by empirical data. Characterisation and quantification of contemporary glacial sediments in transport is now required to address the conceptual and numerical models that have been developed over the past two decades or so. These data will help further our comprehension of entrainment and transport processes, which directly affect interpretations the geological record.

This review summarizes current concepts of glacial and glaciofluvial sediment transport mechanisms operating within small valley glaciers. The principal mechanisms governing these processes are explored to provide a framework for empirical data collection. Glacial sediment transport is presented within the context of different sediment entrainment mechanisms: incorporation into the snowpack (Section 2.2.1.1); crevasse-fill (Section 2.2.1.2); regelation across the glacier bed (Section 2.2.1.3); regelation into sediments at the bed (Section 2.2.1.4); entrainment of pre-existing ice (Section2.2.1.5); adfreezing by conductive cooling (Section 2.2.1.6); adfreezing by glaciohydraulic supercooling (Section 2.2.1.7); entrainment at sub-freezing temperatures (Section 2.2.1.8, and post-entrainment advection mechanism: ductile flow (Section 2.2.2.1) and basal mixing (Section 2.2.2.2).

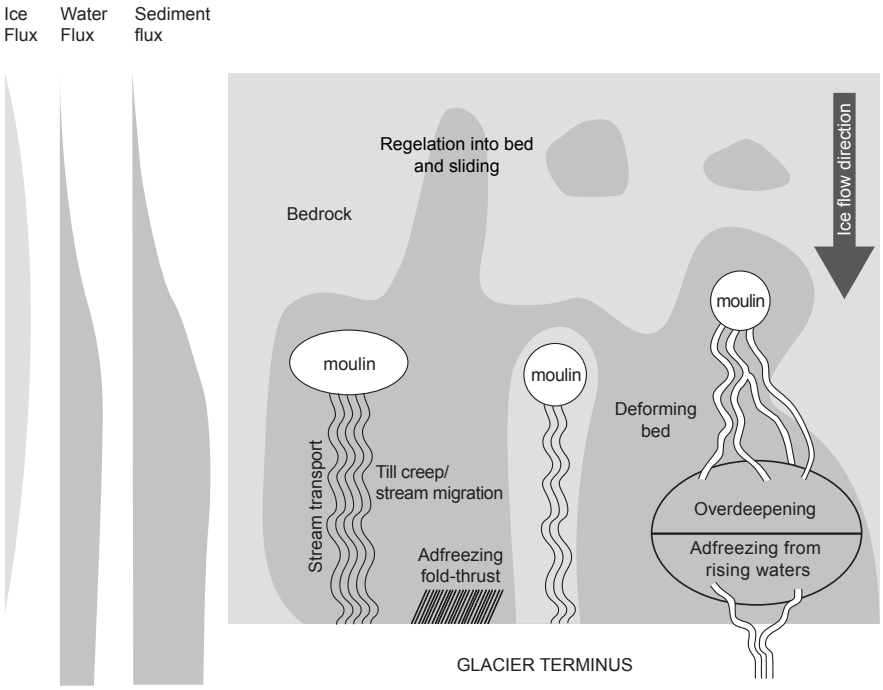

Figure 2.1: Schematic diagram of possible subglacial conditions - illustrating the interaction between subglacial sediment-transport mechanisms, total sediment discharge and proximity to the terminus. Sediment flux scales are logarithmic (from Alley et al., 1997; their Fig. 2).

2.2 Glacial sediment transport

Sediments transported by ice, i.e. glacial transport, are conventionally divided into three domains: supra-, en- and sub-glacial (Benn and Evans, 1998; Eyles and Rogerson, 1978b; Menzies, 2002). The position of sediments within a glacier reflects, to some extent, the processes associated with their entrainment and subsequent advection and modification. The distinction between supra-, en- and subglacial sediments thus forms a convenient point from which a more comprehensive classification of glacial sediment transport can be made. A number of different classification systems exist that have distinguished different ice facies on the basis of styles of sediment suspension, concentration and transport zones (englacial or basal)(e.g. Hubbard and Sharp, 1995a; Knight, 1987; Lawson, 1979). Lawson's (1979) classification consists of two types of englacial subfacies, 'diffuse' and 'banded', and two types of basal subfacies, 'dispersed' and 'stratified'. Following the modifications of Hunter et al. (1996) a further two subfacies were included: a 'solid' subfacies to the basal facies and a 'diffuse-stratified' subfacies to the englacial facies (Fig. 2.2; Table 2.1) .

While other classification systems treat basal ice facies in a great deal more detail (Hubbard et al., 2009; Hubbard and Sharp, 1995a; Knight, 1987), based on range of physical characteristics (e.g. isotopic composition, sediment concentration, bubble content and

Table 2.1: Lawson's (1979) classification of ice facies with modifications by Hunter et al. (1994) and Evenson et al. (1999)

Zone	*Facies*	*Sub-facies*	*Origin*
Supraglacial			surface phenomena
Englacial	diffused		surface firnification
		stratified	intense foliation
	banded		surface firnification
	vent	frazil	supercooling
		anchor	supercooling
Basal	dispersed		combined firnification and basal regelation
	stratified	discontinuous	basal regelation
		suspended	basal regelation
		solid	adfreezing

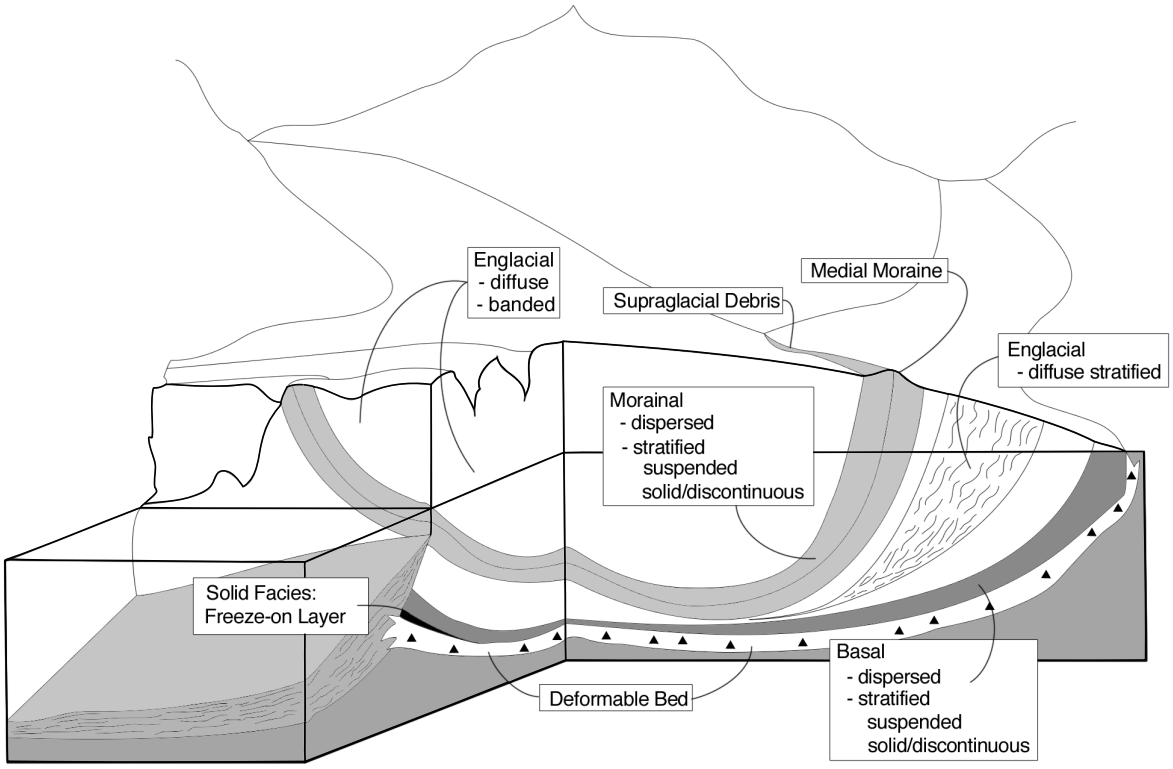

Figure 2.2: Generalised ice facies distribution within a warm-based valley glacier - from Hunter et al. (1996; their Fig. 5)

ice fabric), these are not necessarily any more useful for studies of glacier-wide sediment transport. Nonetheless, they are important to be aware of, in order to appreciate the complex nature of the subglacial domain where sediment transport is typically focused (Lawson et al., 1998).

2.2.1 Entrainment mechanisms

2.2.1.1 Incorporation into the snowpack

Primary stratification is the continuous planar layering of different ice types that reflect the initial composition of the snow pack, prior to the low-grade metamorphism of snow to glacier ice via firnification, i.e. regularly alternating layers of low-density wet snow ice, high-density superimposed ice, and discoloured fine-grained summer ice. The configuration of the snow pack at the end of the ablation season is reflected in the stratified structure of glacier ice (Wadham and Nuttall, 2002). The less dense, wet snow facies, throughout which melting has occurred, form coarse bubble-rich ice facies. Meltwater from wet snow facies percolates to the superimposed ice facies below, composed of lenses, pipes and ice layers; these form coarse-clear ice facies which are bubble-poor. The accumulation of snow in summer, in contrast, is characterized by high rates of ablation, forming discoloured fine-grained, bubble-rich ice facies (Hambrey et al., 2005).

The accumulation of snow on a glacier surface is usually accompanied by the incorporation of rockfall sediments into the snow pack. Successive accumulations of snow ultimately leads to the entrainment of supraglacial rockfall sediments into the ice mass. A knowledge of a glaciers mass balance Q_i and sediment input flux at the glacier surface provide a means by which the overall flux of supraglacial rockfall sediments Q_R can be calculated, so:

$$Q_r = \rho_r Q_i \tag{2.1}$$

where ρ_r is the mass of rockfall sediments per unit area. Rates of rockfall inputs into glacial systems have rarely been quantified, save for studies of specific high magnitude events (Chinn et al., 1992). Concerns over increasing rockfall activity in mountainous regions have prompted a more detail line of investigation into past and contemporary fluctuations (Harris, 2005; Jain et al., 2003; Krautblatter and Dikau, 2007; Perret et al., 2006), leading the way forward for an integrated approach to quantifying glacial sediment budgets.

If a constant rate of rockfall into the system is assumed, ρ_r will vary with precipitation inputs and net energy balance. Accordingly, the subsequent rate of supraglacial sediment transport will be dictated by ice velocities across the glacier, derived from empirical observations. Ice under stress exhibits complex responses governed by the balance between driving

forces, longitudinal stresses and coupling with the bed (Hubbard et al., 1998; Le Meur et al., 2004)(see Section 2.2.2.1).

2.2.1.2 Crevasse-fill

The formation of crevasses and their modification under different stress regimes can be understood roughly in terms of absolute stress values, although the microphysical processes involved lead to considerable complexities (Schulson, 2001). Nye (1952) presented a two dimensional flow model for fracturing at a glacier surface under different stress regimes (Fig. 2.3), which remains a highly relevant model to understanding the nature of ice flow dynamics.

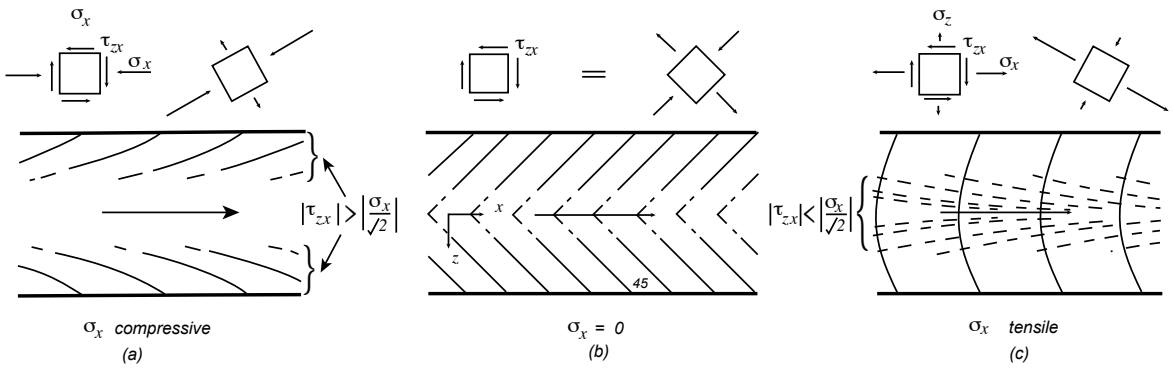

Figure 2.3: The formation of crevasses under different stress regimes - from Nye (1952; their Fig. 9)

Under longitudinally compressive stress (Fig. 2.3a) the direction of maximum tensile stress approaches a flow transverse orientation so marginal crevasses make angles $<45^{\circ}$ to the margin and the tendency for crevasses to form reaches zero in the centre. When laterally compressive stresses σ_x are equal to zero, one principal stress is tensile and the other is compressive (Fig. 2.3b), so tensile stresses decrease to zero at the centre. Under longitudinally tensile stress maximum tension becomes orientated towards the line of flow. Under conditions where σ_x is tensile and horizontal strain τ_{zx} is not too large (Fig. 2.3c), a central strip of crevasses forms, orientated transverse and subparallel to flow as well as in a set of random orientations. These conditions may characterise certain reaches of a straight valley glacier, but are also likely to exist across other areas of a the glacier as well, e.g. on the outside of a bend, at the widening of the valley, under convex bed conditions, under the overburden pressure of accumulation or vice versa.

Basal crevasses are considerably less common than surface crevasses due to the physical forces operating at the bed of a glacier. van der Veen (1998) identified that basal crevassing will only occur if basal water pressures are at or near ice overburden pressure.

High longitudinal stresses are required for appreciable bottom crevasses to form, usually manifested during surge conditions (Lawson et al., 1994) or above very rough subglacial topography (Stewart et al., 2004). From these conditions it can be deduced, that while basal crevassing may be commonly associated with tidewater glaciers (Mickelson and Berkson, 1974), basal crevassing in valley glaciers is only likely to occur under exceptional circumstances; where high basal water pressures exist within an overdeepening (Ensminger et al., 2001), during a jökulhlaup (Kozarski and Szupryczynski, 1973) or an active surge phase (Kamb et al., 1985; Lawson, 1996). The process of basal crevassing is likely to be further limited because it represents a negative feedback mechanism, reducing locally high basal water pressures and forcing glacial flow towards stability.

Research into critical strain rates of crevasse formation have been found to be highly variable (Hambrey and Müller, 1978); to date no consistent values for the tensile strength of ice have been obtained (Epifanov, 2004; Nath and Vaughan, 2003). Recent investigations into the microphysical processes involved in ice fracture have identified causes for discrepancies between empirically derived data (Schulson, 2001). Specifically: (i) ice fracture may occur at subcritical levels (Schulson, 2001; Weiss, 2004), (ii) cyclicity of tension-compression stress regimes increases the tensile strength of polycrystalline ice markedly (Cole, 2003), and (iii) in the presence of multiple crevasses, the stress intensity factor for any one crevasse is reduced (van der Veen, 1998).

Crevasses form points of potential sediment entrainment and transport, specifically rockfall and supraglacial glaciofluvial sediments, in the case of surface crevasses (Goodsell et al., 2005; Hambrey et al., 1999), and subglacial till and subglacial fluvial sediments in the context of basal crevasses (Ensminger et al., 2001; Sharp, 1985). While Nye's (1952) model oversimplifies these processes, it remain a good point of general reference and is highly applicable to a generalized sediment transport model. A knowledge of strain rates and stresses throughout the glacier can therefore be approximated by integration into a generalized glacier flow model (Hubbard et al., 1998). Crevasses may entrain sediments from a number of sources: (i) similar to the entrainment of sediments into the snow pack rockfall material may comprise a large proportion of crevasse-fill (Goodsell et al., 2002; Hambrey et al., 1999); (ii) crevasses may capture supraglacial meltwater streams and form points of fluvial sediment deposition (Goodsell et al., 2005), (iii) basal crevasses may entrain basal sediments by the squeezing of subglacial sediments into a sub-vertical position (Sharp, 1985; Small, 1987), and (iv) basal crevasses may entrain sediments transported by glaciofluvial discharges from artesian upwellings (Ensminger et al., 2001).

Crevasse-fill sediment discharges remain unquantified empirically predominantly due to access difficulties. The englacial orientation of crevasse-fill sediments also precludes the use of remote methods (e.g. ground penetrating radar or seismic sounding) because they tend

Table 2.2: Origins and sedimentological characteristics of transverse supraglacial moraine ridges (from Hubbard et al. 2004).

	Origin	*Sorting*	*Fabric*
Basal crevasse fill	Flow of turbid meltwater into basal crevasses	Very well sorted, unimodal silt-rich sediments, fining towards ice surface	Absent
Crevasse-squeeze	Injection of fluidized till into basal crevasses	Locally well sorted sediments, but generally multimodal poorly sorted with coarse clasts	Locally strong but heterogenous
Thrusts	Thrusting of basal ice facies along shear plane	Poorly sorted multimodal basal sediments with coarse clasts	Strongly unimodal aligned parallel to ridge orientation

to lie parallel to signal pulse direction. The majority of studies documenting crevasse-fill sediments have therefore focused on those exposed by ablation at the ice margin or within meltwater channels (Goodsell et al., 2002; Goodsell et al., 2005; Harris et al., 2004). An alternative means of quantification exists in the form of a crevasse component introduced into a numerical flow model with a supraglacial sediment input element. The volume of rockfall input I_r entrained in crevasses at point i on the glacier surface can be quantified as:

$$V_i^{cf} = I_r^i \frac{N_c^i}{A^i} \tag{2.2}$$

where N_c is the number of crevasses per unit area A.

The origin of planar sediment bands in glaciers has been the focus of a wide body of research (Glasser et al., 2003; Hambrey et al., 1999; Hubbard et al., 2004; Woodward et al., 2002). The processes involved in basal crevasse sedimentation have been commonly linked to turbid supercooled discharges (Ensminger et al., 2001)(Section 2.2.1.7) and the squeeze of subglacial sediments; representing the end members of a fluid-plastic flow continuum. Shearing mechanisms are the result of different set of flow conditions (Section 2.2.2.2) (Hambrey and Lawson, 2000), so distinction between these processes is therefore important. Differentiation can be made on the basis of isotopic signatures, clast shape, texture, roundness and sorting, and glacial flow regime (Hubbard et al., 2004) (Table 2.2).

2.2.1.3 Regelation across basal obstacles

The principles behind regelation melt were first identified by Faraday (cited in Thomson, 1860), who demonstrated that applying pressure to H_20 in the solid phase lowers the melting point. Although Faraday's initial inferences have been shown to be incorrect (Gilpin, 1980) and a fairly poor approximation of the subglacial environment (Dash et al., 1995) the principles involved were correct at the basic physical level.

These principles mean that regelation, via basal sliding across bedrock obstacles under warm ice, is limited by bedrock roughness R (where $R = L/\gamma$, L is the spacing between bedrock obstacles and γ is the spacing of bedrock obstacles). Due to the requirement for latent heat to be transferred through bedrock obstacles, regelation operates most effectively around bedrock obstacles at wavelengths of ∼0.01 m (Kamb and LaChapelle, 1964; Weertman, 1957). Thus under near laminar flow conditions, ice formed on the lee of one obstacle will be destroyed by melting at the stoss side of obstacles downstream (Hubbard and Sharp, 1993). Further refinements to the process have been proposed by Robin (1976) and Lliboutry (1993) to include the possibility of heat loss from an otherwise closed thermal system. This is likely to be manifested via the transport and refreezing of meltwater away from the bed via the intra-granular vein network (Lliboutry, 1993). Potentially up to 50% of basal meltwater could be lost to the intra-granular vein network (Goodman et al., 1979), leading to the development of cold patches on the stoss side of obstacles; a mechanism for small-scale basal adfreezing.

Refreezing of melt produced by regelation and adfreezing on the stoss side of bedrock obstacles clearly has the potential to entrain sediments at the bed. If regelation is linked to basal sliding under warm ice and is controlled by bedrock roughness R, basal shear stress τ_b and the physical and thermal properties of ice and the bedrock α_r (Weertman, 1957), the rate of regelation v_r (m a^{-1}) can be expressed by following relationship:

$$v_r = \alpha_r L^{-1} \left(\frac{\tau_b}{R^2} \right) \tag{2.3}$$

Although more realistic sliding models have been developed (e.g. Fowler, 1987; Gudmundsson, 1997; Hindmarsh, 2000; Lliboutry, 1975; Nye, 1970), observations of laminated basal ice facies have suggested that sediment entrainment via regelation is not a very effective process. Mean sediment concentrations in basal ice facies inferred to the product of regelation have been measured at ∼5% by volume (Hubbard, 1991; Kamb and LaChapelle, 1964). Measurements of bedrock roughness conducted on glacial forefields (Benoist, 1979; Nye, 1970) suggest that the maximum thickness of basal ice facies produced

by regelation alone would be of an order of 0.01 m (Nye, 1970; Hubbard, 1991). Calculations based on a numerical model by Lliboutry (1993) predicted a maximum thickness of 0.2 to 0.4 m, although this was thought to be an unreliable representation of basal conditions. A similar process has also been proposed by Knight (1987) as a mechanism for the formation of clotted ice facies above basal ice facies. Via this process, regelation would not necessary result in the formation of stratified basal ice facies.

Despite the limitations constraining the regelation process, observations of basal laminar facies up to 10 m in thickness at the base of some valley glaciers suggest that alternative entrainment mechanisms must account for their formation (Hubbard and Sharp, 1995a; Knight, 1987). Processes responsible for the formation of laminated and solid basal ice facies $>$0.1 m in thickness include: vertical regelation, apron incorporation, folding, shearing, ductile thickening and basal adfreezing by conductive cooling and supercooling. These processes are discussed in detail below (Sections 2.2.1.4; 2.2.1.5; 2.2.1.6; 2.2.1.7; 2.2.2.2).

2.2.1.4 Regelation into basal sediments

Regelation in the vertical plane is a mechanism via which basal sediments can be accreted under ice masses (Philip, 1980). Regelation in this plane may act as a powerful means of sediment entrainment in the context of large ice sheets (Alley et al., 1997; Christoffersen et al., 2006; Clarke, 2005; Iverson, 2000), but may equally be applicable under certain conditions to small valley glaciers. The process of vertical regelation is dependent upon; (i) the existence of basal ice at the melting point, (ii) establishment of a thermal gradient between basal sediments and (iii) the ice overburden pressure P_i being greater than water pressure in the basal sediment P_w (Iverson and Semmens, 1995). The rate of vertical regelation V_r (mm a^{-1}), into a subglacial sediment will be restricted to a range of physical conditions (Iverson and Semmens, 1995), which can be calculated by:

$$V_r = \frac{K_s(P_i - P_w)}{\rho_i g H_{si}} \tag{2.4}$$

where K_s is the apparent conductivity across the ice-sediment interface and H_{si} is the thickness of the ice saturated sediment layer (Iverson, 2000). Noting that effective pressure $P_e \approx P_i - P_w$, the infiltration rate becomes small at a low P_e as well as when H_{si} becomes large. Regelation will also be influenced by the rate of sliding as a consequence of the production of frictional heat, increasing basal melt rates and reducing P_e (Iverson, 2000). For a small valley glacier where $P_e = 50$ and basal melt rates are 10 mm a^{-1}, maximum thickness of the entrained sediment layer H_{max} will be 0.1 m (Alley et al., 1997).

Regelation will terminate when $H_{max} = H_{si}$, where the rate of regelation will be equal to the rate of basal melting. Subglacial effective pressures under warm-based valley glaciers are principally controlled by the configuration of the hydrological system and the rate of basal sliding (Hubbard et al., 1995b; Iken, 1981; Jansson, 1995). Iverson (2000) asserted that because P_e increases towards meltwater channels, so does the rate of sediment entrainment; larger effective channel pressures resulting in greater ice penetration depths into basal sediments. Estimates of the spatial distribution of sediment entrainment are therefore dependent upon the accurate prediction or prior knowledge of subglacial channel distribution and the calculation of sliding rates (Sharp et al., 1993; Walder and Hallet, 1978; Walder and Fowler, 1994).

Predictive models of regelation into subglacial sediments have been hampered by a lack of knowledge of microphysical processes at the ice-bed interface (Alley et al., 1997; Iverson and Semmens, 1995; Iverson, 2000). Christoffersen et al. (2006) asserted that overestimates of vertical regelation by theory (Iverson and Semmens, 1995) were the result of surface effects operating at the grain-scale for sediments where grain size $r < 0.016$ mm. Conjecture surrounds this point, whether smaller particles rejected are by a freezing front, or whether they act as flocculates. Observations of washed sediments at the ice-sediment interface has provided evidence that clays may be removed at the freezing front (Stone et al., 1997) and although the precise physics remain unknown, laboratory observations have also supported rejection processes (Hubbard, 1991). In any event, this process may not be relevant to warm-based valley glaciers with well developed hydrological systems, where fine sediments are readily transported away from the bed. The model of Christoffersen et al. (2006) represents an improvement over previous approaches to vertical sediment entrainment, in that it predicted the formation of different basal ice facies types under changing bed conditions. In this model, regelation was driven by congelation (the formation of clear congelation ice) and as a result, primarily controlled by the availability of water at the bed. The application of predictive regelation models to polythermal valley glaciers would represent a step up from one or two-dimensional models of sediment entrainment.

The relative contribution of regelation vectors, operating down and across the bed, are likely to be modulated by effective pressure at the bed, basal melting rates, heat fluxes at the ice-sediment interface and the delivery of water to the bed. The presence or absence of a subglacial basal sediment layer will further determine this. In generalized terms, higher rates of sliding will reduce vertical regelation as a result of the production of frictional heat, whist promoting regelation across the bed. Conversely under lower rates of basal melt, sliding is will be reduced and regelation into the bed will be enhanced. Alley et al. (1997) questioned whether regelation has the potential to contribute to rapid sediment flux

given these limiting factors, concluding that large-scale changes in ice flow may enhance regelation-derived sediment transport.

2.2.1.5 Entrainment of pre-existing ice

Glacier advance is likely to involve the contact of the advancing ice front with a considerable volume of proglacial snow, ice and sediment. Depending on thermal conditions of the ice mass and adjacent sediment, this may involve either the over-riding and incorporation of sediment into the base of the glacier, and/or the pushing of sediment in front of the advancing ice front (Benn and Evans, 1998). The over-riding and incorporation of unfrozen proglacial sediment by warm-based ice necessarily involves adfreezing processes and is covered in Sections 2.2.1.6 and 2.2.1.4. Glacially pushed sediment, i.e. glaciotectonism, is not considered within the scope of this review. The incorporation of frozen proglacial sediment into the base of an advancing polythermal or cold-based glacier is typical of regions under permafrost conditions, where ice covered by a thick mantle of debris is preserved following glacier retreat (Evans, 1989). The incorporation of 'dead' or buried ice by re-advancing glaciers has been observed at a number of cold-based and polythermal glaciers (Hooke, 1973; Evans, 1989). Aprons are accumulations of blocks of ice and sediment in front of the termini of advancing glaciers. The over riding and incorporation of these so-called aprons by glaciers has therefore been collectively termed 'apron incorporation'. Basal ice facies resulting from apron incorporation have been recognised at a range of glaciers, including Suess Glacier in Antarctica (Fitzsimons, 1997), Greenland (Knight, 1997) and Skalafellsjökull, Iceland (Sharp, 1984). In extreme cases individual ice or sediment blocks may be observed (Fitzsimons, 1997), but more generally incorporated aprons form alternating layers of sediment-rich and ice-rich folia, formed by the gradual attenuation of sediment and ice under high cumulative stress. The re-advance of ice masses over fluvial, aeolian and marine deposits has been invoked in a number of cases to account for observations of non-glacigenic sediment facies in englacial and supraglacial positions (Fitzsimons, 1997; Evans, 1989). Post-entrainment mixing and advection of these incorporated ice and sediment layers is considered in further detail in Section 2.2.2.2.

2.2.1.6 Adfreezing by conductive cooling

Net adfreezing involves the migration of a 0°C isotherm into subglacial sediments, leading to the formation of solid basal facies (Hubbard and Sharp, 1993). Records of preserved fluvial sediments within marginal subglacial facies strongly support this mechanism, particularly at the margins of polythermal and cold-based glaciers where lateral and/or vertical temperature gradients between the surface and the bed may be very high (Boulton, 1970; Fitzsimons,

1997; Menzies, 1981). Alley et al. (1997) asserted that large-scale changes in climatic conditions (a reduction in temperature of 20°C) could lead to the adfreezing of sediments onto the base of a glacier or ice sheet. Temperature changes of this order of magnitude are improbable in a modern context; adfreezing will therefore be discussed in the context of seasonal temperature fluctuations and changes in ice thickness.

Weertman (1961) argued that contrasts in thermal conditions at a glacier scale may be responsible for widespread adfreezing, rather than climatic changes. Thick ice over the centre of an ice mass insulates the bed from cold surface air temperatures, therefore maintaining melt conditions, leaving the cold periphery frozen to the bed. Water produced at the central region flows to the frozen periphery, leading to the net adfreezing of sediment towards the margin (Weertman, 1961). Rapid adfreezing may occur when a cold wave penetrates to the bed, e.g. at the relatively thin margins of a valley glacier (H <200 m) or during the surge phase of a surge-type glacier (Alley et al., 1997). Cuffey et al. (1995) calculated from first principles the rate of adfreezing F (mm a^{-1}) for any given change in air surface temperature ΔT:

$$F = \frac{\kappa}{\rho L}\Theta \approx 0.22\Theta \tag{2.5}$$

where ρL is the volumetric heat of fusion and κ is the thermal conductivity of ice. Θ is the product of an advection parameter $P\alpha$ (1 if advection is weak, 2 if advection is strong) and the temperature gradient ΔT over the ice thickness H. Based on equation (2.5), when H <100 m at the margins of valley glaciers, adfreezing could occur at a rate of 410 mm a^{-1}, given a surface air temperature drop of 2°C. Cold wave penetrating from the ice surface could be further enhanced by the presence subglacial conduits and crevasses (Anderson et al., 1982; Sugden and John, 1976; Vivian and Bocquet, 1973), although this is only likely to occur in the absence of snow fall. Zones of adfreezing are likely to be spatially restricted, dependent on a set of highly irregular and fluctuating basal conditions, controlled by areas of basal sliding, meltwater production and the subglacial drainage network.

Under surge conditions a rapid increase in thermal gradient, caused by ice thinning, could facilitate high rates of adfreezing (Alley et al., 1997). Following the active surge phase the termination of basal sliding and basal melt would rapidly reduce the thermal heat flux at the bed, enabling a cold surface wave to penetrate into subglacial sediments. Adfreezing rates of high magnitude have been invoked to account for the large volumes of sediment associated with Heinrich events in the North Atlantic (MacAyeal, 1993; Alley and MacAyeal, 1994; Alley et al., 2003).

The above theoretical calculations of adfreezing rates have been difficult to test. The work of Christoffersen and Tulaczyk (2003b) has identified that conditions under the Ross Ice Stream can be modeled using principles adopted from frost-heave mechanics. In this study the rate of adfreezing for different sediment grain sizes and variations in water supply were calculated. The extent of the applicability of these conditions to areas underneath warm-based and polythermal ice masses is unknown at present; experiments have suggested that water supply acts as a limiting factor on adfreezing at ice margins and in warm-based ice (Hubbard, 1991; Souchez et al., 2004). Further concerns regarding the adfreezing process have focused on its overall efficacy. Alley et al. (1997) contended that while low levels of thermal flux in an absence of sliding would promote entrainment, this would limit sediment transport. Conversely the reverse situation is also likely to apply; under rapid sliding adfreezing will not occur. The impact of these limitations are most apparent at the ice margin where adfreezing may be most pronounced. Unless a glacier is advancing, sediment entrained is unlikely to be transported a great distance. In these cases basal facies thickening is more likely to play an active role in sediment transport (Section 2.2.2.2).

2.2.1.7 Adfreezing by glaciohydraulic supercooling

The supercooling of water involves its temperature reduction to a level below its theoretical freezing point for any given pressure. The process is widely documented in a number of fields; in glaciology resulting from the relative configuration of ice surface and subglacial topographies (Cook et al., 2006). The theoretical principles underlying supercooling thermodynamics are well established (Röthlisberger, 1968; Röthlisberger, 1973; Hooke, 1991). Water must undergo a change in pressure which is sufficiently rapid that the rate of energy release is too slow to allow the freezing process to take place. For a subglacial channel flowing up a reverse bedrock slope, where subglacial water pressure p_w is approximately equal to ice overburden pressure p_i, this condition is satisfied when the ratio of the bedrock slope to the ice surface slope reaches a critical value. This can be defined as:

$$\frac{\delta Z_B}{\delta s} = -\frac{(1-\rho_w c_w C_T)\rho_i}{rho_w - (1-\rho_w c_w C_T)\rho_i}\frac{\delta Z_S}{\delta s} \tag{2.6}$$

where Z_B is the height of bed, Z_S is the height of the ice surface, s is slope, ρ_w and ρ_i are the densities of water and ice respectively, C_w is the specific heat capacity of water and C_T is the Clapeyron slope. Depending upon the values of C_T (which change with the air saturation state of water (Röthlisberger, 1968), Equation (2.6) yields a critical ratio in the

range of 1.2 to 1.7, i.e. the bed slope must be 1.2 to 1.7 times steeper than the inverse of the ice surface slope.

Empirical evidence of glaciohydraulic supercooling are relatively sparse (Hooke and Pohjola, 1994; Lawson et al., 1998). Fieldwork undertaken at Matanuska Glacier, USA, over the past thirty years has led to the identification of a number of essential parameters, critical for supercooling to take place (e.g. Ensminger et al., 2001; Lawson et al., 1998). Glaciohydraulic supercooling has been inferred from wide variety of glaciological and sedimentological phenomena (Knudsen et al., 2001; Roberts et al., 2002). Cook et al. (2006) have asserted that the only unequivocal evidence for glaciohydraulic supercooling is the discharge of meltwaters displaying the following characteristics: (i) water temperatures consistently $<0^{\circ}$C surrounded by ambient air temperatures $>0^{\circ}$C; (ii) the formation of frazil ice crystals and flocs within the discharge, and (iii) the growth of anchor ice terraces around discharge vents. However, evidence of supercooling does not necessarily confirm that basal sediments were entrained by the same process.

The formation of frazil ice crystals and flocs within supercooled meltwater leads to the entrainment of suspended sediments as they become trapped within the forming ice crystal matrix (Creyts and Clarke, 2005; Lawson et al., 1998). Sediment entrainment via this mechanism is believed to account for a high proportion of basal ice facies in glaciers which experience supercooling (Alley et al., 1998). Lawson et al. (1998) argued that the formation of sediment-rich stratified basal ice facies by supercooling occurs within hydraulically inefficient glaciofluvial systems with high residence times. Basal ice inferred to have formed by supercooling may form sequences 810 m thick, accreting at rates potentially >0.1 m a^{-1} (Lawson et al., 1998). In addition to basal accretion, supercooled water may rise upwards though basal crevasses (Ensminger et al., 2001). Turbid supercooled discharges, when ascending through basal crevasses, on freezing may form laterally extensive, planar bands of laminated sediment-rich ice facies, although many of these may terminate as blind crevasses in an englacial position (Lawson, unpublished, cited in Ensminger et al., 2001). These sequences consist of complex and highly variable laminae and are potentially difficult to distinguish from ice facies formed by other glacial processes. The sedimentological characteristics of these sequences are presented alongside glacial sediment facies produced by other entrainment mechanisms (Section 2.2.1.2) (Table 2.2).

As ice anneals within a subglacial drainage system, discharges will reduce and the system may eventually shut down, forcing basal waters to flow through either an englacial channel or vein network (Alley et al., 1998; Hooke and Pohjola, 1994). It has been argued that this process, by causing entrainment on the downglacier side of overdeepenings, is self limiting and may therefore be very common features of subglacial topography (Alley et al., 2003). Under steady-state or retreating regimes, entrainment by this mechanism will

limit the development of overdeepenings, by reducing the angle of the adverse bed slope. Conversely, under advancing glacial regimes this process may constitute a positive feedback loop, whereby sediments are continuously transported away from the site of entrainment (Hooke, 1991; Anderson et al., 2006). Intense crevassing caused by steep bedrock topography at overdeepenings enhances meltwater delivery to the bed, facilitating further quarrying and abrasion and thus sediment entrainment (Hooke, 1991). These processes are widely considered to lead to the progressive enhancement of glacial overdeepenings, but are supported by very limited empirical data. Thus the concept that subglacial sediment accretion via supercooling could be responsible for rapid and widespread sediment entrainment has been favored in palaeoglaciological settings. This has particularly been the case where large-scale net adfreezing due to conductive cooling has been considered unlikely due to physical limitations acting on the process (Alley et al., 2003; Roberts et al., 2001) (Section 2.2.1.6).

2.2.1.8 Entrainment at sub-freezing temperatures

Following the theoretical work of Shreve (1984), who considered Gilpin's (1979) laboratory experiments in a broader theoretical context, and the more recent work of Dash et al. (1995) and Rempel et al. (2004), it has been concluded that water may be present at grain boundaries and triple junctions at temperatures as low as 30°C. The implications of this are: (i) that sliding can occur under cold-based glaciers (Echelmeyer and Zhongxiang, 1987); (ii) that entrainment mechanisms may operate in areas of no net melt (Shreve, 1984), and (iii) that cold-based glaciers may be capable of eroding their beds (Atkins et al., 2002). In addition to the laboratory-based observations, empirical evidence of these processes taking place under cold-based glaciers have been presented by Cuffey et al. (2000), Holdsworth and Bull (1970) and Tison et al. (1993). Although evidence for large-scale sediment entrainment at subfreezing temperatures is mounting (Kleman, 2007), the precise mechanics remain largely speculative, suffice it to say that rates of sediment entrainment and transport are likely to be low relative to warm-bedded glaciers (Cuffey et al., 2000).

Tison et al. (1993) considered that entrainment of clay to sand sized particles could occur along an active shear zone under strong longitudinally compressive stress. Detailed strain measurements carried out by Echelmeyer and Zhongxiang (1987) have quantified this process occurring beneath Urumqi Glacier No. 1, China. Tison et al. (1993) suggested that the rotation of ice crystals, in contact with sediments at the bed under simple shear, caused them to become coated with a thin layer of fine sediments. Cuffey et al. (2000) argued that isotopic and gas data collected implied that this mechanism involved the net melt of water and hence could not occur at subfreezing temperatures.

Alternatively, Sugden and John (1976) suggested that regelation may occur under cold-based glaciers. Although the physical processes involved are likely to differ considerably from the pressure-melt cycle presented above (Section 2.2.1.3), the production of water near the bed may facilitate both sliding and entrainment. Water production is enabled by forces operating at the interface between sediment particles and ice crystals (Dash et al., 1995). The disjoining of the two surfaces results predominantly from van der Waals forces at the atom-scale; the volume of water produced is dependent upon particle size, solute concentration and temperature (Clarke, 2005). The confinement of water to grain boundaries and veins, and hence sediment transport pathways, is likely to account for the highly restricted grain-size distributions that have been observed in amber basal ice facies, typically ranging from 1.5 to 0.2 mm (Fitzsimons et al., 1999).

The rate of sediment discharge via entrainment under subfreezing glaciers is likely to be very low. Cuffey et al. (2000) calculated that sediment fluxes at Meserve Glacier, Antarctica, ranged from 10 to 30 m^3 yr^{-1}, equivalent to erosion rates of 9 x 10^{-7} to 3 x 10^{-6} m yr^{-1}. The physical limitations under which these entrainment processes operate suggest that they are unlikely to make a serious contribution to sediment discharges under partially cold-based glaciers.

2.2.2 Advection mechanisms

2.2.2.1 Ductile deformation

The ductile deformation of ice due to gravity is the dominant process by which ice flows from the the accumulation zone in the upper catchment to the ablation zone (Fig. 2.4).

A knowledge of the mechanisms of ice deformation under different stress regimes is instrumental in understanding the nature of glacial sediment entrainment and the changes entrained sediments undergo during transport. Englacial sediment concentrations are typically low (<40% by volume), so it can be assumed that flow is dominated by the physical properties of ice, rather than grain-grain interactions (Jacka et al., 2003; Nickling and Bennett, 1984). The stress fields operating throughout an ice mass can most readily be appreciated through the deformation of primary stratification (Section 2.2.1.1) and formation of foliation. Foliation describes the planar fabric of ice, defined by differences in the small-scale textural and crystallographic characteristics of ice crystals between homogenous layers (Passchier and Trouw, 2005). Foliation is found on almost all glaciers, comprising discontinuous layers of coarse bubble-rich, coarse clear and fine bubble-rich ice, originally described by Allen et al. (1960). Foliation can form parallel (longitudinal foliation) or normal to flow (transverse or arcuate foliation) over a wide range of scales and is observable at wavelengths

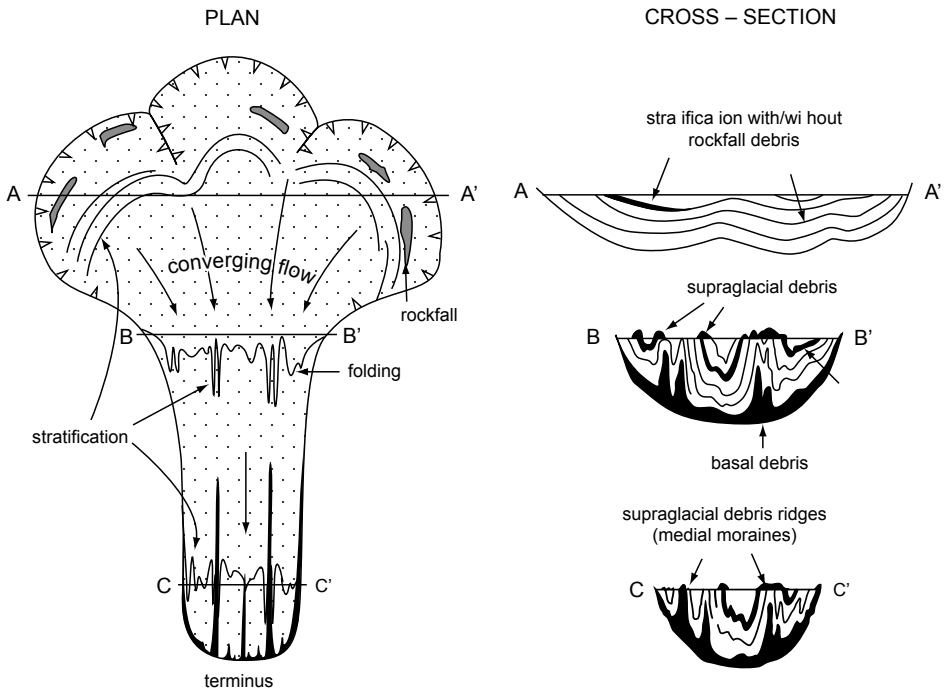

Figure 2.4: Schematic diagram of sediment transport in small valley glaciers originating from composite cirque basins - the diagram illustrates the progressive downglacier large-scale lateral folding of primary stratification, including debris layers, into increasingly vertically orientated planes and isoclinal folds (From Hambrey et al., 1999; their Fig. 15).

ranging from 10^{-3} to 10^{3} m (Hambrey and Dowdeswell, 1994; Lawson, 1996; Ximenis et al., 2000).

At the glacier-scale three distinct stress regimes are observable: (i) vertical loading produces pure shear dominating the upper reaches of a glacier; (ii) a convergent regime as ice flows into the main body, where longitudinal stresses produce progressive uniaxial tension or pure shear in tension, and (iii) a parallel or divergent flow regime towards the terminus, as ice undergoes progressive uniaxial compression or pure shear (Hooke and Hudleston, 1978). In contrast, simple shear dominates the flow of marginal and basal ice. Development of preferential ice fabrics leads to the concentration of strain in thin layers less resistant to glide (Wilson and Marmo, 1999). Rockfall onto the glacier surface has the potential to reach the bed, as ice forming in the accumulation area follows a progressively deeper flow pathway. Below the equilibrium line ice-flow pathways become progressively shallower, elevating sediments towards the ice surface.

The precise origins of foliation are a point of much contention. It is evident that longitudinal foliation can in some cases be inherited from primary stratification, in both pure and simple shear regimes (Hambrey and Lawson, 2000). The development of longitudinal foliation from the folding of primary stratification principally occurs at the glacier margin,

or at the confluence of two flow units where ice flows from a wide accumulation basin into a narrow tongue (Hambrey et al., 1980). The ductile shear of primary stratification occurs under laterally compressive stress and longitudinally extensive stress; manifested as a result in both horizontal and vertical planes (Hambrey et al., 1999; Herbst and Neubauer, 2000). Transverse foliation develops predominantly from crevasse traces, becoming progressively more arcuate downglacier under coaxial shear at the centre of flow units and non-coaxial shear at the margins. This type of foliation can also be inherited from transverse folds associated with thrust faults (Section 2.2.2.2). The development of transverse foliation occurs normal to the maximum compressive strain rate so these structures intensify as longitudinal compression increases, e.g. at the base of an icefall or at a glacier terminus. Foliation has also been observed in an axial planar relationship with primary structures (Hambrey et al., 1999), resembling the folding cleavage relationships observable in low-grade metamorphic rocks.

The influence of these stress regimes is apparent on the transport pathways of entrained rockfall sediments and, to a lesser extent, those entrained at the bed. Passive transportation of structures into new stress regimes however, means that the configuration of foliation and transported sediments may not reflect the stresses at any one point; rather the product of a cumulative strain history (Hambrey and Müller, 1978). In order to explain fully the relationship between cumulative strain, structural evolution and the resultant transport of sediments, strain ellipsoids should be represented in three dimensions (e.g. Goodsell et al., 2005). Such techniques require either extensive empirical data or well parameterized numerical modelling (Hubbard, 2000), although in many cases a two-dimensional approximation may be sufficient to represent the majority of the deformation and strain field (Milnes and Hambrey, 1976).

Glacial sediment flux as a result of ductile flow is spatially heterogeneous and has been presented in three dimensions by (Hambrey and Glasser, 2003, their Fig. 10) (Fig. 2.4). Laterally and vertically, supra-, en- and subglacial sediments become sheared and folded into increasingly linear bands parallel to flow, expressed at the ice surface as medial moraines. This results from: (i) intense shear at the margins of flow units; (ii) laterally compressive stresses acting across a narrowing and deepening ice mass, and (iii) the preferential accumulation of rockfall sediments at the head flow unit boundaries.

2.2.2.2 Basal mixing

Basal ice facies may be advected through a glacier by a range of mechanisms, processes collectively termed mixing. Mixing may occur as a result of shearing, folding and ductile thickening. These mechanisms operate across a range of spatial scales and are responsible for the formation of glacier-wide thrust faults at the medium-scale (Alley, 1989; Hambrey

and Lawson, 2000; Nye, 1951), the thickening of basal ice layers >10 m thick at the small-scale (Knight, 1995; Weertman, 1961), and the intercalation of different basal ice facies types (Hudleston, 1977; Rea et al., 2004).

Shearing results from the brittle failure of ice under compressive stress (Schulson, 2001). Compressive brittle failure occurs from the grain-scale and upwards; observable at the glacier-scale in the formation of thrust or shear-planes; upglacier dipping shear or fracture planes (Hambrey and Lawson, 2000) (Fig. 2.3), or at the small-scale as layers of stacked basal ice facies (Hudleston, 1977). It has been anticipated that the presence of strongly developed fabrics within an ice mass, the existence of healed fractures and presence of bedrock obstacles normal to flow are likely to promote brittle failure (Nye, 1951; Weiss and Schulson, 1995). This behaviour results from the slip/stick motion of post-terminal ice deformation (i.e. following failure) under compressive stresses, occurring at loads lower than the terminal failure load of undeformed ice (Schulson, 1990). This means that the presence of planes of structural weakness within an ice mass (e.g. crevasse traces, transverse foliation or fold axes) preferentially enable shearing. Differential strain at glacier beds causes planes of structural weakness to become progressively rotated upglacier, reaching near horizontal orientations close to the terminus (Hambrey and Müller, 1978; Hooke and Hudleston, 1978). Shearing therefore occurs under regimes of longitudinal compressional flow, along planes of weakness within the glacier, forcing upglacier units of ice to override downglacier ice units (Souchez, 1967).

Röthlisberger (in Weertman, 1961) asserted that a single sediment layer could become highly folded over a period of time, at amplitude scales of 10^1 to 10^4 m. Folding may be initiated by a variety of mechanisms: (i) contrasts in ice viscosity resulting from dynamic recrystallisation, strain softening, the presence of sediment-rich ice or the presence of water and ionic solids at grain junctions and boundaries (Nakamura and Jones, 1970; Obbard et al., 2003; Wilson and Marmo, 1999); (ii) spatial variations in flow velocities between adjacent basal ice layers (Hooke, 1973; Hudleston, 1977), and (iii) roughness elements at the glacier bed (Hudleston, 1977). Small-scale folding at the bed will result in the mixing of juxtaposed ice facies, elevating them away from the bed and forming the characteristic stacked profile observed in many basal ice sequences (e.g. Rea et al., 2004; Tison and Hubbard, 2000).

Pure shear of basal ice layers under compressive stress may result in the thickening of facies units by ductile flow. The extent to which this mechanism contributes to the advection of basal ice facies is uncertain. Field observations have suggested that ductile thickening is most likely to occur as a result of competence contrast between sediment-rich ice and sediment-poor ice at low strain rates, when stresses are lower than critical thresholds of brittle failure (Schulson, 2001; Waller et al., 2000). The physical conditions under which

ductile thickening operates are likely to be spatially restricted, but will preferentially occur where basal ice has a higher viscosity. Modeled flow of basal ice layers have implied that viscosities in the basal ice layer may be nearly an order of magnitude greater than that of englacial glacier ice (Hubbard et al., 2003). However, subcritical brittle failure mechanisms further suggest that shearing may occur preferentially under the majority of compressive stress regimes (Schulson, 2001), although both ductile flow and brittle failure most probably operate in tandem.

The physical conditions outlined above indicate that small-scale to glacier-wide shearing and folding are most likely to occur where contrasts in velocity are high and high deviatoric (especially longitudinally compressive) stresses are present. Well developed thrust faults are particularly prevalent at the margins of polythermal glaciers (Hambrey et al., 1996). Typically the terminal and marginal zones of polythermal glaciers are frozen to the bed, creating an obstructing that warm-based interior ice overrides. In the case of surge-type polythermal glaciers during an active surge phase, longitudinal stresses experienced at the surge front may be very high (Kamb et al., 1985; Lawson, 1996; Lawson et al., 1994). Inactive thrusts in non-surge-type polythermal glaciers have been suggested to reflect the configuration of the glacier during a period when the glacier had been surge-type (Hambrey et al., 2005). High longitudinal compressional stresses, resulting from by changes in bed topography, may be sufficient to cause the formation of thrust faults and folds in warm-based glaciers (Nye, 1951), e.g. at the base of an icefall or at a reverse bedrock slope (Chamberlin, 1928; Goodsell et al., 2002; Kamb and LaChapelle, 1968; Lliboutry, 2002), or the presence of stagnant ice at a terminus during periods of negative mass balance (Herbst et al., 2006). At the small-scale, high tensional and compressive stresses may be further enhanced by the development of cold patches at the bed as a result of regelation (Robin, 1976). The overall intensity of basal mixing processes at warm-based glaciers, however, is liable to be orders of magnitude lower than those processes operating at polythermal glaciers, predominantly because the frictional heat produced by basal sliding pervades across the majority of the glacier bed, not only removing basal ice facies already formed, but also reducing the likelihood of basal mixing occurring.

The importance of thrust faults and folds to glacial sediment budgets relates to whether the upward advection of sediments to the surface of the glacier influences the overall rate of sediment transport. Shearing in warm-based glaciers has never been explicitly associated with sediment transport, at the small-scale in the stacking of basal ice facies, or at the glacier-scale. The fundamental importance of shearing to glacial sediment budgets is in the context of frozen ice margins. Shearing has only ever been quantified by pioneering glaciologist RT Chamberlin (1928). Rates of displacement across thrust faults are unknown

at present, so it remains to quantify sediment transport by this mechanism in tandem with records of fluvial sediment discharges at a polythermal glacier.

It is proposed here that glacier-wide shearing and to a certain extent folding, is likely to play an important role in the glacial sediment budget of polythermal glaciers, primarily because of the selectivity of glaciofluvial discharges in polythermal glaciers (Pearce et al., 2003). Sediment-rich basal ice facies transported towards a glacier surface comprise a wider range of sediment grain-sizes (Table 2.2), suggesting that there will be a marked change in sediment discharge, depending on the relative contribution of the two processes.

2.3 Conclusions

Current concepts of glacial sediment transport mechanisms operating within small valley glaciers have been reviewed above. The relative importance of sediment entrainment and structural deformation processes is largely dictated by basal-thermal regime, which therefore has a controlling influence on the composition of glacigenic sediment-landform-assemblages. While these processes are well known *a priori*, support for conceptual models of glacial sediment transport in the form of reliable empirical data are lacking and many remain vehemently contested.

To assess and refine existing conceptual model of sediment transport within glacierized catchments and address the aims of this study (outlined in Section 1.2), within the process-based framework established by the this review, this study develops and applies a series of new and existing techniques to the fields of structural glaciology and sedimentology (Chapter 3, Chapter 4). Structural mapping, sedimentological analyses and first-order calculations of glacial sediment discharge provide insights into the nature and intensity of sediment transport processes operating at two small valley glaciers of contrasting basal thermal regime: Glacier de Tsanfleuron and Midre Lovénbreen (warm-based and polythermal glaciers respectively).

Chapter 3

Methods

3.1 Introduction

This chapter summarises the methods used: (i) during fieldwork campaigns at Glacier de Tsanfleuron, Switzerland and Midre Lovénbreen, Svalbard, (ii) to analyse sediment samples collected, and (iii) to calculate glacial sediment discharges at Glacier de Tsanfleuron. Field mapping of structure at both glaciers (Section 3.2.1.2) was preceded by mapping from aerial photographs (Section 3.2.1.1). Mapping internal glacier structure was performed using an optical televiewer in ice for the first time (Section 3.2.2), initially for testing at Glacier de Tsanfleuron (Hubbard et al., 2008), and secondly at Midre Lovénbreen to map internal glacier structure in three dimensions using a multiple-borehole array (Section 3.2.2.1). Sediments sampled at both glaciers included a sample of fine matrix sediments ($\leq$ 2 mm) and coarse particles ($\geq$ 200 mm). Analysis of the fine samples is detailed in Section 3.3.1, while morphological analysis is described in Chapter 4 as part of a self-contained methodological investigation. The statistical methods used to analyse sediments samples include: standard descriptive statistics (Section 3.3.2.1), $\cos\theta$ analysis, Gaussian component analysis (Section 3.3.2.2) and fractal analysis (Section 3.3.2.3). modelling of glacial sediment discharges (Section 3.4) briefly describes the finite-difference model used in this study and modifications to it (Section 3.4.1), and also includes descriptions of surface velocity measurements made at Glacier de Tsanfleuron used to refine the model. Finally, details of the calculations made to derive first-order estimates of glacial sediment discharge are given in Section 3.4.5.

3.2 Glacier structure

3.2.1 Surface structure mapping

3.2.1.1 Aerial photography

Surface structures at Glacier de Tsanfleuron were mapped using 1998 aerial photography. Aerial photographs were georectified in ENVI 4.2 to a WGS84 geoid and a UTM grid using a 1:25000 topographic map provided by SwissTopo. Vector drawing tools were used in ArcMap 9.0 to map the surface features identified. A preliminary structural interpretation was made: S_0 primary stratification; S_1 longitudinal foliation; S_2 fractures; S_3 shear planes. Surface structures were mapped at Midre Lovénbreen from high resolution 2004 aerial photography, 2004 CASI data and 2005 Lidar data, provided by NEODC. Vector drawing tools were used to map the surface features identified and a preliminary interpretation was made. Structural elements are classified and coded according to standard convention, with stratification being labelled from S_0 upwards and folds being labelled from F_1 upwards (Hambrey and Lawson, 2000).

3.2.1.2 Ground-based mapping

Transects across the surface of both Glacier de Tsanfleuron and Midre Lovénbreen were taken to map the orientation and dip of planar structures, fractures and folds. The location of the start and end of each transect at both glaciers was recorded using a Garmin eTrex handheld GPS (accurate to $\pm$15 m). Distances along transects was paced and the position of structures sampled were recorded relative to the transect start point. Structures were recorded according to as many of the following as possible: dip, direction of dip, orientation, width, length, depth, sediment content, ice crystal size, colour and microfabric. The orientation of structures was measured using a compass and their length was measured using a tape measure or paced. The dip of planar structures was measured with a compass-clinometer (accurate to $\pm1^\circ$), using an ice pick to excavate along the plane and then aligning the shaft of the ice-axe along the plane.

3.2.2 Optical televiewing

An optical televiewer (OPTV) is a borehole camera system with the capacity to provide a complete and continuous, orientated 360° true colour, optical image of the wall of a water-filled or air-filled borehole. The probe is 2.03 m long, 50 mm diameter and is manufactured and marketed by Robertson Geologging Ltd., UK. A 360° annular image is acquired by via the projection of the adjacent borehole wall by a hyperboloidal mirror onto a probe-aligned

768 x 494 element CCD sensor. The borehole wall is illuminated by a circular array of white LEDs mounted in the probe head directly adjacent to the mirror. The voltage supplied to these LEDs can be controlled from the surface in order to optimize their luminosity and the exposure of the borehole wall. The instrument is raised or lowered along the borehole by a winch, which, along with the OPTV probe, relays dip, azimuth and image data back to a data-logger (RG USB Micrologger 2) located at the ice surface (Fig. 3.1a).

Depth is measured by a potentiometer attached to the cablehead (Fig. 3.1a). These data allow the image acquired to be orientated in three-dimensional space. Azimuth and dip are provided by a triaxial magnetometer and three accelerometers mounted within the probe. The logger transfers probe and winch data to a surface computer which is also used to optimize probe settings in real time. These settings include LED illumination and selection of which pixel row is recorded from a broad annulus reflected by the hyperboloidal mirror (Fig. 3.1b). Precise winch control allows the sensor to acquire image data at a vertical resolution of 1 mm (requiring probe transit speeds of probe transit speeds of $\leq$1 m per minute) and a horizontal resolution of 720 pixels per row. This equates to a horizontal pixel size of $\backsim$0.8 mm in a borehole of diameter 180 mm, typical of large-scale ice coring programmes. Optimum logging at a rate of 1 m min^{-1} can be achieved at a horizontal resolution of 360 pixels per row.

3.2.2.1 Hot-water drilling

Eight boreholes were hot-water drilled only at Midre Lovénbreen using a Kärcher pressure washer HDS1000DE (Fig. 3.2) following methods detailed in (Hubbard and Glasser, 2005, p.116). The borehole sites were sited near a flow unit boundary, in an attempt to characterise the complex ice structure in that region. The stakes also follow a line of mass balance stakes monitored by Norsk Polarinstitut, as well as a ground-penetrating radar survey line taken earlier in the season by Tavi Murray (Murray, pers. comm.). In order to avoid small-scale bends in the borehole, past which the 2050 x 51 mm OPTV sonde would not pass, a particularly long ($\sim$3 m) drill stem was used. While this had the desired effect of smoothing out small-scale bends in the boreholes, it did result in holes that dipped at increasingly shallow angles ($\leq$45°) with depth at a uniform azimuth. Borehole spacing was 180 m at the upper drill site (two boreholes) and 20 to 30 m at the lower drill site (four boreholes) (Fig. 3.2). Repeat OPTV logging recorded a total of ten borehole logs from the six boreholes drilled (four logs were carried out in both the down and the up directions, revealing no notable difference), with a cumulative length of 690 m. The position of each borehole in Cartesian coordinates (x, y, z) at the glacier surface was measured using a Garmin GPSMap 60CSx (accurate to $\pm$10 m).

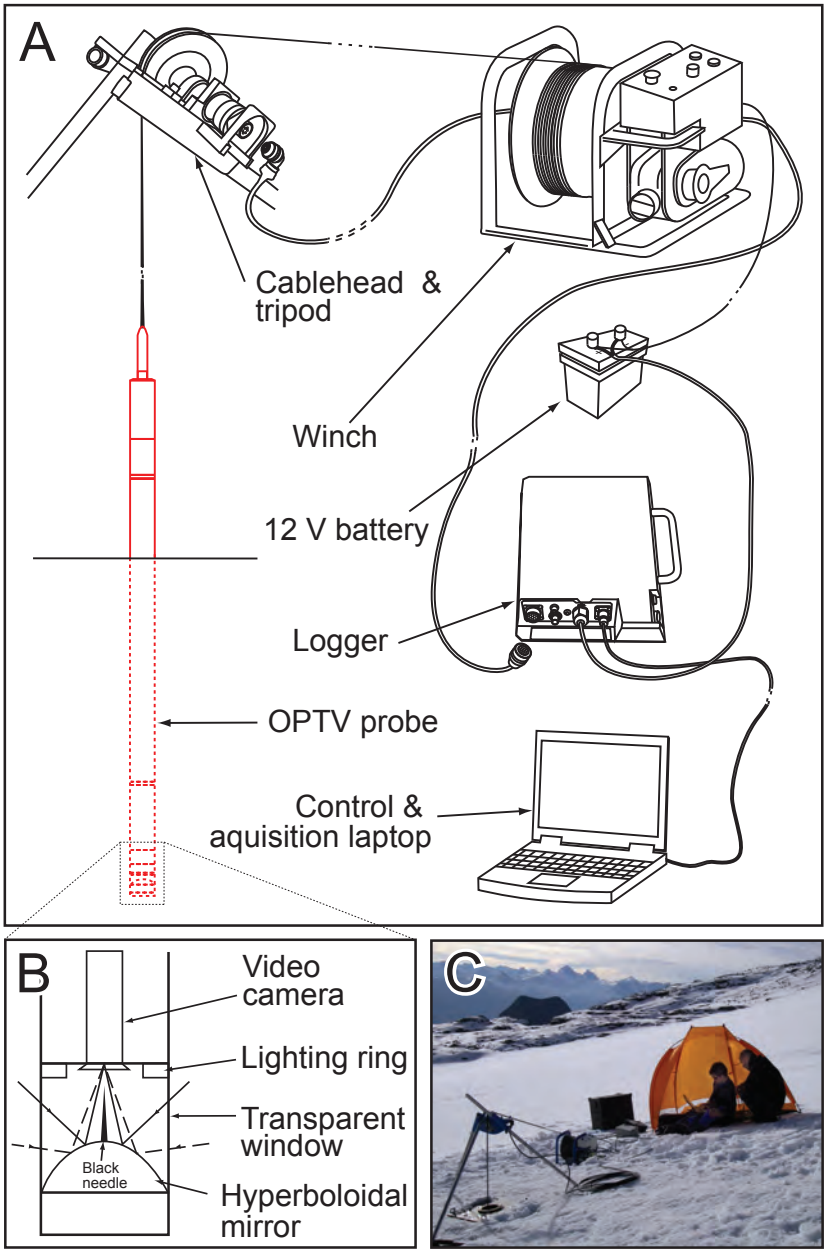

Figure 3.1: Optical televiewer (OPTV) system setup - the main system components: (A) illustrated as a line drawing; (B) a detailed drawing of the OPTV probe head, illustrating the principles of image acquisition, and (C) a photograph of the system operating at the glacier surface.

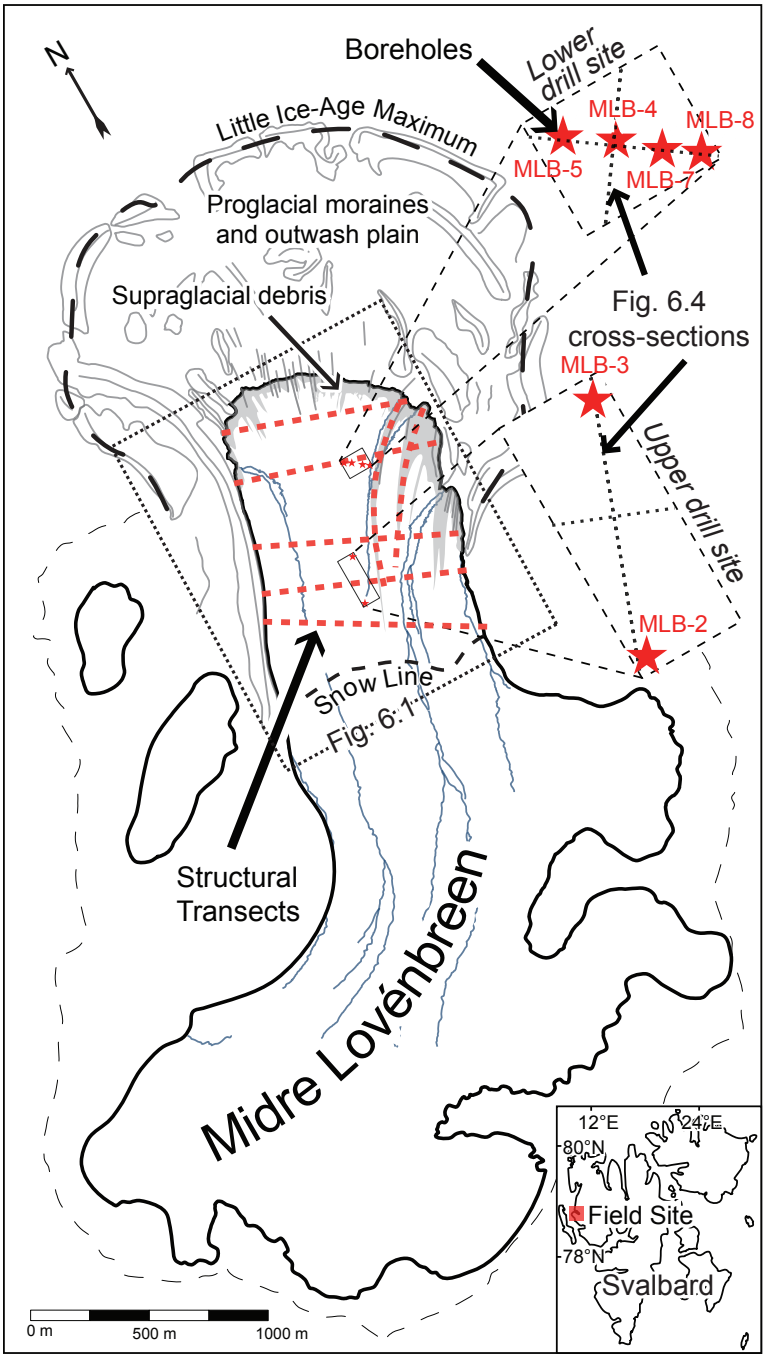

Figure 3.2: Map of Midre Lovénbreen with position of borehole sites and structural mapping transects - orientation of Figs 6.1 and 6.4, and location map of Midre Lovénbreen in Svalbard shown (inset).

3.2.2.2 Image analysis

OPTV borehole logs collected at only Midre Lovénbreen are presented in the form of unrolled images orientated $N-E-S-W-N$ (Fig. 3.3), forming the basis of subsurface structural investigations.

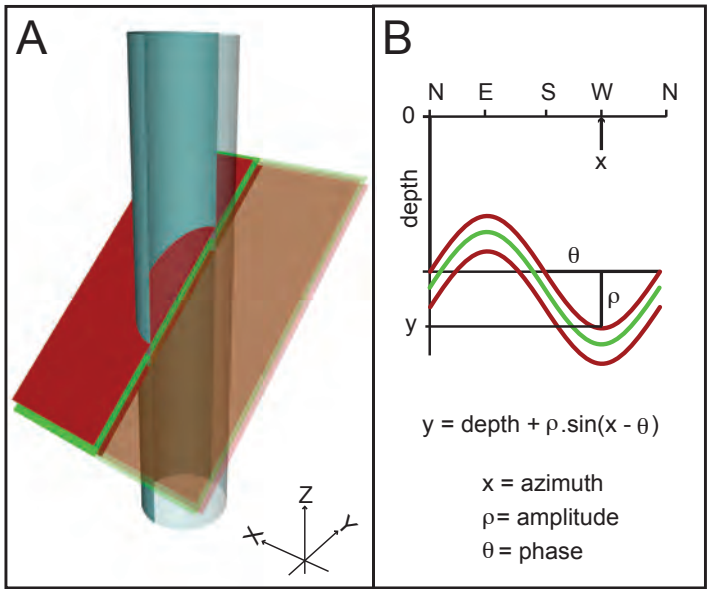

Figure 3.3: Illustration of the relationship between structures intersected by a borehole and seen in an unrolled image - (A) steeply dipping planes intersected by a borehole, and (B) the representation of the planes as sinusoids on a raw (unrolled) OPTV image.

Planar structures intersected by the borehole are translated by cylindrical projection into a sinusoid in the unrolled image. Processing is performed using proprietary software (RGIdip), an integrated suite of applications designed for borehole data analysis and presentation. A feature picking element allows structures to be identified on the basis on their visual properties. The program offers an automated, semi-automated and manual picking; trial and error indicated that the last method provided the best results. Features identified were classified by type, form, state and remark, e.g. primary structure, planar, fresh, bubble-rich. The software automatically calculates depth, dip, thickness and azimuth for each feature identified. The depth of each feature is only related to the borehole, so it is necessary to export the data in *ascii* format in order to register data into Cartesian grid space.

3.2.2.3 Three dimensional visualization

Georegistration of data was triangulated using (x, y, z) coordinates for the borehole at the ice surface and dip and azimuth data recorded by the OPTV. Dip and azimuth data were

extrapolated between boreholes to create a regular three-dimensional lattice of glacier structure. Interpolation was performed for each structural feature identified within the borehole logs: S_0 primary stratification; S_1 longitudinal foliation; S_2 crevasse traces; S_4 fractures. Structural data were interpolated in two spatial subsets: MLB-1 and MLB-2 (labelled *upper drill site* (Fig. 3.2)) and between boreholes MLB-3, MLB-4, MLB-5 and MLB-6 (labelled *lower drill site* (Fig. 3.2). The horizontal extent of both of interpolation areas is also provided in Fig. 3.2. An interpolation across the entire data set was also performed, but the large sample spacing resulted in too many artifacts and was not considered for further analysis. Interpolation used a simple inverse power law algorithm, in which dip and direction of dip data were processed as pseudo-vectors (u, v, w). Each node $\hat{C}_j$ within the regular lattice is defined as:

$$\hat{C}_k = \frac{\sum_{i=1}^{n} \frac{C_i}{h_{ij}^{\beta}}}{\sum_{i=1}^{n} \frac{1}{h_{ij}^{\beta}}} \tag{3.1}$$

where C_i are neighbouring points, β is the power weighting parameter and h_{ij} is:

$$h_{ij} = \sqrt{d_{ij}^2 + \delta_2} \tag{3.2}$$

where d_{ij} is the distance between grid node j and neighbouring point i and δ is the smoothing parameter. Interpolation was executed at a horizontal resolution of 10 m and a vertical resolution of 0.5 m at the upper drill site, and at a horizontal resolution of 1.5 m and at a vertical resolution of 0.5 m at the lower drill site. β the power weighting parameter was equal to 2 and smoothing was turned off ($\delta = 0$). This created a lattice where nodes that coincide with empirical data were equal to the empirical data, and where the influence of empirical data on each lattice node decreases with distance. These parameters were optimized following manual iteration to create the best approximation whilst minimizing artifact propagation.

Planar structures were generated as a series of directional elements, or streamlines, located within a vector lattice, and visualized as nodes in a virtual three dimensional space (a so-called *scene graph*). Certain vertically dipping structures were identified only at the ice surface and not in the OPTV logs, and were consequently of unknown vertical extent. In order to allow these features to be visualized in the scene graphs and structural diagrams (e.g. Fig. 6.4) they were assumed to have a uniform depth of 25 m.

Interpretations based on OPTV however, need to be mindful of several limitations that arise from the interpolation of two dimensional OPTV and surface data into three dimensions. These limitations may be classified into three categories following Thomas (1991):

i. Missing vertical structures,

ii. Misinterpretation of folded structures,

iii. Misjudging lithological characteristics.

While supplementing surface mapping with borehole OPTV analysis undoubtedly increases the power of structural investigations, interpolation and geometrical limitations cannot be eliminated completely.

3.3 Sedimentology

At Glacier de Tsanfleuron 0.5 kg samples of matrix sediments were taken at ninety locations from sediment-landform assemblages on the glacier and proglacial area (Fig. 3.4).

Where sediment cover was sufficiently thick they were obtained at a depth of 0.1 to 0.2 m below the surface. Particles >10 mm were excluded in the field. Sample locations included supraglacial deposits, the 1855-1865 terminal moraine complex, the northern lateral moraine, the glaciofluvial outwash plain, talus cones and proglacial debris stripes. Five debris stripes were sampled, every 100 to 200 m along their length. Nine basal ice samples were collected at Glacier de Tsanfleuron (Coulson, unpublished). Samples of pebble-sized particles were taken at fifty-five points at Glacier de Tsanfleuron for morphology analyses (see Chapter 4).

At Midre Lovénbreen 0.5 kg samples of matrix sediments were taken at 82 locations on the glacier and proglacial area (Fig. 3.5). Sampling focused on supraglacial sediment-landform assemblages and proglacial sediment-landform assemblages $\leq$500 m away from the terminus. Seventeen samples of matrix sediment from subglacial till were also collected at Midre Lovénbreen (Coulson, unpublished). Seventy samples of pebble-sized particles were also collected at Midre Lovénbreen for morphological analyses (see Chapter 4).

Sediment-landform assemblages at both glaciers were described in terms of their morphometry and constituent sedimentary composition. Sedimentary facies are described in terms of their structure, particle-size-distribution and particle morphology.

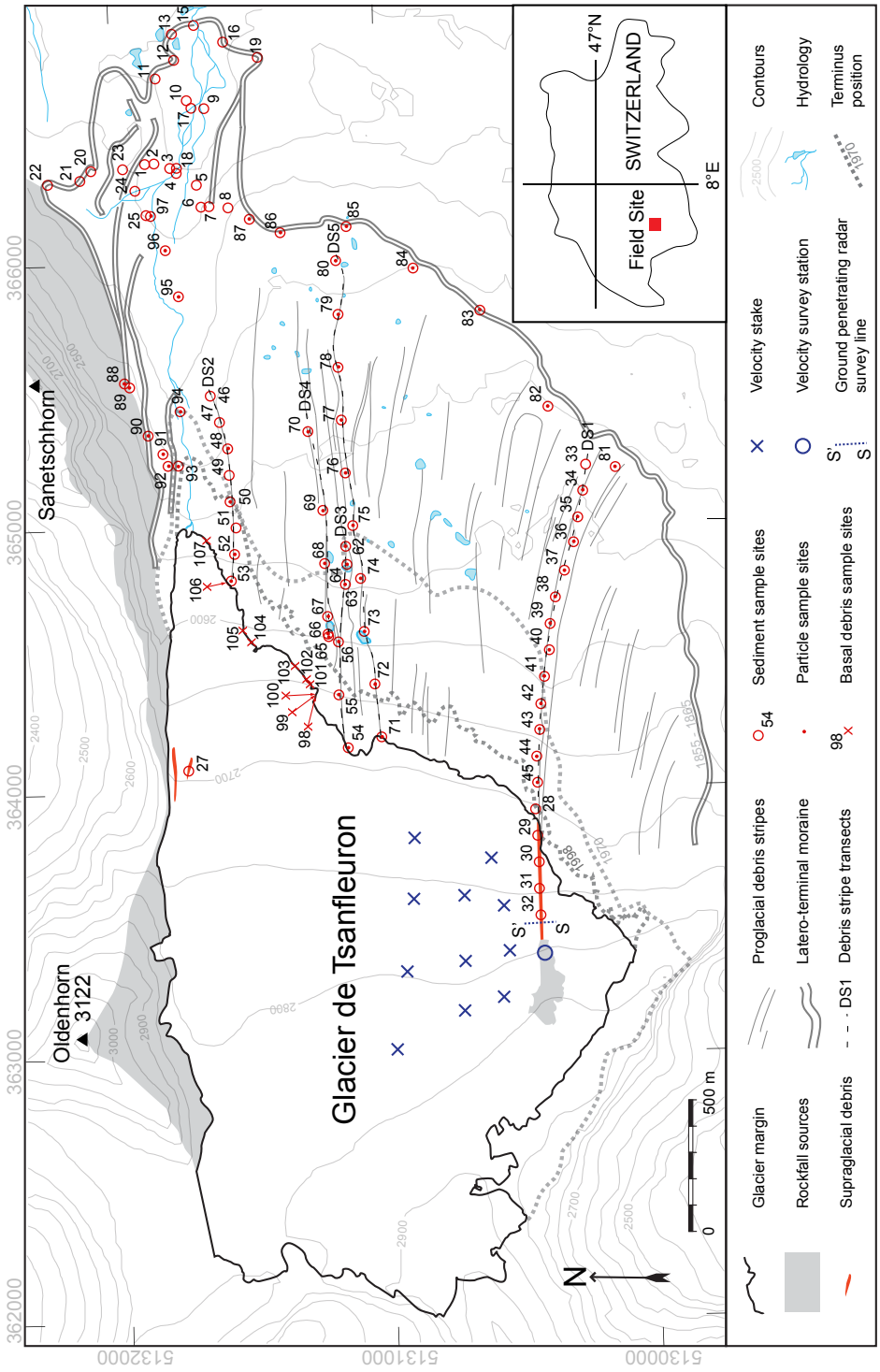

Figure 3.4: Map of Glacier de Tsanfleuron - overview map of sediment-landform assemblages, sample locations, position of surface velocity stakes, survey station and GPR transect.

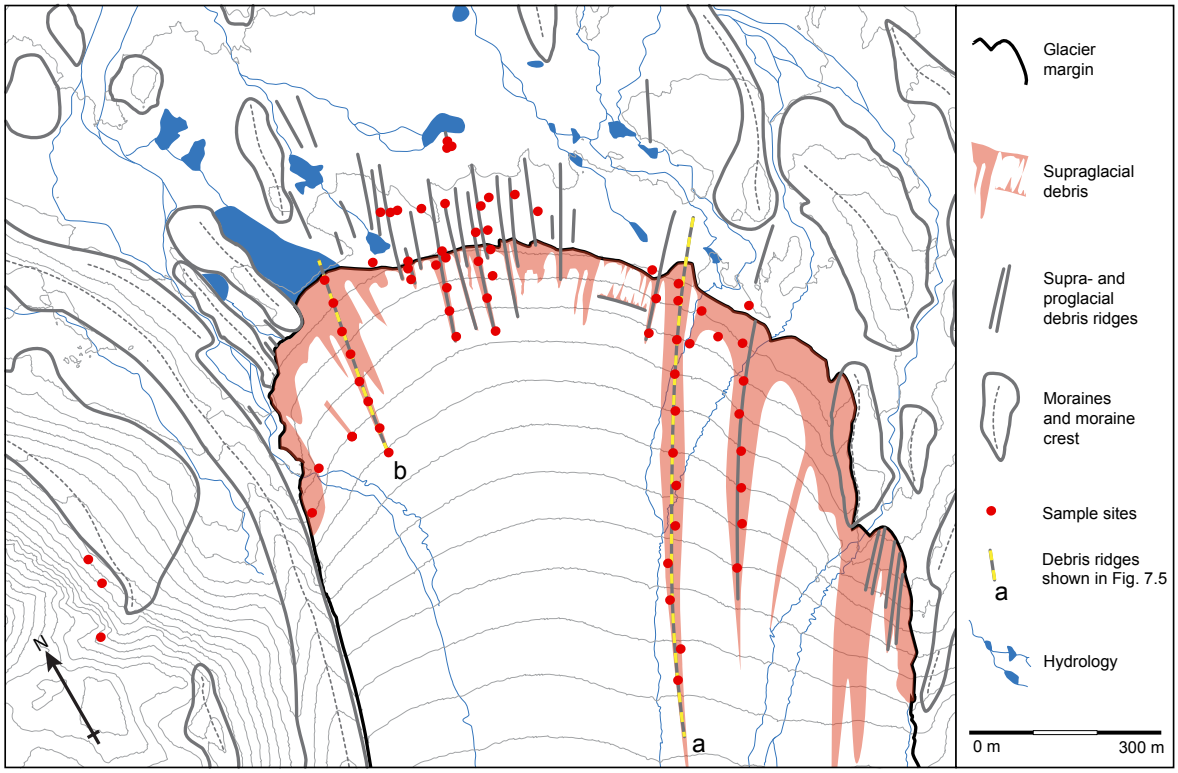

Figure 3.5: Map of glacial sediment-landform assemblages and sediment sample sites at the frontal- and proglacial zone of Midre Lovénbreen - see Fig. 3.2 for positioning

3.3.1 Particle size analysis

The particle-size-distribution of each sample was determined in the laboratory by dry sieving and laser granulometry. Dry sieving used half-ϕ intervals from -1 ϕ to 4 ϕ (2 mm to 0.63 mm) following Gale and Hoare (1992).

The size distribution of particles from 4 ϕ to 12 ϕ (0.63 mm to 0.0002 mm) was determined using laser diffraction (Malvern Mastersizer 2000). Samples were introduced into the Mastersizer using a Hydro 2000 MU pump to achieve an obscuration of 10 to 20%. Analyses were run following initial tests using a refractive index of 1.6 and an absorption value of 0.01. This produced a weighted residual of $<$0.5% between the observed and predicted particle-size-distributions for all samples. The percentage volume distribution of particles measured by the laser granulometer were converted into percentage mass to allow them to be amalgamated with the results from dry sieving.

Comparison of laser diffraction size distributions with those from wet sieving and settling columns has shown that the size of platy clay minerals measured using laser diffraction are overestimated relative to wet sieving or settling methods (Konert and Vandenberghe, 1997; Blott and Pye, 2006). This disparity arises because the granulometer measures the particle diameter in random orientations, whereas sieving and settling techniques

preferentially measure the b - axis of a particle. Amalgamation of these data was performed with a four, two and zero size class shift, i.e. matching the 6 ϕ laser size class with the 4 ϕ dry sieve class, the 5 ϕ laser size class with the 4 ϕ dry sieve class and the 4 ϕ laser size class with the 4 ϕ dry sieve class. A zero size class shift was found to perform best across the range of particle-size-distributions. The close match between the two data sets suggests that the majority of particles $<$4 ϕ were closer to spherical in form, rather than platy clay minerals and that combining these techniques was a robust approach.

Considerable ambiguity surrounds the use and application of sedimentary nomenclature, so it is appropriate here to specify which classification system is used henceforth. Rather than employ the detailed classifications of poorly sorted sediments, typically used in sedimentological investigations of glacierized environments, e.g. Moncrieff (1989) and Hambrey (1994), a simpler classification will be used here: NEN 5104 (Anonymous, 1989), the widely used Dutch classification system for unconsolidated sediments. NEN 5104 defines diamicton for example, as poorly sorted unconsolidated terrigenous sediment characterized by a broad range of particle sizes, closely following Flint et al. (1960). Although lacking the precision of the former systems, the scheme is applicable to a broad range of environments and can easily be supplemented by additional descriptive statistics. These will be given in terms of particle size, sorting, modality, structure, contact type and grading.

3.3.2 Statistical analyses

The combined particle-size-distributions were subjected to a range of statistical analyses.

3.3.2.1 Descriptive statistics

Descriptive statistics for particle-size-distributions were calculated using Minitab 14.0. Statistics extracted include: the mean, standard deviation, kurtosis and skewness for arithmetic, geometric and logarithmic distributions; D_{10}, D_{50} and D_{90}; percentage distributions of gravel, sand and mud (Wentworth, 1922).

The degrees of similarity between particle-size-distributions was quantified using the $\cos\theta$ index of Imbrie and Purdy (1962), following Syvitski (2007). Similarity between N samples i and j of p size intervals is calculated from:

$$\cos\theta_{ij} = \left(\sum_{k=1}^{p} X_{ik}X_{jk}^{2}\right)\sqrt{\left(\sum_{k=1}^{p} X_{jk}^{2}\right)} \tag{3.3}$$

where X_{ij} is the amount of sediment in the k^{th} size interval for sample i and the same for sample j. The index calculates the normalized angular separation between samples by the proportion of sediment in each size class, so the absolute mass of sediment is ignored. A $\cos\theta$ value of 1.0 indicates perfect similarity and a $\cos\theta$ value of 0.0 no similarity. Equation (1) forms an NxN similarity matrix which can then be used to group the samples using a Q-mode principal component analysis. Calculations were performed in Mathworks Matlab using a series of automated scripts. Although $\cos\theta$ values are less good at distinguishing between poorly sorted samples than well-sorted samples (Syvitski, 2007), the calculation of the similarity matrix via this method still yields useful insights.

3.3.2.2 Sediment modality

Sample modality was examined by using a Gaussian component analysis (GCA) following Sheridan et al. (1987). GCA was carried out in Mathworks Matlab using a series of off-the-shelf scripts linked together. These follow the approach of Sheridan et al. (1987) and consist of: (1) increasing the number of particle-size divisions by a factor of one hundred, (2) fitting a cubic-spline curve to the new particle size distribution data, (3) fitting an optimal number of Gaussian components to each particle size distribution using the freely available function `fit_mix_gaussian.m`. Fitting Gaussian components to a particle-size distribution involves

implementing an iterative Newton-Raphson method, in which convergence occurs once a specified threshold value is reached, in this case $1.0e^{-3}$ (See Appendix A for the Matlab code).

3.3.2.3 Fractal analysis

Sediment texture was quantified following the fractal dimension method of Hooke and Iverson (1995). These authors postulated that glacial sediments deforming by grain fracture tend towards a self-similar distribution. This can be quantified by measuring the slope m of particle mass plotted against particle diameter d on a log-log scatterplot. In the case of a self-similar or fractal material, the number N of particles of diameter d is $2m$ times the number of size $2d$, where m is the fractal dimension, hence:

$$N_d = N_0 \left(\frac{d}{d_0} \right)^{-m} \tag{3.4}$$

where N_0 is the number of particles of reference size d_0.

3.4 Sediment discharge modelling

The methods used to derive first-order estimates of sediment transport have been largely developed and documented by other researchers where they are described in detail (Hubbard et al., 1998; Chandler et al., 2008). These methods are therefore described briefly here, with specific details pertaining only to any modifications made during application in this study.

3.4.1 A finite-difference ice-flow model

The ice-flow model used in this study is derived from the Hubbard-Blatter three-dimensional, finite-difference model, first successfully applied to Haut Glacier d'Arolla (Hubbard et al., 1998). Briefly, the model takes ice surface and bed topography to calculate three-dimensional stress and the resultant shear based on the assumption that surface shear stress values are equal to zero. This is achieved through a Runga-Kutta step that integrates stresses calculated at the bed up through the ice column to the surface.

The ice-flow model developed for Glacier de Tsanfleuron is that of Chandler et al. (2008) and uses the optimized values for model parameters provided (Chandler et al., 2008, their Table 2). The parameters used by Chandler et al. (2008) are listed in Table 3.1, with the

parameters used in this study highlighted in bold. r^2 values indicate the closeness of fit between modeled and observed surface velocity fields. A 5 m DEM of the surface geometry is supplied by SwissTopo and the basal elevation from radar data collected by Hubbard et al. (2003) and Chandler (2005). The model is run at a horizontal grid spacing of 100 m and assumes a steady-state geometry.

Table 3.1: Empirical data and optimum parameters for finite-difference ice-flow model (after Chandler et al., 2008: their Table 2)

	n	A (Pa^{-1} s^{-n})	E_{LZ}	max. vel_{nz} (m a^{-1})	r^2
Empirical	–	–	1.8 – 3	40.62	–
Modeled	**1**	**2.5** e^{15}	**1.9**	**40.48**	**0.9996**
Modeled	3	$5.7e^{-26}$	2.5	40.48	0.9997

A sliding module is added in this work to provide an estimate for basal sliding using a finite-difference convergence scheme, based on the methods detailed by Chandler et al. (2008). In this case, basal sliding ($vel_{(i,j,0)}$) is calculated by subtracting the modeled surface velocity field ($vel_{(i,j,nz)}$) (3.4.2) from an empirical surface velocity field ($\widehat{vel}_{(i,j)}$) until convergence criterion λ is satisfied:

$$vel_{(i,j,0)} = vel_{(i,j,0)} + \beta * \left(\widehat{vel}_{(i,j)} - vel_{(i,j,nz)}\right) \tag{3.5}$$

where $\beta = 0.3$, $\lambda = 0.0$, subscripts i, j, k are dimensional indices in the model domain and nz, ny and nz are the number of horizontal (x, y) and vertical (z) grid cells respectively.

The surface velocity field for Glacier de Tsanfleuron is provided by Chandler (2005), and is supplemented in the southern area of the glacier by velocity measurements from this study, taken during spring and summer fieldwork in 2007 (Section 3.4.2).

The model is additionally modified by the application of an exponential transformation parameter to vertical grid cells in order to focus computational power towards the bed. This follows the approach of Hildes (2001):

$$z_j = exp\left[-3\left(\frac{1}{j}\right)\left(\frac{1}{nz}\right)j\right] \tag{3.6}$$

3.4.2 Surface velocity measurement

At Glacier de Tsanfleuron surface velocity measurement was measured during the spring and summer of 2007 using a network of velocity stakes (Fig. 3.4). A geodometer total station (Trimble 5600) was mounted on a surveying tripod on top of a nunatak near the south margin of the glacier (Fig. 3.4). The location of the surveying station was determined using a Magellan ProMark X differential GPS (accurate to $<\pm$1.0 m in pseudo-range mode following post-processing (Higgitt and Warburton, 1999). The area covered by surveying encompassed the south western edge of the glacier, including an area of potentially high glacial sediment transport originating from the nunatak. Eleven wooden stakes were driven into the snowpack or drilled into the glacier surface using a battery-powered ice-drill (DeWalt DC901KL). A Trimble survey prism was mounted on each velocity stake $\sim$1.5 m above the snow or ice surface. The surveying stakes were distributed north and north-west of the geodometer. A reference prism was located at the nunatak summit $\sim$70 m west of the survey station. The centre of an instrument on top of the meteorological station above the Glacier 3000 cable-car station was used to calibrate the instrument's horizontal angle. The location of all eleven velocity stakes and the reference prism was measured using spherical co-ordinates (horizontal angle, vertical angle, sighted distance). Specified distance-measurement accuracy of the Trimble 5600 is $\pm$3 mm + 3 ppm in single-prism mode (Höglund and Large, 2003), which when considering the survey distances involved yields an error of $\pm$4 mm.

During the 2007 summer fieldwork season, following the failure of the Trimble 5700 total station on 04.08.2007, a pair of Magellan ProMark X dGPS were used to measure the position of each velocity stake. A base station was set up at on top of the nunatak, and the position of each stake was measured using pseudo-range differential mode, to generate a position averaged over $\geq$10 minutes. The roving GPS was placed on the downglacier side of each velocity stake on its case with the antenna orientated parallel to the velocity stake. Post-processing of GPS data using MStar (Magellan International) provided a single co-ordinate reference for each velocity stake accurate to $<\pm$1.0 m (Higgitt and Warburton, 1999).

3.4.3 Sediment concentration and distribution

Supraglacial sediment distribution at Glacier de Tsanfleuron was mapped from 1998 aerial photography. The thickness of supraglacial sediment was measured during 2007 summer fieldwork by digging down to the ice surface using an ice-axe. The depth of sediment was measured using a tape measure accurate to $\pm$0.5 mm.

Englacial sediment concentrations were calculated from GPR data (Section 5.2.3.2) and measurements of sediment thickness at the glacier margin (Section 3.4.4, Fig. 3.4). It was assumed that the mass of sediment within the debris stripe was constant downglacier from the nunatak, so sediment mass was taken as the volume of sediment present at sample site 28 (Fig. 3.4), multiplied by an average density value for Urgonian limestone (taken as 2690 kg m^{-3} (Frayssines and Hantz, 2009) and an assumed void ratio of 0.8 following Small et al. (1984).

Sediment concentrations in basal ice facies and their distribution were measured and kindly provided by Hayley Coulson (Coulson, unpublished).

3.4.4 Ground-penetrating radar

A ground-penetrating radar (GPR) common-offset survey line 120 m long was acquired at Glacier de Tsanfleuron, during fieldwork in spring 2007, across the large supraglacial debris stripe east of the nunatak, from S to S' (Fig. 3.4). Data were collected with a Sensors and Software PulseEKKO 100 GPR, using 100 MHz antennae, with an antennae separation of 1.0 m and a step size of 0.5 m to minimize aliasing. Topographic data for the profile were collected using a Magellan ProMark X differential GPS, with a base station set up at on top of the nunatak. Topographic data were acquired in kinematic mode and post-processed with base station data in MStar software (Magellan International) to yield coordinates with a vertical and horizontal accuracy of ∼2.0 to 3.0 m (Higgitt and Warburton, 1999).

The GPR profile (Figure 1) was processed using ReflexW software (Sandmeier Scientific Software) using the following standard functions to reduce noise, amplify the signal and accentuate continuous layering:

i. subtract mean (DEWOW),

ii. static correction,

iii. energy decay,

iv. diffraction stack migration (assuming a constant velocity of 0.167 m ns^{-1}) with a summation window of 10 traces,

v. topographic correction using dGPS data (above).

3.4.5 Glacial sediment discharge calculation

Glacial sediment discharge (Q_s) is calculated by combining empirical measurements of basal ice, englacial and supraglacial sediment distribution (Tt) and sediment concentration (Sc) with modeled ice velocities (vel), hence:

$$Q_s = \int_{(i=nx,j=ny,k=nz)}^{(i=0,j=0,k=0)} \left[Sc_{(i,j,k)} * vel_{(i,j,k)} * Tt_{(i,j,k)} \right] \tag{3.7}$$

where subscripts i, j, k are dimensional indices in the model domain and nx, ny and nz are the maximum number of elements in each dimension, respectively.

Glacier de Tsanfleuron is considered to be hard-bedded (Hubbard and Hubbard, 1998), a claim supported by the low volume of proglacial sediments and observations beneath the glacier, which revealed a very thin ($\leq$ 10 mm) or absent subglacial till layer. Sediment transport by deformation of a subglacial till layer was therefore excluded from estimates of total sediment discharge [3.7].

Chapter 4

Automated image-based analysis of particle morphology

> The seductive ease with which measurements of form and roundness can be made is in contrast with the difficulties encountered in ascribing a geological meaning to them
>
> (Barrett, 1980)

4.1 Introduction

The morphology of sedimentary particles can be described by three largely independent attributes: form, roundness and surface roughness (Barrett, 1980; Orford, 1981). Barrett (1980) identified these properties as affecting particles at different scales: form, a first-order effect; roundness a second-order effect and surface roughness a third-order effect (Fig. 4.1). Form reflects the relative length of a particle's length, width and depth; roundness reflects variations at the particle's corners, superimposed on form; and surface roughness reflects small-scale ($<$1-2 m) variations in the z - axis relative to the x-y plane of particle form and roundness (Sayers and Karamihas, 1997).

Experimental investigations into the processes contributing to the evolution of particle morphology have yielded useful insights into their relative influences (Haldorsen, 1981; Hooke and Iverson, 1995; Kuenen, 1959). However, the timescales over which these processes operate and difficulties in measuring environmental conditions hinder the application of insights gained from laboratory work to data collected in the field. In spite of these limitations, particle morphology is widely recognised as a key line of evidence in deducing the transport history of particles. This is particularly evident in glaciological settings, where processes affecting the morphology of particles may differ considerably over scales

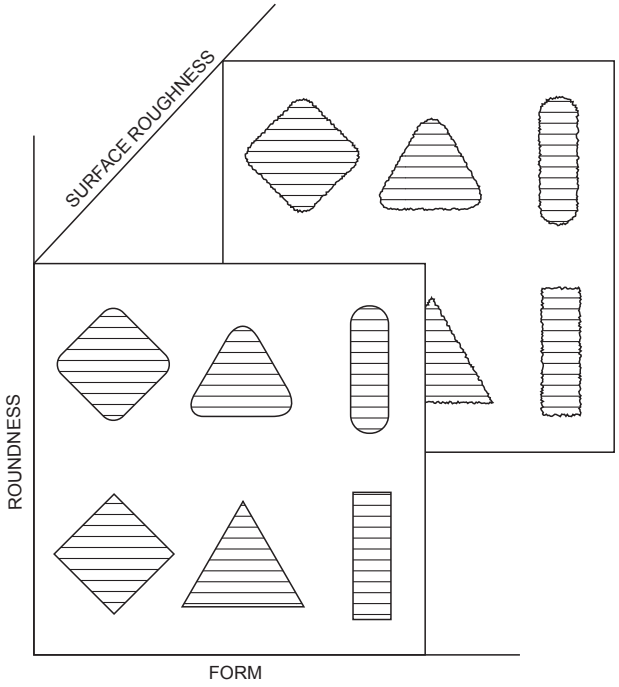

Figure 4.1: Schematic representation of particle morphology - form, roundness and surface roughness can be considered as three independent axes (taken from Barrett, 1980: their Fig. 1).

of hundreds of metres or less. Studies of glacigenic sediment landforms have traditionally used low-tech methods to characterise the form, roundness and surface roughness of pebble-sized particles (Boulton, 1978; Sharp, 1982; Dowdeswell et al., 1985). Attempts to improve the rigor with which statistical analyses were performed have been made most notably by Benn and Ballantyne (1994), who came up with the concepts of C_{40} and RA indices. These were essentially subsets of existing form and roundness scales, modified to accentuate changes occurring within a glacierized catchment. This particular study was able to differentiate a range of sediment facies from one another on the basis of graphical representation in a bivariate scatterplot. Although this was termed a covariance analysis by Benn and Ballantyne (1994), no actual statistical analysis of covariance was undertaken, so it is difficult to assess the statistical significance of these findings. Motivations for the methodological appraisal in this chapter (below) stem directly from the author's own use of these techniques (Roberson, 2008). In a number of glacial environments, the methods of Benn and Ballantyne (1994) have failed to provide the distinction between sediment facies required to make meaningful observations. Of key concern when using these methods, is the statistical robustness of the initial data collection. If the data collected are prone to significant error, all subsequent analyses are therefore invalid. If particle morphology data

are to be useful, it is imperative to be able to quantify them reliably at a spatial resolution high enough to be able to distinguish between particle populations affected by different processes.

The quantification of particle morphology requires measurements in three dimensions (x, y, z). With the exception of measuring form, this has been very time consuming until quite recently (e.g. Hulbe, 1955). More commonly one or more two-dimensional sections of a particle have been measured. From this, equivalent two-dimensional morphologies are derived and used as proxies for overall particle morphology. Dowdeswell (1982) demonstrated that the surface roughness values of 2D particle profiles were representative of particles as a whole. This assumption is clearly invalid for form analyses and it is unlikely to apply to measurements of particle roundness either. Digital analysis systems designed to measure particle morphology automatically have been in use, but not widely used, for many years (Kennedy and Mazzullo, 2007; Kung, 2005; Mazzullo and Kennedy, 1985; Schafer, 1982; Schneider et al., 2003). These systems have typically been computationally demanding, requiring careful sample preparation and high operator times to ensure quality of results. As a result, most operations have been restricted to laboratory or industrial settings (Carter and Yan, 2003; Thomas et al., 1995; Young et al., 2008). Although analysis of surface roughness has been of considerable importance to industrial applications for many years, in the field of geology its potential has only recently been recognised (Finnegan et al., 2007; Haneberg, 2006). This has largely been facilitated by an increase in the affordability and portability of terrestrial laser scanning and digital imaging systems, allowing high resolution three-dimensional data to be acquired in the field (e.g. Brasington et al., 2007; Chandler et al., 2003; Graham et al., 2005).

To address the issues associated with time-consuming and low-precision approaches to measuring particle morphology, using a cheap and efficient means, the specific aims of this chapter are:

i. To review the shortcomings of traditional methods of measuring particle morphology,

ii. To offer a feasible solution using digital imagery and an automated digitally based analysis,

iii. To demonstrate the application of automated methods to particles collected at Glacier de Tsanfleuron, Switzerland,

iv. To quantify the advantages of digital methods over traditional methods in terms of reliability and accuracy.

4.2 Methods

All digital processing and mathematical functions listed in Chapter 4 were performed using Mathworks Matlab (see Appendix B for programming code).

4.2.1 Image acquisition

Samples of fifty particles, where a - axis $\geq$20 mm and $\leq$100 mm, were collected from each of 55 locations in the proglacial area at Glacier de Tsanfleuron. All 2750 particles were photographed using a 10 million pixel Nikon D80 against a high-contrast matt background under a four bulb lighting rig to provide a consistent and even exposure (Fig. 4.2). The images were acquired in RAW format to preserve as much pixel level detail as possible. Each particle was photographed from three different angles at a constant focal length of 55 mm, orientated along a, b and c - axes, yielding 8250 separate images in total.

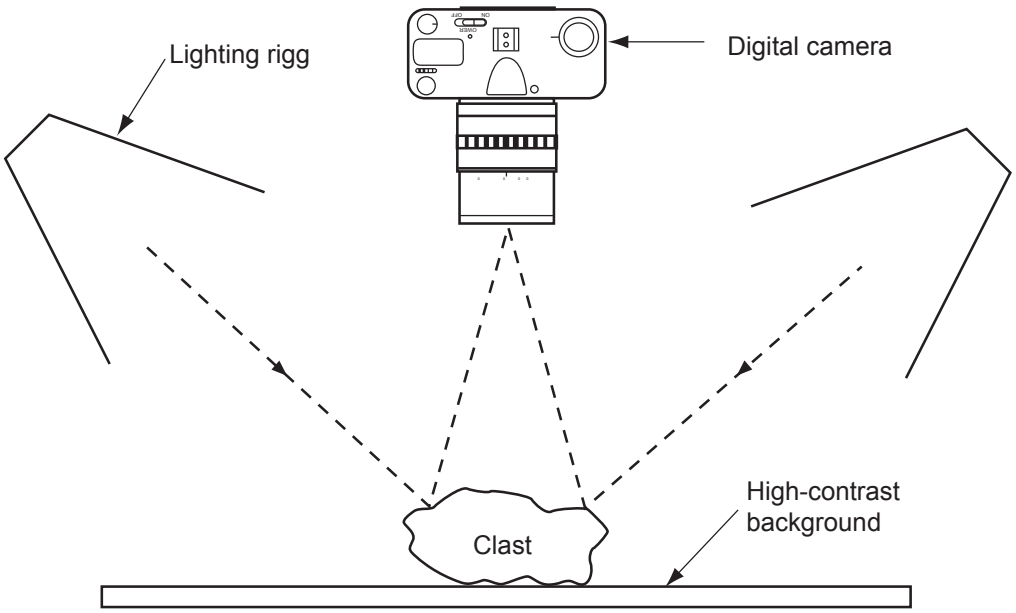

Figure 4.2: Schematic representation of lighting rig and camera setup - camera has a fixed focal range and is mounted at a fixed height on a tripod.

4.2.2 Image processing

Image processing was performed using a series of algorithms run in Mathworks Matlab. Each image was subjected to the following processing sequence to extract a digitized particle

outline:

i. The image was imported (Fig. 4.3a) and the red band and the blue band were isolated and their contrast enhanced using an optimum threshold value estimated from each bands' brightness levels.

ii. The red band was subtracted from the blue band to produce a greyscale image, where image background appeared dark grey and the particle light grey (Fig. 4.3b).

iii. The greyscale image was converted to a binary black and white image using a threshold value equivalent to the geometric mean of the image brightness (Fig. 4.3c).

iv. The image was tidied using a range of standard image-processing algorithms (Fig 4.3d):

   a. A dilation algorithm using 3 pixel vertical linear and 3 pixel horizontal linear structuring elements was applied to the binary image, which catches stray pixels at the edge of the particle.

   b. Apparent holes within the particles were removed using an image fill algorithm, which converts pixels with a value of 0 (i.e. background) that had no connection with the rest of the background to 1.

   c. Pixel clusters $<$30 were removed to tidy the image using an open area algorithm.

   d. Holes of less than 2 pixels between white pixels were filled using a close algorithm.

   e. The edge of the particle was tidied up using an erode algorithm, which helps to counter the effects of pixel dilation.

   f. The remaining stray white pixels in the background were removed by using the open area algorithm to clear pixel clusters $<$5000 pixels.

v. The particle outline was extracted from the processed binary image using a boundary algorithm (Fig. 4.3e). The boundary algorithm detects the continuous boundary between pixels with a value of 1 and pixels with a value of 0 and returns their position using a pixel-based (x, y) - axis Cartesian co-ordinate system. The co-ordinates were saved as an n x 2 matrix in a text file, where n is the length of the particle outline in pixels.

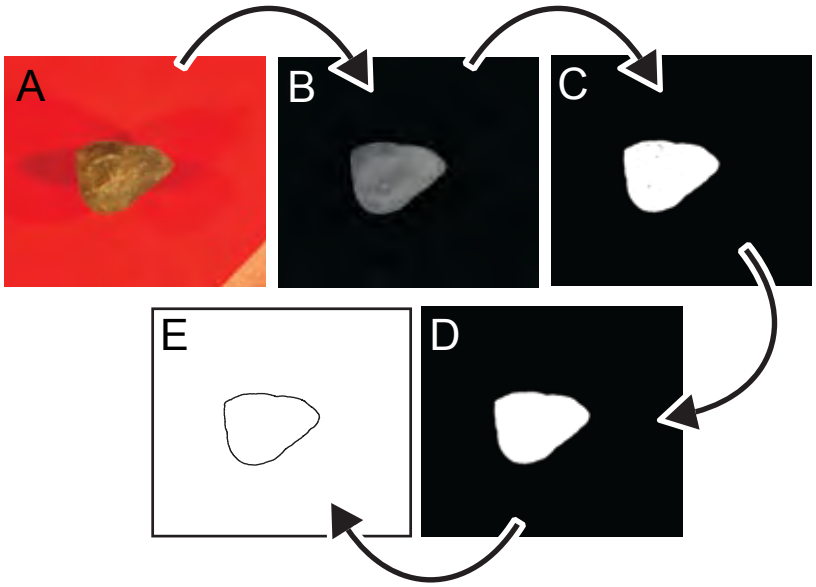

Figure 4.3: Digital image processing steps - (a) image imported into Matlab; (b) r-band subtracted from the b-band; (c) conversion of greyscale image to binary image; (d) application of 'tidying' algorithms to the binary image (e) particle outline plotted as (x, y) Cartesian co-ordinates following boundary extraction.

4.2.3 Form analysis

Particle form has typically been quantified by a measure of the smallest enclosing cuboid around a particle (Krumbein, 1941). From this, long, intermediate and short (a, b, c) orthogonal particle axes may be derived (Wentworth, 1922). Although there may be some error in defining these axes, which is not entirely eliminated through digital image acquisition, it is typically in the range of 0.5 - 2.8 % (Blott and Pye, 2008). A large number of different particle form indices exist that are reliant on the relative measures of a, b and c - axes (see Blott and Pye, 2008, for a review). Krumbein's (1941) intercept sphericity I_s is used here as a quantitative measure of particle form, as it provides the best overall means of distinguishing particle form:

$$I_s = \sqrt[3]{\frac{bc}{a^2}} \tag{4.1}$$

In this case particle axes were calculated in Matlab by using an ellipsefit algorithm to obtain the length of semi-major and semi-minor axes of the particle's best-fit ellipse.

4.2.3.1 Form comparisons

A representative range of 350 particles sampled from in the field (sites 50, 54, 71, 83, 88, 90 and 95 (Fig. 4.7)) was measured manually using calipers to visually determine a, b and c - axes. These data were used to quantitatively compare the results of automated and traditional form analyses.

4.2.4 Roundness analysis

The roundness of a particle is most often defined as a measure of the relative sharpness of its corners (e.g. Krumbein and Pettijohn, 1938; Wadell, 1932). Alternatively a number of authors have defined roundness, or sometimes circularity, as the ratio of particle-area to that of a circle with the same perimeter or a particle's smallest inscribing circle (e.g. Cox, 1927; Tickell, 1948). Wadell's (1932) roundness index measured the ratio of the mean diameter of a particles corners to the diameter of its largest inscribing circle. This has been widely adopted, predominantly in the form of the visual comparison charts prepared by Krumbein (1941), Powers (1953) and Russell and Taylor (1937). The approach of Powers (1953) has been the most widely adopted, as it considered particles in three-dimensions and had an optimum number of classes. Visual comparison charts make the process of measuring particle shape more efficient, although these can suffer from significant operator errors (Folk, 1955; Rosenfeld and Griffiths, 1953).

Schwarcz and Shane (1969) first introduced the Fourier-transform to particle analysis, which have most frequently used a centrally weighted polar co-ordinate system $\rho(\theta)$ to describe a particle outline. Herein lies the computational strength of Fourier analyses, as it quantifies both convex and concave curvatures along the particle outline. The majority of researchers have used a fast-Fourier Transform (FFT) to save computational processing time (e.g. Czarnecka and Gillott, 1977; Drevin, 2000; Ehrlich and Weinberg, 1970). Drevin (2000) found that the normalized sum of the first 23 FFT harmonic amplitudes provides the best correlation with Krumbein's (1941) roundness index. This has the advantage of allowing FFT analyses to be compared with existing data derived from Wadell's (1932) roundness index and visual comparison charts of Krumbein (1941) and Powers (1953).

Despite its potential utility, the numerical complexities of FFT analyses have often dissuaded researchers from its application in the field of glacial sedimentology. However, herein I demonstrate a straightforward approach to FFT particle analysis using conventional software (Mathworks Matlab) following the techniques detailed in Diepenbroek et al. (1992). Processing can be entirely automated using digital photographs and can be performed by a single computer or a server with a host of clients.

4.2.4.1 Digital processing

Particle boundary (x, y) co-ordinates extracted from raster images were filtered to 1024 edge points by linear interpolation:

$$x = \frac{[x_{i+1} - x_i]y_{i+1} - x_{i+1}y_i}{y_{i+1} - y_i} \tag{4.2}$$

Cartesian co-ordinates were converted into polar co-ordinates $\rho(\theta)$ by finding the centre point (x_c, y_c) of the particle outline (Ehrlich and Weinberg, 1970). Particle centre point was calculated by finding the centre of gravity:

$$x_c = \left(x_i + \sum_{i=2}^{N} x\right) \left[\frac{\left(x_i\left(y_i + \sum_{i=2}^{N} y\right) - \left(x_i + \sum_{i=2}^{N} x\right)y_i\right)}{\left(0.5 * A_{NxN}\left(x_i\left(y_i + \sum_{i=2}^{N} y\right) - \left(x_i + \sum_{i=2}^{N}\right)y_i\right)\right)} \Big/ 6\right] \tag{4.3}$$

$$y_c = \left(y_i + \sum_{i=2}^{N} y\right) \left[\frac{\left(x_i\left(y_i + \sum_{i=2}^{N} y\right) - \left(x_i + \sum_{i=2}^{N} x\right)y_i\right)}{\left(0.5 * A_{NxN}\left(x_i\left(y_i + \sum_{i=2}^{N} y\right) - \left(x_i + \sum_{i=2}^{N}\right)y_i\right)\right)} \Big/ 6\right] \tag{4.4}$$

where x_i and y_i are the i^{th} co-ordinate, N is the total number of co-ordinates and A is an N x N matrix of ones. Following Schwarcz and Shane (1969) the FFT of the resultant polar co-ordinates $\rho(\theta)$ are:

$$\rho(\theta) = \frac{a_0}{2} + \sum_{k=1}^{m} a_k \cos k\theta + b_k \sin k\theta \tag{4.5}$$

where m is the number of FFT harmonics calculated, in this case equal to the number of $\rho(\theta)$ co-ordinates, k is the harmonic number and constants a_0, a_k and b_k are given as:

$$a_0 = \frac{1}{\pi}\int_{-\pi}^{\pi} \rho(\theta)\Delta\theta \tag{4.6}$$

$$a_k = \frac{1}{\pi}\int_{-\pi}^{\pi} \rho(\theta)\cos k\theta \,.\, \Delta\theta \tag{4.7}$$

$$b_k = \frac{1}{\pi}\int_{-\pi}^{\pi} \rho(\theta)\sin k\theta \,.\, \Delta\theta \tag{4.8}$$

The amplitude of the 2^{nd} harmonic (R_2) perfectly describes the ellipse of the particle outline (Diepenbroek et al., 1992). The equation of the ellipse may be calculated as:

$$\frac{r_b}{r_a} = 1 - 1.74R_2 + 0.86R_2^2 \tag{4.9}$$

where r_a and r_b are the radii of the semi-major and semi-minor axes respectively. Subtracting the FFT of the best-fit ellipse (R_{ek}) from the sum of all FFT harmonics of the particle outline (R_1 to R_m) therefore removes the influence of shape. Accordingly this is calculated as:

$$\rho_t(\theta_t) = \left[a_0 + \sum_{k=1}^{m} a_k \cos k\theta + b_k \sin k\theta\right] - [a_0 + a_2 \cos 2\theta + b_2 \sin 2\theta] \tag{4.10}$$

The resultant polar co-ordinates $\rho_t(\theta_t)$ are transformed into the frequency domain with the influence of particle form removed:

$$P_{pre} = \sum_{3}^{m}(R_k - R_{ek}) \tag{4.11}$$

where R_{ek} is the influence of the particles best-fit ellipse on the k^{th} harmonic. The effect of particle size on the amplitude of each harmonic is removed by dividing R_1 to R_m by R_0, where R_0 is the summation of all amplitudes (Diepenbroek et al., 1992).

The amplitude of each harmonic decreases exponentially with frequency (k), so in order to give each harmonic an equal influence on the overall roundness value, a standard normalization weighting c_k is applied using an exponential transformation (Diepenbroek et al., 1992):

$$c_k = 0.56\exp(0.2k) \tag{4.12}$$

Accordingly the roundness calculation is modified to:

$$P_{pre} = \sum_{3}^{m} c_k(R_k - R_{ek}) \tag{4.13}$$

Resolution calibration The effect of pixel noise on the amplitude of different harmonics was investigated using a perfect circle at a range of image resolutions and hence number of edge points. Image resolutions of 10, 6, 4, 3 and 2 million pixels were used. These corresponded to 3257, 2553, 2127, 1815 and 1481 edge pixels per circle respectively. Fig. 4.4 shows the effect of pixel resolution across the range of harmonics sampled. The differences between harmonic amplitudes at different resolutions shows that the majority of pixel noise is described by the higher frequency harmonics, as one would expect. The overall effect of pixel noise on particle roundness is shown in Fig. 4.5. The mean increase in harmonic value is given by:

$$R_{npts} = \frac{0.17}{npts} \tag{4.14}$$

where $npts$ is the number of edge pixels.

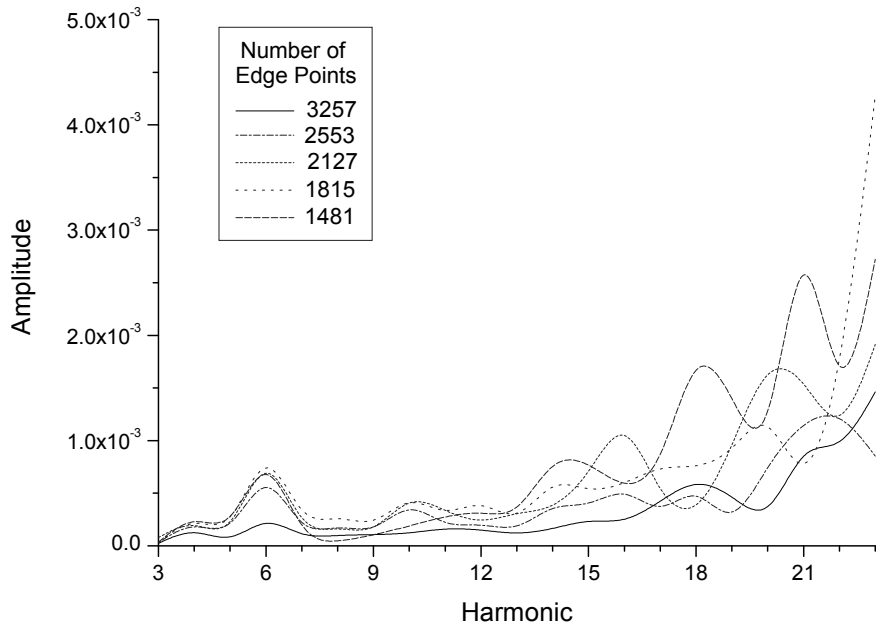

Figure 4.4: Bivariate plot of amplitude against harmonic number taken from identical images processed at different image resolutions - Image resolutions used: 10, 6, 4, 3 and 2 million pixels.

To account for the effect of pixel noise, the calculation of roundness is further modified to:

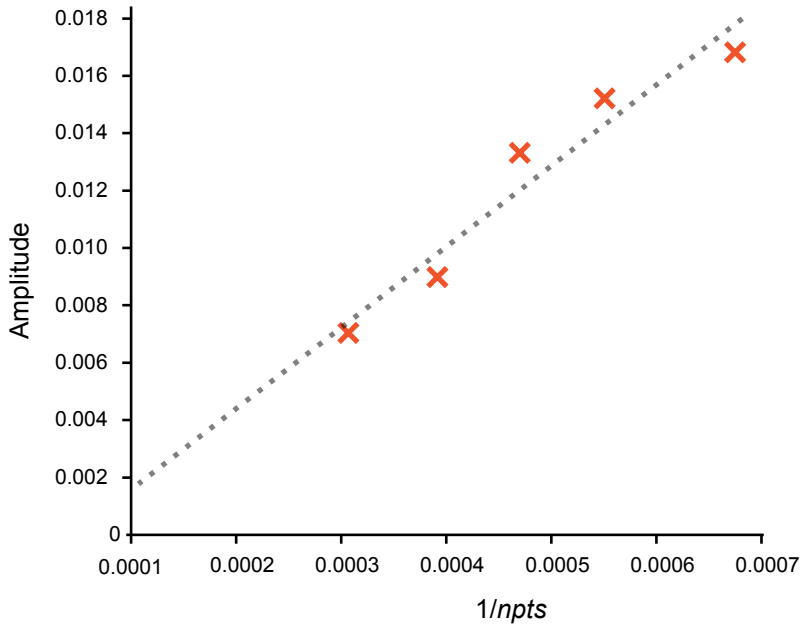

Figure 4.5: Bivariate scatterplot of amplitude against $1/npts$ for a perfect circle processed at a range of different image resolutions - Equation of the best-fit line derived is used to adjust for the influence of pixelation. Image resolutions used: 10, 6, 4, 3 and 2 million pixels.

$$P_{pre} = \sum_{3}^{m} c_k(R_k - R_{ek} - R_{npts}) \tag{4.15}$$

where R_k is the amplitude of the k^{th} harmonic, R_{npts} is the effect of pixel noise and $m = 23$.

Data normalization P_{pre} yields results of $0 \rightarrow \infty$, where 0 is a perfect ellipse. In order to produce data that are homologous to other roundness indices, P_{pre} is normalized to 1 using an exponential transformation:

$$P = \exp(-3P_{pre}) \tag{4.16}$$

On the normalized scale P ranges from 0 to 1, where 1 is a perfect ellipse and 0 is an infinitely angular particle.

4.2.4.2 Roundness comparisons

To assess the difference between automated and traditional roundness analyses, a representative range of particles sampled from the field (sites 50, 54, 71, 83, 88, 90 and 95 (Fig.

3.4)) was subjected to a manual Powers's (1953) roundness classification. To assess operator reliability, a further thirty-six particles from a range of Powers's (1953) roundness classes was also analysed digitally using Wadell's (1932) roundness index. Factors affecting the traditional (visually based) classification analyses were further investigated by re-analyzing the particle outlines used in Krumbein's (1941) visual comparison chart. Krumbein (1941) used eighty-one particle outlines to represent nine different particle roundness categories, which were digitized and quantified using automated (digital-based) roundness analysis. These data are compared to their corresponding Wadell (1932) roundness values, upon which the comparative charts were originally based (Krumbein, 1941).

4.2.5 Surface roughness analysis

Surface roughness can be the most difficult of all morphological parameters to define and quantify and has largely been avoided in glaciological studies, save noting the presence of striae or minor indentations. Proposed ISO specifications for measuring and analyzing surface roughness include: interferometry, stereogrammetry and digital-optical profiling (ISO, 2008). However, quantitative approaches to surface roughness suffer from an overabundance of analytical methods, referred to by Whitehouse (1982) as a 'parameter rash' (Fig. 4.6).

In geology, approaches have included: Fourier transforms (Ehrlich et al., 1980; Hubbard, Siegert and McCarroll, 2000), standard deviation (McCarroll, 1997), root-mean-square error (Haneberg, 2006) and fractals (Schwarcz and Exner, 1980; Stephen and W.H., 1986). Glaciological studies quantifying surface roughness have been predominantly concerned with planar surfaces (e.g. large boulders, bedrock outcrops and large-scale topography) in the context of surface exposure times (McCarroll and Ballantyne, 2000; Nesje et al., 1994), subglacial sliding conditions (Benoist, 1979; Hubbard, Siegert and McCarroll, 2000; Nye, 1969), the basal topography of ice sheets (Taylor et al., 2004; Rippin et al., 2006; Young et al., 2007; Siegert et al., 2005) and ice, snow and sea ice surface roughness (Andreas, 1987; Manninen, 1997). Surface roughness investigations at the particle-scale have been mainly restricted to micro-scale surface features of sand-sized (1 - 0.1 mm) quartz grains (see Dowdeswell, 1982; Mahaney, 2002), although increasingly other lithologies have been considered (Bowman et al., 2001; Mahaney et al., 2008). Broadly, it has been assumed that more weathered surfaces have a higher surface roughness resulting from chemical surface weathering, and that conversely, smooth surfaces and sharp angles are indicative of recent mechanical fracture (Mahaney, 1995). However, although these contrasting surface types may be easy to distinguish qualitatively, it is often difficult to assign causality (Sharp and Gomez, 1986). Currently the use of such evidence is almost entirely qualitative (Fuller and

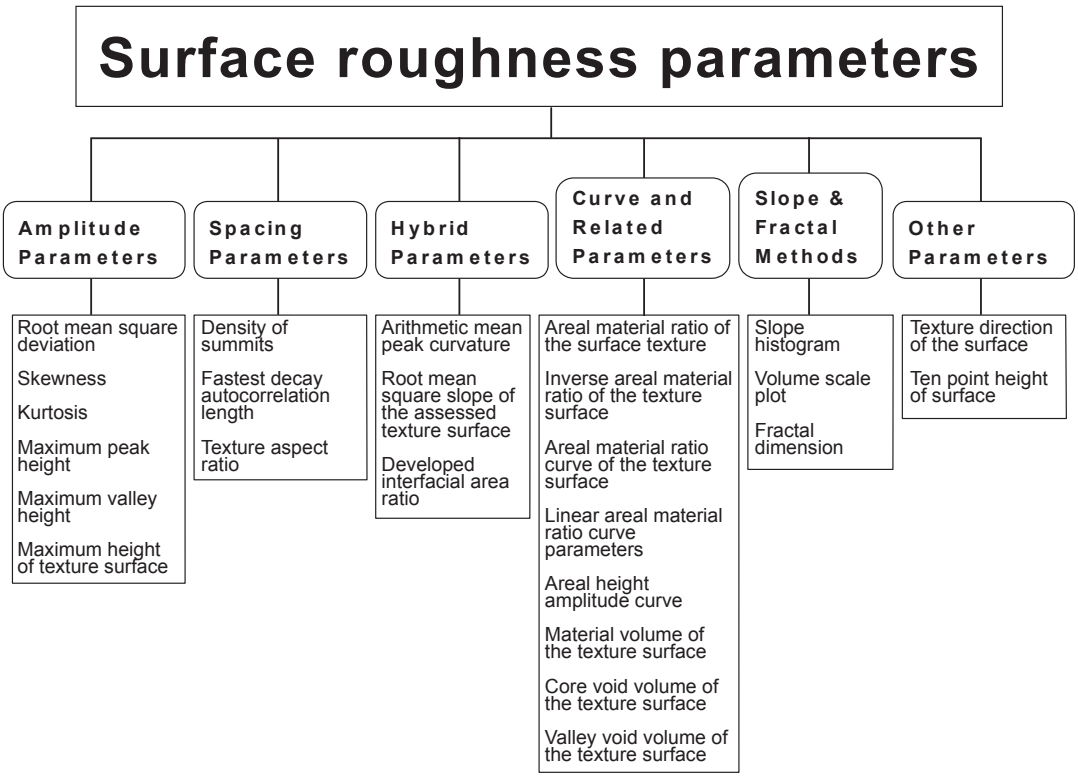

Figure 4.6: Flow diagram of surface roughness parameters -
(after Brown, 2006; his Figure 4.3.11)

Murray, 2002; Owen et al., 2003; Rose and Hart, 2008) and attempts to analyze sand-sized particles with FFT have been concerned with overall shape and roundness, rather than surface roughness *sensu stricto* (e.g. Bowman et al., 2001; Dowdeswell, 1982; Thomas et al., 1995). For familiarity and to allow glaciological comparisons to be made, the spectral power density SPD of a Fourier transform is used in this study following applications by Benoist (1979) and Hubbard, Siegert and McCarroll (2000) to glaciated bedrock surfaces in the Alps.

4.2.5.1 Surface roughness scale

To generate fully quantified roughness values, particle boundary co-ordinates were converted into metres using a scaling factor equivalent to pixel resolution. This converts frequency into wavelengths in metres, yielding roughness values comparable between surfaces of different scales, whether they are particle surfaces or planar surfaces. In order to generate a consistent transformation into the frequency domain, the length of every particle outline was extended to 400 mm. Use of Fourier analysis in the past to analyze particle surface roughness has suffered from a failure to remove the influence of particle shape and size (see discussion in Dowdeswell, 1982). In this study particle outlines were extended following removal of shape,

which otherwise would have been more mathematically complex and hence computationally intensive. Accordingly, Cartesian co-ordinates were converted to polar co-ordinates and the influence of shape R_{ek} removed (4.10). To extend a particle outline, points $\rho_i \rightarrow w$ between the actual particle outline length f and the extended length f_w were padded with existing values of ρ:

$$\rho_{i \rightarrow w} = \rho_{i+l} \tag{4.17}$$

where $w = \left[\frac{l}{f}\right] / f_w$ and l is the initial length of vector ρ. A value of total surface roughness ξ is calculated from the sum of the spectral power density of frequencies between 400 and 100 per particle length (corresponding with wavelengths from 1 to 4 mm):

$$\xi = \sum_{100}^{400} SPD_k \tag{4.18}$$

where SPD_k is the spectral power density of the k^{th} harmonic:

$$SPD = \frac{Y_k \overline{Y}_k}{n_k} \tag{4.19}$$

where Y_k is the amplitude of the k^{th} harmonic, $\overline{Y}_k$ is the complex conjugate of the k^{th} harmonic and n_k is the number of harmonics.

Following other works (e.g. Blott and Pye, 2008), ξ - values are categorized into a classification scheme with eight individual classes based on trends observed in empirical data and the covariance of surface roughness data with particle form and roundness data (Table 4.1). Following Powers's (1953) classification scheme, this surface roughness classification scheme uses a log-normal division of class sizes to create a system that is meaningful for the end-user and representative of conditions likely to be encountered when dealing with empirically derived data.

4.2.5.2 Surface roughness comparisons

To assess differences between automated and traditional surfaces roughness analyses, a representative range of particles sampled from the field (sites 35 to 80, (Fig. 3.4)) was subjected to a manual count of particles with striations. Surface roughness profiles taken by Hubbard, Siegert and McCarroll (2000) on limestone bedrock in front of Glacier de Tsanfleuron were analysed following the procedure above (4.18) in order to situate particle surface roughness measurements in a wider context. These surface roughness profiles were

taken at 0.001 m intervals for 0.1 m. The raw (x, y) - axis profiles were de-trended to remove the influence of large-scale slope effects and padded to a length of 400 mm following (4.17).

4.3 Results and discussion

4.3.1 Form analysis

The results of automated particle form analysis for samples from Glacier de Tsanfleuron are presented as a map of intercept sphericity values (Fig. 4.7a) and also presented as a bivariate scatterplot of b/a - axes against c/b - axes ratios (a so-called Zingg diagram) (Fig. 4.8). Fig. 4.7a shows an overall trend for the intercept sphericity of particles sampled from proglacial debris stripes to increase with distance from the glacier. Quantitatively, this can be described by a regression relationship between particle I_s – values and distance from the glacier margin. Correlation between the two variables is moderate ($r = 0.62$) and I_s – values increase at a mean rate of 3 x 10^{-5} m^{-1}. Qualitatively, this can be described as a decrease in the proportion of blade-shaped particles and, correspondingly, as an increase in the proportion of blocky particles. This trend is not exhibited by particles sampled from the northern zone of the proglacial area, adjacent to the large lateral moraine complex and proglacial stream. In this area, particle intercept sphericity values have a high degree of variability, with no obvious spatial trend.

The percentage difference between intercept sphericity values measured digitally and values measured manually is $\pm$2.15%. This very close correspondence indicates that form can be successfully reconstructed from field-based digital images. If the latter (traditional, visual-based method) is assumed to be correct, then digital analysis does not significantly improve the reliability of particle shape measurement (at a 99% confidence level). The error can be decomposed into two different sources: (i) the increased accuracy of the digital

Table 4.1: Suggested descriptive categories for a particle surface roughness index using log divisions to delimit class sizes, based on empirical data.

	Upper Limit	Lower Limit
Extremely Rough	–	1.83 x 10^{-6}
Very Rough	1.83 x 10^{-6}	1.49 x 10^{-6}
Rough	1.49 x 10^{-6}	1.07 x 10^{-6}
Moderately Rough	1.07 x 10^{-6}	7.11 x 10^{-7}
Moderately Smooth	7.11 x 10^{-7}	4.00 x 10^{-7}
Smooth	4.00 x 10^{-7}	1.68 x 10^{-7}
Very Smooth	1.68 x 10^{-7}	4.90 x 10^{-8}
Extremely Smooth	4.90 x 10^{-8}	–

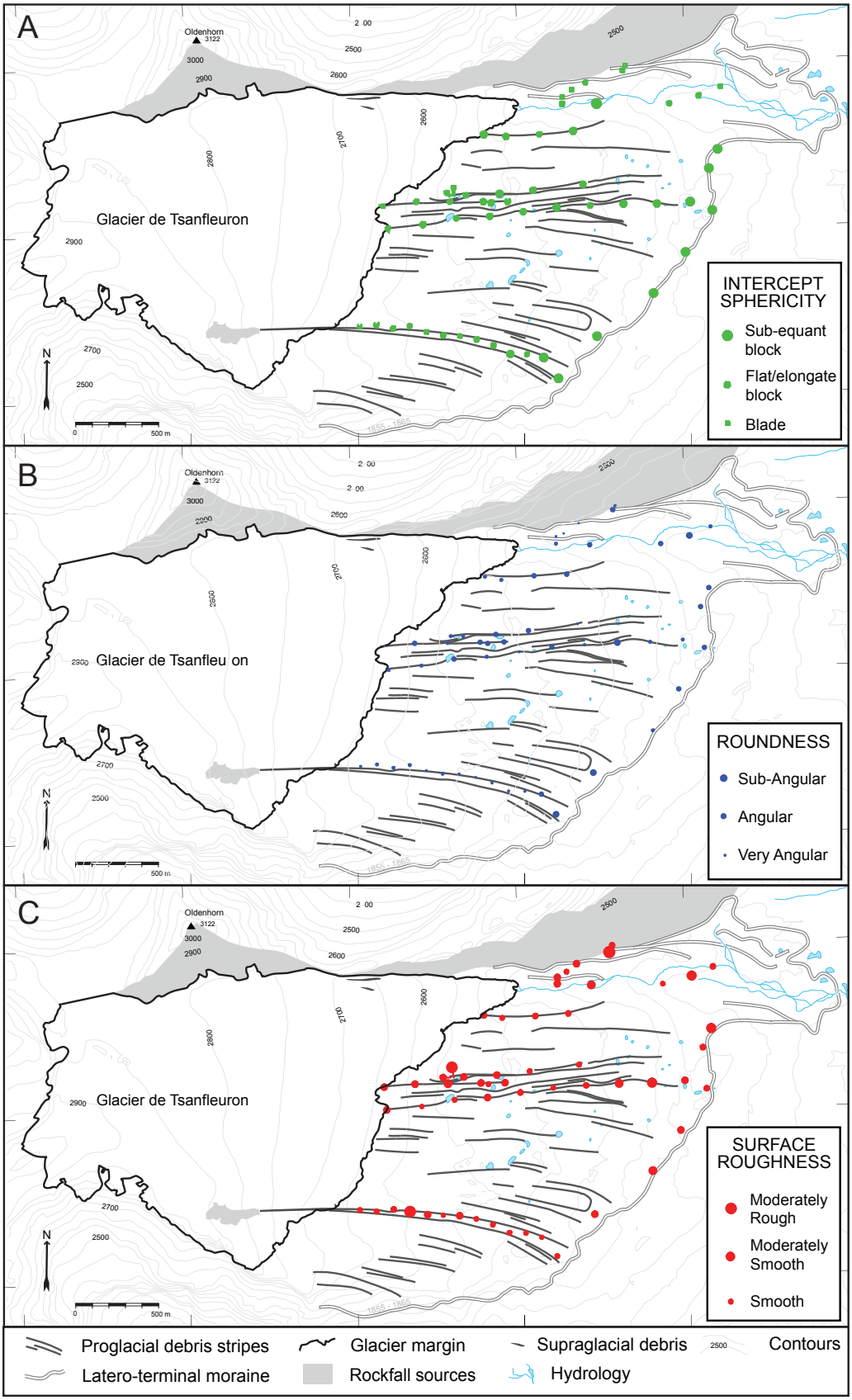

Figure 4.7: Maps of Glacier de Tsanfleuron and forefield displaying results of automated particle analyses for all sediment samples - (A) particle form (intercept sphericity values); (B) particle roundness (P - values), and (C) particle surface roughness (ξ - values).

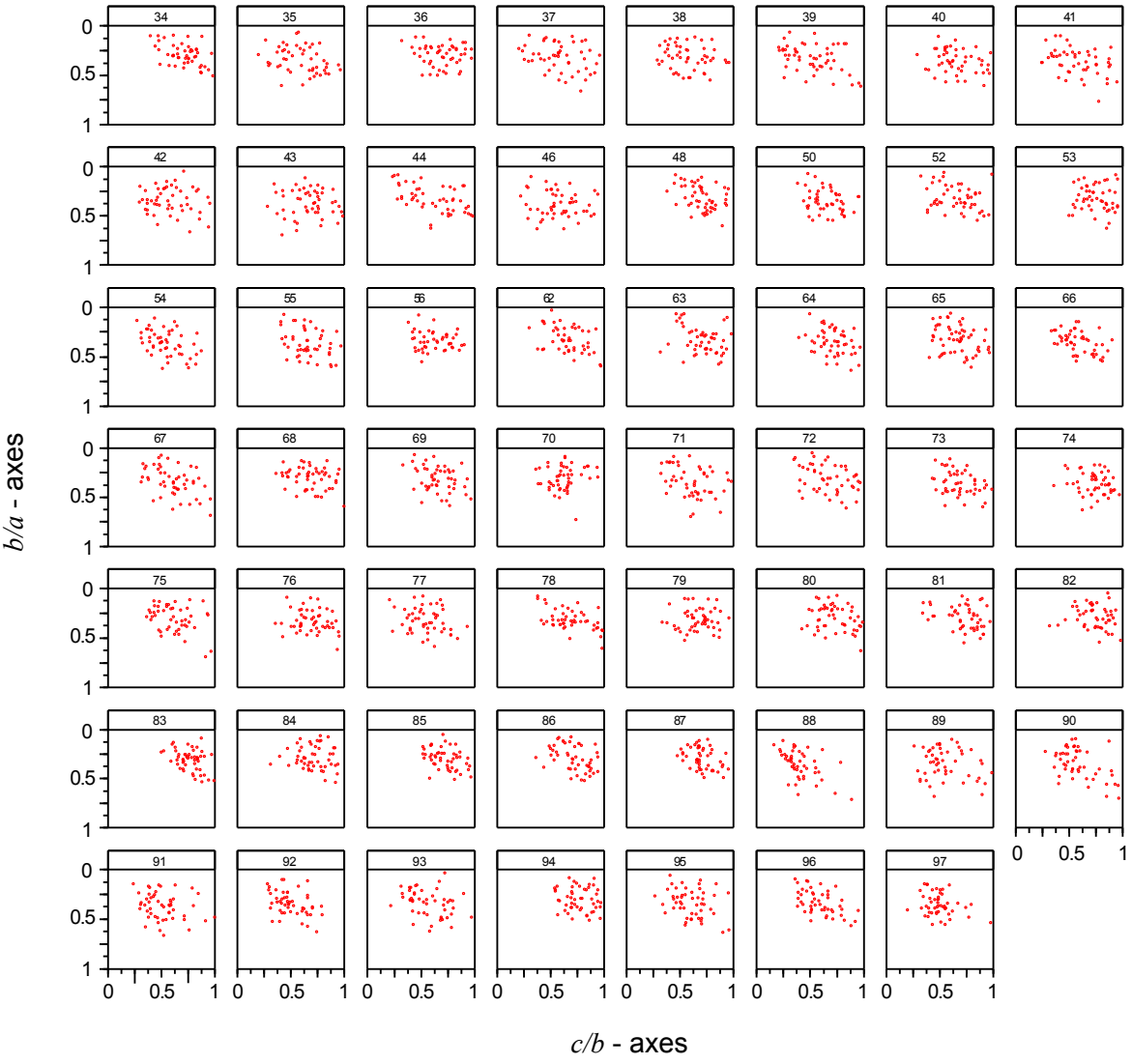

Figure 4.8: Bivariate scatterplots of particles b/a - axes plotted against c/b - axes (Zingg diagrams) - grouped by sediment samples taken from the proglacial area at Glacier de Tsanfleuron. See Fig. 3.4 for sample locations.

imaging method (∼0.9%), i.e. to 10 x 10^{-7} metres in the case of the automated method rather than 10 x 10^{-2} metres in the case of the manual method, and (ii) operator error to which the remaining unexplained variability (1.26%) is attributed. These data agree with operator variability quantified by other workers (Folk, 1955; Blott and Pye, 2008). Operator error in this study, as with others, is probably associated with inconsistencies in the definition and identification of a, b and c - axes. This highlights the overall problem of quantifying particle form using a pseudo-three-dimensional approach, i.e. it is often difficult to define a, b and c - axes with a high degree of precision.

4.3.2 Roundness analysis

The results of automated particle roundness analysis for samples from Glacier de Tsanfleuron are presented as a map of P - values (Fig. 4.7b). Particles P - values of samples from Glacier de Tsanfleuron range from 0 to 0.61 and have a mean value of 0.25, with a standard deviation of 0.09. Particles P - values of samples from Glacier de Tsanfleuron vary spatially with relation to sediment-landform association (see Section 5.2.2). In contrast with the correlation observed between I_s – values and distance away from the glacier (Section 4.3.1), P – values along proglacial debris stripes show no spatial trend with distance from the glacier. The absence of this observed trend may be because: (i) the mechanisms of wear operating on a particle during subglacial transport (i.e. increased wear leading to production of 'bullet-shaped' clasts) cannot be quantified using an automated (digitally based) analysis; (ii) in direct contradiction to the evidence provided by I_s – values, particles from proglacial debris stripes have not undergone a significant amount of wear, or (iii) post-depositional sub-aerial weathering removes any evidence of subglacial wear (Section 4.3.3).

The increased accuracy of the automated method is demonstrated in Fig. 4.9, where data are binned 0.05 intervals, rather than the large bins used in Powers's (1953) roundness histograms. The higher resolution of these data permits samples to be differentiated more easily from one another. For example, with bin sizes of 0.05, the 'Very angular' category of Powers's (1953) is subdivided into three different categories, allowing distinctions to be made between samples 88, 89 and 90, which indicate that particles comprising the lateral moraine at Glacier de Tsanfleuron are more angular than particles from the adjacent talus cone (Fig. 4.10). Using the traditional (visually based) Powers's (1953) roundness classification this distinction is lost and the samples are classified identically. The capability to make distinctions like these is particularly important in certain glaciological setting, such as within or beneath cold-based ice masses and debris-poor glacierized catchments, where the intensity of geomorphic processes may be low and the evolution of particle roundness is slow.

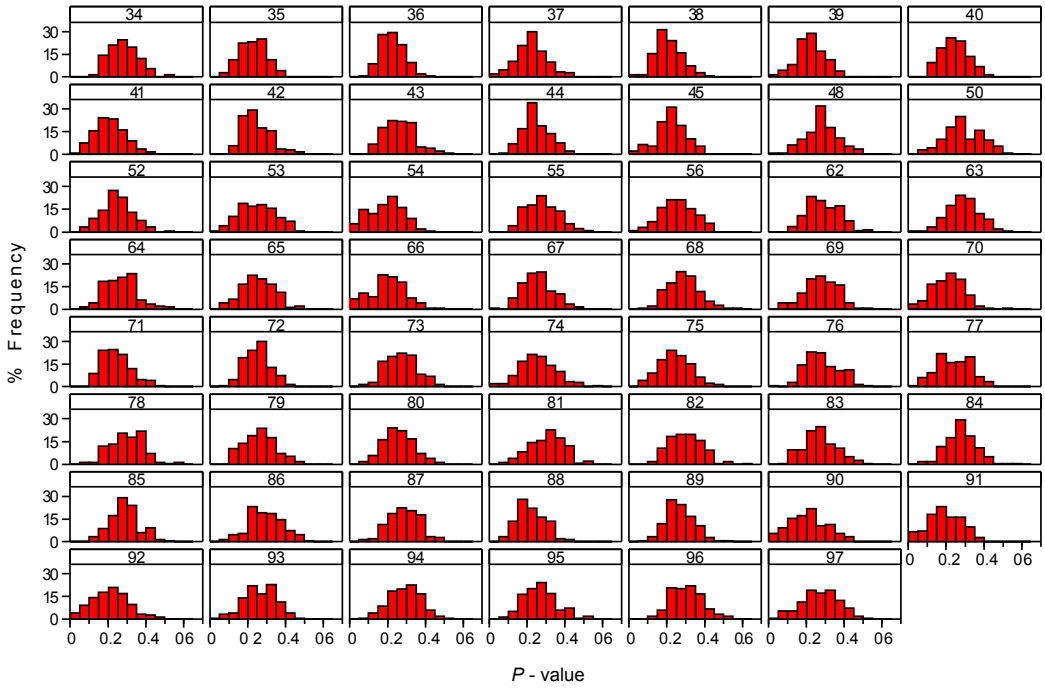

Figure 4.9: Percentage frequency histograms of automated particle roundness (P - values) for proglacial samples from Glacier de Tsanfleuron - See Fig. 3.4 for sample locations

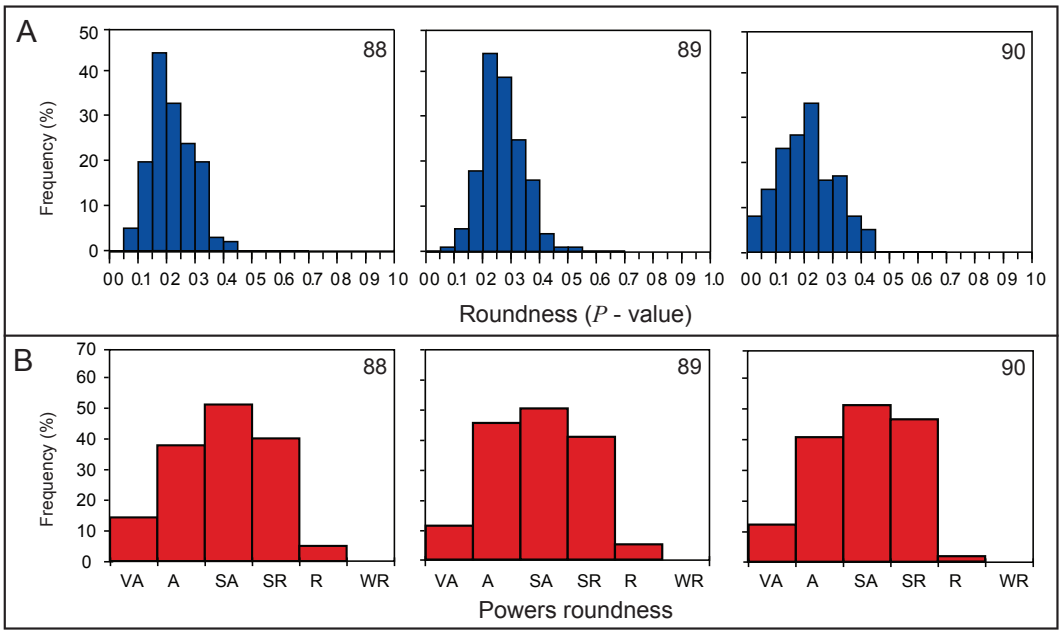

Figure 4.10: Percentage frequency histograms comparing automated and manual approaches to measuring particle roundness for samples 88, 89 and 90 from the proglacial area at Glacier de Tsanfleuron - using (A) an automated digitally based approach and (B) a visually based Powers (1953) roundness scale

Comparison of (visually derived) Powers's (1953) roundness classifications of 1050 particles with their respective (automatically derived) P - values shows only moderate correlation (Pearson's $r = 0.45$) and considerable variance ($R^2 = 20.7\%$). Indeed, a one-way ANOVA test indicated that while 'Very angular', 'Angular' and 'Subangular' classes were significantly different from each other (at a 95% confidence interval), there was no significant difference between 'Subrounded' and 'Rounded' classes at the same level, where $n = 192$ and 11 respectively (Fig. 4.11). The poor distinction between the latter two classes derives from the low number of particles in the 'rounded' class, resulting in a high of variance away from the mean. These statistics indicate that if samples of particles are sufficiently large (i.e. in the this study $n \geq 118$) the influence of outliers is reduced and a visually derived Powers roundness analysis is reliable. However, in the case of classes where the number of samples is relatively low, outliers have a greater influence and operator bias is high. This presents a sampling issue in environments where the number of particles in a particular Powers roundness class is low. Folk (1955) identified a similar problem when describing populations of 50 sand-sized particles using a Powers roundness classification. It is evident from these statistical data that a digitally derived continuous roundness scale eliminates a considerable amount of operator bias, rendering samples more reliable.

The capacity for a visual comparison scheme to be used to distinguish between particles of different roundness is explored further by re-analysing the particle outlines originally used by Krumbein (1941). P - values of the 81 particle outlines originally used by Krumbein (1941) are plotted against their respective (visually determined) Krumbein roundness scores as a bivariate scatterplot (Fig. 4.12). These data are strongly correlated (Pearson's $r = 0.953$) with low variance ($R^2 = 0.908$). The high goodness of fit of Krumbein's (1941) roundness classes to P - values may be largely accounted for by the large number of classes and the idealized morphology of the particles used by Krumbein (1941). Krumbein's (1941) roundness values are rounded to the nearest 0.1, which suggests that the variance between the two indices is probably lower than the R^2 value indicates. To test this relationship further, an ANOVA test was conducted, using P - values from the automated roundness analysis of the 81 idealized particle outlines originally used by Krumbein (1941), to determine whether the classes used were significantly different from each another. The ANOVA test indicated that the Krumbein (1941) index is low precision, because only three of the classes were significantly different from each other (at a 95% confidence level).

The Krumbein (1941) comparison chart uses particle outlines which are superficially different, but which are insufficiently distinct from one another. To examine the factors behind this limitation, a representative range of particles sampled in the field and geometric shapes were analysed manually using Wadell's (1932) roundness analysis method, the index on which Krumbein's classification scheme was originally based. A regression test of 36

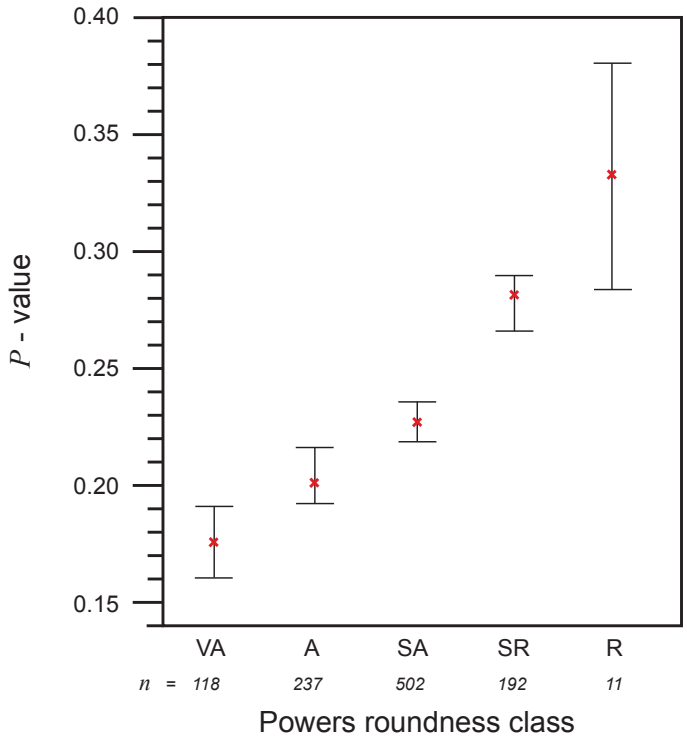

Figure 4.11: Bivariate plot of particle roundness (P - values) derived from automated roundness analysis against corresponding (visually derived) Powers' (1953) roundness class - with mean and 95% confidence levels for Powers roundness classes shown (n = number of samples per class).

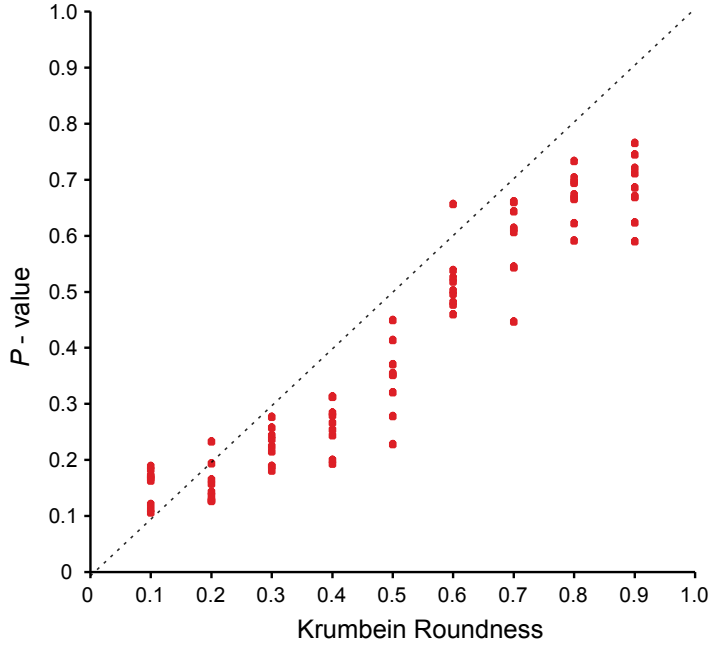

Figure 4.12: Bivariate scatterplot comparing roundness values of Krumbein's (1941) original particle outlines against their corresponding P - values - this uses Krumbeins original particle shape outlines, digitally analyzing them to derive equivalent P - values

particles, analysed both by Wadell's roundness index and automated FFT analysis, show that the data are strongly correlated (Pearson's r=0.85). The test also shows that 28% of the variability in the Wadell's roundness values remains unaccounted for (Fig. 4.13). Other researchers have demonstrated that the Wadell roundness index is limited by its use of a circle as a descriptor of a perfectly rounded particle (Barrett, 1980). To determine whether shape had a significant influence on the Wadell scores a multiple regression analysis was performed using particle elongation (width/length ratio) as a secondary explanatory variable. The multiple regression indicated that elongation only accounted for 0.03% of the variability in the Wadell (1932) roundness scores. Further consideration of the particle outlines used leads to the conclusion that Wadell's (1932) roundness index is therefore limited by its inability to quantify concavities along the particle outline. In some cases these are likely to be considerable sources of angularity and will to lead to an overestimate of particle roundness by Wadell's index. Similarly Wadell's index may underestimate the roundness of a particle if all corners are angular. In the case of a cube, the Wadell index gives a score of 0, compared to a P - value of 0.27 on the basis of automated (digitally based) analysis. Likewise, the Wadell (1932) index is unable to differentiate a cube from a tetrahedron, which has a P - value of 0.15.

4.3.3 Surface roughness analysis

Automatic (digitally derived) values of surface roughness (ξ - values) for all particles sampled at Glacier de Tsanfleuron range from 3.75 x 10^{-5} to 4.46 x 10^{-8}, with a mean value of 9.8 x 10^{-7} and a geometric mean of 4.6 x 10^{-7}. Automatic surface roughness data (ξ - values) are strongly positively skewed (skewness = 5.96) and have a standard deviation of 1.52 x 10^{-6}. Central tendency values of particle surface roughness (ξ values) for each sample from Glacier de Tsanfleuron are displayed as a map (Fig. 4.7c) and the frequency of surface roughness values for each sample are plotted as frequency histograms (Fig. 4.14). In contrast with both automatically derived particle form and roundness data, particle surface roughness data (ξ - values) exhibit no spatially dependent variability. The failure of the automated surface roughness data to characterize any spatial trends can be potentially accounted for by at least three factors: (i) the technique fails to capture surface roughness at a scale meaningful to wear or weathering processes; (ii) the particles sampled at Glacier de Tsanfleuron have a limited potential to preserve evidence of abrasive wear processes, or (iii) evidence of abrasive wear processes have been removed post deposition by sub-aerial weathering. In an attempt to explore the factors affecting these data, automatic (digitally derived) particle data are compared with traditional indices of surface roughness (percentage striations) and surface roughness data collected by Hubbard et al. (2000),

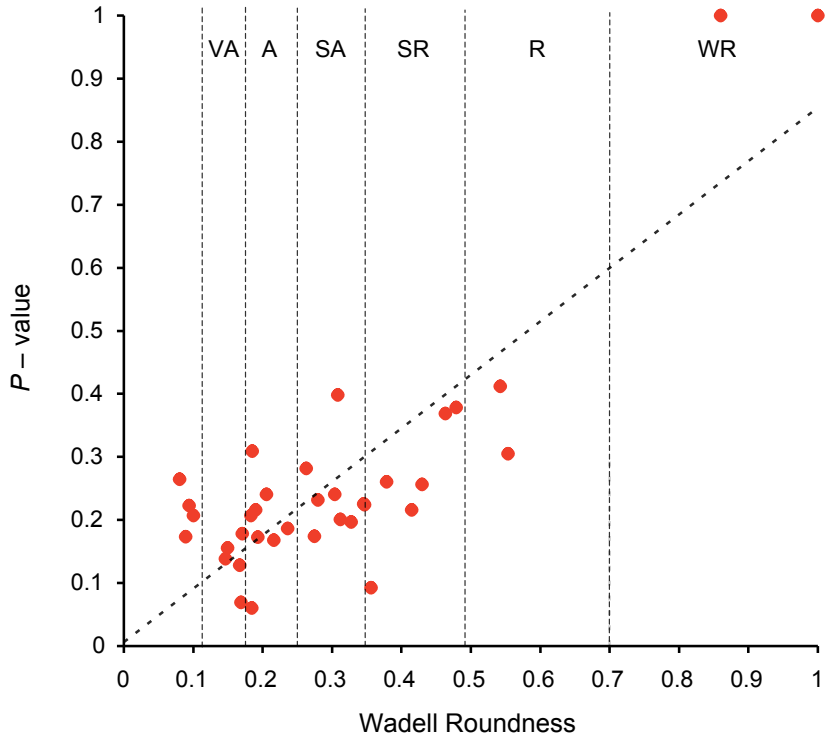

Figure 4.13: Bivariate scatterplot comparing Wadell's (1932) roundness index against P - values - uses particles from a representative range of sediment samples taken from the proglacial area at Glacier de Tsanfleuron ($n = 36$). Powers (1953) roundness classes are included for reference.

which are re-analysed in this study using the digitally based automated analysis procedure [4.18].

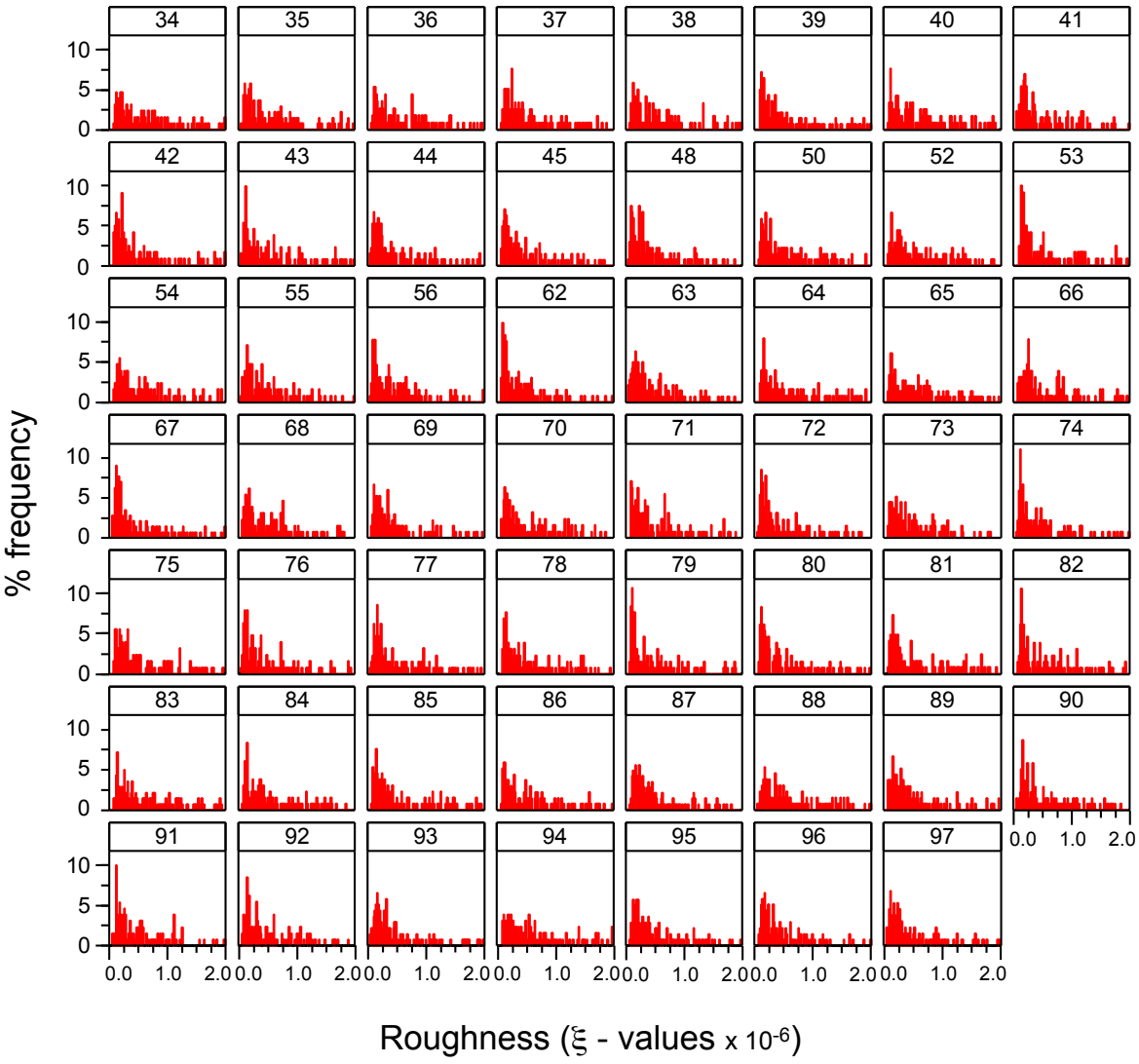

Figure 4.14: A percentage frequency histogram of particle surface roughness (ξ) values - particle samples taken from the proglacial area at Glacier de Tsanfleuron. See Fig. 3.4 for sample locations

Comparison of automated surface roughness (ξ - values) data against traditional (visually derived) percentage striation values show that there is no correlation (Pearson's $r = 0.09$) between these data (Fig. 4.15). The overall proportion of particles where striations are present is strikingly low (2.4%) and exclusively restricted to particles sampled at or near the glacier margin. The plateaux area at Glacier de Tsanfleuron is dominated by Urgonian limestone, with a small amount of Tertiary limestone (Fig. 1.2). Surface texture appears qualitatively variable at the particle scale due to the presence or absence of different fossils (Fig.4.16c) mineral veins and bedding planes (Fig.4.16e). While striations are observable

across a large section of the limestone bedrock in front of Glacier de Tsanfleuron (see Chapter 5), visual examination of the surface texture of particles collected at Glacier de Tsanfleuron permits the following observations to be made: (i) striations are short relative to the size of the clast (Fig.4.16a, b); (ii) striations are not uniformly orientated (Fig.4.16b); (iii) striations are very superficial ($\ll$1 mm deep) (Fig.4.16a, b), and (iv) surface weathering of particles removes all traces of abrasive wear (Fig.4.16c, d, e). Automated digital analysis of limestone particle outlines therefore fails to characterise small-scale wear products in the form of striations for the following reasons: (i) striations are very small and hence difficult to detect; (ii) striations are rapidly removed by surface weathering, and (iii) the volume of debris transported at Glacier de Tsanfleuron is small, hence the number of clast-to-clast and/or clast-to-bedrock interactions is probably quite low.

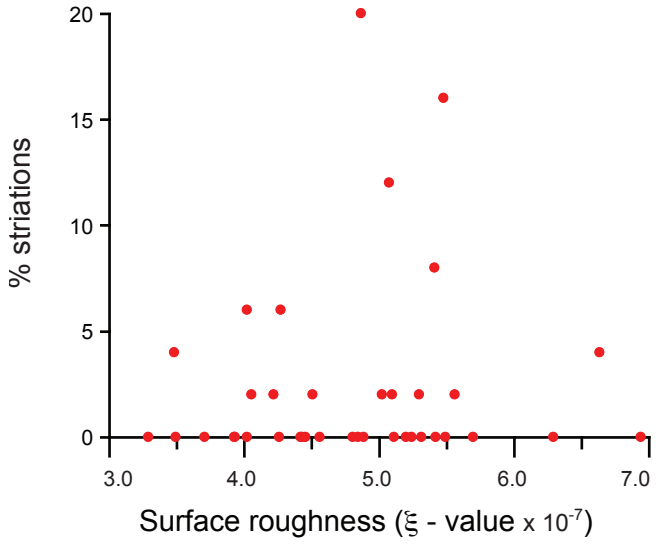

Figure 4.15: Bivariate plot of automated (digitally derived) surface roughness (ξ- values) against traditional (visually derived) striation percentages for particles sampled at Glacier de Tsanfleuron -

Re-analysis of surface profiles collected on bedrock by Hubbard, Siegert and McCarroll (2000) using automated (digitally based) surface roughness analysis provides additional insight into the nature of wear and weathering processes occurring at Glacier de Tsanfleuron. Hubbard, Siegert and McCarroll (2000) collected surface profiles on bedrock in former cavities and on glacially eroded bedrock at two sites, $\sim$0.1 km and $\sim$1.2 km away from the glacier margin, taking profiles parallel and normal to former ice flow direction at both sites. Automated surface roughness analysis (ξ - values) data show that the surface roughness (ξ - values) of glacially eroded bedrock increase with distance from the glacier margin, from extremely smooth (2.97 x 10^{-8}) to moderately smooth (5.4 x 10^{-7}) at 0.1 and 1.2 km respectively. In contrast, the surface roughness of bedrock surface profiles measured in former subglacial cavities decreased from extremely rough (1.8 x 10^{-6}) to rough (9.6 x 10^{-7}) at 0.1 and 1.2 km respectively. These data demonstrate that processes operating on the Urgonian limestone result in very different surface profiles, depending on whether the surfaces are corroded by meltwater or abraded by subglacial debris. Additionally, it is apparent from the response of both types of surfaces (former cavities and glacially eroded bedrock) that exposure to subaerial weathering eventually results in the formation of a bedrock surface roughness that is somewhere between rough and moderately smooth. The implications of these findings for individual particles are that a particle entrained in subglacial transport should become rougher following deposition by the glacier. That this trend is not observed implies that: (i) not all the particles in transport have been in contact with the bedrock surface, and (ii) the processes acting on particles in englacial transport are very different from those acting on subglacial bedrock.

The implications of these findings for an automated surface roughness analysis are that any measurements of surface roughness are strongly limited by particle lithology. In order to overcome this limitation it is apparent that a qualitative survey of particle surface texture is required to focus the sampling strategy. In catchments of more resistant lithology, however, it is probable that rates of subaerial weathering will be much lower and hence allow rates of surface roughness change to be quantified. In the case of particle sampling at Glacier de Tsanfleuron, it would be necessary to increase sampling density towards the glacier terminus to try and capture rates of particle surface modification.

4.4 Conclusions

The aims of this chapter were to review the shortcomings of traditional visually based approaches to measuring particle morphology and develop an alternative, low-cost, automated digitally based alternative. The automated method developed is based on inexpensive digital photography and uses a series of Matlab-based algorithms to extract particle outlines

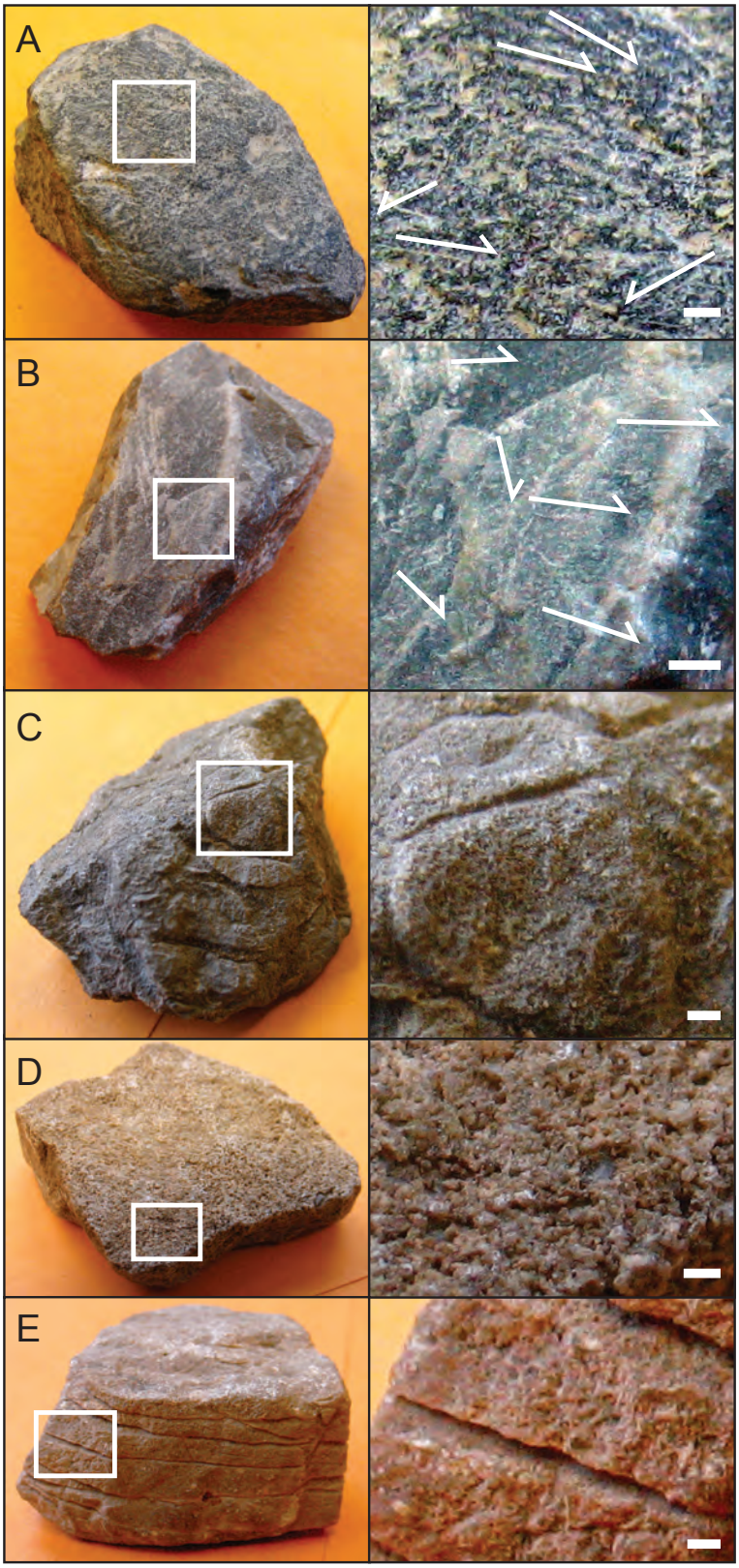

Figure 4.16: Photographs and close-ups (white boxes) of Limestone particles sampled at Glacier de Tsanfleuron for automated analysis of particle morphology - (A) and (B) particles from debris stripe emerging at the glacier margin (sample site 53); (C), (D) and (E) particles from distal end of debris stripe (sample site 34). Arrows indicate striation direction. Scale bars ∼1 mm.

and quantify particle form, roundness and surface roughness. These automated algorithms are applied to samples of 50 particles taken from Glacier de Tsanfleuron, Switzerland and compared to traditional (visually based) analyses of the same particle samples to quantify the advantages of automated digital analysis methods. Development and analysis of automated techniques for the quantitative description of particle morphology have resulted in these findings:

1. Automated (digitally based) measurement of particle form can be successfully reconstructed from field-based images. Comparisons with traditional (visually based) methods indicate that this technique is still subject to operator error, probably caused by uncertainties in identifying a, b and c - axes. Improvements in accuracy offered by an automated (digitally-based) approach are not a significant improvement over a traditional (visually-based) approach.

2. Automated (digitally based) roundness analysis are corollary with traditionally (visually based) Powers's (1953) roundness index. Automated (digitally based) roundness analysis represents a considerable improvement over traditional (visually based) analyses by providing a continuous roundness scale and reducing operator bias associated with visual comparison charts. The automated (digitally-based) approach also offers a means of identifying particles where roundness $\leq$0.12, which is notably absent from the traditional Power's roundness scale. Particles where roundness $\leq$0.12 represented up to 10% of the overall population in 15 samples analysed in this study.

3. Automated (digitally based) approaches to surface roughness measurements do not correlate with measurements made traditionally by counting particles with striated surfaces. Close inspection of particles sampled from Glacier de Tsanfleuron indicate that surface weathering of exposed clasts and bedrock surfaces rapidly removes traces of abrasive wear and that automated values of particle surface roughness are determined by local variations in lithological composition. Re-analysis of surface profiles collected from glaciated limestone bedrock at Glacier de Tsanfleuron (Hubbard, Siegert and McCarroll, 2000) indicate that processes operating on bedrock are very different to processes operating on particles in englacial transport. It is recommended that qualitative reconnaissance should direct a sampling strategy of particles for automated surface roughness analysis in any one environment.

Chapter 5

Structure and Sedimentology of Glacier de Tsanfleuron

5.1 Introduction

This chapter presents and interprets the results of structural mapping from aerial photography and fieldwork and of laboratory analyses of sediment samples collected at Glacier de Tsanfleuron from a range of sediment-landform assemblages during fieldwork in 2007. These data were collected to identify the processes involved sediment transport and the formation of sediment-landform assemblages at a small temperate valley glacier.

The aims of this chapter are:

i. To examine the extent to which the structural dynamics of Glacier de Tsanfleuron influence glacial sediment transport,

ii. To determine whether proglacial debris stripes in front of Glacier de Tsanfleuron can be characterised by spatially distinct trends in particle-size-distribution and particle morphology indices,

iii. To make a first-order approximation of glacial sediment discharge at Glacier de Tsanfleuron.

To address these aims, the structure of the glacier was mapped below the snow-line and one hundred and three sediment samples were collected across the glacier surface and proglacial area. Section 5.2 presents the results of structural mapping and laboratory analyses (detailed in Section 3.3). Interpretations of structures and sediment-landform assemblages are made on the basis of the data collected in the context of observations from previous studies (Section 5.3). The processes involved in glacial sediment transport

and sediment landform assemblage formation are discussed in Section 5.4. Section 5.5 summarises the findings of the research presented and discussed in this chapter.

5.2 Results

5.2.1 Glacier structure

Glacier de Tsanfleuron is composed of two structural Flow Units: a northern unit A and a southern unit B (Fig. 3.4, 5.1). These can be identified by the folding of arcuate planar structures (S_0) into flow-parallel planar structures (S_1). The development of two Flow Units is the result of ice divergence around a west-east orientated subglacial ridge at (364000, 5131000) (Chandler, 2005).

Arcuate planar structures (S_0) are laterally continuous across the exposed ice surface, becoming progressively more elliptical and folded towards the terminus. Arcuate planar structures in Flow Unit A are more steeply dipping on average than in Flow Unit B (central tendencies = 25° and 14° respectively). Three different ice types comprising S_0 structures were observed at Glacier de Tsanfleuron: (a) coarse clear ice, with crystal sizes ranging from 50 to 180 mm; (b) coarse bubbly ice with crystal sizes ranging from 50 to 180 mm, and (c) fine yellow bubbly ice, composed of crystals of size from ∼2 to 7 mm in diameter. Debris concentrations in these ice types was low, <0.1% by weight. These occurred in a range of combinations, including: (a) coarse clear and fine bubbly; (b) coarse-bubbly and fine-bubbly; (c) coarse-clear, fine-bubbly and coarse-bubbly, and (d) coarse-clear and coarse-bubbly. However, planes of fine, yellow, bubbly ice, 20 to 100 mm wide, interposing planes >2 m wide of coarse clear ice were the most common combination. In Flow Unit A arcuate planar structures are often folded into open isoclinal folds with upglacier-dipping fold axes (Fig. 5.1b).

Longitudinal planar structures (S_1) are concentrated at the glacier's northern margin and at the boundary between the two Flow Units. These S_1 structures generally become more closely spaced and steeply dipping towards the glacier margins, such that they they dip at a mean angle of 47°. These longitudinal planar structures are compositionally similar to S_0 continuous layering, with which they form a structural continuum, with S_0 planes becoming gradually transposed downglacier into S_1 planes.

Brittle fractures (crevasses and crevasse traces (S_2)) are ubiquitous across the glacier. In the upper and middle sections they are orientated broadly north-south, orthogonal to ice flow. Towards the terminus numerous upglacier-orientated chevron crevasses in Flow Unit A occur at the north ice margin, associated with the higher surface velocities and marginal shear stress here (Nye, 1952). The dip of these fractures is consistently vertical

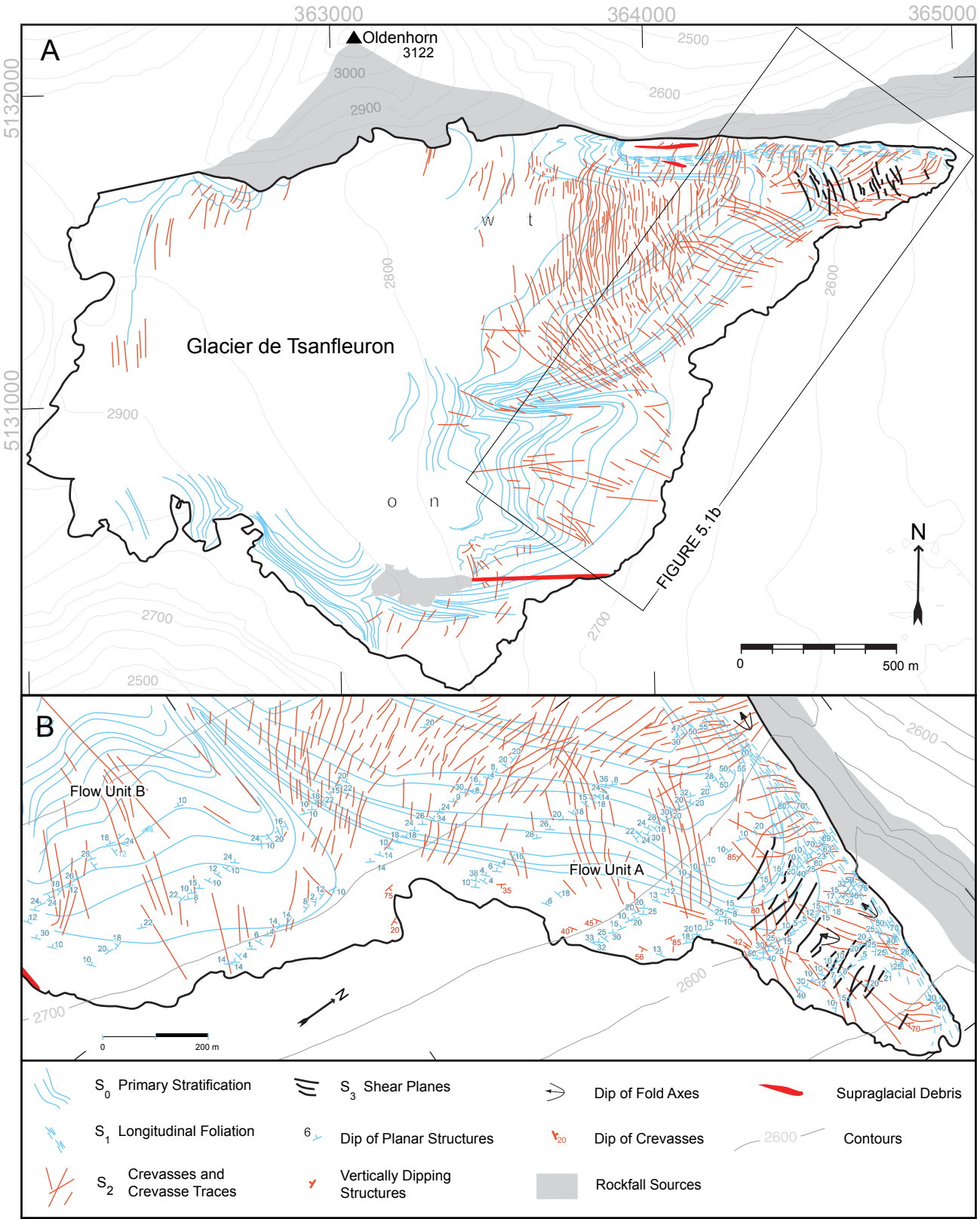

Figure 5.1: Map of structures identified at Glacier de Tsanfleuron - (a) Overview of glacier structure from 1998 aerial photography with 2007 terminus extent, (b) detail of glacier structure measured by surface mapping during 2007 fieldwork.

to sub-vertical, with no downglacier rotation. Crevasses in the lower sections of Flow Unit B are predominantly orientated longitudinally, parallel to ice flow, and are consistent with laterally unconstrained ice flow on the limestone plateau (Section 5.2.3.1). These fractures also have a consistently vertical to sub-vertical dip.

A second generation of brittle fractures (S_3) occurs in the lower section of Flow Unit A. These form transverse planar structures, up to 200 m long, which cut across S_0 continuous layering, S_1 longitudinal planar structures and S_2 brittle fractures. S_3 brittle fractures were also observed in cross-section at the glacier bed in subglacial cavities close to the terminus in Flow Unit A and at the boundary between Flow Unit A and B. S_3 fractures dip upglacier at a mean angle of 40°, and are often observed in association with the folding of S_0 continuous layering into hook-shaped asymmetric folds (Fig. 5.2). In subglacial cavities S_3 fractures are associated with the folding of sequences of subglacial ice facies.

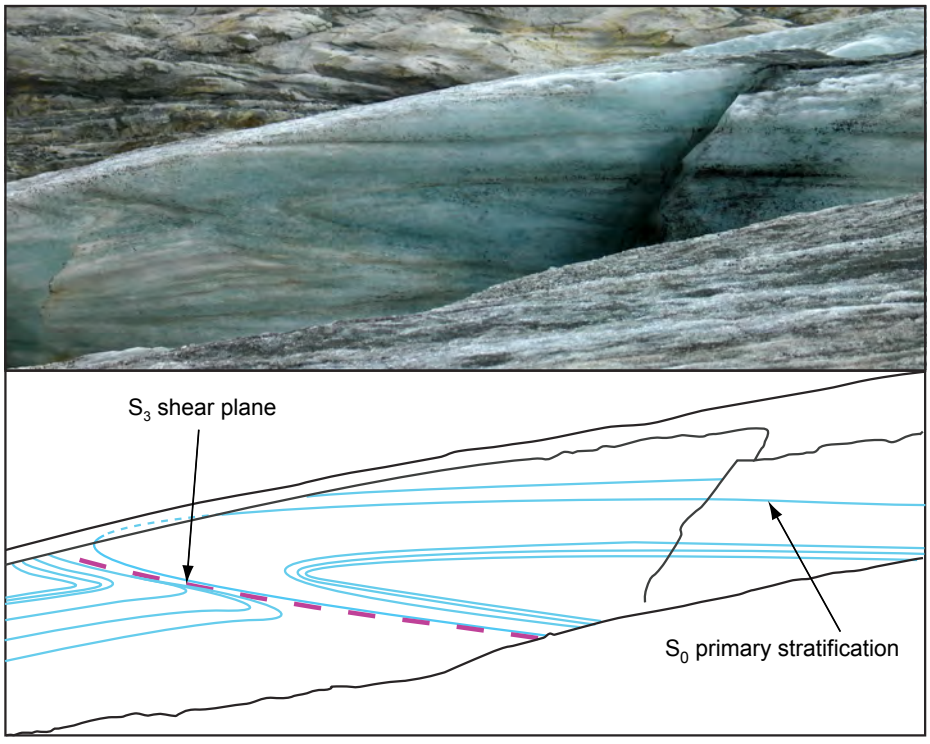

Figure 5.2: Annotated photograph of S_0 continuous layering dissected by an S_3 shear plane - S_0 continuous layering is deformed into asymmetric hook-shaped fold by vertical displacement across S_3 shear plane.

5.2.2 Sediment-landform assemblages

Seven distinct sediment-landform assemblages are identified at Glacier de Tsanfleuron: talus cones, supraglacial debris stripes, subglacial debris stripes, lateral moraines, termi-

nal moraines, glaciofluvial outwash plain and proglacial debris stripes (Fig. 3.4). Table 5.1 presents summary statistics of sediment textures for each sediment-landform-association, including: percentage gravel, sand and mud; geometric mean particle size; median particle size, and fractal dimension of the particle-size-distribution. The mean particle-size-distribution of each sediment-landform assemblage is presented in Fig. 5.3. The similarity between the mean particle-size-distribution of each sediment-landform assemblage is quantified by a $\cos\theta$ similarity index (Table 5.3). Table 5.2 and Fig. 4.7) summarize the mean particle size, dispersion and probability of the modal sizes as identified by Gaussian Component Analysis (GCA). Fig. 5.4 presents a bivariate scatterplot of particle size against sorting for each mode identified by GCA. Table 5.4 summarizes central tendencies of particle intercept sphericity (Fig. 4.7a), roundness (Fig. 4.7b) and surface roughness (Fig. 4.7c) for sediment-landform assemblages sampled in the proglacial area.

Table 5.1: Statistical characteristics of mean particle-size-distributions for matrix samples from sediment-landform assemblages at Glacier de Tsanfleuron. Note that these samples only represent particle sizes from 2000 to 0.01 μm (-1 to 12 ϕ)

	Gravel	Sand	Mud	D_{50}	Mean particle size	σ	m	r^2
		% mass		μm	μm			
Talus cones	12	68	20	380	284	5.60	2.42	-0.993
Supraglacial debris	11	73	15	552	371	2.30	2.26	-0.988
Subglacial debris	13	73	14	674	395	2.40	2.45	-0.995
Lateral moraine	11	73	16	419	314	2.40	2.42	-0.996
Terminal moraine complex	8	73	19	436	297	2.45	2.43	-0.996
Proglacial debris stripes	9	76	15	503	347	4.77	2.40	-0.983
Glaciofluvial outwash plane	8	79	13	521	375	2.19	2.30	-0.994

Table 5.2: Results of analyses of particle morphology of samples from sediment landform assemblages at Glacier de Tsanfleuron: mean values of intercept sphericity, roundness and surface roughness.

	Intercept sphericity	Roundness	Surface roughness
Talus cones	0.54	0.20	4.55×10^{-7}
Supraglacial debris	–	–	–
Subglacial debris	0.70	0.23	4.87×10^{-7}
Lateral moraine	0.60	0.19	5.55×10^{-7}
Terminal moraine complex	0.70	0.27	5.14×10^{-7}
Proglacial debris stripes	0.65	0.23	4.78×10^{-7}
Glaciofluvial outwash plain	0.64	0.26	5.15×10^{-7}

Table 5.3: Cosθ matrix of similarity - A comparison between mean particle-size-distributions of matrix samples from each sediment landform assemblage: (i) talus cones; (ii) supraglacial debris; (iii) subglacial debris; (iv) lateral moraine; (v) terminal moraine complex (vi) proglacial debris stripes; (vii) glaciofluvial outwash plain.

	i	ii	iii	iv	v	vi	vii
i		0.982	0.943	**0.992**	0.971	0.970	0.956
ii	0.982		0.966	0.989	0.982	0.987	0.982
iii	0.943	0.966		0.964	**0.992**	**0.991**	**0.993**
iv	**0.992**	0.989	0.964		0.987	0.986	0.976
v	0.971	0.982	**0.992**	0.987		**0.998**	**0.996**
vi	0.970	0.987	**0.991**	0.986	**0.998**		**0.998**
vii	0.956	0.982	**0.993**	0.976	**0.996**	**0.998**	

Table 5.4: Results of Gaussian component analysis for mean particle-size-distributions of matrix samples from sediment landform assemblages at Glacier de Tsanfleuron.

	Mode 1			Mode 2			Mode 3		
	ϕ	σ	p	ϕ	σ	p	ϕ	σ	p
Talus cones	-0.32	0.48	0.29	3.24	2.22	0.71	–	–	–
Supraglacial debris	-0.33	0.47	0.35	3.12	2.09	0.65	–	–	–
Subglacial debris	-0.52	0.54	0.32	1.97	1.27	0.49	6.27	1.86	0.19
Lateral moraine	-0.43	0.40	0.25	1.97	1.39	0.55	5.40	2.03	0.20
Terminal moraine complex	-0.15	0.55	0.30	2.08	1.34	0.50	5.69	2.03	0.20
Proglacial debris stripes	-0.21	0.53	0.32	1.99	1.33	0.48	5.39	1.90	0.20
Glaciofluvial outwash plain	-0.11	0.57	0.35	1.91	1.27	0.47	5.02	2.08	0.18

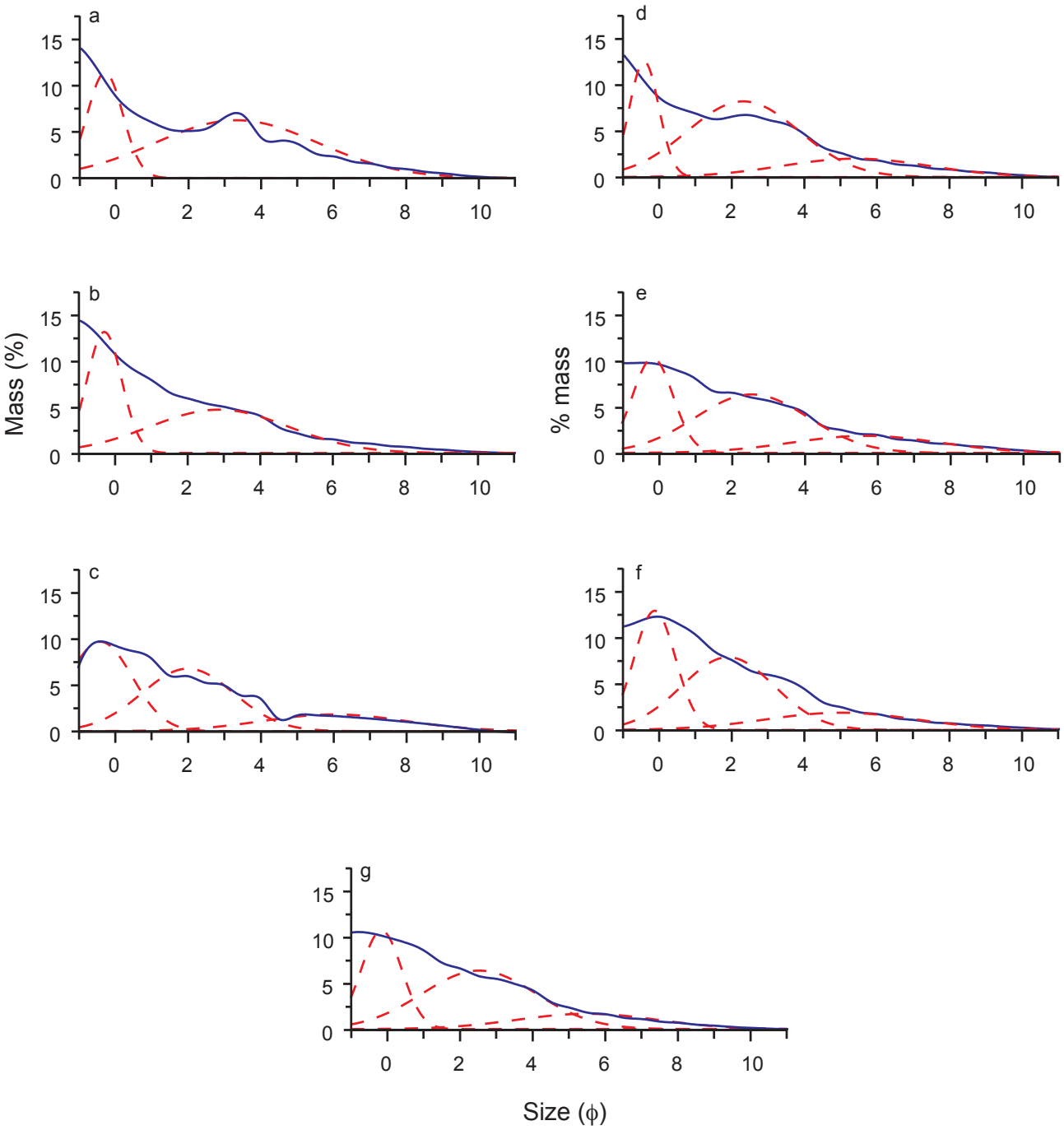

Figure 5.3: Bivariate scatterplots of mass against mean particle-size-distribution for matrix samples taken from sediment-landform assemblages - (a) talus cones; (b) supra-glacial debris; (c) subglacial debris planes; (d) lateral moraine; (e) terminal moraine complex; (f) glaciofluvial outwash plain, and (g) proglacial debris stripes.

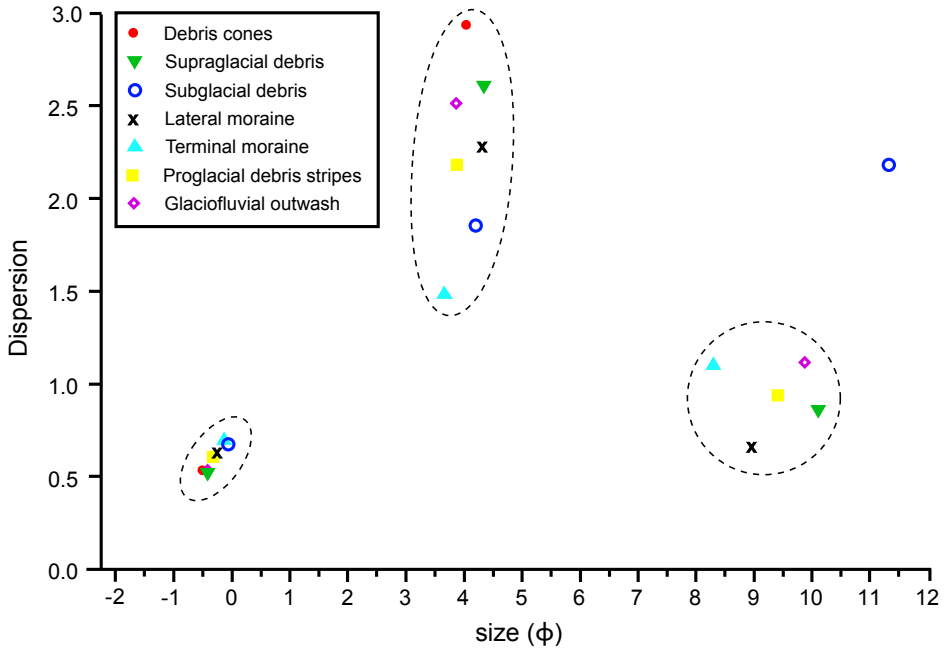

Figure 5.4: Bivariate scatterplot of particle size plotted against standard deviation of sediment modes - identified by Gaussian-component-analysis of matrix samples from sediment-landform assemblages

5.2.2.1 Talus cones

Debris in cone-shaped accumulations up to 100 m high occurs below the free-faces of the Oldenhorn and Sanetschhorn, abutting the northern lateral margin of Glacier de Tsanfleuron (Fig. 5.5a). These consist of clast-supported boulder gravel, with an extremely poorly sorted matrix (σ = 5.6) comprising ~10% of the sediment. Median matrix particle size (D_{50}) is 284 μm, with mud and silt comprising 20% and 68% of the matrix respectively. Particle-size-distributions of matrix samples from talus cones are significantly similar ($\cos\theta$ = 0.99) to matrix samples from lateral moraine sediments. GCA identified a mode at 1249 μm (-0.3 ϕ) and a mode at 106 μm (3.2 ϕ). These modes account for 29% and 71% respectively of the probable Gaussian component of the particle-size-distribution. Particle-diameter-abundance plots indicate that the particle-size-distributions has a mean fractal dimension of 2.42 (r^2 = -0.993). Particles are slightly elongate and slightly flat in form, with an intercept sphericity of 0.57. Mean particle roundness is angular (P – value = 0.20) and mean surface roughness is moderately smooth (ξ – value = 4.55 x 10^{-7}).

5.2.2.2 Supraglacial debris stripes

Supraglacial debris stripes occur at two locations: (1i) as a 1 to 10 m wide debris stripe trending eastwards of a nunatak towards the glacier terminus (Fig. 5.6 and (ii) as two

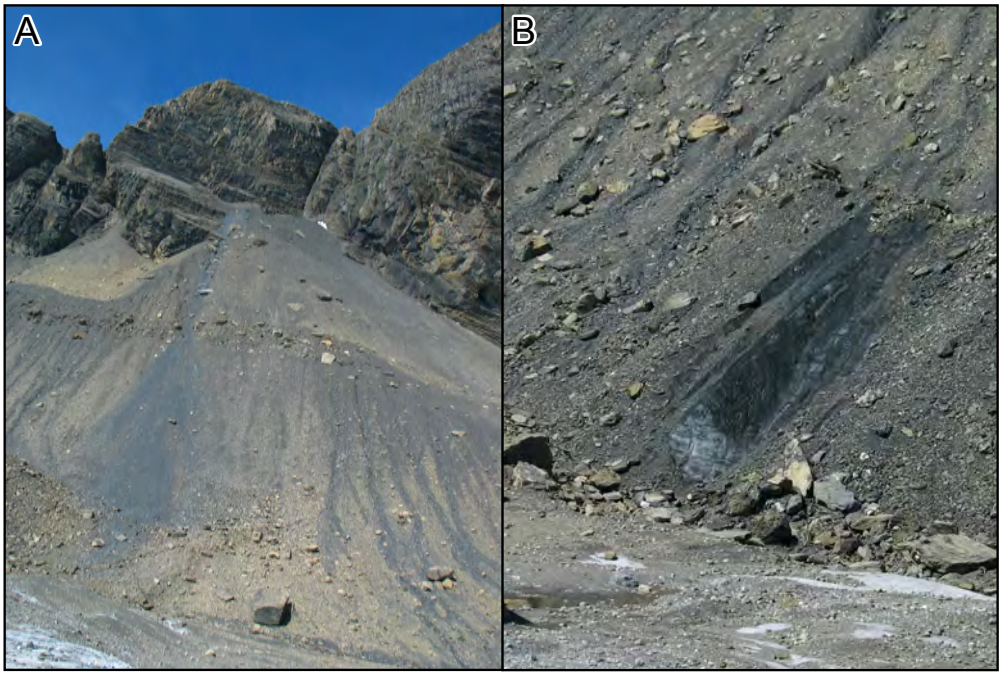

Figure 5.5: Talus cone and lateral moraine at Glacier de Tsanfleuron - (a) talus cone on the southern face of the Sanetschhorn above the 'Little Ice Age' lateral moraine (boulder at bottom centre is ~4 m high) and (b) ice-cored inner later moraine ridge dating from an advance during the late 1970s.

isolated west - east trending deposits ~10 m long and ~5 m wide with a thickness of 1 or 2 clasts near the glaciers northern margin (Fig. 5.6b). Supraglacial debris is very poorly sorted (σ = 2.3), with a median particle size of 551 μm. Mud and sand make up between 13% and 21%, and 67% to 76% of the facies respectively. The $\cos\theta$ similarity index does not identify any matrix samples from other sediment-landform assemblages that are similar to matrix samples from supraglacial debris stripes (at a significance level of 0.99). GCA identified 2 modes, centered on 1254 μm (-0.3 ϕ) and 115 μm (3.12 ϕ) respectively. These modes account for 35%, 65% respectively of the probable Gaussian component. Particle-diameter-abundance plots indicate that particle-size-distributions have a mean fractal dimension of 2.26 (r^2 = -0.988). Particles from supraglacial debris stripes were not available for morphological analyses.

5.2.2.3 Subglacial debris planes

Subglacial debris occurs in planar debris-rich basal ice, which is pervasive at the glacier terminus, ranging in thickness between 0.1 and 10 m. Debris-rich basal ice at Glacier de Tsanfleuron typically has a massive structure with mean debris concentrations of ~40 g l^{-1} (Coulson, Unpublished). Silt- to clay-sized particles are predominantly transported as

Figure 5.6: Photographs of supra- and proglacial debris stripes
- (A) Debris Stripe 1 taken from nunatak looking downglacier (people for scale); (B) Debris Stripe 3 emerging from the glacier at the terminus, (C) Debris Stripe 4 passing over and capturing sediment from a sinkhole in the karst forefield. Note the sharp boundary between the debris stripe and bare bedrock (backpack left of centre for scale).

aggregate clots (Fig. 5.7b), in contrast to boulder- to sand-sized particles, which are mainly transported as isolated or dispersed clasts (Fig. 5.7a). Crude layering and flow-parallel debris trains are observable at many locations, frequently dominated by a small range of particle sizes <1 mm. Particles comprising flow-parallel debris trains have a discernible planar fabric, parallel to ice flow and in some locations are continuous with proglacial debris stripes (e.g. DS_2). Subglacial debris are very poorly sorted ($\sigma = 2.3$), with a median particle size of 395 μm. Mud and sand comprise between 8% and 22% (mean = 14%), and 63% and 80% (mean = 73%) of the facies respectively. Particle-size-distributions of matrix samples from subglacial debris planes are significantly similar ($\cos\theta = 0.99$) to matrix samples from the terminal moraine complex, proglacial debris stripes and glaciofluvial outwash sediments. GCA identifies 3 modes, at 1435 μm (-0.5 ϕ), at 255 μm (1.9 ϕ) and at 13 μm (6.3 ϕ). These modes account for 32%, 49% and 19% respectively of the probable Gaussian component of the particle-size-distribution. Particle-diameter-abundance plots indicate that particle-size-distributions have a mean fractal dimension of 2.45 (r^2 = -0.995). Particle form is moderately elongate and slightly flat, with a mean intercept sphericity of 0.70. Striations were observed on 17% of the particles sampled. Particle roundness is angular (P – value = 0.23) and a mean surface roughness is moderately smooth (ξ – value = 4.87 x 10^{-7}).

5.2.2.4 Lateral moraine

A lateral moraine complex extends eastwards from the northern margin of the glacier for 1500 m. It is composed of a 150 m high outer moraine, a 120 m high central moraine and a 50 m high inner moraine (Fig. 5.5a,b). The middle of these moraines is likely to be associated with a period of glacier stability from 1905 to 1919 (ETHZ, 2008), while the innermost moraine coincides with an Alpine-wide glacier advance that occurred during the late 1970s (Vincent et al., 2005). The outermost moraine ridge is thought to indicate the maximum extent of the glacier during the 'Little Ice Age' ~1855 to 1865 (Marie, unpublished; cited in Tison et al., 1989). Sediments comprising the lateral moraine complex are very poorly sorted (σ = 2.4), and have a median particle size of 419 μm. Mud and sand make up between 9% and 26% (mean = 11%), and 66% and 80% (mean = 73%) of the sediment respectively. Particle-size-distributions of matrix samples from lateral moraine sediments are significantly similar ($\cos\theta = 0.99$) to matrix samples from debris cones. GCA identifies 3 modes at 1344 μm (-0.4 ϕ), 255 μm (2.0 ϕ) and at 24 μm (5.4 ϕ). These modes account for 25%, 55% and 20% respectively of the probable Gaussian component of the particle-size-distribution. Particle-diameter-abundance plots indicate that particle-size-distributions have a mean fractal dimension of 2.42 (r^2 = -0.996). Particle form is moderately elongate and slightly flat, with a mean intercept sphericity of 0.60. Mean

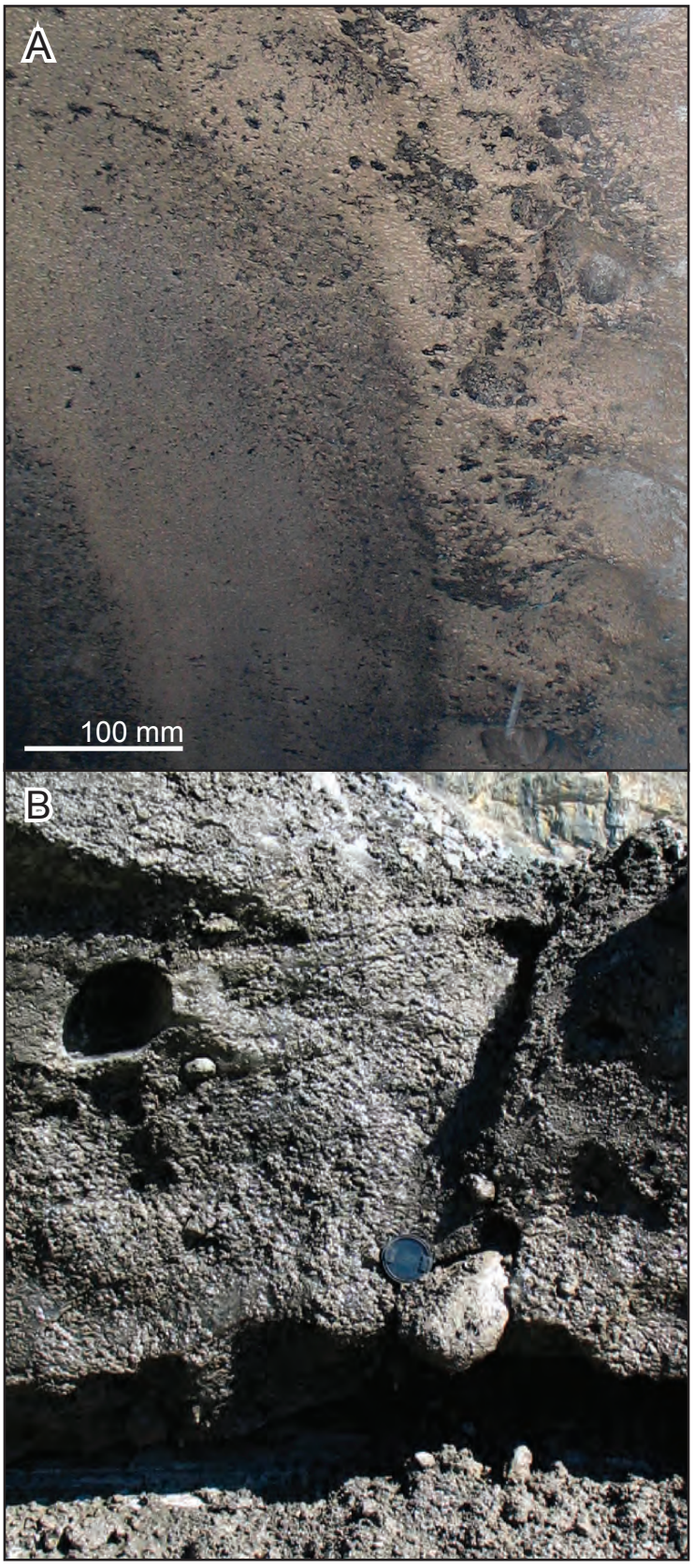

Figure 5.7: Photographs of subglacial debris at Glacier de Tsanfleuron - (A) linear stripes of silts and clays melting out from the base of the ice at the start of debris stripe 2, (B) boulder and cobble-sized clasts above subglacial debris planes at the start of debris stripe 3. 53 mm lens cap in centre for scale.

particle roundness is angular (P – value = 0.19) and mean surface roughness is moderately smooth (ξ – value = 5.55 x 10^{-7}). The lateral moraine is subject to a large amount of post-depositional reworking, due, in part at least, to the melt-out of the ice core within the inner moraine (Fig. 5.5b).

5.2.2.5 Terminal moraine complex

A terminal moraine complex is present ∼2000 m from the present glacier margin, forming a near-continuous ridge 5 to 30 m high, which extends from the northern lateral moraine, across the limestone plateau, to south of the glaciers present day margin. Historical data have identified this moraine as marking the maximum extent of the glacier between 1855 and 1865, coinciding with the Little Ice-Age maximum (Maire, unpublished, cited in Tison and Lorrain, 1987). Terminal moraine sediments are very poorly sorted (σ = 2.45), with a median particle size of 436 μm. Mud and sand comprise between 12% and 37% (mean = 12%), and 58% and 81% (mean = 73%) of the sediment respectively. Particle-size-distributions of matrix samples from terminal moraine sediments are significantly similar ($\cos\theta$ = 0.99) to matrix samples from subglacial debris, proglacial debris stripes and glaciofluvial outwash sediments. GCA identifies 3 modes, at 1110 μm (-0.2 ϕ), 237 μm (2.1 ϕ) and 19 μm (5.7 ϕ). These modes account for 30%, 50% and 20% respectively of the probable Gaussian component of the particle-size-distribution. Particle-diameter-abundance plots indicate that particle-size-distributions have a mean fractal dimension of 2.43 (r^2 = -0.996). Particle form is slightly elongate and slightly flat, with a mean intercept sphericity of 0.70. Mean particle roundness is subangular (P – value = 0.27) and mean surface roughness is moderately smooth (ξ – value = 5.14 x 10^{-7}).

5.2.2.6 Proglacial debris stripes

Proglacial debris stripes form a series of linear sediment ridges, from 0.05 to 0.4 m thick, 10 to 100 m wide and up to ∼2000 m long, that extend eastwards from the glacier margin, in some cases as far as the terminal moraine complex (Figs 5.8a, 5.6a, c). The debris stripes are aligned parallel to former ice-flow direction, as indicated by proglacial striation directions, and originate at the ice margin in association with the melt-out of subglacial debris planes (Fig. 5.6b) or, in the case of DS1, a supraglacial debris ridge (Fig. 5.6a). Although proglacial debris stripes predominately trend eastwards, lateral migration at the 10 m scale, which occurs and coincides with the presence of large (100 m in diameter and 50 m deep) sinkholes in the palaeokarst forefield (Gremaud et al., 2009) (Figs 5.8b,5.6c).

Matrix samples from proglacial debris stripe sediments are extremely poorly sorted (σ = 4.77), with median particle grain sizes (D_{50}) ranging from 197 to 516 μm (mean D_{50} = 503

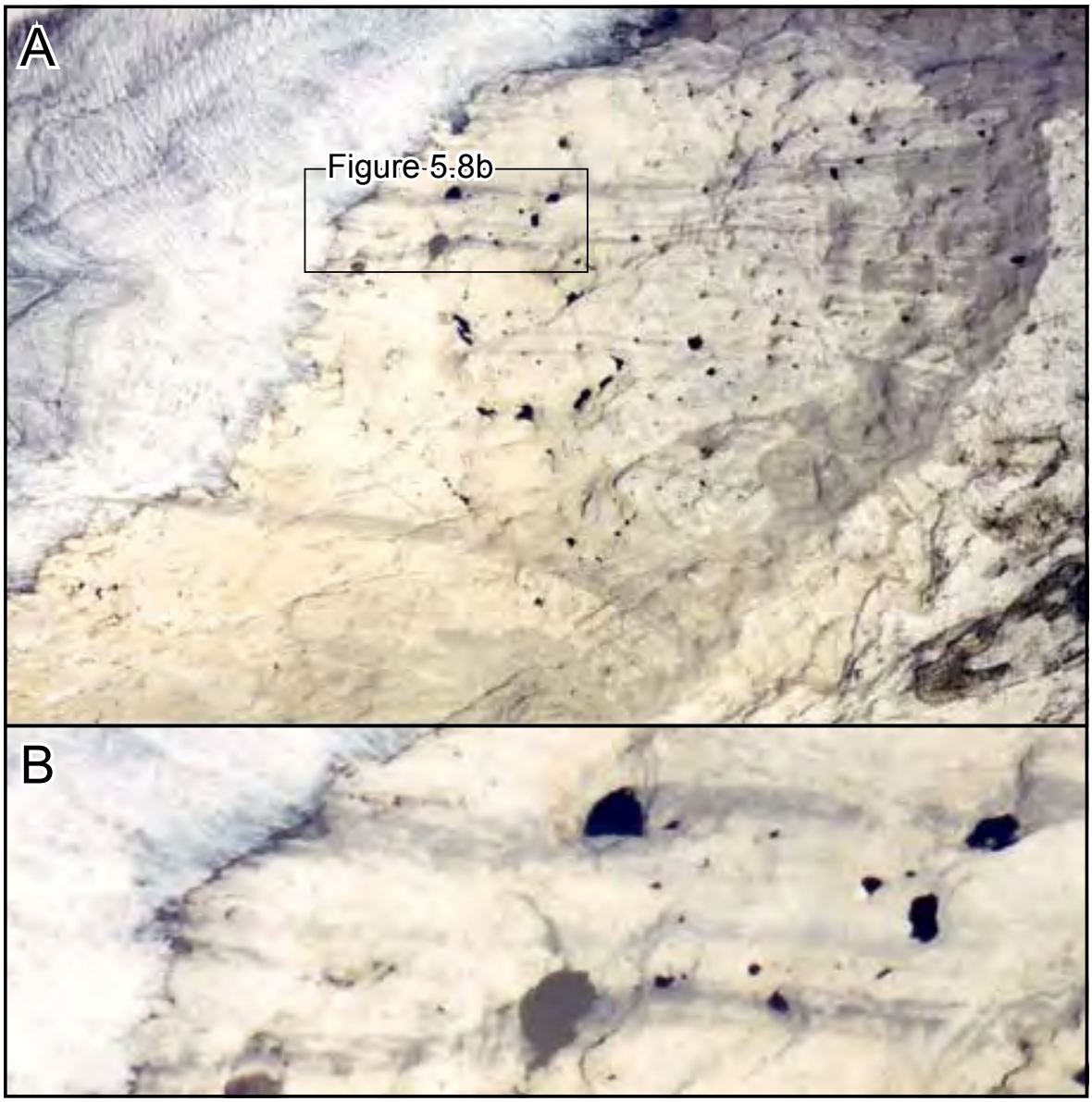

Figure 5.8: Uncorrected aerial photograph of Urgonian limestone forefield at Glacier de Tsanfleuron - (A) overview showing all proglacial debris stripes, and (B) detail showing lateral migration of DS4 and DS5 into large sinkholes in the palaeokarst

μm). Mud and sand comprise between 4% and 19% (mean = 15%), and 65% and 90% (mean = 67%) respectively. Particle-size-distributions of matrix samples from proglacial debris stripes are significantly similar ($\cos\theta$ = 0.99) to matrix samples from subglacial debris, terminal moraine and glaciofluvial outwash sediments. GCA identifies 3 modes, at 1157 μm (-0.2 ϕ), at 252 μm (2.0 ϕ) and at 24 μm (5.4 ϕ). These modes account for 32%, 48% and 20% respectively of the probable Gaussian component of the particle-size-distribution. Particle-diameter-abundance plots indicate that particle-size-distributions have a mean fractal dimension of 2.4 (r^2 = -0.983). Particles are elongate and slightly flat, with mean I_s – values of 0.62 to 0.71. Mean particle roundness is angular (P – value = 0.23) and mean surface roughness is moderately smooth (ξ – value = 5.15 x 10^{-7}). Striations occur on 2.3% of particles from proglacial debris stripes. Samples where the percentage of striations on particles is >10 are restricted to sample sites adjacent to the glacier margin (Sites 53, 54 and 71).

Sampling of proglacial debris stripes at Glacier de Tsanfleuron was conducted in transects along the debris stripes at 50 to 100 m intervals to characterise spatial trends in particle-size-distributions and particle morphology indices. Regression analysis of the relationship between median particle size (D_{50}) and distance away from the terminus show that there is no correlation between the two variables (r^2 = 0.025) (Fig. 5.9). Regression analysis of the relationship between particle form (I_s) and distance eastwards from the glacier terminus (Fig. 5.10a) show that these variables have a moderate positive correlation (r = 0.62) and moderately high variance away from the regression trend (r^2 = 0.39). The slope of the regression line shows that I_s – values increase at a mean rate of 3 x 10^{-5} m^{-1} away from the glacier margin. A number of samples with markedly lower I_s – values deviate away from this overall trend. These include five samples from nunatak-derived DS1 (samples 35, 36, 37, 38 , 39) and a sample taken from DS3 on the steep east-facing wall of a sinkhole (sample 66). Regression analysis of the relationship between particle roundness (P – value) and distance away from the terminus show no no correlation between the two variables (r = 0.17). Similarly, regression analysis of the relationship between particle surface roughness (ξ – value) and distance away from the terminus show no no correlation between the two variables (r = 0.02).

5.2.2.7 Glaciofluvial outwash plain

Extensive glaciofluvial deposits surround the modern proglacial meltwater stream eastwards of the terminus. The depth of glaciofluvial deposits ranges from ~0.1 to 1 m at the glacier margin, reaching an unknown thicknesses as the deposits open into a wide braid plain (~250 m wide) near the 'Little Ice Age' limit. Glaciofluvial sediments are poorly sorted (σ = 2.19), with a median particle size of 521 μm. Mud and sand comprise between 4% and 23%

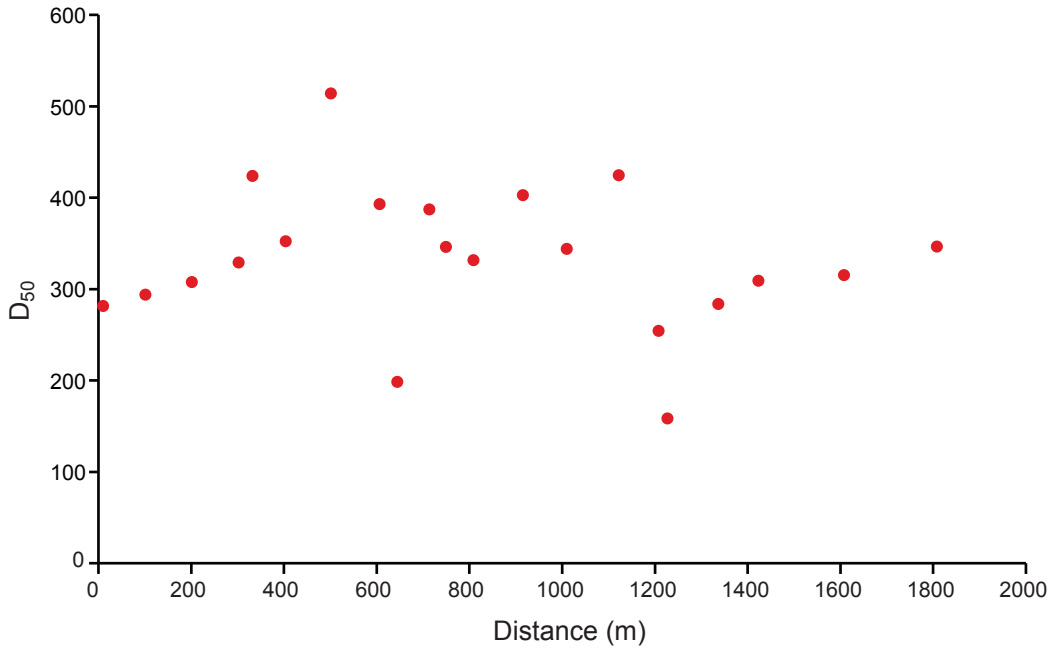

Figure 5.9: Bivariate scatterplot of median particle size (D_{50}) for matrix samples taken from proglacial debris stripes plotted against distance from the glacier terminus

-

(mean = 8%), and 71% and 86% (mean = 79%) of the sediment respectively. Particle-size-distributions of matrix samples from glaciofluvial outwash sediments are significantly similar ($\cos\theta$ = 0.99) to matrix samples from subglacial debris, terminal moraine and proglacial debris stripe sediments. GCA identifies 3 modes: at 1078 mm (-0.1 ϕ), at 266 μm (2.0 ϕ), and at 31 μm (5.0 ϕ). These modes account for 35%, 47% and 18% respectively of the probable Gaussian component of the particle-size-distribution. Particle-diameter-abundance plots indicate that particle-size-distributions have a mean fractal dimension of 2.3 (r^2 = -0.994). Particles are slightly elongate and slightly flat in form, with a mean intercept sphericity of 0.64. Mean particle roundness is subangular (P – value = 0.26) and mean surface roughness is moderately smooth (ξ – value = 5.15 x 10^{-7}).

5.2.3 Sediment discharge modelling

5.2.3.1 Ice-flow modelling

The results of modelling three-dimensional ice-flow at Glacier de Tsanfleuron using Hubbard and Blatter's first-order solution (Hubbard et al., 1998) are presented as two-dimensional vector maps and three-dimensional vector scene graphs (Figs 5.11). Comparisons between modeled and observed surface velocities show that they are not significantly different at a 99.96% confidence level. Ice velocities range from 0 m a^{-1} to 40.48 m a^{-1}. Ice flow

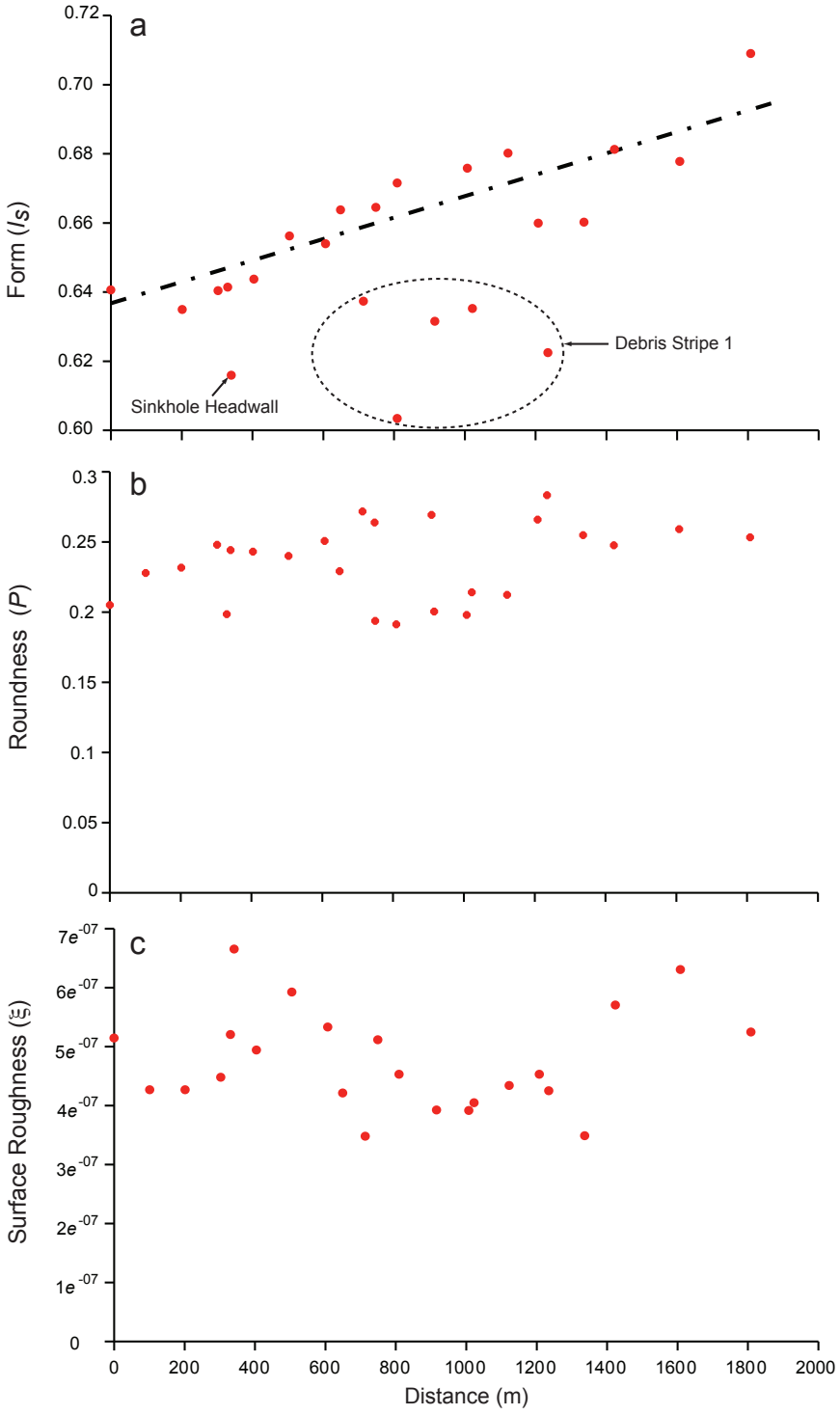

Figure 5.10: Bivariate scatterplots of particle morphology indices for proglacial debris stripe particles plotted against distance from the glacier terminus - (a) intercept sphericity values; (b) roundness values, and (c) surface roughness values.

is predominately to the east and highest in the thicker northern half of the glacier (Flow Unit A), where ice velocities increase with distance downglacier, reaching maximum values in the steep, narrow ice tongue. The southern half of the glacier (Flow Unit B) has much lower average annual velocities ($\leq$10 m a^{-1}). Model results simulated basal sliding under 55% of the glacier, accounting for an average of 50.6% of the glacier's surface velocity. Vertical variations in velocity up through the ice column from the bed are correspondingly small.

5.2.3.2 Ground-penetrating radar

The results of the GPR survey are presented as a topographically corrected greyscale radar profile (Fig. 5.12a). Four continuous or near-continuous reflection horizons are identified from the radar profile: (i) a continuous horizon composed of a direct coupling wavelet of the radar antennae loaded on the snow surface (+−+ pulse) (Reynolds, 1997) ; (ii) at $\sim$2 m below the surface coupling reflector horizon, a continuous reflection horizon with a +−+ phase polarity; (iii) a continuous reflector horizon (+−+ pulse) starting at 24 m depth at the southern end of the radar profile (0 m) rising at a constant gradient to 10 m depth at the northern end of the profile (123 m), and (iv) a semi-continuous horizon (+−+ and −+− pulses) thickening from $\sim$ 5 m near the southern end of the radar profile to $\sim$10 m at the northern end of the profile. An area of faint, but dense, horizontally discontinuous reflectors are also identified, occurring from $\sim$70 m to $\sim$100 m along the profile, extending vertically from the uppermost continuous reflector horizon to the lowermost near-continuous reflector horizon ($\sim$16 m thick).

5.2.3.3 Glacial sediment discharge

Glacial sediment discharges from the terminus at Glacier de Tsanfleuron are presented as a map of the glacier in model domain space, showing the discharge in kg a^{-1} at the ice margin as bars (Fig.5.13). Sediment discharge rates range from 0 to 2746 kg a^{-1}, with the total annual rate of sediment discharge at the ice margin of 4734 kg a^{-1}. Glacial sediment discharge is highest at the southern section of the margin, corresponding with sediment input from the nunatak and the presence of a large supraglacial debris stripe (DS1) (Fig. 5.6ca). The central part of the the glacier margin is characterised by regularly alternating areas (cells) of high and low sediment discharge ($\sim$500 to 1200 kg a^{-1} and $\sim$10 to 50 kg a^{-1}). Glacial sediment discharge is zero in areas south of DS1.

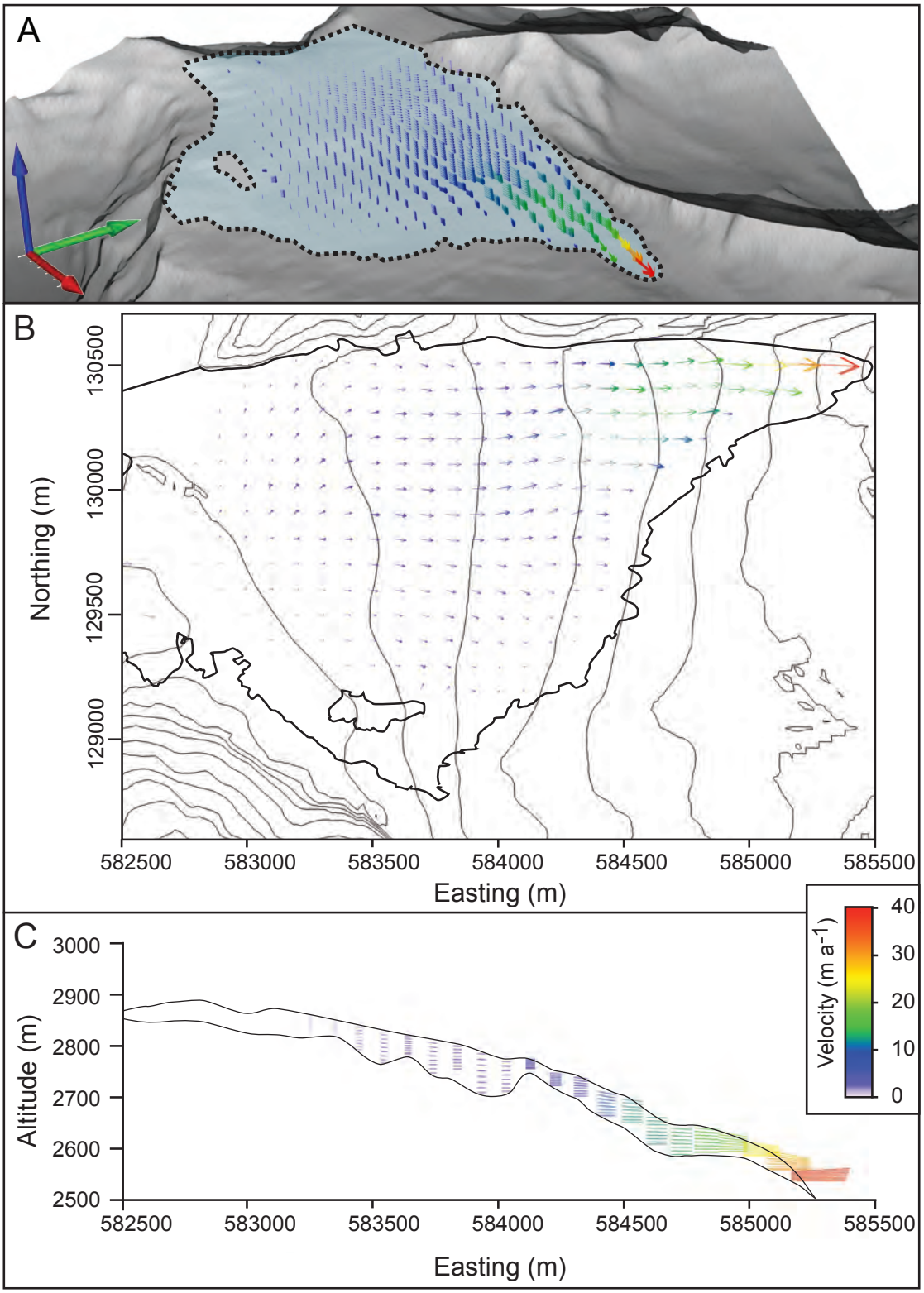

Figure 5.11: Vector field output from ice-flow model of Glacier de Tsanfleuron calibrated to measured ice surface velocities - presented as: (A) an orthographic view of a digital elevation model with three-dimensional ice-flow vectors (u, v, w); (B) a map of longitudinal and lateral components of ice flow (u, v), and (C) a cross-section along central flow-line showing ice surface and bed elevation with easterly and vertical components of ice flow (u, w). Vertical scale exaggerated by two, coordinates in Swiss Grid (CH1903)

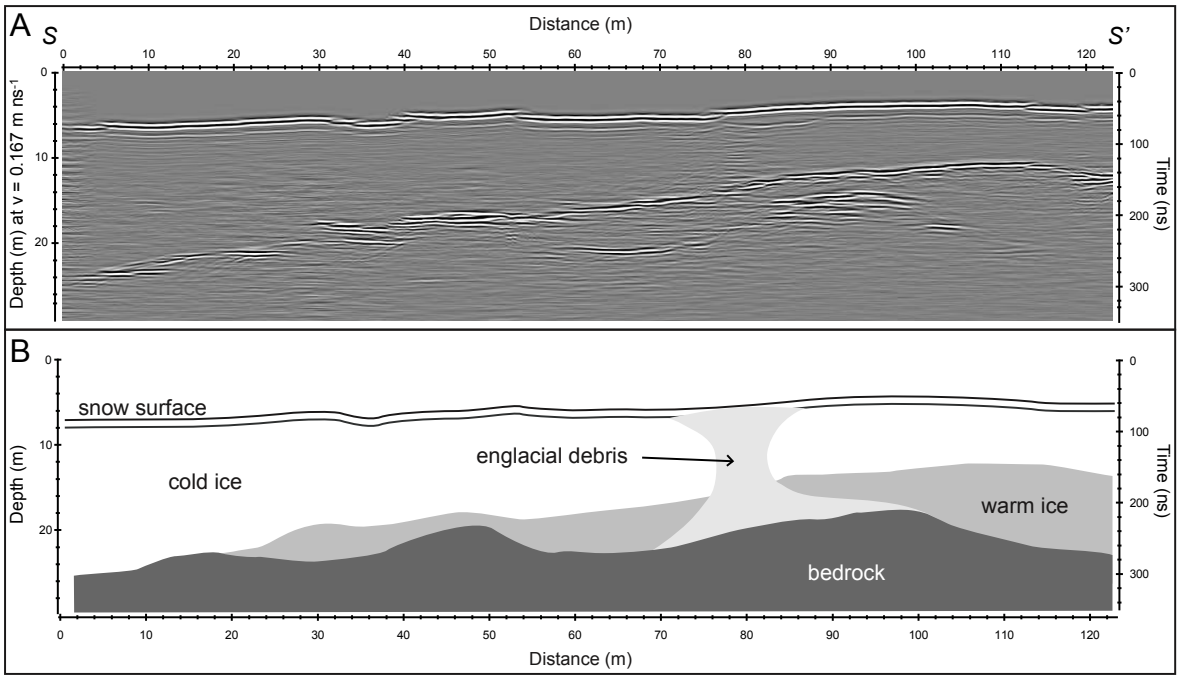

Figure 5.12: Results and interpretation of ground-penetrating-radar survey at Glacier de Tsanfleuron - (a) greyscale profile of GPR survey corrected for topography, and (b) interpretation of radargram showing bedrock, warm-based and cold-based ice and englacial debris from DS1 (for survey orientation refer to Fig. 3.4)

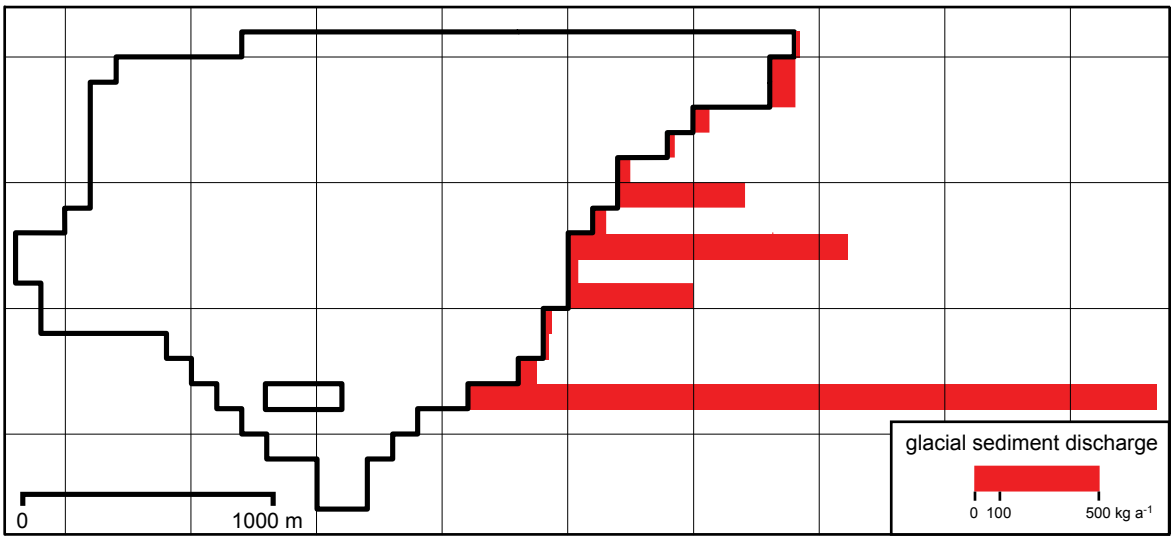

Figure 5.13: Map of Glacier de Tsanfleuron showing modeled glacial sediment discharge at the terminus (kg a^{-1}) - presented in model domain space (100 m x 100 m grid cells)

5.3 Interpretation and discussion

The structures described at Glacier de Tsanfleuron are interpreted on the basis of their crystallographic composition, superposition relative to other structures and similarity to structures described by previous researchers. Sediment-landform assemblages investigated at Glacier de Tsanfleuron are interpreted in a process-based context on the basis of particle-size-distributions and particle morphology data presented above and their relationship with glacier structures. Modeled glacial sediment discharges are interpreted with reference to ice flow velocities, basal ice thicknesses and the formation of proglacial sediment-landform assemblages, with reference to other relevant studies at Glacier de Tsanfleuron.

5.3.1 Glacier structure

Continuous layering (S_0) is interpreted as primary stratification, on the basis of their lateral continuity (Fig. 5.1) and the regular alternation of coarse clear, coarse-bubbly and fine-bubbly ice. The composition of these strata are consistent with descriptions of initial snowpack formation and of meteoric, firnified glacier ice (e.g. Wadham and Nuttall, 2002; Souchez and Lorrain, 1991). Here, layers of low-density coarse bubbly crystals represent winter accumulation layers which have undergone partial melt and refreezing. In contrast, dense layers of coarse clear crystals are a product of snow-melt refreezing at the base of the snowpack. Fine bubbly crystals are the product of snow accumulation during the ablation season, characterised by thin strata ($<$100 mm), some discolouration and fine crystal diameter ($<$5 mm). Differential flow velocities within Flow Units A and B result in progressive downglacier deformation, such that the tighter folding of primary stratification measured in Flow Unit A relative to Flow Unit B reflects the higher flow speeds ($\sim$38 m a^{-1}) associated with thicker ice ($\sim$120 m) and basal sliding at the glacier's northern outlet lobe (Chandler, 2005). The uniform low velocities in Flow Unit B (Fig. 5.11) are reflected by the low degree of deformation apparent in (S_0) primary stratification in this area (Fig. 5.1).

Longitudinal planar structures (S_1) are interpreted as foliation on the basis of their compositional similarity with primary stratification and the continuity observed between them and S_0. The concentration of S_1 foliation at the glacier's northern margin is interpreted as the result of intense simple shear and folding under a longitudinally tensile and laterally compressive stress regime associated with comparatively high surface velocities present in Flow Unit A. These high velocities are associated with a narrowing and deepening of the glacier tongue at this point, where the thrust fault at the junction between Hauterivian and Urgonian lithologies has been exploited by glacial erosion.

Brittle fractures (S_3) are interpreted as shear planes on the basis of their cross-cutting relationship with S_0 primary stratification and the vertical displacement of primary stratification across the fracture, evident in section, resulting in the formation of asymmetric hook-shaped folds (Hudleston, 1989) (Fig. 5.2). The development of shear planes, or thrusts as they are often referred to, involves brittle failure as a result of longitudinally compressional stress, leading to fracture perpendicular to the maximum strain-rate tensor and dynamic recrystallisation of ice along the fracture plane (Schulson, 1999; Wilson and Marmo, 1999; Nye, 1952). In warm-based glaciers this has been linked to obstructions to flow at the margin, e.g. a reverse bedrock slope or fallen snow blocks (Herbst et al., 2006; Roberson, 2008). Alternatively, shear planes may be associated with the reactivation of pre-existing structural weaknesses, e.g. rotated crevasses (Nye, 1952), requiring lower longitudinal compression than newly generated compressive fractures (Schulson, 2001). Examination of a digital elevation model (DEM) of the glacier bed (Chandler, 2005) reveals that a reverse bedrock slope is present $\sim$200 m upglacier (west) from the observed S_3 shear planes. Surface velocity data further show that this area on the glacier surface coincides with a point of deceleration. The restriction of (S_3) shear-planes to structural unit A suggests that the development of a longitudinally compressive stress regime in association with a reverse bed slope is most likely mechanism of (S_3) shear plane formation at Glacier de Tsanfleuron.

5.3.2 Sediment-landform assemblages

5.3.2.1 Talus cones

Rockfall debris from the glacier's adjacent peaks and nunatak towards the southern margin supply the majority of the debris visible at the glacier surface. Fracture of sedimentary rocks in cold environments occurs preferentially along existing incipient fractures and mineral veins (Nicholson and Nicholson, 2000), hence talus cones are thought to provide a good example of the initial composition of freshly weathered debris at Glacier de Tsanfleuron and are a useful end-member for understanding the formation of other sediment-landform assemblages.

Gaussian component analysis of particle-size distributions from talus cone matrix samples reveals that weathering of Hauterivian lithologies produces a strong mode at 3.3 ϕ, which may reflect the composition of the lithology's component minerals (Haldorsen, 1981). However, other researchers have suggested that clast-to-clast contacts occurring during rock avalanches may be responsible for the production of a significant volume of fines (van Steijn et al., 2002; Whalley et al., 2004). Particle intercept sphericity data support the view that talus cone sediments represent an end-member of the sediment transport continuum, i.e.

intercept sphericity values of talus cone particles are lower than adjacent lateral moraine sediments (Table 5.2; Fig.4.7a). In contrast, particle roundness data do not support this interpretation (Table 5.2). Particles sampled from talus cones have slightly higher roundness (P – values) than particle sampled from the adjacent lateral moraine. This apparent discrepancy may be interpreted in at least two ways: i) that talus cone particles have undergone some degree wear as a result of clast-to-clast interactions within debris flows, or ii) that the recently fractured particles in the talus cone are more regular than particles that have experienced a small but slightly higher degree of wear and therefore have a higher number of faces. The latter situation may arise as a result of the roundness analysis procedure (Chapter 4). In Section 4.3.2, comparison of geometric shapes revealed that a perfectly cuboidal particle may be less angular than a particle with more faces (e.g. a dodecahedron), because of the contribution of both particle convexities *and* concavities to roundness. In the context of the wider catchment, all other sediment-landform assemblages, with the exception of the lateral moraine, are composed of particles that are more rounded than particles sampled from the talus cone. This suggests that the latter hypothesis is correct, and that recently fractured particles have more regular faces than particles that have undergone a small degree of wear.

5.3.2.2 Supraglacial debris stripes

Supraglacial debris stripes are frequently observed on the surface of valley glaciers. Their formation is associated with a number of distinct, but often difficult to isolate processes: (i) the accumulation of rockfall deposits at the margins of convergent Flow Units, producing an avalanche-type moraine (Eyles and Rogerson, 1978a); (ii) the folding of primary stratification into large-scale lateral folds, elevating englacial debris into flow-parallel fold-hinges (Hambrey and Glasser, 2003); (iii) the exposure of subglacially derived sediments originating from a point source at the bed (e.g. a bedrock knob or roche moutonnée) (Eyles, 1979; Small, 1987), and (iv) the reorientation of a surface rockfall deposits into flow-parallel stripes, deformed under high cumulative shear (Goodsell et al., 2005; Woodward et al., 2002). The morphology of supraglacial debris stripes and their relationship with glacier structures lead to a number of insights: (i) Boulder- to cobble-sized rocks cascading down from the nunatak directly onto the 1 to 10 m wide debris stripe (DS1) close to the glacier's southern margin lead to the interpretation that DS1 is primarily formed by rockfall, which is then transported downglacier to the terminus. The widespread absence of large-scale lateral folding at the glacier surface strongly indicates that the composition of DS1 is not controlled by structural dynamics at Glacier de Tsanfleuron. (ii) Visual comparison of the particle-size distributions of matrix samples from supraglacial debris stripes and talus cones suggest that these two sediment-landform assemblages are texturally similar

(Fig. 5.4). However, $\cos\theta$ analysis (Table 5.3) shows that similarity is not significant at a 0.99 level. Matrix samples from supraglacial debris stripes are depleted in fines relative to talus cone samples, from which they are inferred to be derived. This loss of sediment is reflect post-depositional eluviation by surface meltwater streams or the ablating snowpack (Fischer and Hubbard, 1999). The similarity between sediment matrix samples from talus cones and the the two isolated debris stripes at the northern margin of the glacier strongly support the interpretation that these are isolated rockfall deposits. Their linear flow-parallel morphology is interpreted to be the result of high-cumulative strain at the northern margin of the glacier, caused at Glacier de Tsanfleuron by a strong gradient in surface velocities between the flow-line in Flow Unit A and the glacier margin (Fig. 5.11).

5.3.2.3 Subglacial debris planes

Gaussian component analyses of matrix samples from subglacial debris planes identify a strong trimodal sediment, enriched in fine silts relative to supraglacially transported sediments. The enrichment of subglacial debris planes in fine silts relative to supraglacial sediment-landform assemblages is consistent with the occurrence of abrasion or adhesion processes, which Haldorsen (1981) and Rabinowicz (1995) identified during laboratory experiments of sediment crushing and deformation. Additionally, the small particle-size range and flow-parallel fabric of planar, subglacial debris trains indicates that they have probably been transported away from points of sediment production at the bed. Iverson et al. (1996) suggested that the production of fine silts was the result of clast-to-clast contacts within a deforming sediment. The absence of a thick till layer beneath Glacier de Tsanfleuron and presence of striations on subglacially transported particles and exposed bedrock suggests that rather than reflecting clast-to-clast contacts, the tertiary mode in subglacial debris plane sediments is indicative of clast-to-bed contacts. Analysis of the fractal dimension of particle-size-distributions was not instructive in this study in interpreting the specific processes involved in the formation of glacigenic sediments. Furthermore, the data also indicate that the technique, developed by Sammis et al. (1987), is unable to distinguish between particle-size-distributions with fractal and non-fractal signals, which in this study are successfully decomposed into multi-modal Gaussian components (Table 5.2). Similar conclusions have also been reached by other workers employing this analytical technique (Fischer and Hubbard, 1999; Khatwa et al., 1999; Benn and Gemmell, 2002), who have concluded that the fractal analysis of particle-size-distributions was unable to differentiate between highly deformed and undeformed glacigenic sediments.

Particle intercept sphericity and roundness data provide further evidence of subglacial abrasion processes. Particles from subglacial debris planes are more blocky and more rounded than particles from supraglacial debris stripes and talus cones. These data lend

support to Boulton's (1978) conceptual model of 'passive' and 'active' sediment transport zones. At Glacier de Tsanfleuron, particles transported subglacially undergoing considerably more wear than particles transported en- and supraglacially. Particle surface roughness data are not useful indicators of subglacial abrasion, as they fail to quantitatively distinguish between particles with striations and particles without striations (see Fig. 4.3.3). The reasons underlying this analytical limitation have been discussed previously (Section 4.3.2).

5.3.2.4 Lateral moraine

The large lateral moraine at Glacier de Tsanfleuron is interpreted to be the product of deposition of supraglacial debris sourced from rockfall deposits. This inference is based on the similarity between matrix samples from lateral moraine sediments and those from talus cones (Table 5.1). Particle intercept sphericity values indicate that particles from the lateral moraine have undergone more wear than particles from adjacent talus cone sediments, although particle roundness data are ambiguous (see discussion in Section 4.3.2). Fig. 5.5 illustrates the large volume of sediment contributed to the lateral moraine by talus cones forming beneath the free-face of the Sanetschhorn. This observation suggests that a large proportion of the lateral moraine is likely of non-glacigenic origin. The extent to which lateral moraine sediments have been transported en- and subglacially is difficult to assess, firstly because the subglacial environment is difficult to sample in the area of the glacier bed adjacent to the moraine, and secondly, because lateral moraine sediments have clearly been modified post-depositionally, following glacial retreat.

5.3.2.5 Terminal moraine

The terminal moraine complex at Glacier de Tsanfleuron is interpreted to have formed predominantly as the result of the deposition of subglacially transported sediments. This interpretation is supported by the nature of particle-size-distributions from terminal moraine matrix samples, which have strong tertiary mode centred around fine silts, and the similarity of this mode to subglacially transported debris ($\cos\theta = 0.992$). Analyses of particle-size-distributions from subglacial debris planes matrix samples (Section 5.3.2.6) support the interpretation that an enrichment in fine silt-sized particles is indicative of abrasive processes occurring between particles in transport and the glacier bed (Haldorsen, 1981; Rabinowicz, 1995). This inference is further supported by particle form and roundness data for samples from the terminal moraine complex. These particles are more blocky and more rounded than particles sampled from adjacent proglacial debris stripes (Fig. 4.7a,b), which is thought to reflect the increased wear of these particles with transport distance. Spatial trends in the morphology of particles transported subglacially are discussed further in Section 5.3.2.6.

Fischer and Hubbard (1999) asserted that particle abrasion occurred during subglacial sediment deformation at Haut Glacier d' Arolla, and suggested that the sedimentary products of abrasion could be isolated by subtracting the particle-size-distribution of a headwall sediment sample from that of a sample of subglacial sediment. Applying this hypothesis to Glacier de Tsanfleuron results in a percentage difference plot that is very similar to that obtained by Fischer and Hubbard (1999) (their Fig. 4) and by Iverson et al. (1996) (their Fig. 5a) during laboratory shear experiments ($\cos\theta = 0.992$). The two former studies obtained sediment samples from a deforming sediment, although a thick till layer largely absent beneath Glacier de Tsanfleuron, with the exception of sediment beneath the narrow north ice tongue. The findings from this study therefore suggest that the production of fines via abrasion beneath a hard-bedded involves the same wear process that occur within a deforming-layer beneath a soft-bedded glacier.

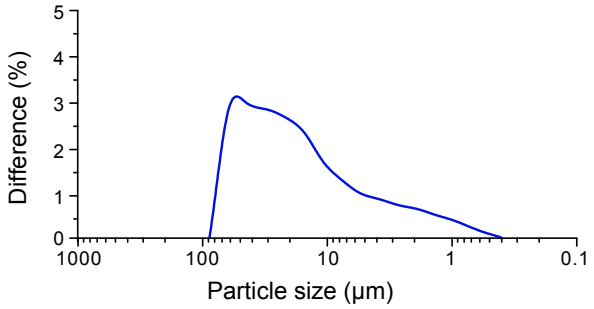

Figure 5.14: Difference between particle-size-distributions of matrix samples from talus cone sediments and terminal moraine sediments - produced by subtracting the particle-size-distribution of talus cone matrix sediment samples from those of terminal moraine matrix sediment samples.

5.3.2.6 Proglacial debris stripes

Flow-parallel debris stripes have been observed in front of a large number warm-based glaciers(e.g. Boulton, 1976; Eyles, 1979; Gordon, 1992; Hambrey and Lawson, 2000; Roberson, 2008). The formation of proglacial flow-parallel debris stripes has been attributed to: (i) the deposition of medial moraine-type supraglacial debris ridges (Benn and Evans, 1998); (ii) the ablation of subglacially transported debris originating from point-sources (Eyles, 1979); (iii) the deposition of supraglacial debris ridges formed by large-scale lateral folding of en- and sub-glacial debris (Hambrey and Lawson, 2000; Goodsell et al., 2005); (iv) the exposure of flutes formed by deformation of till into subglacial cavities, and (v) the post-depositional erosion of proglacial till by meltwater channels (Roberson, 2008). At Glacier de Tsanfleuron the formation of proglacial debris stripes is attributed to the ablation

of both a medial moraine-type debris ridge and the flow-parallel transportation of sediment from a subglacial point source.

Proglacial debris stripes DS2, DS3, DS4 and DS5 are interpreted to be deposited from subglacially transported debris planes, originating from point sources of sediment production at the bed. This interpretation is based on the following areas of evidence. (i) The similarity between particle-size-distributions of matrix samples from proglacial debris stripes and subglacial debris planes, with which they are morphologically continuous, indicates that sediment in proglacial debris stripes has been subject to abrasion at the bed. (ii) The progressive increase in particle I_s – values with distance from the glacier margin (3 x 10^{-5} m^{-1}) along proglacial debris stripes is interpreted as an indication of increased particle wear with distance from the point of entrainment at the bed. The absence of any correlation between inferred transport distance and other particle morphology indices (i.e. P – values and ξ – values) is attributed to the rapid surface weathering of particles following deposition (Fig. 4.16; Section 4.3). (iii) Sharp et al. (1989) and Grust (2004) have suggested, on the basis of dye-tracer experiments and the distribution of former subglacial cavities in the proglacial area, that the topography of the glacier forefield is characteristic of the topography underlying Glacier de Tsanfleuron. On the basis of these conclusions and the geometric relationship between proglacial debris stripes and sinkholes in the palaeokarst forefield, it is suggested that sinkholes act as point sources beneath the glacier for subglacial debris planes and proglacial debris stripes.

The largest proglacial debris stripe at Glacier de Tsanfleuron (DS1) is interpreted to be a medial moraine-type debris stripe, forming as a result converging ice, in this case, around a nunatak. This interpretation is supported by observations of rockfall-sediments from the nunatak onto the debris stripe and detection of dense, horizontally discontinuous reflectors in GPR profiles, which are interpreted to be englacial sediment bodies $>$0.4 m in diameter (Section 5.3.3.1). Supraglacial sediment volumes at DS1 are relatively low, which would suggest that sediment transport should be relatively passive, following Boulton's (1978) theory of passive and active glacial sediment transport. However, while a number of particle samples from DS1 have relatively low I_s – values compared to particles from other debris stripes (Fig. 5.10a), this trend is by no means universal. In addition, the similarity in particle-size-distribution between matrix samples from DS1 and subglacial debris planes, indicates that a large proportion of the particles from DS1 have been transported en- or subglacially. Such an interpretation is consistent with conceptual models of ice-flow dynamics in areas of confluent ice-flow (Boulton, 1978).

5.3.2.7 Glaciofluvial outwash plain

The high degree of similarity between particle-size-distributions of matrix samples from glaciofluvial outwash and those from subglacially transported debris ($\cos\theta = 0.991$) suggests that the influence of proglacial meltwater on the characteristics and morphology of proglacial sediment-landform assemblages is limited. This is also conveyed by the morphology of particles sampled from the glaciofluvial outwash plain. Proglacial sediment deposits that have been modified by, or deposited by, glaciofluvial meltwater are typically blocky in form and sub-rounded to rounded (Hambrey and Ehrmann, 2004; Fischer and Hubbard, 1999; Roberson, 2008), equivalent to I_s – values of $>$0.8 and P – values from 0.35 to 0.43. In contrast, particles sampled from the outwash plain in front of Glacier de Tsanfleuron have comparatively low mean I_s and P – values (0.64 and 0.26 respectively).

The limited impact of proglacial meltwater on the characteristics of sediment-landform assemblages may be accounted for by the comparatively low proportion of the glacier's total meltwater discharge draining across the glaciofluvial outwash plain. Research into the composition of the glaciers drainage network concluded that only 5% of total ice melt discharges via the portal at the northern edge of the terminus (Grust, 2004), with the remainder draining through the subglacial karst system. These findings suggest that sediment transport processes at Glacier de Tsanfleuron are atypical of small warm-based valley glaciers and that glaciofluvial sediment discharge rates are probably lower than glaciofluvial sediment discharge rates from other warm-based valley glaciers of a similar size.

5.3.3 Sediment discharge modelling

The results of glacial sediment discharge modelling are interpreted here within the context of three-dimensional ice-flow velocities, the thickness and extent of basal ice facies (provided by Coulson, unpublished) and ground penetrating radar data. Chandler et al. (2008) provide a rigorous assessment of the three-dimensional ice-flow model, where the choice of parameters used is justified and related to other empirical data.

5.3.3.1 Ground-penetrating radar

Continuous and near-continuous reflector horizons identified from GPR data (above) are interpreted on the basis of signal pulse, geometry and relationship with other field measurements.

(i) The direct coupling wavelet is interpreted as the air-snow interface, on the basis of the consistently large amplitude of the $+$-$+$ signal pulse.

(ii) The continuous horizon at 2 m depth is interpreted as the snow-ice interface on the basis of lateral continuity, the transition from a lower-density to a higher-density layer

(indicated by the +-+ pulse) and snow-depth measurements (generously provided by Alun Hubbard), which indicated that the ice surface was consistently at a depth of 2 m.

(iii) The continuous reflector horizon at ∼24 m depth may be interpreted as a number of features, on the basis that the lower layer has a higher dielectric permittivity than the upper layer: (a) sediment-rich basal ice with a high liquid-water content (Murray et al., 2007); (b) the ice bed interface, where the lowermost reflector horizon is a ghost of the horizon above, or (c) a boundary between cold-ice and warm-ice, caused by penetration of a winter cold front into the ice mass by conductive cooling (Weertman, 1961). The third hypothesis is tentatively accepted here by a process of elimination. The first hypothesis is rejected because observed basal ice thicknesses at the margin at Glacier de Tsanfleuron in the proximity of the supraglacial debris stripe (DS1) were much lower than the vertical extent of the lowermost layer observed in the radar profile. The second hypothesis is rejected on the basis that the morphology of the lowermost discontinuous horizon is markedly different from the continuous reflector horizon above it. This interpretation is consistent with down-borehole thermistor data collected by Bailey (2007) at Glacier de Tsanfleuron.

(iv) The +-+ pulse of the lowermost reflection horizon is typical of an ice-bed interface (Brandt et al., 2007), and in this profile morphologically similar to the relief of the limestone forefield.

The area of dense, horizontally orientated discontinuous reflectors at ∼70 m to ∼100 m across the profile may be consistent with the presence of small, dispersed solid bodies within the ice column. The parameters used for the GPR survey indicate that these bodies are ≥0.4 m wide, so may correspond with englacial boulders, air-spaces or water bodies. The area of horizontally orientated discontinuous reflectors corresponds at the ice surface with the large supraglacial debris stripe originating from the nunatak, suggesting that it is the englacial distribution the supraglacial debris stripe.

5.3.3.2 Glacial sediment discharge

Spatial variations in rates of glacial sediment discharge correspond well with the distribution and size of proglacial debris stripes (Fig. 3.4) even at the model grid-scale (100 x 100 m). Modeled rates of glacial sediment discharge for proglacial debris stripes (DS2, DS3, DS4, DS5) in the centre of the glacier margin support the assertion that they form as the result of subglacial transport of sediment from point sources (Section 5.3.2.6). On the basis of the interpretations made above and modeled rates of glacial sediment discharge, areas of relatively high glacial sediment discharge must therefore correspond with point-sources upglacier, which may indicate the position of sinkholes.

Rockfall-derived sediment supplied from the nunatak accounts for ∼58% of total glacial sediment discharge through the ice terminus. This high discharge (2746 kg a^{-1}) coincides

with an area of relatively thin ice (30 to 20 m thick) and correspondingly low ice velocities. Modeled velocities along DS1 are due to diffusion creep, with no contribution from basal sliding, although velocities along DS1 are not calibrated by empirical surface measurements. Empirical studies of the behaviour of rock-ice mixtures have shown that the shear strength of ice increases markedly once sediment concentrations exceed 40% per volume (Nickling and Bennett, 1984). Spatial variations in creep rates have been incorporated into the ice-flow model, but only consider an enhancement factor a Lower Zone of softer ice $\sim$10 m thick. While failure to include a viscosity parameter for ice with high sediment concentrations (¿ 40% per volume) is unlikely to greatly affect the total error of the modeled velocity field, this may result in an overestimation of glacial sediment discharge rates at the local-scale. Rather than consider small-scale variability in ice softness, this potential source of error may be most effectively addressed by measuring ice velocities along and around the debris stripe.

Despite the high ice velocities observed and modeled at the northern section of the glacier tongue ($>$40 m a^{-1}), sediment-rich basal ice facies are largely absent and glacial sediment discharge rates are correspondingly very low ($<$10 kg a^{-1}). The absence of basal ice facies at the northern part of the ice terminus is thought to be related to the high rates of basal sliding in northern Flow Unit A. Basal sliding accounts for 92% of total surface velocity along the glacier flow-line, resulting in a net loss of sediment-rich ice at the bed. The northern half of the glacier is also thought to be underlain by an efficient arborescent drainage network during the summer (Grust, 2004), effectively removing any basal sediments ablating at the bed. In addition, access to the glacier bed at the northern part of the margin is very difficult, due to the steep, unstable terminus and an absence of subglacial cavities.

5.4 Glacial sediment transport at Glacier de Tsanfleuron

The distribution and characteristics of glacially transported sediments are not greatly influenced by the structural dynamics of Glacier de Tsanfleuron. The influence of glacier flow dynamics and structure on the characteristics of sediment-landform assemblages is illustrated by the formation of flow-parallel debris ridges and longitudinal foliation at the northern margin of Glacier de Tsanfleuron. The transport of sediment is dominated by the entrainment of subglacial sediment into flow-parallel debris planes and the incorporation of rockfall debris and subglacially derived sediment into a medial moraine-type debris ridge. Sediment discharge modelling demonstrates that the incorporation of rockfall of debris into a medial moraine accounts for the majority (58%) of sediment transport, depositing 2746 kg a^{-1} under steady-state conditions. In contrast, sediment transported subglacially accounts

for 1988 kg a^{-1}, over a much larger area. Medial moraine-type DS1 is correspondingly much larger than DS2, DS3, DS4 and DS5 derived from subglacial point sources of sediments. The total rate of sediment discharge (4734 kg a^{-1}) averaged across the glacier bed corresponds to an erosion rate of 0.5 mm a^{-1}, which is comparable to estimates of erosion rates at other small valley glaciers in the European Alps (Hallet et al., 1996).

The relatively fast-flowing glacier tongue at Glacier de Tsanfleuron occupies a 100 m deep, fault-guided valley (Fairchild et al., 1994), suggesting that erosion has been concentrated here. However, modeled rates of glacial sediment discharge in the main ice tongue are $<$10 kg a^{-1} (Fig. 5.13), implying that sediment evacuation in this comparatively deep valley has instead occurred by glaciofluvial transport. In contrast to this study, the majority of other studies have provided sediment discharge rates based exclusively on meltwater discharge (e.g. Gurnell and Clark, 1987; Swift et al., 2002; Warburton and Beecroft, 1993), usually made by measuring meltwater discharge and suspended sediment concentrations. The low percentage of meltwater draining from the terminus at Glacier de Tsanfleuron, $\sim$5% of total meltwater discharge according to Grust (2004), suggests that any estimates of glaciofluvial sediment discharge made on the basis of suspended sediment concentrations in the proglacial meltwater stream are likely to be erroneous.

Conceptual models of glaciated valley landsystems (Benn et al., 2003; Roberson, 2008) have suggested that glaciofluvial deposition and reworking are the dominant processes affecting the characteristics of proglacial sediment-landform assemblages in front of valley glaciers with low sediment discharge rates. The relative importance of glacially transported sediments in the formation of proglacial sediment-landform assemblages at Glacier de Tsanfleuron, however, suggests that the transport processes operating at Glacier de Tsanfleuron are atypical of glaciated valley landsystems in general.

5.5 Conclusions

The aims of the research presented in this chapter were to determine whether structural dynamics exert a controlling influence on sediment transport at Glacier de Tsanfleuron and to determine whether sedimentological characteristics of proglacial debris stripes at Glacier de Tsanfleuron exhibited spatially distinct trends. This chapter also aimed to make a first-order approximation of glacial sediment transport rates and evaluate whether glacial sediment transport processes at Glacier de Tsanfleuron were typical of small warm-based valley glacier systems. The findings derived from these investigations have resulted in the following conclusions:

1. Glacially transported sediment at Glacier de Tsanfleuron is derived from two main sources: (i) rockfall debris from a nunatak close to the glacier's southern margin, and (ii)

plucking of subglacial point sources, probably the upglacier face of sinkholes in the subglacial palaeokarst. Sediment transported from these sources form, respectively, a medial moraine-type supraglacial ridge and flow-parallel subglacial debris planes. The medial moraine-type ridge forms a large (2 km long, $<$100 m wide) continuous ridge from the glacier margin to the Little Ice Age terminal moraine complex, while flow-parallel subglacial debris planes ablate to form a series small ($<$0.8 km long, $<$30 m wide) longitudinal proglacial debris stripes.

2. Samples of particles from proglacial debris stripes at Glacier de Tsanfleuron exhibit an increase in blockiness (quantified by I_s – values) with increased distance from the glacier terminus as a result of increased wear with transport distance at the glacier bed. This spatial trend is not reflected by other indices of particle morphology (P – values or ξ – values), nor by particle-size-distributions of matrix samples from proglacial debris stripes. This conflict of evidence is believed to be caused by post-depositional weathering of the limestone particles that comprise the proglacial debris stripes. Qualitative evidence demonstrates that particles of Urgonian limestone, the lithology underlying the majority of Glacier de Tsanfleuron, have a relatively low potential for preserving evidence of subglacial abrasion, e.g. striations.

3. Modeled rates of glacial sediment discharge reflect the size and morphology of proglacial sediment-landform assemblages at Glacier de Tsanfleuron. Calculated erosion rates (0.5 mm a^{-1}) are comparable to erosion rates measured at other small, warm-based valley glaciers in similar settings. Glacial sediment transport rates in the northern half of the glacier are low relative to the rest of the glacier and the modeled velocity field. Sediment transport in the northern half of the glacier is probably dominated by glaciofluvial sediment transport, although this is difficult to determine empirically, as the majority of the the glacier's meltwater drains through sinkholes at the bed (Grust, 2004). Modification of proglacial sediment-landform assemblages by meltwater is correspondingly spatially restricted and superficial, atypical of traditional models of glaciated valley landsystems.

Chapter 6

Three dimensional glacier structure at Midre Lovénbreen

6.1 Introduction

The manner in which sediment is transferred through glaciers is important because it links glacial processes to the landscape record. Research is increasingly revealing that the pathways taken by this sediment are more complex than originally considered. For example, research at polythermal valley glaciers over the past 10 years has shown that the pathways followed by englacial debris appear to be closely associated with the complex internal structure of those glaciers (Hambrey et al., 1996; Hambrey et al., 1999). Consequently, investigations of englacial debris transport pathways have been closely allied to parallel investigations of structural glaciology. The research presented in this chapter builds upon the methodological study conducted by Hubbard et al. (2008) at Glacier de Tsanfleuron, exploring the subsurface structure of a glacier. In this research an OPTV is used in arrays of multiple boreholes to produce a pair of three-dimensional structural visualizations. The results of borehole logging provide key evidence to support existing conceptual models of glacier flow dynamics and structural evolution. These data, in combination with surface mapping, allow for the identification of eight structural elements and the refinement of conceptual models pertaining to structure-sediment dynamics.

The specific aims of the research therefore are:

i. to map the surface structures at Midre Lovénbreen using a combination of high-resolution digital imagery and surface surveying,

ii. to drill and log multiple boreholes using an optical televiewer to map the internal structure of Midre Lovénbreen,

iii. to develop a method of visualizing glacier structure in three-dimensions from OPTV data,

iv. to improve upon existing conceptual models of structure-sediment dynamics using interpretations made on the basis of three-dimensional structural data.

Suites of structural generations identified from surface mapping and OPTV logs are presented in Section 6.2. Interpretations of these structures are made on the basis of their juxtaposition with one another and results from the previous studies (Section 6.3). The significance of these interpretations are discussed in Section 6.4, with relation to the wider literature and existing conceptual models of structural dynamics. The principal conclusions of the research presented in Chapter 6 are summarised in Section 6.5.

6.2 Results

Several structural generations are identified on the basis of OPTV images and surface observations. These are illustrated and characterized below.

6.2.1 Continuous layering (S_0)

At the glacier surface primary stratification is apparent below the snow line as laterally continuous broadly arcuate planar structures dipping upglacier between 2° to 40 (Fig. 6.1) composed of regularly alternating layers of coarse bubble-rich ice, coarse bubble-poor ice and fine bubble-rich ice. In borehole logs S_0 primary stratification occurs as continuous sub-parallel layers of bubble-rich ice and bubble-poor ice, 0.01 to 0.1 m thick and 0.001 to 0.01 m thick respectively (Fig. 6.2a).

Bubble-rich ice can be divided into two subfacies: coarse-grained bubble-rich ice and fine-grained bubble-rich ice, with the ice crystals being 35 to 100 mm and 0.5 to 3 mm in diameter respectively. Bubble-poor ice occurs only as coarse crystals 35 to 100 mm in diameter. Borehole log analyses identify 1358 stratification layers with highly variable dips, ranging from near-horizontal to 71° (Fig. 6.3). Contacts between layers are predominantly gradational between coarse bubble-poor ice and coarse bubble-rich ice facies. Upper boundary contacts between fine bubble-rich ice and coarse ice are noticeably sharper. Paraconformities in the primary structure occur at 15 locations within borehole logs, characterised by an irregular sharp contact between a fine bubble-rich lower plane and a bubble-poor upper plane (Fig. 6.2a). Three-dimensional reconstructions of internal glacier structure (Fig. 6.4) reveal that the dip of S_0 continuous layering is highly variable, plunging upglacier at angles from 10 to 40° and dipping across glacier at angles of 10°

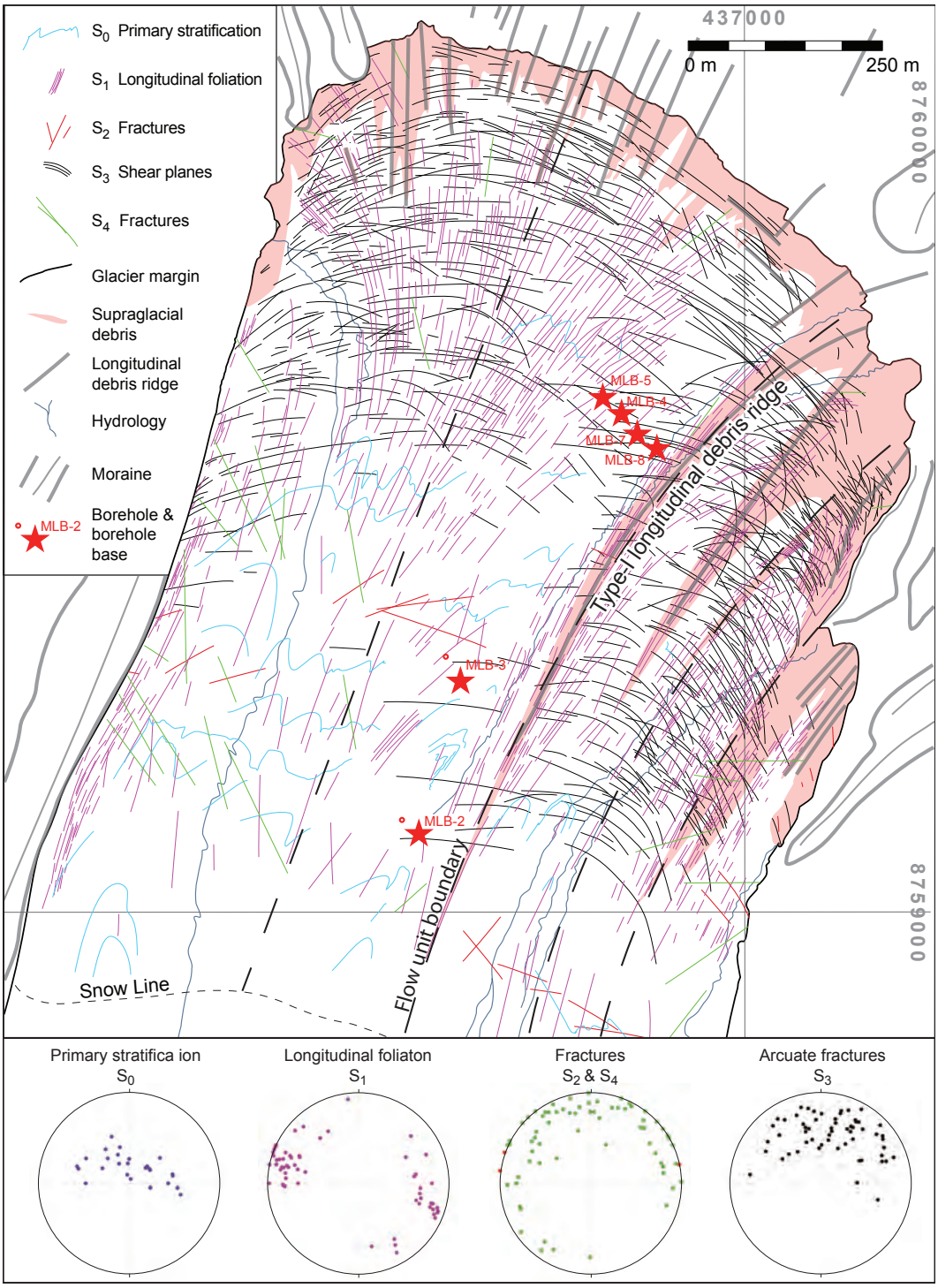

Figure 6.1: Map of structures and sediment identified at the glacier surface from field-work and 2005 aerial photographs - poles to planes Schmidt equal-area lower-hemisphere stereoplots showing orientation and dip direction of structures measured below the snow-line: S_0 continuous layering, S_1 longitudinal planes; S_2 transverse fractures, S_3 shear planes, and S_4 fractures. Position of boreholes, flow unit boundaries and supraglacial debris ridges also shown.

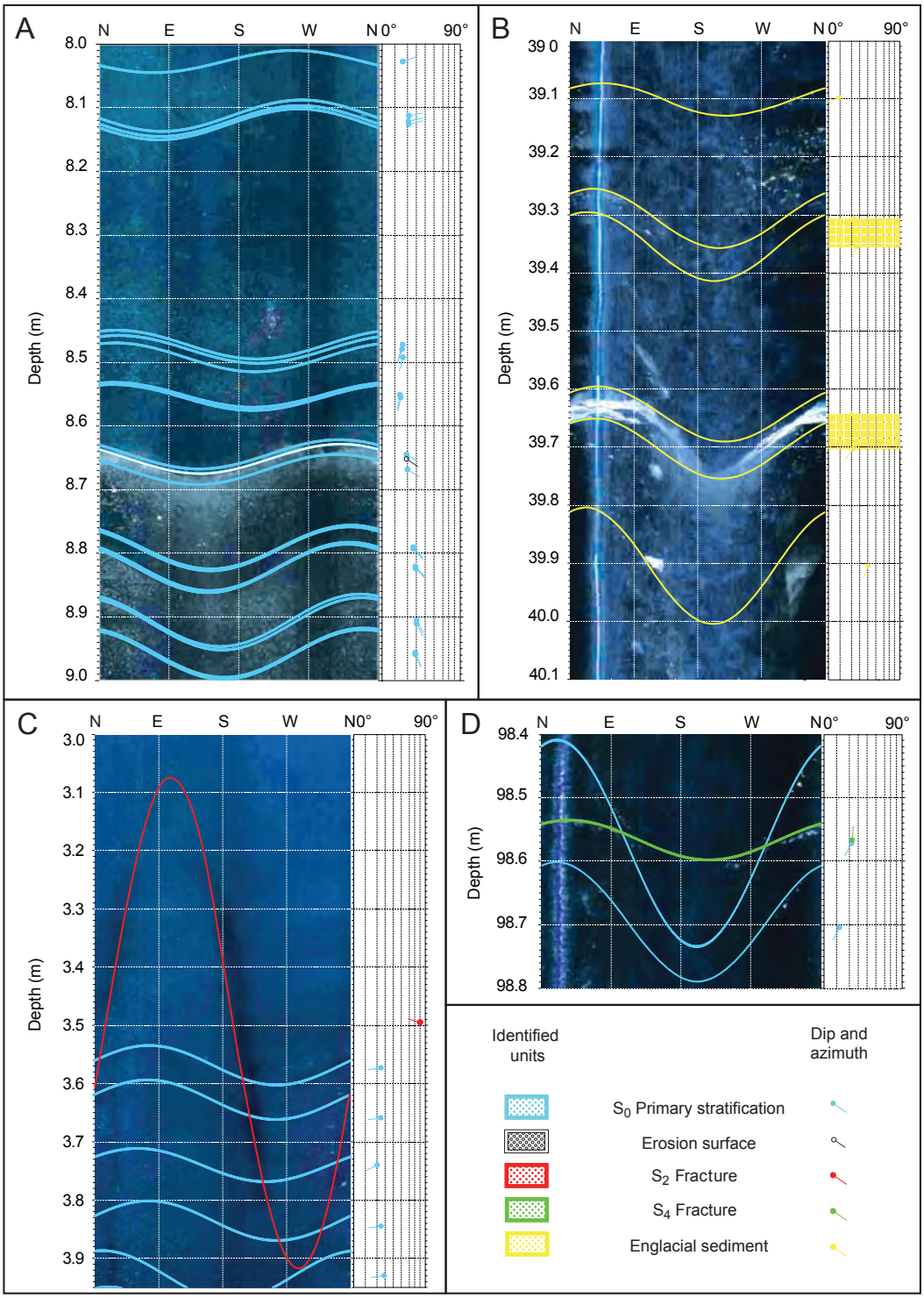

Figure 6.2: Unrolled borehole logs illustrating contrasting ice types - (a) S_0 continuous layering displaying paraconformity (8.65 m) interpreted as a summer erosion surface, (b) continuous layering intercalated with laminated and sheared basal ice (at 39.65 m) and sand to cobble sized clasts, (c) S_0 continuous layering cross-cut by S_2 transverse fractures, and (d) primary stratification cross-cut by S_4 oblique fracture from MLB-3.

to near-vertical. The dips of S_0 continuous layering are described in greater detail in the context of fold structures (below).

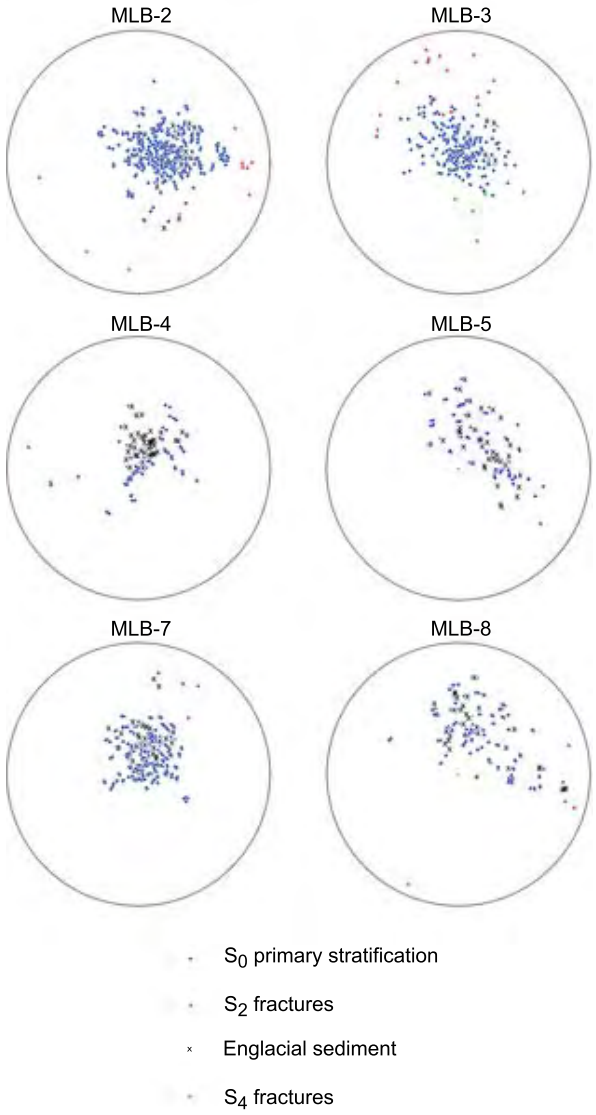

Figure 6.3: Poles to planes Schmidt equal-area lower-hemisphere stereoplots for surveyed boreholes - MLB-2, MLB-3, MLB-4, MLB-5, MLB-7 and MLB-8 showing dip and azimuth of structures identified and englacial sediment layers.

6.2.2 Fold structures (F_1,F_2,F_3)

Large-scale (10 to 50 m) lateral folding (F_1) of S_0 continuous layering into similar or chevron-type folds is visible from aerial photographs. Fold axes are orientated parallel to flow unit boundaries (Fig. 6.1) and surface flow vectors (Rees and Arnold, 2007). At the glacier surface, below the snow line, small-scale (1 to 10 m) parasitic folds are ubiquitous on

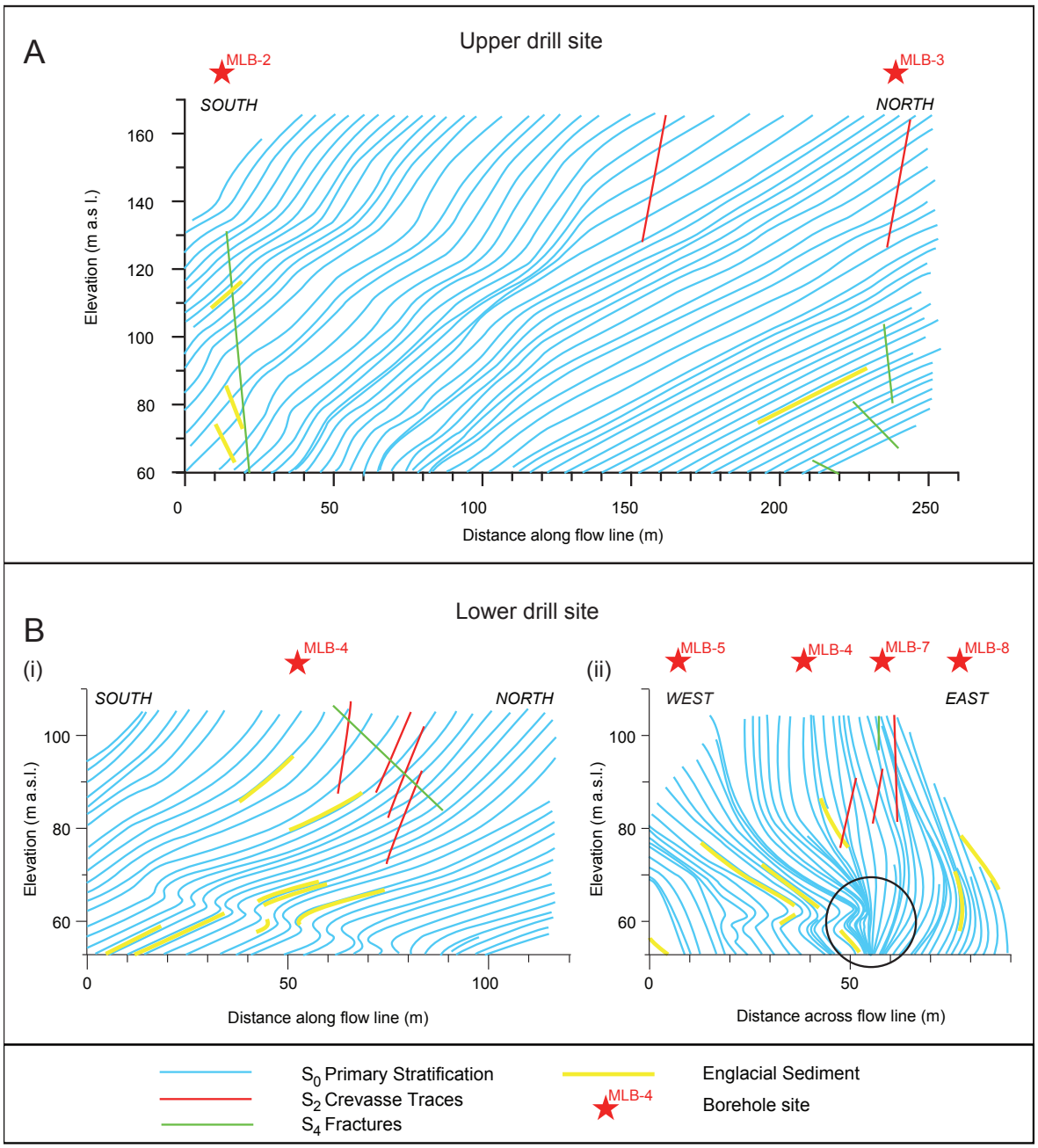

Figure 6.4: Cross-sections through interpolated 3D scene graphs of glacier structure - (A) the upper drill site; and (B) the lower drill site (i) parallel to flow, and (ii) orthogonal to flow. Hinge of large-scale lateral fold (F_1) is highlighted by circle. For orientation of cross-sections see Fig. 3.2.

the large-scale lateral folds, being more easily identifiable at the ice surface than large-scale folds. These are also lateral similar folds; with flow-parallel fold axes that consistently dip gently upglacier. The orientation of S_0 continuous layering as revealed by three-dimensional interpolation (Fig. 6.4b(ii)) within a flow-normal borehole array at the lower drill site (Fig. 3.2) is consistent with large-scale lateral folding. The dip of S_0 continuous layering increases from east to west transverse to ice flow, from 35° at MLB-5 to near-vertical at MLB-4. At MLB-7 the dip of S_0 continuous layering decreases to 70°. At depth within the ice mass (at an elevation of 60 m a.s.l.) S_0 continuous layering form a large-scale lateral fold hinge (highlighted in Fig. 6.4b(ii)), characterised by near-vertical dips at the fold axis and planes dipping less steeply away from the central fold hinge, trending upglacier at angles of 10 to 40°. The configuration of the F_1 fold hinge (as revealed in Fig. 6.4b) is complicated by further medium-scale horizontal (F_2) folding. This decimetre-scale horizontally orientated similar fold (F_2) occurs in S_0 continuous layering at a depth of 40 to 50 m within MLB-4 (Fig. 6.2b), 10 m above the bed (Rippin et al., 2003). The fold axes are sub-parallel and dip downglacier at 30°, with an azimuth parallel to flow direction. S_0 primary stratification is further overwritten by recumbent folding (F_3) at the small scale (0.1 to 1 m) in association with S_3 arcuate fractures (Fig. 6.5a,b). The axes of F_3 folds are orientated parallel to the dissecting S_3 arcuate fracture, and dip steeply upglacier at angles of 35 to 70°. Vertical displacement (a few centimetres to several decimetres) across the fracture is evidenced in a number of locations by the offset of S_0 primary stratification across the S_3 fracture.

6.2.3 Longitudinal planes (S_1)

Longitudinally orientated layers of intercalated coarse bubble-rich and coarse bubble-poor ice, 3 to 100 mm thick, occur at the glacier surface below the snow line (Fig. 6.5c). Layering is most pronounced at the glacier margins and flow unit boundaries, but is pervasive across the entire glacier (Fig. 6.1), becoming obscured close to the terminus due to the development of S_3 planes and an increase in supraglacial debris cover. Longitudinal planes have an axial-planar relationship with S_0 primary structure, being consistently orientated parallel to F_1 fold hinges and surface flow vectors (Rees and Arnold, 2007). Longitudinal planes dip consistently between 80° and 90°, with strike orientated parallel to surface flow vectors. No longitudinal planes were observed in any of the OPTV borehole logs - unsurprising considering the parallel orientations of the planes and the boreholes.

6.2.4 Transverse fractures (S_2)

S_2 transverse fractures occur as both open fractures and fracture traces orientated transverse to modeled ice flow vectors (Hambrey et al., 2005). Open transverse fractures were observed

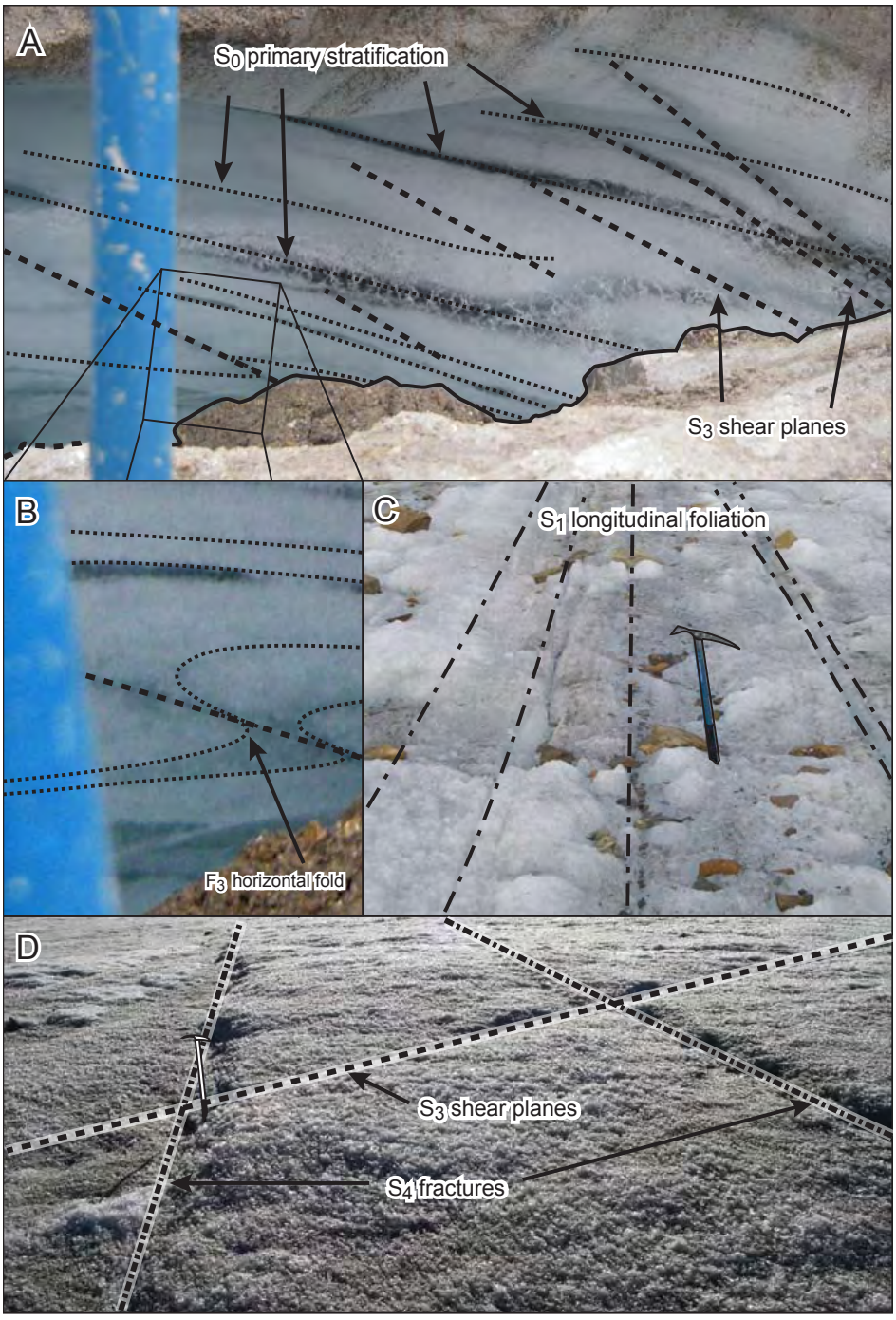

Figure 6.5: Photographs taken at the glacier surface illustrating structural relationships - (A) the relationship between S_0 continuous layering, S_3 shear planes and F_3 small-scale recumbent folds seen in section in a meltwater channel; (B) detail of A showing the displacement of S_0 primary stratification by a shear plane (S_3) forming a small-scale (F_3) recumbent fold; (C) the nature of S_1 longitudinal stratification and the exposure of a Type-I debris ridge; (D) the cross-cutting relationship between S_3 arcuate shear planes and S_4 oblique fractures.

from aerial photography in the accumulation area, but are absent below the snow-line or within borehole logs. Transverse fracture traces occur infrequently at the glacier surface below the snow-line (Fig. 6.1). Fracture traces are assumed to be either (i) open crevasses that have since closed with transport downglacier from the accumulation area; (ii) fractures that have formed at subcritical tensional stresses (Schulson, 2001), or (iii) fracture traces that were continuous with open crevasses that were formed at the ice surface but have since ablated. Fracture traces are observed within OPTV logs at depths of 30 m at both the upper drill site and the lower drill site, being more common at the upper site than the lower. Fracture traces are composed of fine bubble-rich crystals (1 to 3 mm in diameter) orientated normal to the fracture orientation, dissected by a central fissure. S_2 fracture traces observed in OPTV logs dip between near-vertical and 60° in an upglacier direction.

6.2.5 Arcuate fractures (S_3)

A dense series of upglacier-dipping arcuate fractures, cross-cutting S_0 continuous layering, S_1 longitudinal planes and S_2 transverse fractures, develop 1 km upglacier of the terminus and increase in spatial frequency towards the terminus (Fig. 6.1). The fractures are 50 to 300 m long, comprised of planes of fine bubble-rich ice crystals (1 to 3 mm in diameter) up to 35 mm wide, interposing coarse bubble-rich ice, as evidenced by surface observations (Fig. 6.5a). S_3 fractures dip at angles of between 30° and 80°, becoming shallower towards the terminus. Arcuate fractures are not consistently orientated at any one point of the glacier surface, but frequently intersect at low angles (Fig. 6.1). Observed in vertical section in meltwater channels (Fig. 6.5a), S_3 fractures cut across S_0 continuous layering. This often coincides with the folding of S_0 layers into hook-shaped asymmetric folds, indicating displacement along the S_3 fracture plane (Hudleston, 1989). S_3 arcuate fractures are not identified within borehole logs. Surface excavations along S_3 fracture planes down through the ice mass with an ice axe reveal thin films of muddy debris ($<$1 mm thick) occurring in high concentrations along the fracture planes.

6.2.6 Oblique fractures (S_4)

At the glacier surface closed fractures orientated obliquely to the ice margin occur 1 km upglacier from the terminus (Fig. 6.1, Fig. 6.5d). The dip of these fractures, measured at the glacier surface, range from near vertical to 50°, with 70% of the features dipping upglacier and 3% dipping downglacier. The fractures are crystalographically similar to S_2 transverse fractures (above). Oblique fractures are also observed at seven locations in OPTV logs (Fig. 6.5d; Fig. 6.3), in all cases dipping downglacier at angles between 80° and 23° (Fig. 6.2).

6.2.7 Englacial sediment layers

Intercalation of S_0 stratification with layers of sediment-rich ice occurs in one or more instances in all six borehole logs (Fig. 6.2b). Englacial sediment layers dip from 9.3° to 71° upglacier sub-parallel to adjacent S_0 primary stratification and are observed in borehole logs from depths of 20 to 100 m (Fig. 6.2b). At the lower drill site, sediment layers are associated with the lateral folding (F_1) of S_0 stratification into steep fold limbs, elevating englacial sediment layers into flow-parallel near-vertical planes on both sides of the fold hinge (Fig. 6.4b(ii)). Englacial sediment layers are composed of two distinct facies types. (i) Planes of sediment 0.01 to 0.1 m thick composed of sheared fines (mud to gravel sized particles) in high concentrations. These layers appear to be similar to the laminated or solid basal ice facies described by Hubbard and Sharp (1995a), Knight (1988), Knight (1997) and Waller et al. (2000). (ii) Layers of bubble-rich ice containing individual clasts or particle inclusions up to 700 mm in diameter, where particle long axes appear to be orientated parallel to the dip of the adjacent S_0 continuous layering (Fig. 6.2b). Included clasts show no bedding relationships and are very angular to sub-rounded, occurring in isolation or in association with sheared englacial sediment facies.

6.2.8 Supraglacial debris ridges

Longitudinal debris ridges composed of very angular to sub angular sandy gravel occur up to 1 km upglacier of the terminus (Fig. 6.1). These are ice cored, up to 1 m high and 10 m wide, widening downglacier and coalescing to form a near-continuous cover of supraglacial debris at the terminus. Longitudinal debris ridges are orientated parallel to ice flow and S_1 longitudinal planes and have an axial planar relationship with large-scale lateral (F_1) folds. Longitudinal debris ridges can be divided into two morphological types: (Type-I) ridges that appear gradually, as isolated clasts, widening downglacier until they form a continuous cover of debris; and (Type-II) ridges that originate abruptly in association with S_3 arcuate fracture planes from which point they propagate downglacier. At one location Type-II ridges are laterally continuous, forming a transverse debris stripe 50 m wide and 0.5 m high.

6.3 Interpretation

Each of the structures described above can be interpreted individually and in relation to each other within the framework of the glacier's overall structural evolution, englacial and supraglacial sediment transport and thermal setting. These interpretations, although, need to be mindful of several limitations that arise from the interpolation of two dimensional

OPTV and surface data into three dimensions. These limitations may be classified into three categories following Thomas (1991):

i. Missing vertical structures,

ii. Misinterpretation of folded structures,

iii. Misjudging lithological characteristics.

While supplementing surface mapping with borehole OPTV analysis undoubtedly increases the power of structural investigations, interpolation and geometrical limitations cannot be eliminated completely: each of these limitations is considered in the interpretations presented below.

6.3.1 Primary stratification (S_0)

The composition of continuous layering (S_0) is consistent with descriptions of initial snowpack formation at Midre Lovénbreen (Wadham and Nuttall, 2002), i.e. regularly alternating layers of low-density wet snow ice, high-density superimposed ice, and discoloured fine-grained summer ice. The metamorphosis of seasonal snow layers to glacier ice forms corresponding regularly alternating seasonal glacier ice facies: (i) coarse bubble-rich crystals represent winter accumulation layers that have undergone partial melt and refreezing; (ii) coarse bubble-poor crystals are a product of snowmelt refreezing at the base of the snowpack; (iii) fine bubble-rich crystals are the product of snow accumulation during the ablation season, characterized by thin strata ($<$100 mm) and small crystal diameter ($<$5 mm). The occurrence of paraconformities is consistent with the ablation of summer ice surfaces overlain by winter accumulation layers, i.e. they are erosion surfaces.

6.3.2 Fold structures

6.3.2.1 Large-scale lateral folds (F_1)

Large-scale lateral folds (F_1), observed at the glacier surface from aerial photographs and within three-dimensional structural visualizations of OPTV logs, are interpreted to be formed by the folding S_0 primary stratification under convergent ice flow, as ice from the glacier's constituent cirque basins combine to form a narrow ice tongue. Hambrey and Glasser (2003) reasoned that this convergent flow is associated with high laterally compressive stresses, deforming S_0 stratification into fold limbs and flow-parallel fold-hinges. These authors further argued that lateral folding is most intense at flow-unit boundaries, forming isoclinal folds with near-vertical fold-limbs, whereas towards to centre of flow units

folding is more gentle and the dip of fold limbs are correspondingly less steep. The F_1 fold revealed in cross-section by three-dimensional visualization of borehole data from the lower drill site (Fig. 6.4b(ii)) is structurally consistent with the concepts advanced by Hambrey and Glasser (2003), although in this case the fold represents the lower hinge of an isoclinal fold, rather than the surface exposure of the upper hinge. Further support for this concept may be taken from the position of the flow-unit boundary 10 m to the west of MLB-8, where the dip of S_0 stratification remains near-vertical, whereas, in contrast, the dip of S_0 stratification decreases away from the flow-unit boundary towards MLB-4 and MLB-5.

6.3.2.2 Meso-scale recumbent folds (F_2)

Horizontal similar folds F_2 similar to those reported herein have been observed in section at a number of glaciers, commonly associated with basal ice facies (Knight, 1988; Sharp et al., 1994; Hambrey and Lawson, 2000; Chandler et al., 2008). Indeed the presence of sediment-rich basal-ice facies in the upper and lower limbs of F_2 folds in the present study strengthens this association further. Here, the orientation of the fold hinge indicates that ice located within some metres of the glacier base is moving faster than that immediately overlying it. Enhanced flow of the lower layer may be accounted for by the presence of a local slippery spot, e.g. caused by a subglacial drainage conduit (Willis et al., 2003) or by ice flow within a deep bed undulation (Gudmundsson, 1997). Geophysical data collected by King et al. (2008) identified that ice at the lower drill site is frozen to the bed and that subglacial drainage is either poorly developed or absent from the area. In contrast, Rippin et al. (2005) concluded (on the basis of force-balance modelling, surface velocity and hydrological measurements) that small areas of locally reduced basal drag could be generated due to the penetration of basal melt through and under the glacier's peripheral cold-based ice from its warm-based core. Gudmundsson's (1997) model of ice flow over a sinusoidal bed predicts accelerated flow over the crest and trough of the sinusoid on the basis of heterogeneous basal shear stress distributions across the asperity. The lateral extent of the fold layer measured at Midre Lovénbreen is unknown; however the restriction of fold F_2 to observations in MLB-4 suggest that it is most likely to be caused by the presence of a bedrock asperity or slippery-spot on the scale of metres to decimetres. It is difficult to determine, on the basis of observations made here, which of these mechanisms is more likely to be responsible, particularly because they probably do not act independently from one another.

6.3.2.3 Small-scale recumbent folds (F_3)

Small-scale recumbent folds (F_3) are interpreted as having formed by vertical displacement of S_0 stratification, indicated by the offset of the hook-shaped folds across S_3 fractures (Fig. 6.5b). These structures are indicative of simple shear under compressive stress (Hudleston, 1989), and are discussed in the context of S_3 arcuate fractures (below).

6.3.3 Longitudinal foliation (S_1)

S_1 are interpreted as foliation on the basis of: (i) their orientation parallel to surface ice flow vectors and F_1 fold axes (Rees and Arnold, 2007), and (ii) the small diameter of their constituent ice crystals relative to adjacent coarse-grained bubble-rich ice, indicative of dynamic recrystallisation under simple shear (Wilson and Marmo, 1999). Two alternative formation mechanisms for foliation in glacier ice have been proposed: (i) they arise from the deformation of pre-existing inhomogeneities, i.e. primary stratification or crevasses, under laterally compressive and longitudinally tensile stresses (Hambrey, 1977; Hooke and Hudleston, 1978), and (ii) they form via the dynamic recrystallisation of ice crystals parallel to the maximum strain rate tensor (Hambrey and Lawson, 2000). The latter mechanism is considered to be more important at Midre Lovénbreen because S_1 planes are observed to cut across S_0 primary stratification at the surface and there is no reason to believe that this is not the case at depth. Although S_1 foliation was not observed at depth in our OPTV logs, this is of little bearing to the existence of S_1 at depth because the chance of (sub-vertical) boreholes intercepting these (sub-vertical) planes is minor.

6.3.4 Transverse fractures (S_2)

The absence of open fractures below the snow-line indicates that strain rates in the main trunk of Midre Lovénbreen are well below the critical threshold for active crevasse formation (Weiss and Schulson, 2000). Fracture traces occurring at or close to the surface are inferred to reflect former flow conditions when ice extent and velocities were much greater, probably during the Little Ice Age, a period when some researchers have suggested the glacier was underlain by more extensive warm-based ice (Hambrey et al., 2005) and may even have undergone episodic surging (Liestøl, 1988; Hagen et al., 1993).

6.3.5 Arcuate shear planes (S_3)

S_3 arcuate fractures are interpreted as shear planes on the basis that: (i) they cut across S_0 primary stratification at low-angles, resulting in the formation of hook-shaped asymmetric F_3 recumbent folds (Fig. 6.2a, b) indicative of vertical displacement along the plane

(Hudleston, 1989); (ii) they are composed of fine-grained bubble-rich ice, indicative of dynamic recrystallisation (Wilson and Marmo, 1999), and (iii) the vertical displacement of upglacier ice units relative to downglacier ice units indicates that the ice is subject to high compressive stresses parallel to the ice flow vector (Souchez, 1967; Rees and Arnold, 2007). Structurally S_3 shear planes are similar to arcuate fractures identified in the terminal zone of other valley glaciers (Hambrey et al., 1996; Glasser et al., 1998; Glasser et al., 2003; Roberson, 2008), where it has frequently been suggested that compressive brittle failure is facilitated by pre-existing structural weaknesses, e.g. strongly anisotropic crystal fabrics or rotated fractures (Nye, 1952; Weiss and Schulson, 2000). However, at Midre Lovénbreen the low density of S_2 open fractures and fracture traces indicate that S_3 shear planes form as an entirely new generation of structures. The compressive stresses required to initiate arcuate shear plane development are considered to be caused by the transition between warm-based ice in the main trunk of the glacier and cold-based ice at the glacier terminus and margins (Rippin et al., 2003; King et al., 2008). The reduction in flow velocity between the two basal regimes leads to high longitudinally compressive stresses, forcing ice upglacier to override obstructing downglacier ice, resulting in the vertical offset of S_0 stratification across the shear plane (Hambrey and Huddart, 1995).

6.3.6 Oblique fractures (S_4)

Oblique fractures are frequently observed near the lateral margins of ice masses, caused by friction-induced stresses at the ice-bed interface (Nye, 1952). Surface observations of S_4 oblique fractures have only reported upglacier-dipping fractures. However, downglacier-dipping S_4 oblique fractures observed in OPTV borehole logs have not been reported in the literature, either at the surface or within an ice mass. However, Nye's (1952) model of fracture formation does predict slip-line fields under extending flow (Nye, 1952, ;his Fig. 6), which form parallel to the maximum strain rate tensor and dip downglacier at depth. Until now it has been very difficult to observe these fractures. The geometry of the glacier indicates that such fractures would be most likely to form in the accumulation area where ice flows over steep bedrock. Basal strain rates at Midre Lovénbreen modeled by Hambrey et al. (2005) indicate that englacial or basal fractures will not form under current stress conditions, according to the parameters outlined by van der Veen (1998). Previous studies have hypothesized that transverse surface crevasses and proglacial landform assemblages are indicative of former wet-based conditions during the Little Ice Age, when the flow of the glacier was considerably faster than today. Correspondingly higher strain rates during a more active phase could therefore account for the formation of downglacier-dipping englacial fractures observed within OPTV logs.

6.3.7 Englacial sediment layers

The intercalation of sediment layers within S_0 primary stratification can be reasonably accounted for by at least two processes: (i) incorporation of rockfall debris synchronously with the accumulation of snow on a glacier surface, or (ii) entrainment of particles at the bed (probably via regelation and/or freeze-on), coupled with advection through the ice mass by shearing and folding. The former mechanism is invoked to account for sediment layers observed close to the ice surface in the upper drill site (Fig. 6.2a) where, very angular to sub-angular gravel to cobble-sized particles orientated parallel to the dip of primary stratification are indicative of high-level transport through the ice mass (Boulton, 1978; Owen et al., 2003). In contrast, the similarity in visual appearance of the high-concentration sheared sediment layers observed deeper in the OPTV logs at the lower drill site (Fig. 6.2b) with basal ice facies described by several authors beneath a range of ice masses (Hubbard and Sharp, 1995a; Knight, 1988; Knight, 1997; Waller et al., 2000) supports the interpretation that these are formed at the bed by regelation and/or the freeze-on of subglacial sediment. This interpretation is supported by the presence of large-scale vertically orientated F_1 fold structures close to the bed, and upglacier-dipping arcuate shear planes (S_3), which have frequently been invoked to account for the advection of sediment through an ice mass (Souchez, 1967; Hudleston, 1977; Hambrey and Lawson, 2000). The occurrence of isolated pebble to cobble sized clasts in association with sheared englacial sediment layers provides evidence that regelation and/or adfreezing may also be responsible for the incorporation of larger particles into the ice mass.

6.3.8 Supraglacial debris ridges

Type-I longitudinal debris ridges are interpreted as englacial sediment layers intercalated within S_0 primary stratification that has been elevated into flow-parallel ridges by F_1 lateral folding under convergent flow. This interpretation builds on the conceptual model advanced by Hambrey and Glasser (2003), by providing evidence of englacial sediment layers similar in physical characteristics to laminated basal ice facies described by Hubbard and Sharp (1995a), Knight (1988), Knight (1997) and Waller et al. (2000). Three-dimensional reconstructions of internal glacier structure, based on data interpolation from multiple OPTV logs, indicate that these basally derived englacial sediment layers are elevated into flow-parallel sub-vertical planes around a fold-axis by large-scale lateral folding (F_1) (Fig. 6.4b(ii)). The proximity of the fold limbs to a flow unit boundary and a large Type-I longitudinal debris ridge strongly suggests that the fold axis is the lower hinge of an isoclinal fold exposed at the ice surface. Contributions to this large (1 km long) longitudinal debris stripe by rockfall from a headwall spur are clearly also significant, however OPTV

data provide evidence that subglacially derived sediment layers also supply a major proportion of the sediment input. Concurrently, smaller longitudinal debris ridges (100 to 50 m long), occurring within the centre of flow units (Fig. 6.1), are inferred to receive a proportionately higher contribution to their mass from basally derived englacial sediments and a proportionately lower contribution from rockfall-drived sediments.

The formation of Type-II longitudinal debris ridges, occurring abruptly in association with S_3 shear planes, is interpreted to be the result of sequential deformation of large-scale F_1 flow-parallel fold hinges by small-scale F_3 horizontal-folds (Fig. 6.6). It is envisaged that englacial sediments are folded laterally into large-scale F_1 fold hinges under convergent ice flow, similar to the formation of Type-I debris ridges, but rather than the fold hinges being gradually exposed (as is the case for Type-I ridges) they are cut across by S_3 shear planes and incorporated into F_3 recumbent folds. Vertical displacement across S_3 shear planes then concentrates englacial sediment into a tight recumbent fold, aligned parallel to the dip of the associated S_3 shear planes, with which they appear explicitly associated when exposed at the ice surface.

6.4 Discussion

The data and interpretations presented above raise several points for further discussion.

6.4.1 Type-I longitudinal supraglacial debris ridges

A large body of research has provided evidence that longitudinal supraglacial debris ridges, frequently observed at polythermal glaciers, and at Svalbard glaciers in particular (Hambrey and Glasser, 2003; Hubbard et al., 2004), include a major component of basally derived sediment. Empirical evidence for this includes: particle morphology, grain-size distribution, isotopic composition, and relationship to glacier structure and ice crystallography ((Bennett et al., 1996; Hubbard et al., 2004; Hambrey et al., 2005). In this study shear structures in englacial sediment layers intercalated within S_0 primary stratification are identified, which are physically similar to laminated or solid basal ice facies described by Hubbard and Sharp (1995a) in the western Alps and by Knight (1997) in Greenland. Three-dimensional visualizations of internal glacier structure, based on data interpolation between borehole arrays (Fig. 6.4), provide evidence that basally derived englacial sediment layers are incorporated into large-scale lateral folds (F_1) and elevated into fold limbs. These fold limbs have a near-vertical dip proximal to flow unit boundaries and a more gentle dip distal from flow unit boundaries. Hambrey and Glasser's (2003) model of longitudinal debris ridge formation proposes that debris stripes formed at flow unit boundaries are flow-parallel isoclinal

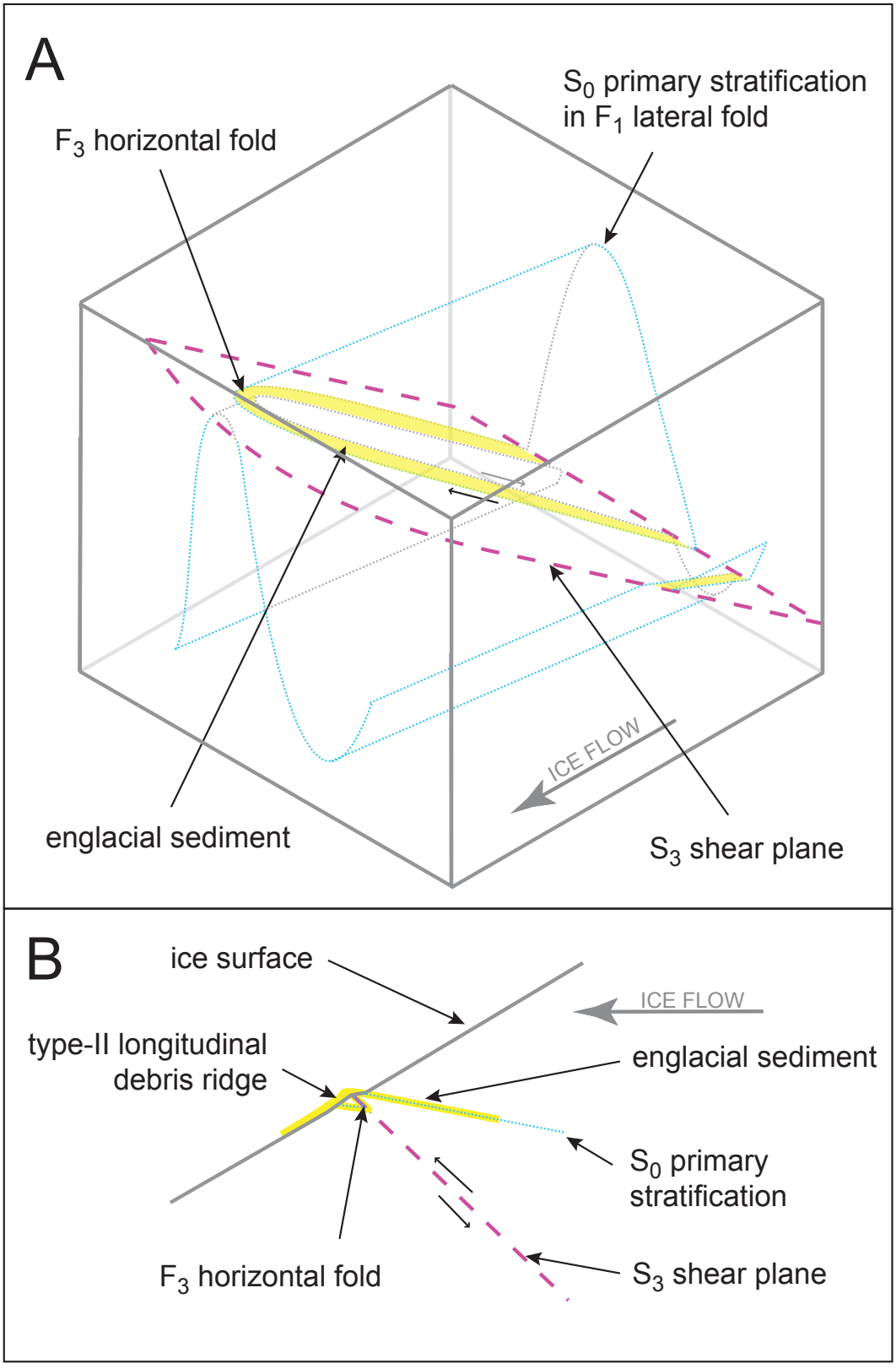

Figure 6.6: A schematic illustration of the deformation of an F_1 fold hinge by an F_3 fold in associated with S_3 arcuate shear plane - (A) a three-dimensional orthographic view within the ice mass, and (B) in cross-section outcropping at the glacier surface to form a Type-II longitudinal debris ridge.

fold hinges. In contrast, Woodward et al. (2002) envisaged that supraglacial longitudinal debris ridges might be formed by the reorientation of basal crevasse-fill sediments that have deformed under high cumulative strain following successive surge events. While it has been demonstrated that crevasse fills may become progressively rotated into a flow-parallel orientation under steady-state flow conditions (Hubbard and Hubbard, 2000), the low density of surface crevasses at Midre Lovénbreen suggests that this process is unlikely to account for the volume of material observed in longitudinal supraglacial debris stripes at the glacier. Furthermore basal crevassing is unlikely to occur at Midre Lovénbreen as the physical conditions for deep crevasse formation require high basal water pressures and high strain rates at the bed (van der Veen, 1998). In contrast to nearby Kongsvegen, which terminates in water and is thought to have undergone episodic surging (Woodward et al., 2002), these conditions are not met, and were unlikely to have been met in the recent past, at Midre Lovénbreen (Hambrey et al., 2005; Irvine-Fynn et al., 2005b). The relationship between large-scale lateral folding, as revealed by three-dimensional visualizations (Fig. 6.4b(ii)), and supraglacial longitudinal debris ridges at the surface of Midre Lovénbreen is consistent with the interpretation that it is the lower hinge of an isoclinal fold formed by high laterally compressive stresses at the flow unit boundary under convergent ice flow. OPTV logs also provide evidence that large-scale lateral folding is responsible for the elevation of coarse pebble to cobble sized clasts, inferred to be of subglacial origin by their close association with sheared englacial sediment layers.

6.4.2 Type-II longitudinal supraglacial debris ridges

The association between S_3 shear planes and thin ($<$1 mm) films of muddy debris observed in section (above) is at odds with the geometric relationship between S_3 shear planes and Type-II longitudinal debris stripes observed at the ice surface at Midre Lovénbreen (above). The textural composition of Type-II longitudinal debris ridges (i.e. sandy gravel) is incompatible with the advection of well-sorted muddy debris along S_3 shear planes. Small-scale recumbent folding (F_3) in S_0 primary stratification, associated with vertical displacements across S_3 shear planes, is invoked to account for the surface morphology of Type-II longitudinal debris ridges in this study (Fig. 6.6). It is proposed that englacial sediment layers, deformed into flow-parallel fold hinges by large-scale lateral folding (F_1), are subsequently intersected by S_3 shear planes and folded again into small-scale recumbent folds (F_3). This deformation sequence is envisaged to concentrate englacial sediment into a shear plane-parallel fold axis. As the F_3 fold hinge outcrops at the ice surface, the englacial sediment appears abruptly, in association with the S_3 shear plane (Fig. 6.6b), thus obscuring the relationship that the debris ridge has with large-scale F_1 folding and S_0 stratification.

This mechanism is suggested tentatively, as conclusive empirical evidence of this structural relationship is lacking. The proposed mechanism implies that folding of an existing Type-I debris ridge could transpose it into a Type-II debris ridge, while conversely, continued melt-out of a Type-II debris ridge might lead to its reclassification as a Type-I debris ridge. This hypothesis could be therefore easily tested by comparisons between time-series aerial photographs or by time-lapse photography of the glacier.

6.4.3 Geometric relationships between glacier morphology and structural analysis

Surface mapping of glacier structures is heavily influenced by the nature of the ice surface texture and the geometric relationship between the orientation of the ice surface and the structures being mapped. This problem is highlighted by Woodward et al.'s (2002) critique of Glasser et al.'s (1998) proposed mechanism of longitudinal debris ridge formation by large-scale lateral folding. Woodward et al. (2002) discounted Glasser et al.'s folding mechanism on the basis of observations of unfolded stratification exposed in the terminal ice cliff-face at nearby (surge-type and tidewater) Kongsvegen. Woodward et al. (2002) expressed considerable uncertainty in the interpretations of Glasser et al. (1998) on the basis of the geometric relationships between the observed ice surface and the structures in question. Three-dimensional reconstructions of internal glacier structure (Fig. 6.4) reveal that the orientation of S_0 primary stratification is highly variable at scales ranging from metres to hundreds of metres. Mapping of these structures on an irregular sloping ice surface or at an ice cliff are likely to result in observational difficulties. This work demonstrates that three-dimensional structures are easier to conceptualize and hence interpret using on-screen three-dimensional visualization techniques, rather than in two-dimensional cross-sections. Furthermore, cross-sections taken through our three-dimensional reconstructions (Fig. 6.4) are presented both orthogonal and parallel to surface flow vectors (Rees and Arnold, 2007) in an attempt to reduce interpretational ambiguity.

6.4.4 Limitations of OPTV-based structural analyses in ice boreholes

A specific set of problems, some restricted to ice masses and some more widely relevant, are encountered when applying an OPTV system to logging boreholes in a glacier. These are presented and discussed below with reference to the interpretations made above.

Firstly, a general problem encountered is the largely monomineralic composition of ice. It is possible to identify both fractures and foliation from OPTV logs in rock boreholes,

primarily because they are commonly characterised by contrasting minerals (Williams and Johnson, 2004; Spillmann et al., 2007). Correlations between strata in solid rock boreholes are also frequently facilitated by being able to trace specific marker horizons. Such marker horizons are largely absent from ice masses, which are best regarded as single sedimentary units undergoing low-grade metamorphism. The lack of distinct boundaries was addressed in this study when interpolating S_0 primary stratification between borehole logs, by treating each layer identified as a Lagrangian vector rather than as a lithological unit with specific characteristics.

Secondly, it is in the nature of vertically orientated boreholes to systematically miss vertically orientated structures. This limitation could potentially be addressed by use of an inclined borehole, although this might fail to produce a dramatically higher level of fracture detection. The failure of OPTV logs to detect either S_1 foliation; S_2 or S_3 fractures in ice may be related to the role of differential erosion associated with surface weathering which does not occur at depth. Alternatively, it may be that ice that has undergone dynamic recrystallisation in fracture and foliation planes is undetectable in OPTV logs, because of the 1 mm vertical resolution of the OPTV and the small size of the ice crystals involved (Schulson, 2001). More sensitive, perhaps spectrally based, procedures for feature discrimination may therefore need to be developed for OPTV adaptation to ice-based investigations.

Thirdly, the inability to detect fractures in ice boreholes is likely to result in an oversimplified interpolation of strata between boreholes, that otherwise may be offset across fractures. It is suggested that S_2 fractures at Midre Lovénbreen are unlikely to result in marked offset across S_0 primary stratification, firstly because they are vertically dipping and form under tensile stress normal to the direction of flow, and secondly because relatively few are identified on the glacier surface. Observations of S_0 primary stratification offset across S_3 arcuate shear planes demonstrates that S_0 interpolation is oversimplified at Midre Lovénbreen. Despite these limitations, it is clear from individual OPTV logs (e.g. MLB-4 and MLB-7 (Fig. 6.45b(ii)) that offsets in S_0 primary stratification, caused by both F_1 large-scale and F_2 medium-scale folds, can be detected due to the high vertical resolution of the technique.

6.5 Conclusions

The use of OPTV in multiple boreholes has successfully allowed the internal structure of two regions of the frontal zone of Midre Lovénbreen to be logged in Cartesian space with geometric accuracy. Interpolation between individual borehole logs has also allowed several distinctive englacial structures to be visualized in three-dimensions. Combining

measurements from OPTV logs with surface mapping reveals the visual and geometrical characteristics of numerous structural elements. OPTV analysis of hot-water drilled boreholes can yield significant new evidence relating to the three-dimensional internal structure of glaciers, particularly when combined with surface mapping. The research on Midre Lovénbreen presented in this chapter has resulted in several novel findings, including:

1. The identification of eight structural elements (i) S_0 primary stratification; (ii) S_1 longitudinal foliation; (iii) S_2 transverse fracture traces; (iv) S_3 arcuate shear planes; (v) S_4 oblique fractures; (vi) F_1 large-scale lateral folds; (vii) F_2 medium-scale recumbent folds and (viii) F_3 small-scale recumbent folds. S_4 oblique fractures, predicted by Nye (1954), are identified empirically here for the first time.

2. The differentiation and hypothesized formation of two texturally similar longitudinal debris ridge morphologies: Type-I ridges appear gradually at the ice surface in association with large-scale lateral folds (F_1), while (newly recognised) Type-II ridges appear more abruptly in association with S_3 arcuate shear planes and small-scale recumbent foldFig. 6.2bFig. 6.2bs (F_3).

3. The visualization of debris-rich basal ice elevated into an englacial position. The visual characteristics of englacial sediment layers identified within our OPTV logs are consistent with laminated and solid basal ice facies described by Hubbard and Sharp (1995). Three-dimensional visualization of internal glacier structure, based on the inter-borehole interpolation of OPTV logs, reveal that these englacial sediment layers are incorporated into large-scale F_1 lateral folds and elevated into near-vertical planes in association with lateral compressive stress and Type-I longitudinal debris ridge formation, consistent with the structural model of Hambrey et al. (2005).

4. Despite these successes, the application of borehole OPTV to reconstructing the three-dimensional structure of ice masses is still limited by difficulties in (i) intersecting and imaging borehole-parallel structures, (ii) the requirement for inter-borehole spatial interpolation, and (iii) imaging layers whose constituent crystals are either difficult to distinguish visually or are too thin to be identified at a resolution of 1 mm. All three of these issues represent challenges that require addressing by continuing technique development.

Chapter 7

The sedimentology of Midre Lovénbreen, Svalbard

7.1 Introduction

This chapter presents and interprets the results of laboratory analyses of sediment samples collected from a range of sediment-landform assemblages at Midre Lovénbreen (Section 7.2). These data were collected to identify the processes involved sediment transport and the formation of sediment-landform assemblages at a small polythermal valley glacier. The hypotheses presented complement structural interpretations made at the glacier (Chapter 6) and build on existing conceptual models to provide new insights into ways in glacial sediment transport operates at polythermal valley glaciers (Section 7.3).

Specifically, the aims of the research presented in this chapter are:

i. To examine the extent to which glacier structure influences the characteristics of glacially transported sediment at Midre Lovénbreen.

ii. To determine the origin of supraglacial debris cones at Midre Lovénbreen.

iii. To evaluate and contribute to existing conceptual models of glacial flute formation on the basis of sedimentary data collected at Midre Lovénbreen.

To address these aims, ninety nine sediment samples were taken from sediment-landform assemblages across the glacier surface and proglacial area. The results of laboratory analyses (detailed in Section 3.3) are presented in Section 7.2. The processes involved of sediment-landform assemblage formation are discussed in Section 7.3. Section 7.5 summarises the findings of the research presented and discussed in Chapter 7.

7.2 Results

Geomorphological observations and mapping reveal the presence of at least nine distinct sediment-landform assemblages at Midre Lovénbreen: (i) talus cones (ii) subglacial debris layer, (iii) longitudinal debris ridges, (iv) transverse debris ridges, (v) debris cones, (vi) proglacial debris layer and (vii) proglacial debris layer ridges. The morphology, texture and particle shape of these sediment-landform assemblages are described below, supplemented by key figures and tables.

7.2.1 Talus cones

Talus cones composed of talus cones are present above the glacier's lateral margins. Talus cones is predominantly composed of very poorly sorted massive sandy-muddy gravel, with mud, sand and gravel contributing 2%, 4% and 94% volume respectively (Table 7.2). The matrix is bimodal, with modes centred at 1839 μm (-0.9 ϕ) and 163 μm (2.6 ϕ), accounting for 59% and 41% of the probable particle-size-distribution respectively (Table 7.4; Fig. 7.3a, 7.2a). The *cos* θ matrix of similarity (Table 7.3) indicates that the particle-size-distribution of matrix samples from talus cones are very similar to those from both Type-I and Type-II longitudinal supraglacial debris ridges and debris cones. Particle form is slightly elongate and blocky, with a mean intercept sphericity of 0.64 (Table 7.1, Fig. 7.4). Particles range from very angular to sub-angular and are predominantly angular with a mean P – value of 0.26. Particles are predominantly extremely rough (mean ξ – value $= 1.25 \times 10^{-6}$), but range from extremely rough to very smooth.

Table 7.1: Results of analyses of particle morphology for samples from Midre Lovénbreen: mean values of intercept sphericity, roundness and surface roughness.

	Intercept sphericity	Roundness	Surface roughness
Talus cones	0.64	0.26	1.25×10^{-6}
Subglacial debris layer	0.68	0.24	9.99×10^{-7}
Longitudinal debris ridge (Type-I)	0.59	0.24	1.27×10^{-6}
Longitudinal debris ridge (Type-II)	0.60	0.23	1.46×10^{-6}
Transverse debris ridge	–	–	–
Debris cones	0.68	0.38	6.63×10^{-7}
Proglacial debris layer	0.65	0.25	1.04×10^{-6}
Proglacial debris stripes	0.67	0.30	8.16×10^{-7}

Table 7.2: Statistical characteristics of mean particle-size-distributions for matrix samples from sediment landform assemblages at Midre Lovénbreen.

	Gravel	Sand	Mud	D_{50}	Mean particle size	σ
		% mass		μm	μm	
Talus cones	84.50	11.25	4.25	1294.77	759.70	3.80
Subglacial debris layer	65.00	20.00	15.00	417.24	334.26	5.17
Longitudinal debris ridge (Type-I)	74.74	16.29	8.97	896.48	620.98	3.86
Longitudinal debris ridge (Type-II)	85.00	9.88	5.13	1022.93	619.08	4.32
Transverse debris ridge	3.50	58.45	37.24	609.97	468.44	3.45
Debris cones	32.50	36.63	30.00	1180.48	858.80	3.00
Proglacial debris layer	78.21	15.57	6.21	340.13	274.54	5.21
Proglacial debris stripes	44.72	34.64	20.00	233.03	201.31	5.65

Table 7.3: Cos θ matrix of similarity - a comparison between mean particle-size-distributions of matrix samples from each sediment-landform assemblage identified at Midre Lovénbreen: (i) talus cones; (ii) subglacial debris layer; (iii) supraglacial longitudinal debris ridge (Type-I); (iv) supraglacial longitudinal debris ridge (Type-II); (v) supraglacial transverse debris ridge (vi) debris cone; (vii) proglacial debris layer; (iix) proglacial debris stripes.

	i	ii	iii	iv	v	vi	vii	iix
i		0.862	**0.977**	**0.992**	0.823	**0.979**	0.820	0.710
ii	0.862		0.944	0.916	**0.959**	0.879	**0.989**	**0.955**
iii	**0.977**	0.944		**0.996**	0.917	**0.978**	0.915	0.829
iv	**0.992**	0.916	**0.996**		0.883	**0.985**	0.881	0.784
v	0.823	**0.959**	0.917	0.883		0.859	0.943	0.901
vi	**0.979**	0.879	**0.978**	**0.985**	0.859		0.833	0.725
vii	0.820	**0.989**	0.915	0.881	0.943	0.833		**0.980**
iix	0.710	**0.955**	0.829	0.784	0.901	0.725	**0.980**	

Table 7.4: Results of Gaussian component analysis of mean particle-size-distributions of matrix samples from sediment-landform assemblages at Midre Lovénbreen.

	Mode 1			Mode 2			Mode 3		
	ϕ	σ	p	ϕ	σ	p	ϕ	σ	p
Talus cone	–0.88	1.61	0.78	2.62	1.74	0.19	–	–	–
Subglacial debris layer	–0.32	1.61	0.78	4.02	1.74	0.19	–	–	–
Longitudinal debris ridge (Type–I)	–0.84	1.12	0.80	2.72	1.53	0.18	–	–	–
Longitudinal debris ridge (Type–II)	–0.99	0.95	0.76	2.81	1.70	0.21	–	–	–
Transverse debris ridge	0.83	1.14	0.88	3.61	1.65	0.10	–	–	–
Debris cone	0.61	0.80	0.83	2.19	1.44	0.17	–	–	–
Proglacial debris layer	0.21	1.71	0.78	3.34	1.67	0.22	–	–	–
Proglacial debris stripes	0.21	1.37	0.60	3.34	1.65	0.28	5.47	1.16	0.13

Table 7.5: Morphometric characteristics of proglacial debris stripes and boulders associated with proglacial debris stripes at Midre Lovénbreen.

	Boulder axes			Flute ridges		
	a	b	c	Length	Width	Height
Average	0.39	0.29	0.17	22.50	23.18	0.10
Maximum	1.54	0.95	0.73	99.85	48.81	0.51
Minimum	0.23	0.15	0.06	1.13	6.80	0.05

Figure 7.1: Photograph of adfrozen subglacial debris layer - taken in a subglacial cavity on the glacier's western margin and here shows the normal grading of entrained sediment, from pebbles to sands, overlain by dispersed basal ice facies (ice axe for scale)

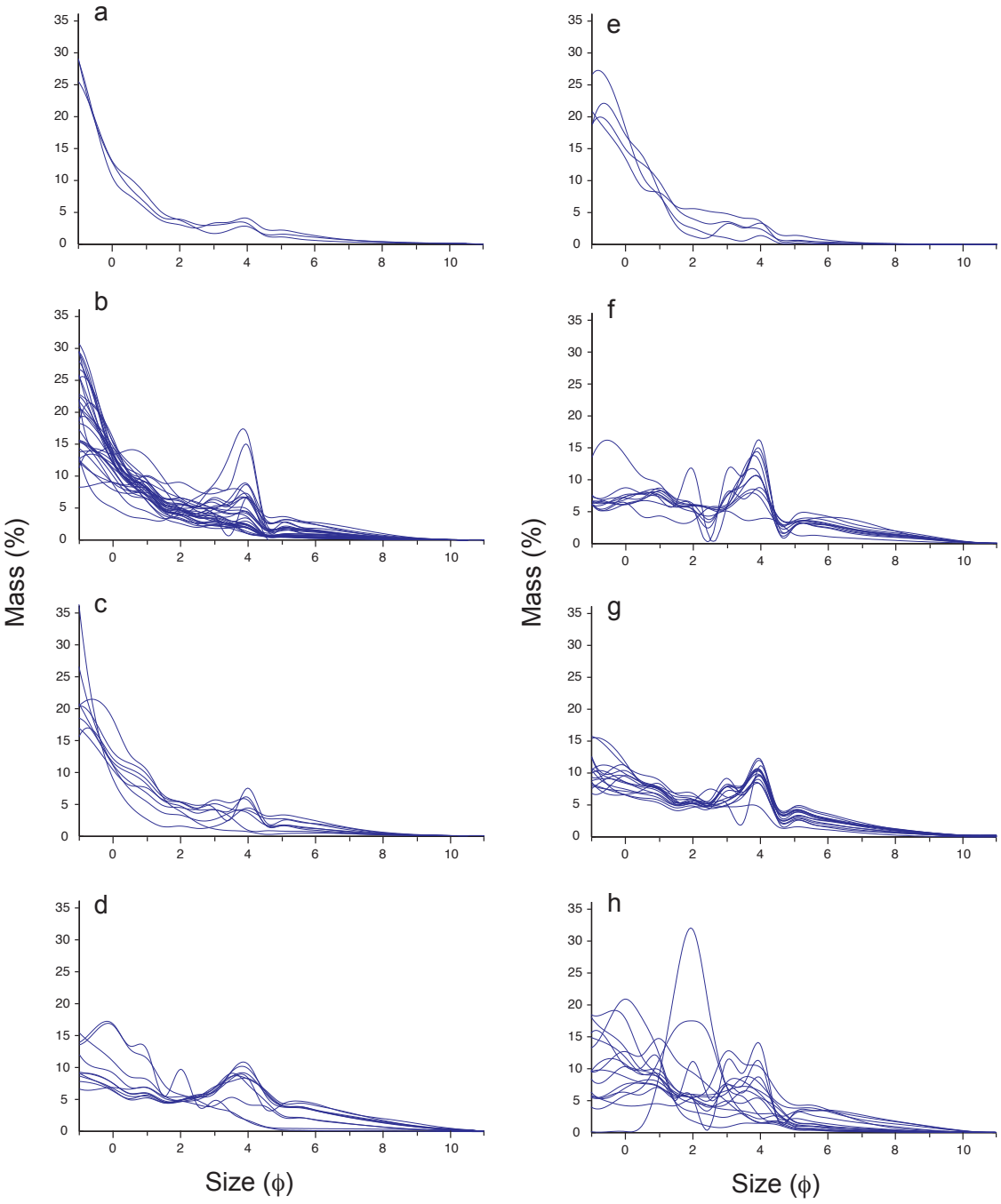

Figure 7.2: Bivariate plots of mass against particle size for sediment samples taken at Midre Lovénbreen - (a) talus cones; (b) Type-I longitudinal supraglacial debris ridges; (c) Type-II longitudinal supraglacial debris ridges; (d) supraglacial transverse debris ridges; (e) debris cones; (f) subglacial debris layer; (g) proglacial debris layer; (h) proglacial debris stripes. Data are smoothed with a cubic spline interpolation.

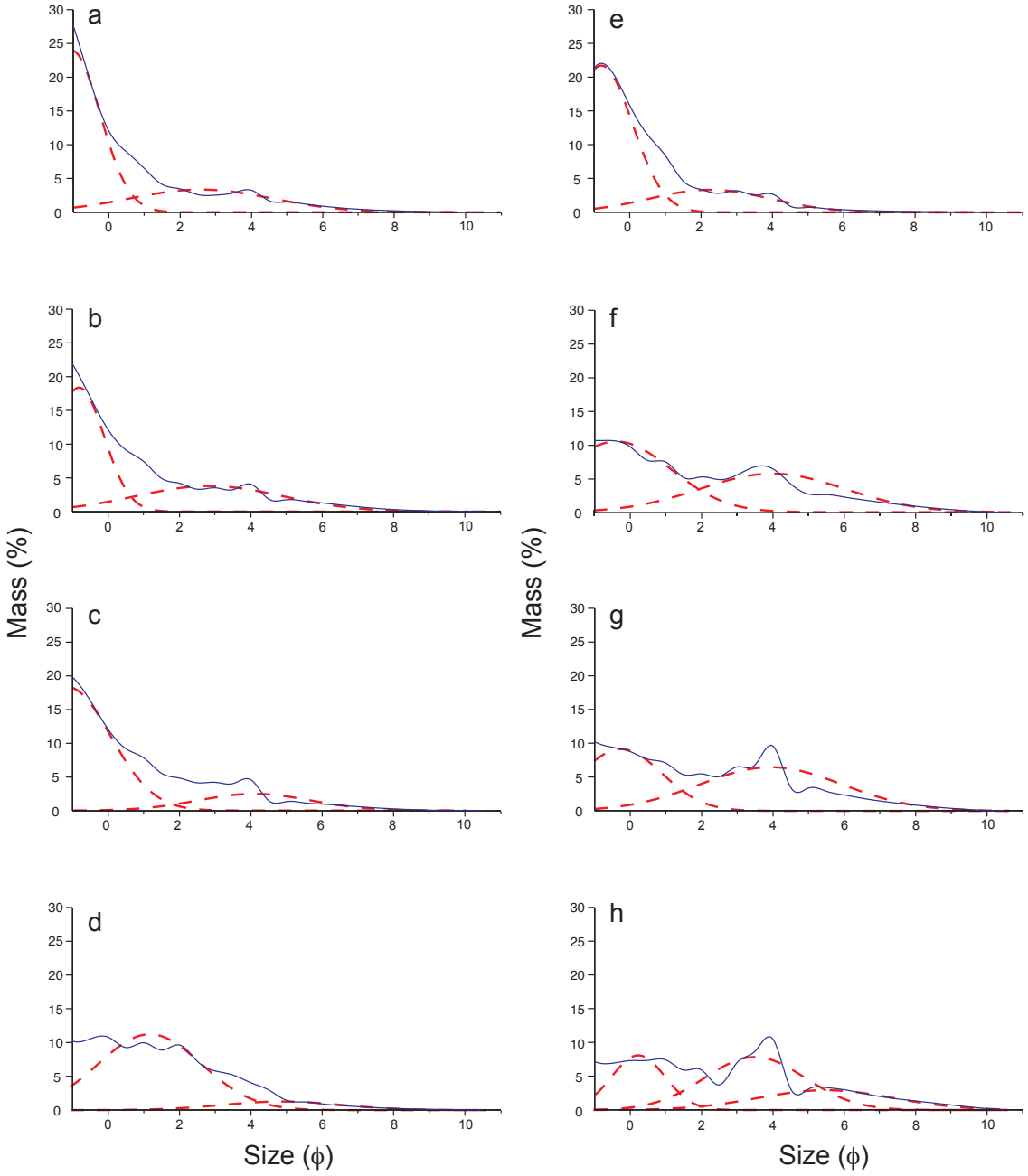

Figure 7.3: Bivariate plots of mass against particle size averaged for each sediment-landform assemblage (blue line) with their respective Gaussian components (red dashed line) - (a) talus cones; (b) longitudinal debris ridge (Type-I); (c) longitudinal debris ridge (Type-II); (d) transverse debris ridge; (e) debris cones; (f) subglacial debris layer; (g) proglacial debris layer; (h) proglacial debris stripes. Data are smoothed with a cubic spline interpolation.

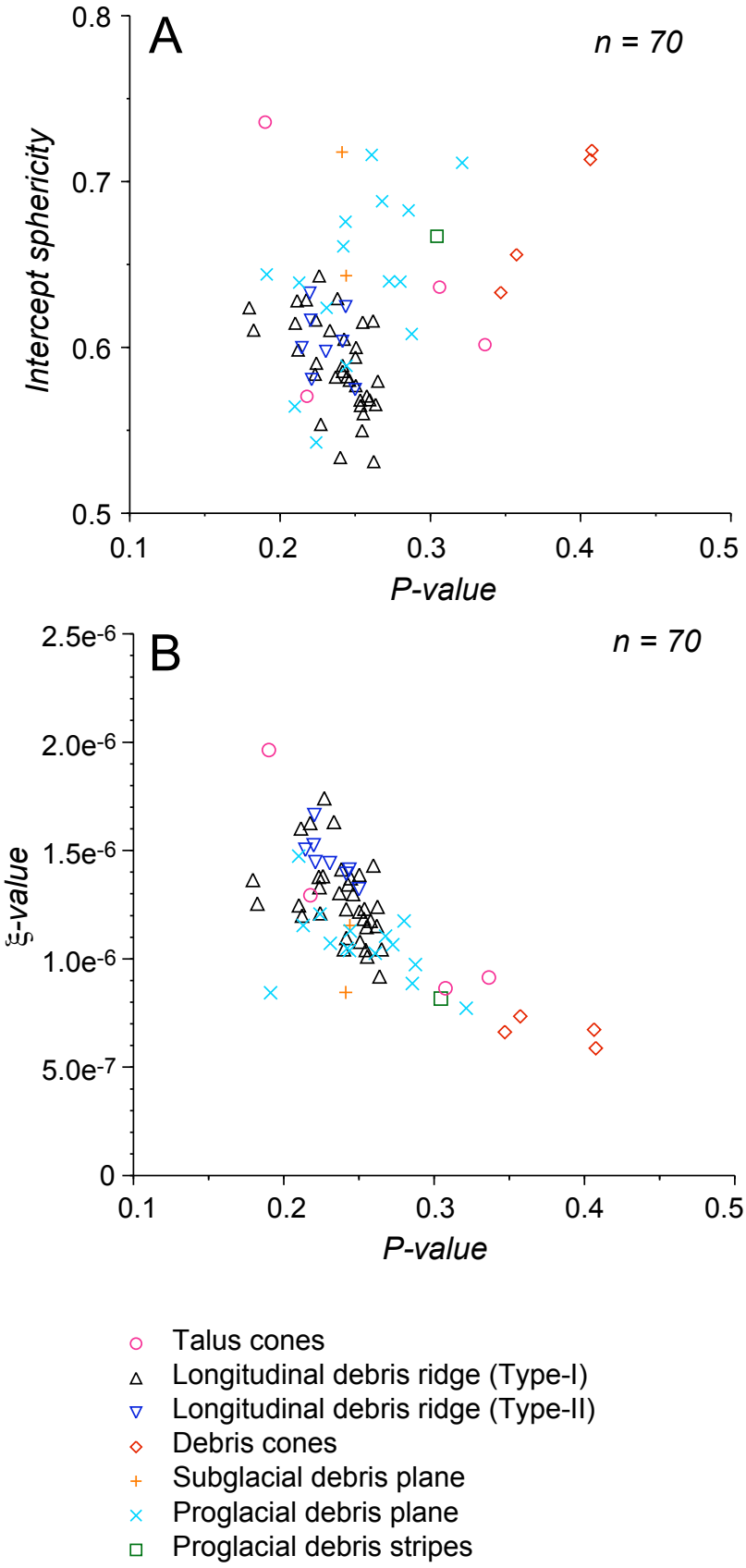

Figure 7.4: Covariance plots of particle morphology statistics - (A) intercept sphericity (form) against P – value (particle roundness), and (B) ξ – value (surface roughness) against P – value (particle roundness).

7.2.2 Subglacial debris layer

A subglacial debris layer is visible in exposures up to 1 m thick at the eastern and western lateral margin and within an abandoned subglacial meltwater channel at the eastern margin (Fig. 7.1b). The sediment is frozen on to the glacier base and grades normally into the overlying ice, from a clast-dominated pebble-sized gravel through to fine sands. Although the subglacial debris layer is not exposed at the frontal area of the glacier terminus, geophysical data indicate that it is likely to underlie much of the glacier where the ice is cold-based (King et al., 2008).

The sediment facies that make up the subglacial debris layer is poorly sorted, with mud, sand and gravel contributing 15%, 20% and 65% volume respectively (Table 7.2). The matrix of the sediment facies is bimodal, with modes centred at 1251 μm (-0.3 ϕ) and 62 μm (4.0 ϕ), accounting for 53% and 47% of the probable particle-size-distribution respectively (Table 7.4; Fig. 7.3f). The $\cos\theta$ matrix of similarity (Table 7.3) indicates that the particle-size-distribution of matrix samples from subglacial debris layer are very similar to those from transverse debris ridges, proglacial debris layer and proglacial debris stripes. Particle form is slightly elongate and slightly flat, with a mean I_s – value of 0.68 (Fig. 7.4). Particles range from very angular to sub-rounded and are predominantly angular with a mean P – value of 0.24 (Table 7.1). Particles range from extremely rough to moderately rough and are predominantly moderately rough with a mean ξ – value of 9.99e^{-7}.

7.2.3 Longitudinal supraglacial debris ridges

Flow-parallel supraglacial longitudinal debris ridges can be classified into two different types according to their morphology and structural relationships.

7.2.3.1 Type-I longitudinal supraglacial debris ridges

Type-I longitudinal supraglacial debris ridges are low relief ($<$1 m high) linear stripes of gravel extending up to 1 km upglacier of the terminus. The ridges are ice-cored, appearing gradually and widening downglacier and coalescing to form broad swathes of near-continuous debris cover approaching the terminus, $<$10 m wide and $<$0.2 m thick (Fig. 7.6a). Type-I longitudinal supraglacial debris ridges are orientated parallel to ice flow and longitudinal foliation (S_1), melting out at the glacier surface in association with large-scale lateral (F_1) folds. Type-I longitudinal supraglacial debris ridges are composed of very poorly sorted diamicton, with mud, sand and gravel contributing 9%, 16% and 75% volume respectively. GCA indicates that the matrix is bimodal, with modes centred at 1791 μm (-0.9 ϕ) and 152 μm (2.7 ϕ), accounting for 76% and 24% of the probable particle-size-distribution respectively (Fig. 7.3b). Detailed inspection of these analyses demonstrates,

while the entire feature is bimodal, the relative contribution of the primary and secondary modes to the overall particle-size-distribution exhibit a distinct spatial trend. Fig. 7.5 shows changes in the relative contribution of the coarse sand and fine gravel modes and the very fine sand to coarse silt modes to the overall particle-size-distribution of matrix samples along two Type-I longitudinal supraglacial debris ridges (for sample locations see Fig. 3.5). At the upglacier end the coarse sand to fine gravel modes account for ∼65% of the particle-size-distribution and decreases roughly linearly with distance to between ∼27 to ∼40% approaching the terminus. Concurrently, the contribution of the very fine sand to coarse silt modes increases with distance downglacier, from 2 to 3% at the upglacier end of the debris stripes to 13 to 18% approaching the terminus.

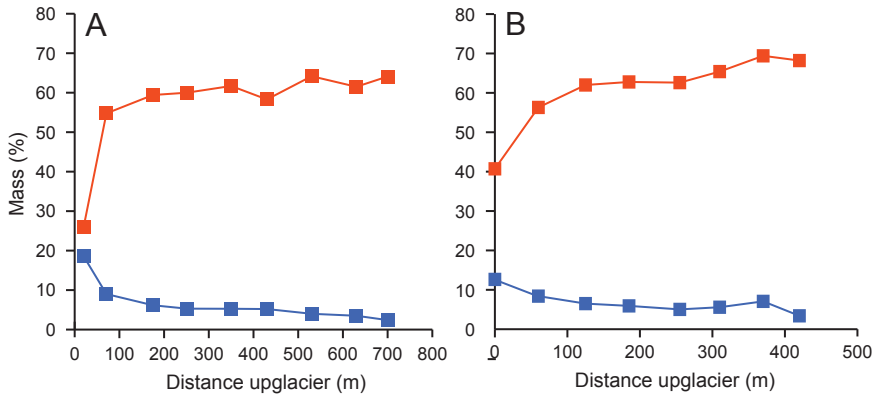

Figure 7.5: Bivariate plots of percentage mass against distance upglacier from the terminus for matrix sediment samples from two Type-I longitudinal supraglacial debris ridges - these plots illustrate spatial trends in the percentage contribution of primary and secondary modes to overall particle-size-distribution (red line: -1 to 0 ϕ; blue line: 3 to 4 ϕ). See Fig. 3.5 for position of supraglacial longitudinal debris ridges (A) and (B).

The $\cos\theta$ matrix of similarity indicates that the particle-size-distribution of matrix samples from Type-I longitudinal supraglacial debris ridges sediments are very similar to both those from Type-II longitudinal supraglacial debris ridges and debris cones. Particle form is moderately elongate and moderately flat, with a mean I_s – value of 0.59. Particles are predominantly angular (mean P – value = 0.24) and range from very angular to sub-rounded (Fig. 7.4). Particles are predominantly rough (mean ξ – value = 1.27 x 10^{-6}) and range from extremely rough to moderately smooth and. In contrast with the spatial trends observed in particle-size-distribution data, particle morphology statistics exhibit no consistent spatial variability with distance along Type-I longitudinal supraglacial debris ridges.

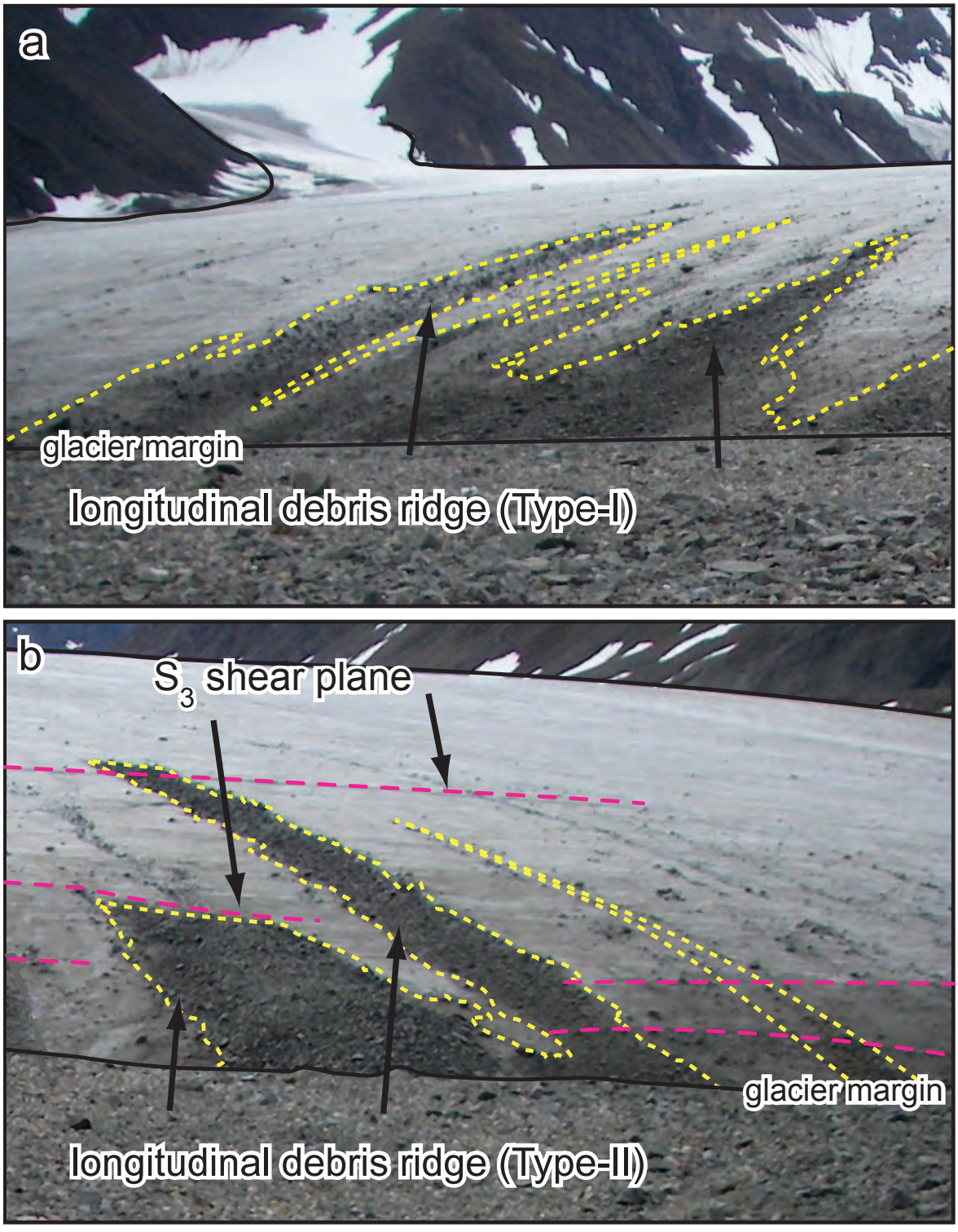

Figure 7.6: Annotated photographs illustrating the morphological contrast between Type-I and Type-II longitudinal supraglacial debris ridges at Midre Lovénbreen - (a) Type-I supraglacial longitudinal debris ridges at the centre of the glacier margin, and (b) Type-II longitudinal supraglacial debris ridges at the centre of the glacier margin.

7.2.3.2 Type-II longitudinal supraglacial debris ridges

Type-II longitudinal supraglacial debris ridges occur abruptly at the glacier surface in direct or close association with arcuate shear planes (S_3). These ridges are orientated parallel to ice flow, are 2 to 5 m wide, 100 m long and form a surface debris cover up to 0.2 m thick that merges indiscriminately with Type-I longitudinal supraglacial debris ridges towards the terminus (Fig. 7.6b). Type-II longitudinal supraglacial debris ridges are composed of very poorly sorted diamicton, with mud, sand and gravel contributing 5%, 10% and 85% volume respectively (Fig. 7.3c). The matrix is bimodal, with modes centred at 1984 μm (-1.0 ϕ) and 142 μm (2.8 ϕ), accounting for 77% and 23% of the probable particle-size-distribution respectively. The *cos* θ matrix of similarity indicates that the particle-size-distribution of matrix samples from Type-II longitudinal supraglacial debris ridges are very similar to sediments from Type-I longitudinal supraglacial debris ridges and debris cones. Particle form is slightly elongate and slightly flat, with a mean intercept sphericity of 0.6. Particles range from very angular to sub-rounded and are predominantly angular with a mean P – value of 0.23 (Fig. 7.4a). Particles range from extremely rough to moderately smooth and are predominantly rough with a mean ξ – value of 1.46 x 10^{-6}.

7.2.4 Transverse supraglacial debris ridges

Transverse debris ridges composed of muddy-sand are located on the glacier surface 30 to 50 m from the terminus at the centre of the ice margin. These ridges originate abruptly in association with arcuate shear plane (S_3) and consist of a 50 to 75 m long ice-cored ridge orientated parallel to arcuate shear plane orientation and sub parallel to the glacier margin (Fig. 7.7). The ice-cored ridges are mantled by a carapace of debris $\sim$0.1 m thick, with a steep upglacier face and a gentle downglacier face, the debris thinning to reveal bare ice 15 m downglacier. The coarse fraction is dominated by coarse to fine gravels, with very few pebble to cobble-sized clasts available for particle morphology analysis.

Transverse debris ridges are composed of poorly sorted clast-rich intermediate diamicton, with mud, sand and gravel contributing to 37%, 58% and 4% sediment volume respectively (Fig. 7.3d). The matrix is bimodal, with modes centred at 564 μm (0.8 ϕ) and 82 μm (3.6 ϕ), accounting for 89% and 11% of the probable particle-size-distribution respectively. The *cos* θ matrix of similarity indicates that the particle-size-distribution of matrix samples from transverse debris ridges are very similar to matrix sediments from subglacial debris layer (Table 7.3).

Figure 7.7: Photograph of transverse debris ridge at Midre Lovénbreen - the transverse debris ridge is located 100 m east of the large supraglacial meltwater stream on the western half of the glacier. Note the close association between the emerging sediment and the S_3 arcuate fracture trending from left to right across the image.

7.2.5 Debris cones

Debris cones crop out at three locations at the glacier surface adjacent to large (1 to 3 m wide) supraglacial meltwater channels. These form ridges orientated parallel to ice surface slope, up to 1.5 m high and 15 m long and characterised by an asymmetric long profile, consisting of a steep upglacier face (25° to 35°) and a gentle downglacier face (10° to 15°) (Fig. 7.8). The sediment of the two faces is also different, with the upglacier face being composed of a gravel fraction of cobble to pebble-sized clasts, fining to fine to coarse gravels on the downglacier face. Debris cones occur in close proximity to S_3 shear planes, which contain low volumes of muddy-sand. Debris cones are composed of poorly sorted clast-rich intermediate diamicton, with mud, sand and gravel contributing 30%, 37% and 33% volume respectively. The matrix is bimodal, with modes centred at 1531 μm (-0.6 ϕ) and 219 μm (2.2 ϕ), respectively accounting for 65% and 35% of the probable particle-size-distribution (Fig. 7.3d). The *cos* θ matrix of similarity indicates that the particle-size-distributions of matrix samples from debris cones are very similar to sediments from talus cones and both Type-I and Type-II longitudinal supraglacial debris ridges.

Particle form is moderately elongate and moderately flat, with a mean intercept sphericity of 0.68 (Table 7.1). Particles are predominantly sub-rounded (mean P – value $= 0.38$) and range from angular to rounded (Fig. 7.4). Particles are predominantly moderately smooth (mean ξ – value $= 6.63 \times 10^{-7}$) and range from extremely rough to moderately smooth.

7.2.6 Proglacial debris layer

The proglacial zone up to 0.5 km away from the glacier terminus consists predominantly of a massive diamicton (Fig. 7.9), up to 1.5 m thick where exposed in meltwater channel sections, resting sharply on weathered bedrock. Muddy-sandy gravels are very poorly sorted, with mud, sand and gravel contributing 6%, 16% and 78% of the volume respectively. The matrix is bimodal, with modes centred at 1255 μm (0.2 ϕ) and 68 μm (3.3 ϕ), accounting for 48% and 52% of the probable particle-size-distribution respectively (Fig. 7.3g). The *cos* θ matrix of similarity indicates that the particle-size-distribution of matrix samples from proglacial gravel sediments are very similar to sediments from subglacial debris layer and proglacial debris layer ridges. Particle form is slightly elongate and slightly flat, with a mean intercept sphericity of 0.65 (Table 7.1). Particles are predominantly sub-angular (mean P – value $= 0.25$) and range from very angular to sub-rounded. Particles are predominantly moderately rough (mean ξ – value $= 1.04 \times 10^{-6}$) and range from extremely rough to smooth.

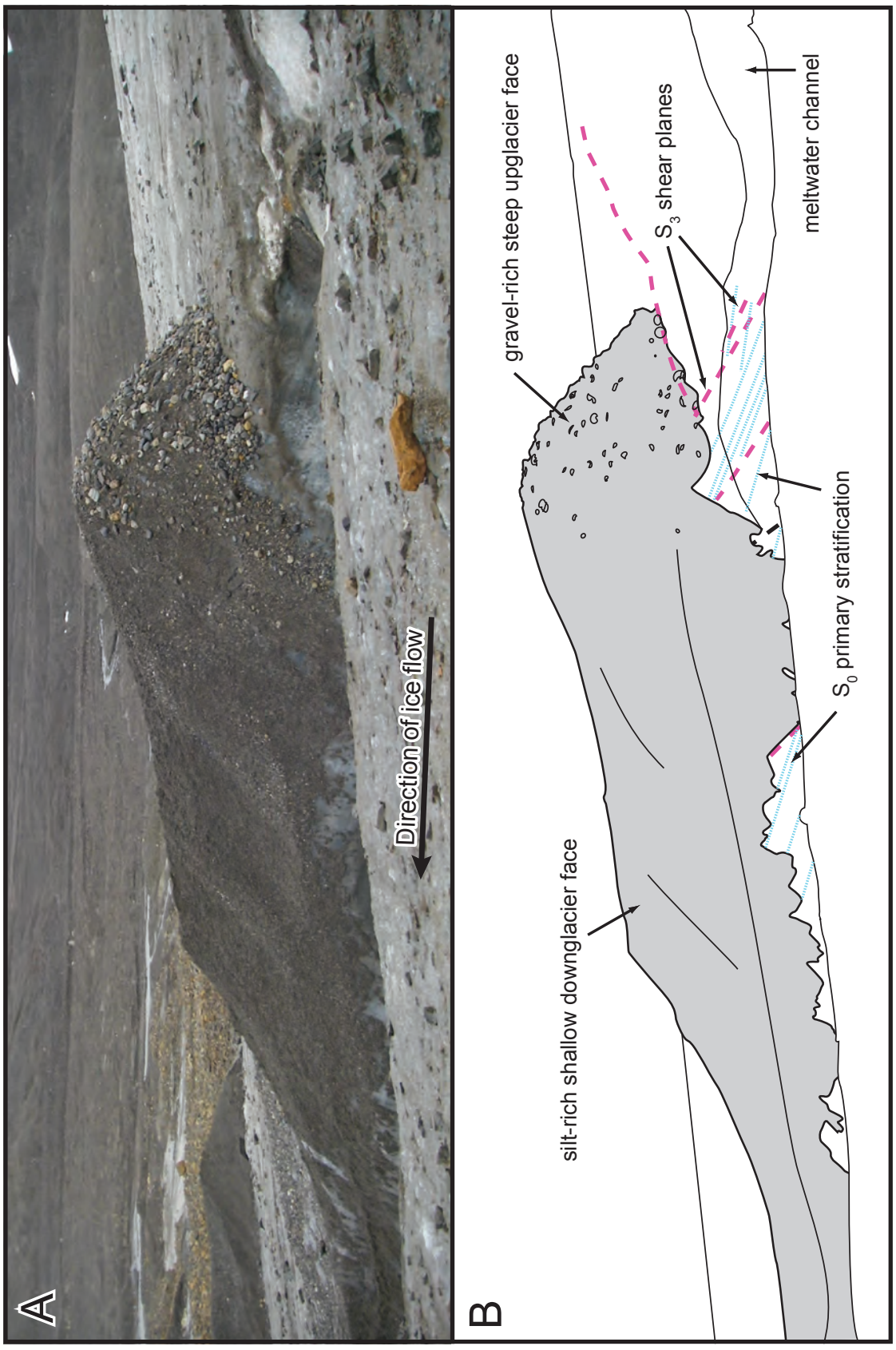

Figure 7.8: Photograph of a debris cones at Midre Lovénbreen - (A) Debris cones forming an asymmetric ridge seen at the ice surface and showing ice structure in section within a meltwater channel, and (B) annotated illustration. The ridge is 1.5 m high.

7.2.7 Proglacial debris stripes

Proglacial debris stripes occur on relatively flat areas of the proglacial zone between the glacier terminus and zones of major proglacial outwash channels (Fig. 3.5). Proglacial debris stripes at Midre Lovénbreen form low linear ridges of diamicton originating in the lee of boulders, trending orthogonal to the terminus, presumably parallel to fornmer ice-flow direction (Fig. 7.9a). The diamicton ridges range in size from 0.05 m to 0.5 m high, 0.06 to 0.5 m wide and 1 to 100 m long (Table 7.5). The height of diamicton ridges decreases with distance away from the boulders, commonly reaching the same height as the adjacent till surface after ∼10 to 25 m. Beyond this point the proglacial debris stripes can still be identified due to the contrast in sediment texture between them and the adjacent till despite the absence of any contrast in relief. Boulders associated with the proglacial debris stripes are subangular to subrounded and boulder $a-$, $b-$ and $c-$axes range respectively from 0.23 to 1.54 m, from 0.15 to 0.95 m and from 0.06 to 0.73 m. The width of flute ridges are typically 1 to 0.5 times the width ($b-$axes) of the boulders. Where boulders a-axes are greater than ∼0.5 m, an area of ploughed sediment ridges of similar width to the boulder can be observed on the leeward side of the boulder, with a corresponding scarp face on the upglacier side (Fig. 7.9a). The dip of boulder a-axes ranges from 0 to 10°, with an azimuth orientated in the direction of the flute long-axis. At some locations (very few), proglacial debris stripes link together longitudinally, to form a linear series of boulder and ridge, boulder and ridge, with no modification or lateral migration of the flute ridge as it meets the next boulder. This contrasts with the morphology of linked proglacial debris stripes documented by Gordon (1992, their Fig. 11), where widening, thickening and/or lateral migration of the flute ridge was observed as the ridge met with the next boulder.

At Midre Lovénbreen the texture of subglacial debris layer matrix samples is extremely similar to that of proglacial debris layer ($\cos\theta = 0.99$) (Fig. 7.2). This is consistent with visual estimates of overall sediment texture (Fig. 7.10) and Gaussian component analysis (Table 7.2). Gaussian component analysis identifies two modes in both subglacial debris layer and proglacial debris layer, located at -0.21 to 0.3 ϕ and 4 to 3.3 ϕ respectively. The texture of subglacial debris layer matrix samples is also generally similar to that of debris-rich basal ice facies ($\cos\theta = 0.95$) and proglacial debris stripes ($\cos\theta = 0.94$). However, visual particle-size analysis over a wide range of particle sizes (Fig. 7.10) indicates that proglacial debris stripes are depleted in gravels, or enriched in sands and muds, relative to both subglacial and proglacial debris layer. Gaussian component analysis reflects this trend (Table 7.2): relative to subglacial and proglacial debris layer, the contribution of the mode centred at 0.21 ϕ is reduced by 18% compared to proglacial debris stripes, and the contribution of the mode centred at 3.3 ϕ is increased respectively by 9% and 6% compared

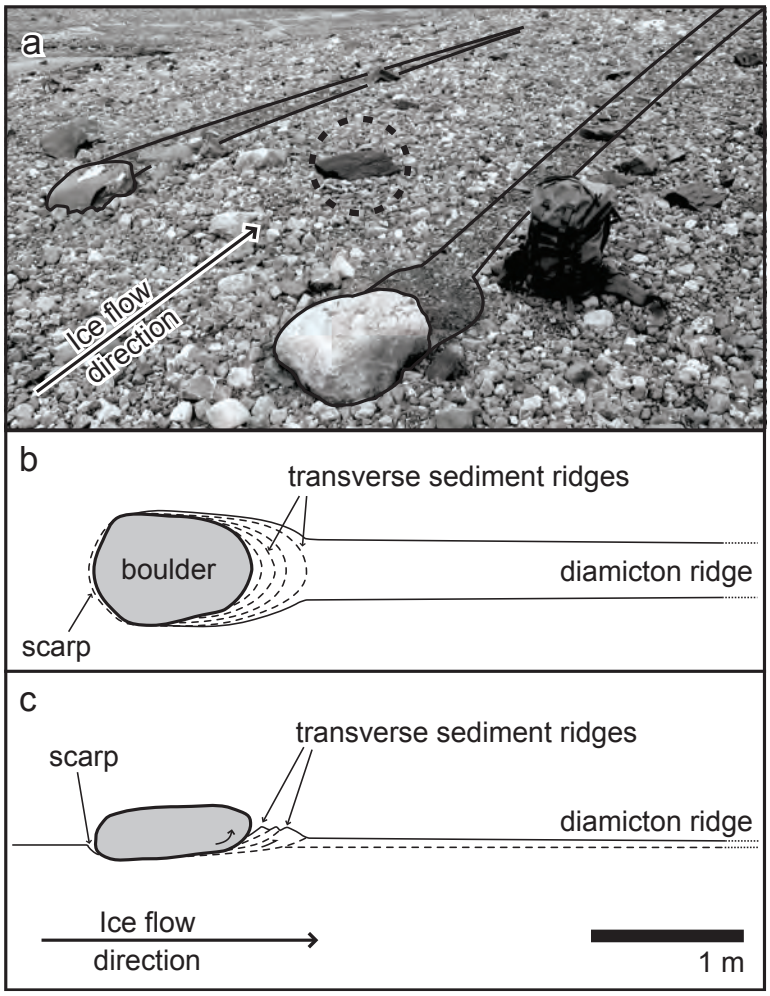

Figure 7.9: The morphology of proglacial debris stripes at Midre Lovénbreen - (a) Photograph of proglacial debris stripes at Midre Lovénbreen showing textural contrast with adjacent proglacial debris layer. Note supraglacially-transported angular boulder in centre without diamicton ridge. Ice flow direction from bottom left to top right. (b) Schematic illustration of proglacial debris stripe showing boulder, ploughed sediment ridges and tail ridge in (i) planform and (ii) cross-section.

to proglacial debris stripes. Gaussian component analysis also identifies a third mode in flute sediment samples at 5.47 ϕ, accounting for 13% of the overall particle-size-distribution.

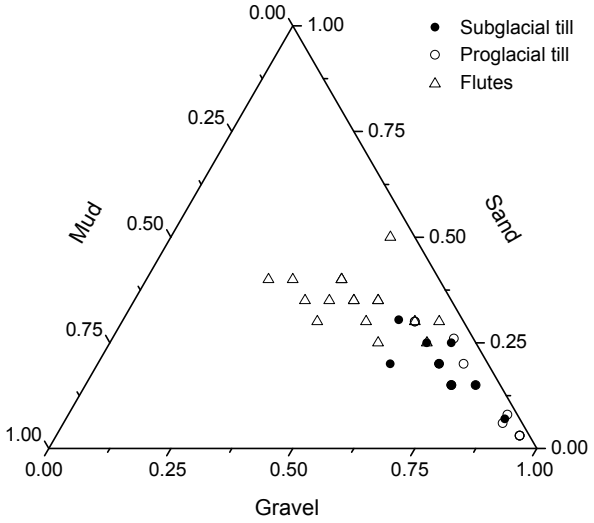

Figure 7.10: Ternary plot of visually-estimated sediment texture showing proportions of gravel, sand and mud for subglacial debris layer, proglacial debris layer and proglacial debris stripes. -

7.3 Interpretation and discussion

Here, sediment-landform assemblages investigated at Midre Lovénbreen are interpreted on the basis of the data presented above (including structural data presented in Chapter 6) and discussed within the context of previous research and the glacier-wide sediment transport system.

7.3.1 Talus cones

The weak bimodality of particle-size-distributions of matrix samples from talus cones is typical of a sediment that has undergone a low amount of shear (Hooyer and Iverson, 2000). The weak secondary mode at 163 μm (Fig. 7.3) may be indicative of grain crushing events taking place within the talus cone during debris flows. The lithology of isolated boulders (phyllite, schist, psammite and quartzite), in contrast with the lithology of weathered bedrock samples, is much more typical of supra-, sub- and proglacial sediment-landform assemblages. This similarity is reflected by the high proportion of very angular to angular particles (P – value 0.25) and the very high surface roughness of the particles (Table 7.1). Values of particle intercept sphericity, although, appear anomalously high, i.e. they are more blocky than particles from any other sample. This relatively high degree of blockiness

is interpreted to reflect the configuration of pre-existing bedrock fractures, implying that the impacts of weathering and transport on particle form are likely to be less than straightforward. The influence of lithology on particle morphology at Midre Lovénbreen has been examined by Bennett et al. (1997), who concluded that, while particle form *is* influenced by lithology, its affect is not systematic; rather it increases the noise present in particle-form data. Additionally, Bennett et al. (1997) observed that the influence of particle lithology on roundness and surface texture is limited.

7.3.2 Subglacial debris layer

Gaussian-component-analyses of subglacial debris layer particle-size-distributions identify that the matrix is dominated by coarse silts with a secondary mode of coarse sands (Fig. 7.3f). The enrichment of subglacial debris layer sediments in coarse silts relative to supraglacial sediment-landform assemblages is consistent with the occurrence of crushing or attrition processes identified by Haldorsen's (1981) laboratory experiments. The results of these experiments were built upon by Iverson et al. (1996), who advanced the concept that fine sands to coarse silts are produced by the failure of grain-bridges, crushing larger grains into a number of particles of similar size. Haldorsen (1981) argued that the size-fraction produced by crushing reflects the mineral size of the parent bedrock. Iverson et al. (1996) associated these types of particle-size-distribution with low-shear glacial sediments. Extension of these theories to Midre Lovénbreen implies that the enrichment of subglacial debris layer in coarse silts relative to supraglacial sediment-landform assemblages is the product of crushing coarse sand-sized particles that act as grain bridges during sediment deformation. On the basis of this evidence subglacial debris layer is interpreted to be a till.

Both Haldorsen (1981) and Iverson et al. (1996) further observed that abrasion processes (i.e. clast to clast impacts or clast to bedrock impacts) are associated with the production of a mode centred around the medium to fine silt-sized fraction. While this mode is present in subglacial till samples, it does not comprise a major component ($<$10%) of the total particle-size-distribution. From these data it can therefore be inferred that the dominant process of communition in the till layer underlying Midre Lovénbreen is crushing rather than abrasion. The absence of a large modal peak in the medium to fine silt size fraction may be accounted for by a number of possible mechanisms: (i) a deformed sediment layer having undergone relatively low shear (Iverson et al., 1996); (ii) the removal of the size fraction from the subglacial till layer by meltwater (Fischer and Hubbard, 1999), (iii) high pore water pressures inhibiting communition (Tulaczyk et al., 1998), or (iv) the dissipation of basal shear stresses by basal sliding or high levels of shear at the ice-bed interface (Iverson et al., 1996). The

glacier's low surface velocity ($\leq$3 cm day^{-1} (Rees and Arnold, 2007)), absence of a well-developed subglacial drainage network and cold-based terminus (King et al., 2008) strongly favours the interpretation that the absence of a significant medium silt-sized sediment mode is due to relatively low levels of shear within the subglacial debris, probably caused by low basal shear stresses. Detailed field-based investigations at Mýrdalsjökull led Kjaer (1999) to conclude that dominant processes of communition could vary over scales of a few hundred metres, depending on local drainage conditions and the impact of pore water pressure on the thickness of the deforming layer. Such high levels of variability are deemed unlikely at Midre Lovénbreen on the basis that, (i) the subglacial drainage network is poorly developed (Irvine-Fynn et al., 2005b), suggesting that pore water pressures are relatively homogeneous at the bed (compared to glaciers with well-developed arborescent drainage networks), and (ii) particle-size-distributions of subglacial debris layer matrix samples and proglacial gravel matrix samples exhibit a remarkably low variability (standard error of the mean = 0.52 and 0.47 respectively) (Fig. 7.2), giving no reason to suppose that they are not characteristic of the subglacial environment as a whole.

Covariance plots of intercept sphericity and roundness and surface roughness and roundness (Fig. 7.4a, b) demonstrate that subglacial till particles are more blocky in form and less rough in surface texture than supraglacial longitudinal debris ridges and talus cones. Correspondingly, they are predominantly less rounded than proglacial gravels and proglacial debris layer ridges. The position of subglacial debris particles on both covariance plots strongly suggests that they represent an intermediate morphology between supraglacial sediments and proglacial sediments. This trend was also observed in subglacial tills at Midre Lovénbreen by Bennett et al. (1997, their Fig. 10) in their RA-C_{40} covariance plots.

7.3.3 Longitudinal supraglacial debris ridges

The formation of longitudinal debris ridges has been discussed in the context of glacier structure in Chapter 6. Here we build on this by discussing longitudinal debris ridge formation in the context of the sedimentological data presented above, the glacier sediment transport system as a whole and the wider literature.

7.3.3.1 Type-I longitudinal supraglacial debris ridges

Sedimentological analyses at Midre Lovénbreen identify downglacier changes in the relative contribution of both coarse sand to fine gravel modes and very fine sand to coarse silt modes to the overall particle-distribution of matrix samples from two Type-I longitudinal supraglacial debris ridges. These changes take the form of a decrease in the percentage

contribution of coarse sand to fine gravel modes and corresponding increase in the percentage contribution of very fine sand to coarse silt modes with distance downglacier along the Type-I supraglacial debris stripes. These trends observed here may be accounted for by at least two different processes: (i) an increase in the volume of basally derived debris exposed at the ice surface, or (ii) an increase in clast-to-clast contacts caused by an increase in sediment volume at the ice surface.

The first hypothesis suggests that longitudinal supraglacial ridges here (Chapter 6), and elsewhere, form from the elevation of basally derived debris due to large-scale lateral folding of primary stratification (Hambrey et al., 1999; Hambrey and Glasser, 2003; Hubbard et al., 2004). In this study, vertical advection of subglacial till due to large-scale lateral folding (Fig. 6.4) would result in the mixing of en- and supraglacially transported debris with subglacial debris layer, consistent with the changes in sediment texture measured. Specifically, Hubbard et al. (2004) demonstrated, using oxygen isotope ratio comparisons, that ice layers at the centre of longitudinal debris ridges at Midre Lovénbreen shared similar characteristics with stratified basal ice facies.

This mechanism may also account for the lack of variability observed in particle morphology indices along longitudinal supraglacial debris ridges. While differences between the mean values of particle roundness and surface roughness from supraglacial debris ridges and subglacial till are identified (Section 7.2.3.1), it is suggested here that they are sufficiently low that mixing of these two sediments is unlikely to result in spatially consistent changes.

The second hypothesis invokes sedimentological studies that have shown supraglacial sediment transport at debris-rich glaciers to be an important contributor to the net production of fines via communition processes (Benn and Evans, 1998; Owen et al., 2003). Communition of coarse sediment particles via crushing is attributed to the production of coarse silts within the subglacial till layer at Midre Lovénbreen (Section 7.3.2). However, Owen et al. (2003) concluded that supraglacial communition processes are unlikely to result in the production of a large mass of fines on glaciers with a thin debris cover ($\leqslant$0.5 m). Since Type-I longitudinal supraglacial debris ridges reach a maximum thickness of 0.2 m, it is therefore unlikely that communition processes are responsible for the observed downglacier increase in very fine sand to coarse silt modes.

In summary, the relationship between sediment particle-size-distribution and particle form data and glacier structure (Chapter 6) strongly support the hypothesis that Type-I longitudinal supraglacial debris ridges are the product of S_1 large-scale lateral folding. The downglacier changes in the relative contribution of two different sediment modes to the overall particle-size-distribution are interpreted reflect the progressive inclusion of subglacial till sediments, elevated into an englacial position by lateral folding processes.

7.3.3.2 Type-II longitudinal supraglacial debris ridges

Gaussian-component-analyses of particle-size-distributions show that the matrix of Type-II longitudinal supraglacial debris ridges is dominated by a primary mode of coarse sands, with a much smaller secondary mode of coarse silts (Table 7.3). The similarity in mean particle-size-distributions of Type-I with Type-II longitudinal-debris-ridges suggests that their constituent particles have been transported along identical, or at least very similar, transport pathways. Contrary to Type-I debris ridges, detailed inspection of individual samples from Type-II longitudinal supraglacial debris ridges reveals no spatial trend in the relative contribution of primary and secondary modes to particle-size-distributions. Structural data (Chapter 6) strongly suggest that Type-II longitudinal supraglacial debris ridges form as the result of a secondary F_3 small-scale horizontal folding of Type-I longitudinal supraglacial debris ridges, associated with vertical displacement across S_3 shear planes. Developing this conceptual model further (assuming that Type-II longitudinal supraglacial debris ridges are derived from Type-I longitudinal supraglacial debris ridges) the following mechanisms may account for the patterns observed: (1) the folding of longitudinal debris ridges results in the mixing of upglacier sediments with downglacier sediments, obscuring a previously existing spatial trend; (2) shearing along S_3 shear planes results in the vertical advection of sediments consistent with those observed in transverse debris ridges (Section 7.2.4).

The validity of these hypotheses is difficult to evaluate within the scope of the current study. Testing of the former mechanism requires repeated sampling over a time-scale of two or more field seasons. Sediment sampling carried out herein is also not of sufficiently high spatial resolution to determine whether S_3 shear planes had a influence on the texture of Type-II longitudinal supraglacial debris ridges. Additionally, increased sediment cover towards the terminus makes reliable mapping of surface structures increasingly difficult. Investigation of the proposed mechanisms, although, would combine well with suggestions for additional work made in Chapter 6.

7.3.4 Transverse supraglacial debris ridges

A great deal of research effort has been directed towards explaining the origin of transverse supraglacial debris ridges at numerous polythermal valley glaciers (Glasser and Hambrey, 2001; Hubbard et al., 2004; Woodward et al., 2002). Although the mechanism remains unproven, it has been argued that this debris may be elevated into an englacial position by folding and thrusting ((Goldthwait, 1951; Tison et al., 1989; Glasser et al., 1998; Hambrey et al., 1999) or as basal crevasse-fills (Mickelson and Berkson, 1974; Sharp, 1985; Bennett et al., 1996; Evans and Rea, 1999; Ensminger et al., 2001; Woodward et al., 2002). For example, Glasser et al. (1998) associated transverse supraglacial ridges on the glaciers

of Kongsfjorden, Svalbard, with structures interpreted as thrusts. Later, Hubbard et al. (2004) analysed the sedimentology and isotopic chemistry of the debris-bearing ice forming the core of these ridges (in this case located on Midre Lovénbreen and Austre Bröggerbreen, Kongsfjorden), concluding that the material was basal ice, elevated intact from the glacier bed. The character of this ice and debris was more compatible with elevation as part of a thrust than as part of a crevasse filled with fluidized or semi-fluidised debris.

In contrast to this interpretation, Woodward et al. (2002) argued that the transverse supraglacial debris ridges at Kongsvegen originated from debris-filled basal crevasses that had been exposed at the glacier surface by ablation of the overlying ice. A similar origin for debris-bands has also been advanced on the basis of research at numerous other glaciers. Ensminger et al. (2001), for example, describe a laminated sequence of debris-rich and debris-poor bands to have originated as basal crevasse-fills at Matanuska Glacier, Alaska. Similarly, Sharp (1985) argued that crevasse-squeeze ridges could form as a result of viscous soft sediment injection into basal crevasses that open during surging. van der Veen (1998) calculated that basal crevasse formation will occur if subglacial water pressure reaches or exceeds ice overburden pressure, where strain rates are greater than 0.1 a^{-1}.

The *cos* θ matrix of similarity data (Table 7.3) shows that transverse supraglacial debris ridges are composed of sediments that are very similar in particle-size-distribution to sediments from subglacial debris layer. In contrast, while those from other supraglacial sediment-landform assemblages were found to be dissimilar. This dissimilarity suggests that englacial sediment bands are not crevasse-fill in origin. Comparisons of particle morphology data between transverse debris stripes and other sediment-landform associations are precluded owing to the low percentage of gravels (3%) within the facies. This possibly reflects the result of an exclusion process taking place during sediment incorporation into the ice.

Although neither basal crevasses nor S_3 shear planes are identified in OPTV logs (Chapter 6), small-scale horizontal folding (F_3) of S_0 primary stratification is inferred in this study to be indicative of vertical displacement along S_3 shear planes (Fig. 6.5b). None of these data revealed by this study, however, provide any evidence of the existence of basal crevasses at Midre Lovénbreen. This lack of evidence is consistent with the predictions of van der Veen (1998), whose calculations suggest, that under existing basal stress conditions (based on Hambrey et al.'s (2005) three dimensional ice flow model), basal crevassing is unlikely to occur.

In summary, statistical analyses of sediment texture provide strong indication that sediments in transverse supraglacial debris ridges are basally derived, rather than supraglacially derived crevasse-fill sediments. Furthermore, structural analyses support the concept that subglacial sediments are advected along S_3 shear planes, rather than incorporated into

basal crevasses. These findings are consistent with Hubbard et al.'s (2004) interpretations of sedimentological and isotopic data from transverse debris stripes at Midre Lovénbreen and Kongsvegen.

7.3.5 Debris cones

Debris cones are morphologically and sedimentologically similar to dirt or ablation cones described in the Himalaya by Swithinbank (1950), Greenland by Drewry (1972), Iceland by Lewis (1940), Svalbard by Boulton (1967), New Zealand by Kirkbride and Spedding (1996) and the Alps by Goodsell et al. (2005). These cones are generally interpreted to form due to the differential ablation of ice overlain by an insulating sediment layer. They are defined as transient features by Swithinbank (1950), forming from the melt-out of isolated sediment deposits. Two main competing mechanisms for dirt or ablation cone formation have been advanced: (1) that they are formed by the melt-out of sediments deposited within a closed moulin or surface crevasse, and (2) that they originate at the glacier bed and are advected to the surface along thrust or shear planes. The two mechanisms are by no means mutually exclusive; debris cones of separate genetic origins were simultaneously observed at Haut Glacier dArolla by Goodsell et al. (2005).

Covariance plots of particle roundness against surface roughness strongly suggest that debris cones at Midre Lovénbreen have been subject to high rates of erosion relative to other sediment facies and in particular other supraglacial debris (Fig. 7.4). These data indicate intense reworking by water. The precise mechanism of this reworking has been a point of much speculation. Huddart et al. (1998) maintained that rounded gravels characteristic of debris cones found on glaciers around Brøggerhalvøya, including Midre Lovénbreen, were the product of the advection of raised beach deposits along thrust planes. Alternatively, Cooke and others (pers. comm.) have suggested that a possible mechanism for reworking may be the trapping of gravel-sized particles within a subglacial overdeepening. Debris cones appear in close juxtaposition with S_3 shear planes (Fig. 7.8), although, S_3 shear planes are not associated with the transport of gravel to pebble-sized particles (Section 7.3.4), strongly suggesting that in this case, the close spatial relationship is a coincidence. The sparsity of open crevasses on the modern-day glacier surface (Section 6.2.4) also largely, but not entirely, contradicts the idea that debris cones may be crevasse-fill sediments. They may of course have been deposited from crevasses which have since ablated. Without sediment samples from the glaciofluvial outwash plain, it is impossible to determine whether relatively short-term erosion by glaciofluvial activity is likely to have caused roundening to such a degree, or whether they are indeed marine in origin as suggested by Huddart et al.

(1998). It is possible to rule out Cook et al.'s mechanism on the basis of geophysical data (Rippin et al., 2003), which show no indication of an overdeepening at Midre Lovénbreen.

7.3.6 Proglacial debris layer

The composition of proglacial sediment facies can provide insight into the relative importance of different sediment transport processes at a glacier However, acquisition of meaningful empirical data relies on selecting areas of the proglacial area where glacigenic sediments are most likely to have retained their original characteristics. To that end, sampling of proglacial sediment facies at Midre Lovénbreen was directed away from meltwater channels and restricted to an area of c. 0.15 km^2 adjacent to the glacier margin.

The similarity between particle-size-distributions of matrix samples from proglacial debris layer and subglacial debris layer (Fig. 7.3, Table 7.2) strongly support the interpretation that they are of the same genetic origin. Gaussian-component-analyses (Table 7.3) underline these similarities, with both facies having sediment modes that correspond closely with each other, while particle morphologies are also similar (Fig. 7.4, Table 7.1).

In summary, both sediment texture and particle morphology data strongly support the interpretation that proglacial debris layer were formed from basal diamicton that has been transported at the bed of the glacier. Additionally, the spatial homogeneity of proglacial debris layer particle-size-distributions (Fig. 7.2) demonstrates that, over the sampling area at least, basal sediment and transport processes influencing it are highly uniform. The similarity between the proglacial debris layer and subglacial till sediments also demonstrates that subglacially transported sediments currently contribute to a relatively high proportion of total glacial sediment discharge at Midre Lovénbreen.

7.3.7 Proglacial debris stripes

Proglacial debris stripes at Midre Lovénbreen are morphologically and sedimentologically similar to fluted moraines or flutes, which have been observed in front of, and beneath, both polythermal and temperate valley glaciers, forming ridges decimetres to metres wide and tens of metres to hundreds of metres long (Hart, 2006; Ottesen and Dowdeswell, 2006). Larger-scale flutes have also been identified beneath modern and palaeo continental ice-sheets (Dowdeswell et al., 2004; Ó Cofaigh et al., 2005; King et al., 2009), forming ridges up to one hundred metres wide and tens of kilometers long. Despite their morphological similarity, there remains some conjecture as to whether a single mechanism of flute formation can operate across such a large range of scales (Schoof and Clarke, 2008).

Mechanisms that have been associated with flute formation can be considered in two main categories: (i) sediment deformation into incipient basal cavities formed down-flow of

boulders, and (ii) secondary lateral flow instabilities at the ice-sediment interface occurring in response to subglacial topographic roughness elements. It is unlikely that these two suites of processes are mutually exclusive, although some researchers have suggested that their relative contribution may be scale-dependent (Hindmarsh, 1998; Schoof and Clarke, 2008), for example, the two may operate in tandem. (Schoof and Clarke, 2008) reasoned that while boulders may be responsible for the initiation of flutes at the small-scale, their formation would establish topographic roughness elements that would result in the domination of lateral flow instabilities in sediment transport at larger scales.

Empirical evidence for flute formation related to sediment deformation has been identified at both warm-based and polythermal ice margins (Boulton, 1976; Schytt, 1963). Evidence for the formation of flutes by sediment deformation into a cavity in the lee of a boulder has been given in the form of both shear and fold structures and macrofabric data (Paul and Evans, 1974; Boulton, 1976). Consideration of the processes acting to preserve subglacial flutes prior to their exposure has led to the suggestion that these processes are likely to differ markedly between basal-thermal regimes (Boulton, 1976; Eklund and Hart, 1996). For example, Boulton (1976) suggested that growth and extension of the flute occured at the distal end of the flute, resulting from further extension of the cavity, arguing that the existing flute sediment maintained the opening of the cavity, which itself migrated down-flow. However, this was envisaged to occur only under relatively thin ice ($<$20 m). Hoppe and Schytt (1953) advanced a mechanism for flute formation beneath polythermal ice masses, suggesting that sediments squeezed into the open cavity would be adfrozen on to the glacier bed and transported away by ice flow. Adfreezing was envisaged to occur due to the relatively low pressure within basal cavities. The continuous widening of the cavity adjacent to the boulder by further ice flow would then allow additional sediment deformation and flute growth to occur. In Hoppe and Schytt's (1953) model however, no explanation was provided to account for the presence of fluidized subglacial sediment under cold-based ice. Alternatively, Eklund and Hart (1996) proposed a cavity-deformation mechanism independent of basal-thermal regime, suggesting that under polythermal glaciers flutes would only form in the warm-based interior, becoming frozen on to the glacier bed due to the low pressure within basal cavities. This sediment, would then be preserved as a basal ice layer within both the warm-based interior and the cold-based margin. While Boulton's (1976) explanation of how cavities may be maintained by unfrozen flute sediments under thin ice ($<$20 m) is satisfactory, it is difficult to extend such a mechanism to thicker warm-based areas of either temerate or polythermal glaciers. Geophysical data presented by King et al. (2008) indicated that at Midre Lovénbreen, warm-based ice exists beneath $>$100 m of ice.

Secondary lateral-flow instabilities have also been proposed for flute formation on the basis of macrofabric data by (Rose, 1989), but have more commonly been linked with the morphology of large-scale streamlined bedforms (Dowdeswell et al., 2004; Ó Cofaigh et al., 2005; King et al., 2009). Schoof and Clarke's (2008) recently published physically-based model argued that flutes can also form as a result of secondary transverse flows within basal ice. Here, Schoof and Clarke (2008) argued that non-uniform normal stresses would be balanced by transverse flow. Where such processes occurred in the presence of undulating bed-forms this would establish a flow instability, which would serve to amplify the existing subglacial topography (Fig. 7.11). Specifically, these authors maintained that the cavity-fill mechanism proposed by Boulton (1976) and Morris and Morland (1976) was improbable, because there would be no reason for the unfrozen and easily-deformable till to maintain the cavity opening. Schoof and Clarke (2008) concluded that secondary transverse flows would be directed from the troughs to the ridges of longitudinally-orientated subglacial bed-forms, establishing a series of spiral flow cells (Schoof and Clarke, 2008, their Fig. 1b). This model may additionally account for the formation of flutes on glacially-eroded bedrock in the absence of a substantial till layer or initiating boulders (e.g. Gordon, 1992).

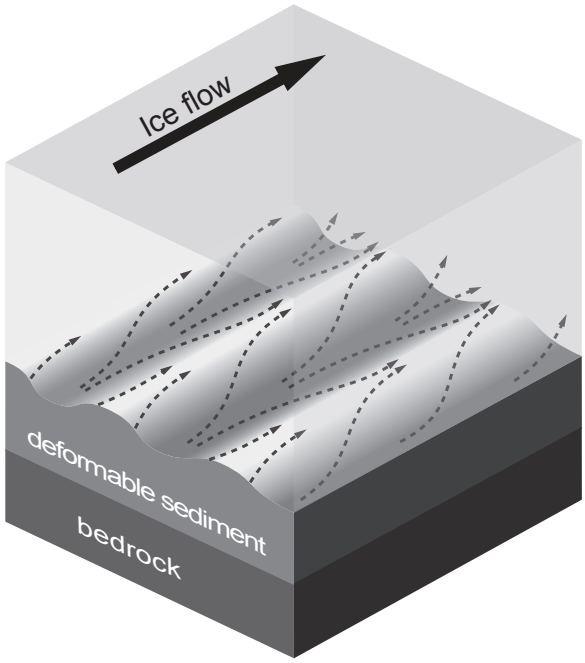

Figure 7.11: Secondary ice flow over regular bed topography - An illustration of the development of secondary lateral flow in basal ice, reinforcing existing topography in the deformable subglacial sediment layer.

The association of the majority of, but not all, flutes with boulders at the margins of valley glaciers suggests that sediment-deformation into lee side cavities is implicitly linked with the formation of flutes at the small-scale. Current conceptual models of flute formation

at polythermal valley glaciers remain unsatisfactory in terms of the processes involved in either sediment deformation under marginal cold-based ice, and/or the formation of an open cavity by fluidized sediments under relatively thick interior warm-based ice.

In this study, sediment texture data demonstrate that flutes are depleted in gravel- to sand-size fractions, relative to proglacial till and subglacial till, and are correspondingly enriched in fine sands to clays. Working on the assumption that flutes are derived from adjacent proglacial till and, by proxy, subglacial till, these data imply that the mechanism responsible for flute formation preferentially excludes particles coarser than medium sands and/or preferentially includes muds. The occurrence of a sorting mechanism of variable effectiveness is also reflected by the high degree of heterogeneity in particle-size-distributions in the coarse sand to coarse silt range in flute sediments, relative to adjacent proglacial debris layer (Fig. 7.3g, h). It is suggested on the basis of these particle-size-distributions, that a fluidization process is likely to be responsible for the preferential sorting of sediments at the bed. The widespread occurrence of flutes across relatively flat areas of the proglacial zone indicate that a fluidization process would require a spatially extensive water source. From this it is inferred that fluidization is unlikely to be caused by action of meltwater beneath the glacier, the delivery of which is highly spatially restricted (Rippin et al., 2005), but rather by the presence of ice at the pressure-melting point, i.e. warm-based ice.

Numerous authors have proposed the squeezing of till into lee side cavities as a mechanism of flute formation beneath warm-based ice (e.g. Schytt, 1963; Boulton, 1976; Benn, 1994). To date the contrast in texture between flutes and adjacent proglacial till have not been noted by other researchers. The formation of cavities in the lee of bedrock obstacles has been both widely considered *a priori* (Lliboutry, 1968; Walder, 1986; Fowler, 1987) and well documented empirically(Boulton et al., 1979; Hubbard, 2002). However, there is no evidence to suggest that sediment, once squeezed into a cavity, is able to support the overburden pressure of ice acting to close the cavity by ice creep (Röthlisberger, 1972). Theoretical treatment of the response of subglacial sediments to basal freeze-on by (Christoffersen and Tulaczyk, 2003a) have demonstrated that the shear strength of subglacial till may increase by one or two orders of magnitude upon freezing. Hence, for sediment squeezed into a cavity to balance or partially balance overburden pressure, a mechanism by which subsequent freezing can occur must also be operating.

Classic regelation theory (Weertman, 1957) argues that ice melting on the stoss side of bedrock obstacles refreezes on its leeward face. However, in the likely circumstance that the transport of meltwater across an obstacle is not 100% efficient (Lliboutry, 1993), a cold patch will develop on the top and/or lee side of the obstacle (Robin, 1976). In addition, a decrease in overburden pressure associated with cavity formation will also lead to the development of a cold patch on the lee side of the boulder due to the local elevation of

the pressure-melting point. It is proposed that the development of these cold patches, in combination with the squeezing of partially-fluidized till, leads to the freeze-on of gravel-poor diamicton at the bed (Fig. 7.12). Following this the frozen-on sediment is transported downglacier as an adfrozen basal-ice lineation. As the sediment is transported away the cavity expands and the process is repeated, entending the flute in a flow-parallel direction.

This mechanism of flute formation is consistent with the model presented by (Schytt, 1963), in which suggesting that sediments squeezed into an open basal cavity would be adfrozen to the glacier bed and transported away by ice flow. Adfreezing was also envisaged to occur due to the relatively low pressure within basal cavities. (Eklund and Hart, 1996) suggested that, in addition to the freeze-on mechanism proposed by (Schytt, 1963), flutes would also form at the boundary between cold and warm-based ice beneath a polythermal glacier. Although these authors had no data to support this argument, geophysical data collated by (Rippin et al., 2007) indicate that the upglacier migration of cold-based ice at Midre Lovénbreen from the margin has occurred within the last 15 years, implying that the flutes observed in this study were probably formed under warm-based ice.

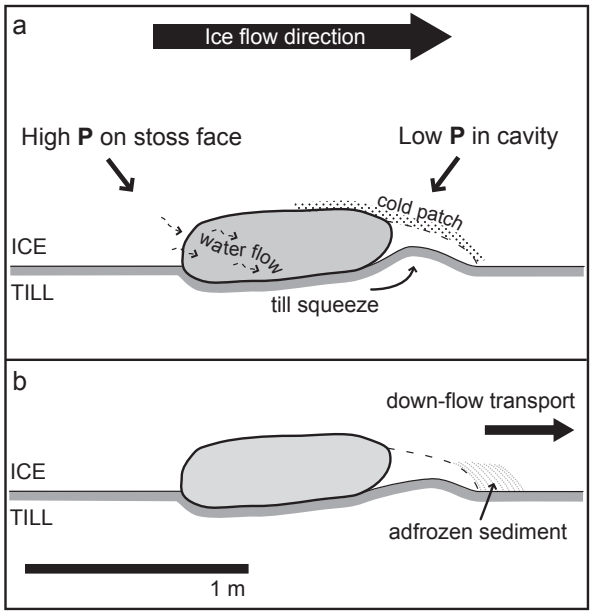

Figure 7.12: Schematic of flute formation via the development of cold patches in the lee of subglacial boulders - (a) A cold patch forms on the lee of a boulder in warm-based ice due to (i) water loss during film and vein flow, and (ii) the elevation of the pressure-melting point within a low-pressure cavity, and (b) the development of a cold patch leads to the freeze-on of till squeezed into the lee side cavity, whic is transported away as a basal ice facies.

7.4 Glacial sediment transport at Midre Lovénbreen

The development of structures and transport of sediment at Midre Lovénbreen are consistent with processes observed at other small valley glaciers (e.g. Glasser et al., 2003; Hubbard et al., 2004; Goodsell et al., 2005; Roberson, 2008). This study identifies eight structural elements at Midre Lovénbreen and eight sediment-landform assemblages. Structures identified at Midre Lovénbreen include: (i) S_0 primary stratification; (ii) S_1 longitudinal foliation; (iii) S_2 transverse fracture traces; (iv) S_3 arcuate shear planes; (v) S_4 oblique fractures; (vi) F_1 large-scale lateral folds; (vii) F_2 medium-scale horizontal folds and (viii) F_3 small-scale horizontal folds. Sediment transport at Midre Lovénbreen is directly influenced by four of these structural elements.

The formation of Type-I longitudinal supraglacial debris ridges is associated with the large-scale lateral folding (F_0) of rockfall debris within primary stratification (S_0) into flow-parallel fold hinges, following the conceptual model advanced by Hambrey and Glasser (2003). These folds develop under a laterally compressive stress regime, as ice converges from the glacier's accumulation zone into a comparatively narrow and deep ice tongue. The emergence of these ridges at the ice surface coincides with the ablation of the ice surface and gradual exposure of F_1 fold hinges.

The formation of transverse supraglacial debris ridges at Midre Lovénbreen is associated with the longitudinally compressive stress-regime that develops towards the glacier terminus. This develops as relatively fast-moving warm-based ice from the glacier's interior abuts against relatively slow-moving ice at the glacier's margins, forming arcuate shear planes (S_3) transverse to ice flow. Sediment from the bed of the glacier is entrained and advected along these shear planes as ice from upglacier overrides slower moving ice downglacier.

The development of previously unidentified Type-II longitudinal supraglacial debris ridges (a subcategory of Type-I longitudinal supraglacial debris ridges) is associated with the evolution of primary stratification (S_0), arcuate shear planes (S_3), large-scale lateral folds (F_1) and small-scale horizontal folds (F_3). Type-II longitudinal supraglacial debris ridges form as a result of the cumulative affect of laterally compressive stresses, which act to concentrate englacial sediments into a flow-parallel fold hinge (F_1, and longitudinally compressive stresses, which shear the fold-hinge (F_1) into a flow-orthogonal plane parallel to the dip of arcuate shear planes (S_3).

The development of other sediment-landform assemblages at Midre Lovénbreen is not explicitly associated with the glacier's structural dynamics. Rather, their evolution is affected by supraglacial meltwater transport (in the case of debris cones), subglacial adfreezing (in the case of subglacial debris layer and proglacial debris layer) and small-scale till melt-squeeze-freeze cycles at the glacier bed (in the case of flutes).

7.5 Conclusions

The aims of this chapter were to characterise the nature of sediment transport at a polythermal glacier, determine the influence of glacier structure on sediment transport process and ultimately their influence on the formation of glacigenic sediment-landform assemblages. Research at Midre Lovénbreen has resulted in several relevant conclusions:

1. Subglacial till sediments have undergone relatively low levels of shear, resulting in a matrix-dominated by coarse silts and the absence of a significant medium silt-sized sediment mode. Crushing is inferred to be the dominant process of debris communition in the subglacial zone.

2. Proglacial debris layer form a sediment-landform association that is very similar to subglacial debris layer. The spatial homogeneity of proglacial debris layer is therefore indicative of former basal conditions at Midre Lovénbreen, suggesting that subglacial sediment transport is the dominant mode of glacial sediment transport at the glacier.

3. Type-I longitudinal supraglacial debris ridges are interpreted to be the product of S_1 large-scale lateral folding, responsible for elevating subglacial till sediment into flow-parallel fold hinges. These are characterised by downglacier changes in sediment texture, interpreted to reflect the altering ratio of rockfall-derived to basally derived sediment. Previously unidentified Type-II longitudinal supraglacial debris ridges are interpreted to result from a secondary F_3 small-scale horizontal folding of Type-I longitudinal supraglacial debris ridges.

4. Transverse supraglacial debris ridges are interpreted to be basally derived sediment which has been advected along S_3 shear planes, rather than squeezed into basal crevasses.

5. A lack of comparative data make the interpretation of debris cones at Midre Lovénbreen difficult. On the basis of their high degree of roundness, they are probably reworked beach deposits, as suggested by Huddart et al. (1998). However, in this study debris cones were not associated with structural elements, e.g. shear planes.

6. Flute formation at Midre Lovénbreen is interpreted to result from the squeeze of partially fluidized diamicton into cavities that form in the lee of boulders under warm-based ice in the interior of the glacier. The fluidization effectively mobilizes finer sediments, excluding coarser gravel-sized particles. A heat-pump effect across ploughed subglacial boulders leads to development of a cold patch in the lee-side cavity, causing squeezed sediments to freeze-on to the bed of the glacier. These adfrozen sediments form a solid basal ice facies that is transported away from the boulder by glacier flow. Continuous cavity squeezing produces a flow-parallel, elongate bedform, extending downglacier from its associated boulder.

Chapter 8

Synthesis and conclusions

8.1 Introduction

The fundamental aim of this project is to investigate the roles of ice deformation and subglacial thermal regimes upon sediment transfer by cold- and warm-based glaciers. The project quantifies the physical relationships between glaciological processes and Arctic and Alpine land-system evolution. New field data sets from Glacier de Tsanfleuron in Switzerland and Midre Lovénbreen in Svalbard are used to calibrate and validate conceptual and numerical models integrating sediment transfer and ice mass behaviour. The aims of this project (outlined in Chapter 1) are to:

i. Develop a new suite of automated methods for quantifying particle morphology to a high degree of precision and accuracy, and apply this suite of techniques to ice facies and sediment-landform assemblages at both Alpine and Arctic valley glacier landsystems,

ii. Map glacier surface and subsurface structure and examine the influence of structure on sediment transport processes at both Alpine and Arctic valley glaciers,

iii. Make a first-order approximation of glacial sediment discharge on the basis of the distribution and concentration of sediments in ice facies and modeled three-dimensional ice-flow velocities,

iv. Evaluate and contribute to existing conceptual models of glacial sediment-transport and glacigenic sediment-landform assemblage formation,

v. Evaluate the influence of basal thermal regime on glacier structure and sediment transport on the basis of these research findings.

These aims were addressed by applying and developing a range of innovative techniques to empirical data collection, at Glacier de Tsanfleuron in 2007, and Midre Lovénbreen in 2008, and subsequent analyses of these data (Table 8.1). The data acquired during fieldwork were used to address the main aims of the this thesis.

Table 8.1: Areas of investigation and data collection and analysis techniques used to characterise and quantify glacial sediment transport dynamics

Area of investigation		Techniques applied
Glacier structure	(i)	Surface mapping from aerial photography and fieldwork
	(ii)	Optical televiewing using hot-water drilled multiple borehole array
	(iii)	Three-dimensional data interpolation and visualization
Sediment-landform assemblages	(iv)	Geomorphological mapping
	(v)	Particle-size-distribution analysis
	(vi)	Automated particle morphology analysis
Sediment discharge rates	(vii)	Surface velocity measurement
	(viii)	Finite-difference modeling

This chapter discusses the sediment-landform assemblages and sediment transport processes identified at Glacier de Tsanfleuron and Midre Lovénbreen within the context of glacier basal thermal-regime and wider environmental settings (Section 8.2). The main findings from this project are summarized in Section 8.3, followed by suggestions for areas of further research (Section 8.4).

8.2 Synthesis: The influence of basal–thermal regime on glacier structure and sediment transport

The influence of basal thermal-regime on glacier structure and sediment transport has been widely recognised, from both theoretical studies (e.g. Weertman, 1961; Boulton, 1972; Alley et al., 1997) and from empirical data (Paterson, 2000; Hallet et al., 1996; Hodson and Ferguson, 1999; Hambrey and Lawson, 2000). Conventionally, glaciers are often referred to as either *warm-based*, when ice at the bed is thought to be close to or at melting point, *cold-based*, when ice at the bed is below the melting point, or *polythermal*, when ice at the bed is below melting point in some areas and above the melting point in others (Paterson, 2000; Harrison, 1972).

Consideration *a priori* of the processes operating at the bed of a valley glacier (e.g. regelation, adfreezing, conductive cooling, supercooling, geothermal heating) suggests that the distribution of heat at the bed is unlikely to be spatially or temporally homogeneous

over a very large area or for a very long time (Alley et al., 1997). For example, Hodson and Ferguson (1999) concluded, on the basis of time series data of suspended sediment discharge rates from three Svalbard glaciers of different basal thermal-regime, that the thermal processes governing sediment availability were responsible for the most obvious differences measured in the timing and rates of suspended sediment discharge between the three glaciers. Alley et al. (1997) also asserted, that while a number of different transport processes could operate simultaneously, the nature of physical factors governing sediment entrainment mechanisms meant that one process in particular would be dominant at any one time. The processes of sediment transport identified in this study focus on sediment transported by ice, rather than by meltwater or by sediment deformation. This is predominantly due to the physical setting of both the glaciers investigated. The following sections discuss the nature of structural evolution, sediment transport processes and the formation of sediment-landform assemblages at both Glacier de Tsanfleuron, Switzerland, and Midre Lovénbreen, Svalbard, with reference to basal thermal conditions, hypsometry and underlying lithology.

8.2.1 Glacier de Tsanfleuron

Glacier de Tsanfleuron has been described by a number of researchers as a warm-based glacier (e.g. Sharp et al., 1989; Hubbard, 2002; Hubbard et al., 2003). More recent research (Murray et al., 2007; Bailey, 2007), however, has demonstrated that the internal temperature distribution is not wholly consistent with theoretical predictions, even averaged at the glacier scale. Both Grust (2004) and Bailey (2007) recognised the important role that the palaeokarst system underlying Glacier de Tsanfleuron had on the glacier's energy balance, subglacial drainage network and velocity dynamics.

Unlike the majority of glaciers in the Alps (Hubbard and Nienow, 1997), Glacier de Tsanfleuron is largely underlain by a drainage network composed of linked-cavities (Sharp et al., 1989; Grust, 2004). Dye tracing experiments carried out at the glacier have indicated that $\sim$95% of the meltwater produced drains through the karst system and that only $\sim$5% leaves the glacier as proglacial runoff. Additionally, Bailey (2007) found that the subglacial karst system was responsible for large positive basal thermal disturbances ($\sim$3.5°), due to the penetration of comparatively warm air to the bed, a phenomenon termed *cave breathing*. The accumulation area of Glacier de Tsanfleuron is also atypical of most valley glaciers in the Alps, in that it occupies a broad upland plateau, rather than one or more cirque basins. Currently, the glacier is retreating rapidly (25 to 50 m per year) and almost the entire glacier surface has been snow or firn-free by the end of the melt season over the past four years,

strongly suggesting the (theoretical) equilibrium line altitude is higher than the maximum altitude of the glacier.

The result of these unusual set of conditions is that spatial patterns of ice flow dynamics, and hence structural evolution and sediment transport are highly atypical of conceptual models of valley glacier landsystems in the Alps (Benn et al., 2003).

The terminus of Glacier de Tsanfleuron can be subdivided into four main zones on the basis of style and rate of sediment transport: (i) a northern zone occupying a fault-guided valley (Fig. 1.2); (ii) a central zone characterised small proglacial debris stripes; (iii) a zone of high sediment transport dominated by a medial moraine, and (iv) a southern zone of no sediment transport.

The northernmost zone is most typical of glacierized valley landsystems, in that the ice tongue is relatively thick ($\sim$100 m), bordered to the north by a large lateral moraine and is underlain by an arborescent drainage system that flows across a glaciofluvial outwash plain (Grust, 2004). Structural elements are most well developed in this zone: S_0 primary stratification is intensely deformed by high velocity gradients across the ice tongue, which leads to the development of S_1 longitudinal foliation at the northern margin, and there is a high density of S_2 fractures. Glacial sediment transport in this northern zone is relatively low ($<$10 kg a^{-1}), probably because high rates of basal sliding (10 to 20 m a^{-1}) result in high basal melt rates. Any sediment produced at the bed is evacuated by the comparatively efficient arborescent drainage network. Despite the presence of a proglacial outlet stream in this northern area, rockfall from the adjacent peaks and ice-cored lateral moraine mean that glaciofluvial processes leave a relatively weak signature, compared to outwash plains in front of other warm-based valley glaciers of a similar size (Goodsell et al., 2005; Roberson, 2008). The implications of these findings are that, in more laterally constrained glaciers generally typical of warm-based valley glaciers in the Alps, the volume of sediment transported by ice will also be quite small.

The central zone of the glacier is characterised by alternating areas of moderate (50 to 100 kg a^{-1}) and low ($<$50 kg a^{-1}) glacial sediment discharge rates. Areas of moderate glacial sediment discharge correspond with the ablation of subglacial debris planes and formation of proglacial debris stripes. The physical controls on stream power (i.e. the erosive potential of a discharge) (Equation 2.8) suggest that water flow through a distributed cavity-based drainage network will have a much lower erosive potential than the same discharge flowing through an efficient arborescent drainage network. At Glacier de Tsanfleuron, these circumstances are likely to result in relatively low rates of sediment evacuation, where cavities and channels are present. Additionally, the geometrical relationship between proglacial debris stripes and karst sinkholes suggest that the sinkholes act as point

sources of subglacial sediment. This theory is born out by the linear fabric of sediment entrained in subglacial debris planes, which ablate to form proglacial debris stripes.

The moraine-dominated zone has the highest rate of glacial sediment discharge at Glacier de Tsanfleuron, in spite of relatively low ice flow velocities ($\lesssim$1 m a^{-1}). While Bailey's (2007) research has shown that large areas of the glacier are cold-based, the results of the GPR survey across this region of the glacier (Section 5.2.3.2) indicate that there is a transition from cold surface ice to warm-based ice where liquid water is present. Modeled ice flow velocities additionally demonstrate that flow in this area of the glacier is entirely due to to internal deformation, with no basal sliding occurring despite the presence of warm ice. The implications of these findings are that sediment discharge rates in this zone of the glacier are likely top be the same irrespective of basal thermal conditions. Additionally, these data suggest that medial moraines account for a very high percentage of total volume of sediment transported by warm-based valley glaciers, particularly if basal sediment reservoirs are evacuated efficiently by subglacial meltwater (see above).

Modeled sediment discharge rates for the southern zone of the glacier suggest that they are equal or close to zero. The GPR profile presented in this study and a borehole drilled in this southern area (Samyn, unpublished data) suggest that ice depth does not exceed 25 m at any point south of the nunatak. Temperature profiles recorded by Bailey (2007) at Glacier de Tsanfleuron at three sites where ice depths were much greater, imply that ice in this southern zone of the glacier is probably cold throughout its depth for much of the year. Expanses of cold-based ice are unlikely to be typical of valley glaciers in the Alps, as terminal areas are generally characterised by high rates of melt.

8.2.2 Midre Lovénbreen

Midre Loveénbreen has been frequently referred to as a type site for small valley glaciers in Svalbard (Hagen and Liestøl, 1990; Rippin et al., 2003; Hambrey et al., 2005); indeed it is probably now the most studied of all glaciers in the Arctic. The glacier is known to be polythermal on the basis of radio-echo soundings, ground-penetrating radar and seismic surveys (Björnsson et al., 1996; Rippin et al., 2003; King et al., 2008). Time-series GPR data indicate that the extent of the core area of warm-based ice has varied over time, although surprisingly, this has been non-synchronous with changes in the glacier's mass balance (Rippin et al., 2007). Recent geophysical data suggest that cold ice at the bed is located along the glacier's flow-line up to $\sim$1.3 km upglacier from the terminus (King et al., 2008). The spatial extent of peripheral cold-based ice determines, to a large extent the behaviour of the subglacial drainage network (Hodson and Ferguson, 1999) and correspondingly, the quantity of sediment available for glacial transport. Investigations at Midre Lovénbreen

have shown the subglacial drainage network to be spatially restricted and have suggested that glaciofluvial suspended sediment discharge rates are largely dependent upon sediment availability from a subglacial reservoir (Irvine-Fynn et al., 2005a). Rippin et al. (2003) successfully demonstrated that the timing and spatial configuration of the glacier's drainage network is heavily dependent on the distribution of cold-based ice, although meteorological inputs to the glacier surface were also found to be strongly influential early in the melt season. Although no calculations of glacial sediment discharge rates were made for Midre Lovénbreen, as they were for Glacier de Tsanfleuron (Section 5.2.3.3), a number of insights into the influence of basal-thermal regime on different transport mechanisms and their relative contribution to total sediment discharge can still be made.

Interpretations made on the basis of sediment analyses in this study (Section 7.3) concluded that subglacial transport is the dominant mode of glacial sediment transport at Midre Lovénbreen. The results from this and other studies conducted at Midre Lovénbreen (Hambrey et al., 2005; King et al., 2008) suggest that shear of the till layer beneath the glacier is relatively low. The results of work by Rippin et al. (2005) contradict this view, however, on the basis of empirical data and force-balance modelling. These authors suggested that surface velocities and basal drag may vary over at the metre-scale, due to the penetration of basal meltwater through and under cold-based ice around the glacier periphery. Rather than the relatively inert subglacial till layer suggested by the results from this study, Rippin et al.'s (2005) study indicates that high rates of shear may occur locally in the till layer for short periods. On the basis of the textural characteristics of flutes in front of and emerging from under Midre Lovénbreen, it is hypothesized that local slippery-spots may be associated with the partial-fluidization of the basal till layer and the formation of flutes by cavity-squeeze processes. The presence of slippery spots at the bed may also explain observations of F_2 medium-scale horizontal folds within borehole logs (Section 6.2.2).

Four types of supraglacial sediment-landform assemblage were identified at Midre Lovénbreen: (i) Type-I longitudinal supraglacial debris ridges; (ii) Type-II longitudinal supraglacial debris ridges; (iii) transverse supraglacial debris ridges, and (iv) debris cones.

Laterally compressive stresses associated with the flow of ice from multiple-cirque basins into a deep, narrow tongue and large-scale lateral folding, result in the elevation of en- and subglacial debris into flow-parallel Type-I longitudinal supraglacial debris ridges. These sediment-landform assemblages resemble, in size and texture, those identified on warm-based valley glaciers in a similar topographic setting (e.g. Goodsell et al., 2005; Roberson, 2008). As such, these landforms cannot be considered diagnostic features of particular thermal conditions.

Type-II longitudinal supraglacial debris ridges have been identified for the first time in this study, and are interpreted to form as Type-I debris ridges are incorporated into F_3 small-

scale horizontal folds. F_3 horizontal folds are found in association with S_3 shear planes, forming under a longitudinally compressive stress regime established due to the stress-gradient between relatively fast-moving ice from the glacier's warm core and relatively slow-moving cold-based ice at the glacier's margins. While these formation mechanism imply that Type-II longitudinal supraglacial debris ridges may be unique to polythermal glaciers, they also suggest that, following deposition, they will be indistinguishable from Type-I debris ridges. Indeed, relicts of neither sediment-landform assemblage were identified in the glacier forefield. In summary, in the unlikely event of longitudinal supraglacial debris ridges being identified in the geological record, this would not prove diagnostic of basal thermal conditions.

The formation of supraglacial debris cones at Midre Lovénbreen is linked to the deposition of glaciofluvially transported sediment in large (2 to 4 m deep) supraglacial channels. The presence of cold-based ice at polythermal glaciers restricts the penetration of surface meltwater to the bed (Tranter et al., 1996), leading to the formation of a well-developed supraglacial stream network. At Midre Lovénbreen, the development of the supraglacial drainage network is also encouraged by the very low density of open S_2 surface crevasses, which otherwise have the potential to re-route surface meltwater en- and subglacially. While debris cones have been observed at the surface of numerous warm-based glaciers (e.g. Swithinbank, 1950; Drewry, 1972; Small et al., 1984; Goodsell et al., 2005), the majority of these have been associated with crevasse-fill or advection along shear planes. It is suggested therefore, that although debris cones are not ubiquitous to polythermal glacier landsystems, they are less likely to be composed of fluvially rounded gravel at a warm-bedded glaciers, which tends to be associated with transport by subglacial meltwater (Hambrey and Ehrmann, 2004; Roberson, 2008). The implications of this hypothesis are that debris cones are less likely to be a feature of polythermal glaciers with less well-developed supraglacial drainage networks. Historical documentation of Midre Lovénbreen (see Norsk Polarinstitutt aerial photograph S36 15 5 2, published in Hambrey et al., 2005, their Fig. 10), has shown that open S_2 surface crevasses were much more common when the glacier was larger and probably faster flowing. The higher density of S_2 surface crevasses suggests that the penetration of surface meltwater to the bed was more widespread than it is under current conditions. It is therefore proposed, on the basis of these observations and the hypothesized mechanism of debris cone formation presented above (Section 7.3.5), that supraglacial debris cones composed of rounded-gravel were probably absent during periods of more rapid flow.

Transverse supraglacial debris ridges identified in this study are associated with the advection of basally derived sediment along S_3 shear planes. However, there is no empirical evidence to suggest that, under a warm-based thermal regime, basally transported

sediments are advected along shear planes. This is probably due to: (i) the evacuation of subglacial sediment reservoirs by well-developed subglacial drainage networks (Gurnell and Clark, 1987); (ii) the lower frequency of S_3 shear planes at warm-based glaciers (Roberson, 2008), and/or (iii) the lower levels of net adfreezing due to the continual melt of ice at the bed of warm-based ice masses (Alley et al., 1997). Investigations at other glaciers have also linked the formation of transverse supraglacial debris ridges to injections of turbid meltwater or fluidized sediment into basal crevasses (Evans and Rea, 1999; Ensminger et al., 2001; Woodward et al., 2002). This study has established that basal crevassing is unlikely to take place at Midre Lovénbreen under current conditions (Section 6.3.5). Empirical and theoretical studies indicate that both faster ice flow velocities and seasonal fluctuations in basal water pressure increase the likelihood of basal crevasse formation (Mickelson and Berkson, 1974; van der Veen, 1998; Harbor, 2009). However, in spite of the implications of these conditions for basal crevasse formation, i.e. that basal crevassing will occur under faster warm-based ice, transverse supraglacial debris ridges at temperate glaciers are almost exclusively associated with the advection of basally supercooled meltwater. The physical conditions outlined by Cook et al. (2006) strongly suggest that supercooling would be unlikely to take place at Midre Lovénbreen, due to the absence of an over-deepened basin, and therefore that transverse debris ridge formation under warm-based conditions is as equally improbable.

8.2.3 Wider implications

It was the intention of this study to draw direct comparisons between two small valley glaciers of contrasting basal thermal-regime, on the basis of parallel investigations conducted at Glacier de Tsanfleuron and Midre Lovénbreen. However, it is concluded that while Midre Lovénbreen, composed of multiple cirque basins feeding into a deep, narrow ice tongue, is fairly typical of small valley glaciers, both in Svalbard and the western Alps, Glacier de Tsanfleuron, occupying broad and highly permeable plateau, is not. The result of these underlying differences, is that the compressive stress regimes identified at Midre Lovénbreen result in structures that are very different from the structures identified at Glacier de Tsanfleuron, which form under a largely tensile stress regime.

Using Midre Lovénbreen and Bakaninbreen as two contrasting examples, King et al. (2008) suggested that the ice-flow dynamics and rates of glacial sediment transport in Svalbard glaciers might be geologically determined. The results of this study show that this assertion is equally applicable to glaciers in the Alps as well. While erosion rates at Glacier de Tsanfleuron are of the same order of magnitude as other small valley glaciers in the Alps, the results of this study demonstrate that styles of sediment transport are rather

different, predominantly due to the highly permeable nature of the glacier's underlying karst system. Additional investigations into glacial sediment discharge rates in the Alps are therefore needed to examine whether the suggestions made in this study, with regards to the distribution and relative proportions of sediment transported by ice and meltwater, are valid.

8.3 Summary of main conclusions

8.3.1 Automated image-based analysis of particle morphology

The techniques developed in Chapter 4 demonstrate that particle morphology can be quantitatively analysed using a low-cost, automated digitally based approach. The automated method uses an inexpensive digital camera and a series of Matlab functions, based on the fast-Fourier transform techniques, to extract digitized particle outlines and quantify particle form, roundness and surface roughness. Automated (digitally based) analyses used: (i) Krumbein's (1941) intercept sphericity index to quantify particle form; (ii) Diepenbroek et al.'s (1992) P – value (analogous to Wadell's (1932) roundness index) to quantify particle roundness, and (iii) Hubbard, Siegert and McCarroll's (2000) ξ - value to quantify particle surface roughness. The automated, digitally based technique was successfully demonstrated using 2500 particles sampled from Glacier de Tsanfleuron, Switzerland. Traditional (visually based) analyses of the same particles enabled the differences in accuracy and precision between traditional and automated approaches to be investigated quantitatively. The traditional (visually based) analyses used were: (i) Krumbein's (1941) intercept sphericity index, for measuring particle form; (ii) Powers's (1953) roundness index, for measuring particle roundness, and (iii) counting striations per sample, for measuring surface roughness.

Comparison of automated and traditional techniques demonstrates that automated measurements of particle form are $\pm 2.15\%$ more accurate than visually based measurements. Both methods still remain subject to operator error however, probably caused by uncertainties in identifying a, b and c - axes.

Comparison of automated and traditional techniques reveals that automated measurements of particle roundness correlate strongly with traditional (visually based) Powers's (1953) roundness index, but that digitally derived P – values show less variance away from the mean, i.e. they are more precise. Automated (digitally based) roundness analysis also represents a considerable improvement over other traditional (visually based) analyses in terms of being able to make distinctions between samples which would otherwise appear identical using traditional (visually based) methods, e.g. Powers's (1953) roundness index. This is due not only to the use of a continuous roundness scale, rather than a discontinuous

classification, but also due to reductions in operator bias associated with visual comparison charts.

Automated (digitally based) approaches to surface roughness measurements do not correlate well with traditional (visually based) measurements made by counting particles with striated surfaces. Close inspection of particles sampled from Glacier de Tsanfleuron indicate that surface weathering rapidly removes traces of abrasive wear and that automated values of particle surface roughness are determined by local variations in lithological composition. Re-analysis of surface profiles collected from glaciated limestone bedrock at Glacier de Tsanfleuron (Hubbard, Siegert and McCarroll, 2000) indicate that processes operating on bedrock are very different from processes operating on particles in englacial transport.

8.3.2 Structure and sedimentology of Glacier de Tsanfleuron

Investigations at Glacier de Tsanfleuron, Switzerland reveal two main sources of glacially transported sediment: (i) rockfall debris from a nunatak close to the glacier's southern margin, and (ii) subglacial point sources, probably sinkholes in the subglacial palaeokarst. Structural elements identified at Glacier de Tsanfleuron have limited influence on sediment transport, with the exception of weak flow-parallel foliation (S_1), which develops close to the glacier's northern margin. Here, rockfall debris are re-orientated by simple shear into flow-parallel debris stripes, due to the high longitudinal tensile stress and high lateral compressive stress operating between the glacier's main ice tongue and northern margin.

Rockfall-derived sediment forms a medial moraine-type supraglacial debris stripe that extends into the glacier forefield and is continuous with a proglacial debris stripe, extending to the terminal moraine complex. Sediment derived from subglacial point sources is transported as flow-parallel subglacial debris planes. These ablate to form a complex series of small ($<$0.8 km long, $<$30 m wide) longitudinal proglacial debris stripes. Samples of particles from these proglacial debris stripes exhibit an increase in blockiness (quantified by I_s – values) with increased distance from the glacier terminus. This is interpreted to be a result of an increase in wear with transport distance at the glacier bed. This spatial trend however, is not reflected by other indices of particle morphology (P – values or ξ – values), nor by particle-size-distributions of matrix samples from proglacial debris stripes. This conflict of evidence is believed to be caused primarily by post-depositional weathering of the chemically soft limestone particles that comprise the proglacial debris stripes. Qualitative evidence demonstrates that particles of Urgonian limestone, the lithology underlying the majority of Glacier de Tsanfleuron, have a relatively low potential for preserving evidence of subglacial abrasion when exposed to subaerial weathering, e.g. striations.

Ice-marginal glacial sediment discharge rates are calculated on the basis of the distribution of ice facies, their respective sediment concentrations and ice-flow vectors generated by a three-dimensional finite-difference model of Glacier de Tsanfleuron. Modeled rates of glacial sediment discharge reflect the size and morphology of proglacial sediment-landform assemblages. Calculated erosion rates (0.5 mm a^{-1}) are comparable to erosion rates measured at other small, warm-based valley glaciers in similar settings. Glacial sediment transport rates in the northern half of the glacier are low relative to the rest of the glacier and the modeled velocity field. Sediment transport in the northern half of the glacier is probably dominated by glaciofluvial sediment transport. However, this is likely to be difficult to determine empirically, as the majority of the the glacier's meltwater drains through sinkholes at the bed (Grust, 2004). Modification of proglacial sediment-landform assemblages by meltwater is correspondingly spatially restricted and superficial. This is atypical of traditional models of glaciated valley landsystems in the Alps. Sediment transport processes at Glacier de Tsanfleuron are predominantly controlled by the composition of its underlying karstic lithology and its unique topographic setting, rather than by variations in prevailing thermal conditions.

8.3.3 Structure and sedimentology of Midre Lovénbreen

The use of OPTV in multiple hot-water drilled boreholes has successfully allowed the internal structure of two regions of the frontal zone of Midre Lovénbreen to be logged in Cartesian space with geometric accuracy. Interpolation between individual borehole logs has also allowed several distinctive englacial structures to be visualized in three-dimensions. Combining measurements from OPTV logs with surface mapping reveals the visual and geometrical characteristics of eight structural elements: (i) S_0 primary stratification; (ii) S_1 longitudinal foliation; (iii) S_2 transverse fracture traces; (iv) S_3 arcuate shear planes; (v) S_4 oblique fractures; (vi) F_1 large-scale lateral folds; (vii) F_2 medium-scale horizontal folds and (viii) F_3 small-scale horizontal folds. S_4 oblique fractures, predicted by Nye (1954), are identified empirically here for the first time.

The transport of sediment and development of sediment-landform assemblages has a strongly structurally controlled component at Midre Lovénbreen. The visual characteristics of englacial sediment layers identified within our OPTV logs are consistent with laminated and solid basal ice facies described by Hubbard and Sharp (1995). Three-dimensional visualization of internal glacier structure, based on the inter-borehole interpolation of OPTV logs, reveal that these englacial sediment layers are incorporated into large-scale F_1 lateral folds and elevated into near-vertical planes in association with lateral compressive stress

and Type-I longitudinal supraglacial debris ridge formation. These findings are also supported by downglacier changes in the relative contribution of two different sediment modes to the overall particle-size-distribution of samples from Type-I longitudinal supraglacial debris ridges. These are changes are interpreted to reflect an increase in the proportion of basally derived sediment elevated from the bed by large-scale lateral folding (F_1), consistent with the structural model of Hambrey et al. (2005). Previously unidentified Type-II longitudinal supraglacial debris ridges (a sub-type of Type-I longitudinal supraglacial debris ridges) are interpreted to result from a secondary F_3 small-scale horizontal folding of Type-I longitudinal supraglacial debris ridges into a plane parallel to S_3 arcuate shear planes, orientated orthogonal to ice flow. S_3 arcuate shear planes are also linked to the advection of basally derived sediment to the ice surface, forming transverse supraglacial debris ridges close to the glacier terminus.

Non-structurally controlled sediment transport is also responsible for the formation of sediment-landform assemblages identified at Midre Lovénbreen include subglacial till, debris cones proglacial diamicton and flute. Textural analysis reveals that subglacial till sediments have probably undergone relatively low levels of shear, resulting in a matrix dominated by coarse silts, where crushing is inferred to be the dominant process of debris communition. Proglacial diamicton form a sediment-landform association that is very similar to subglacial till. The spatial homogeneity of proglacial diamicton is considered indicative of former basal conditions at Midre Lovénbreen, suggesting that subglacial sediment transport is the dominant mode of glacial sediment transport at the glacier. Debris cones located close the glacier's terminus are interpreted to form from the melt-out of raised beach deposits on the basis of particle morphology and size-distribution data. Flutes observed in front of and emerging from under the terminus of Midre Lovénbreen are interpreted form as a result of 'cavity-squeeze' processes, when partially fluidized diamicton is squeezed into cavities forming in the lee of boulders ploughed into the glacier bed. Till fluidization occurs under warm-based ice in the presence of liquid water at the ice-bed interface, which mobilizes finer sediments and excludes coarser particles from the flute. Adfreezing of the squeezed sediment is caused by the formation of a cold-patch within the cavity walls, resulting from: (i) a 'heat pump' effect across the boulder during regelation, similar in nature to the processes identified by Robin (1976), and (ii) the elevation of the pressure-melting point within the cavity due to the comparatively low pressure. The adfrozen sediment forms solid basal ice facies, which is transported downglacier, away from the boulder. The repetition of this processes produces an elongate bedform, extending downglacier parallel to the direction of ice flow. Flutes are not thought to form under cold-based ice at Midre Lovénbreen, but rather they are preserved.

8.4 Recommendations for future research

8.4.1 Instrumentation

This study has demonstrated that particle morphology can be quantitatively measured to a high degree of accuracy and precision using a low-cost digital camera and digitally based analysis techniques. It is the intention of the author to make the Matlab code more widely accessible by integrating it into a cross-platform graphical user interface-based application. A number of limitations were apparent however, most of which are attributable to the use of two-dimensional outlines as proxies for describing three-dimensional particles. This was apparent from errors identified in defining particle a-, b- and c-axes and in particular, quantification of particle surface roughness. This technique failed to characterize the presence of striations on subglacially transported particles and was also unable to characterise particle morphologies considered diagnostic of glacial sediment transport (e.g. bullet-shaped particles). Recent developments (Bridges et al., In Press) in the use of laser scanning technologies to quantify physical environments have indicated that a fully three-dimensional approach to the analysis of particle morphology maybe feasible in the near future.

The application of borehole OPTV to ice boreholes has identified a number of limitations in both data acquisition and post-processing methods. Chief amongst these are problems in intersecting and imaging borehole-parallel structures, which may be potentially overcome through use of the OPTV in non-vertical boreholes. Identification of individual structures is currently restricted by the resolution of the OPTV's charge-coupled device (CCD) digital image sensor, which resolves pixels to a resolution of 1 mm. The irregular geometry of the hot water-drilled boreholes is also a source of uncertainties, particularly in terms of determining the orientation and dip of englacial structures with a high degree of precision. Plans for further development of this technique include the use of parallel instrumentation, including: a borehole caliper to measure the variable borehole geometry; an electrical-resistivity probe to quantify down-borehole changes in ionic concentrations, and an acoustic imager to detect changes in material properties horizontally away from the borehole. For the advantages offered by a multi-system approach to be fully realised, further software developments are also required.

8.4.2 Data collection

Proposed mechanisms for the development of Type-II longitudinal supraglacial debris ridges, identified in this study at Midre Lovénbreen, require verification from additional field-based studies. Use of repeat photography would be particularly effective in identifying trends in the surface development of Type-I and Type-II longitudinal supraglacial debris ridges time.

Wider application of the OPTV system to imaging subsurface structures may also add to our knowledge of folding on englacial sediment transport. An approach using short, steam-drilled boreholes would allow a relatively large area to be covered at the terminal zone of a glacier during a single field season. Such an approach may be particularly useful when it comes to characterizing the distribution of basal ice facies at glaciers where access to the subglacial environment at the terminus is restricted.

Further investigations into the formation mechanism of subglacial flutes is proposed that combines decimetre-scale sediment sampling with numerical modelling of basal shear stress and sediment deformation. Existing finite-difference flow models can be used to predict values of basal shear stress and simulate cavity opening, in combination with a coupled model of meltwater production and sediment deformation to assess mechanisms of till fluidization and sorting.

This study has demonstrated that empirical measurements of sediment concentrations may be used effectively in combination with first order solutions of three-dimensional ice flow to investigate the formation of proglacial sediment landforms. Extension of this approach using either a coupled or uncoupled physically based model of sediment erosion and transport would provide even more insights into the nature of subglacial sediment production and entrainment. Rather than apply this model to Glacier de Tsanfleuron however, where the distribution and behaviour of the subglacial drainage network is difficult to predict and model, it is suggested that it should be applied to an equally well-documented glacier, more typical of small valley glaciers in the Alps (e.g. Glacier de St. Sorlin, France or Haut Glacier d'Arolla, Switzerland).

Appendix A

Automated Gaussian-component analysis: Matlab code

The following is the Matlab code used to perform the Gaussian-component analysis detailed in Chapter 3.

```
% GAUSSIAN-COMPONENT ANALYSIS %

% COMPILED BY SAM ROBERSON %

% AFTER SHARP AND OTHERS, 1994 %


cd 'volume:\directory\subdirectory'

% enter data as variable 'data'  with particle-size-distributions in columns
% or read data in from file

data=open('file.txt');

% Enter particle size range and bin size of data in phi:

max = 11;
min = -1.0;
bin = 0.5;

files = dir('*.ai');

% This code uses blank Adobe Illustrator documents to output graphs.
% The .ai files can either be saved to the directory from Matlab
% or created from a command line interface.
%
% Name the files according to your data labels and re-order your
```

A. AUTOMATED GAUSSIAN-COMPONENT ANALYSIS: MATLAB CODE

```
% data alphabetically so that it matches to way the files are read in by Matlab.

% Enter the number of Gaussian-components required:

p=3;

data=single(data); % to keep the size down

[a,b]=size(data);

for k=1:b
x=data(:,k);
x=x.*100;
x=int16(x);
x=single(x);
d=10;
q=1:length(x);
qs=1:1/d:length(x);

% Apply cubic spline interpolation to the data:

xs=spline(q,x,qs);
% this deals with problems of zeros and negative numbers
ys=(1.0:bin/100:(1-min)+max).';
xs=xs.';
[m,n]=size(xs);
xs=int16(xs);

% This loop reorganizes data into a population-density format

for z=1:m
xf(1:xs(z,1),z)=ys(z,1);
end

xf=reshape(xf,[],1);
xf=sort(xf,'descend');
xf(sum(xs):length(xf))=[];
xf=single(xf);

% fit Gaussian distributions to the data

[u,sig,t,iter] = fit_mix_gaussian(xf,p);

% Formating for graphs:

nbins  = 250;
```

```
points = 250;
[n,x]  = hist(xf,nbins);
dx     = x(2)-x(1);
x_c    = linspace(x(1)-dx/2,x(end)+dx/2,points);

for m = 1:p
y_c(m+1,:)=t(m)/sqrt(2*pi*sig(m)^2)*exp(-((x_c-u(m)).^2)/(2*sig(m)^2));
end

x_c=x_c-2;
y_c(1,:)=x_c;

u=u-2;
u=2.^(u.*-1);
u=u.*1000;

% Data output arranged as n rows x 3p columns,
% where n is the number of samples and p is the number of Gaussian-components:

results(k,1:p)=u; % mean particle size of the Gaussian-component
results(k,p+1:2.*p)=sig; % standard deviation of the Gaussian-component
results(k,(2.*p)+1:3.*p)=t(:,1:p); % probability of the Gaussian-component

g=p+1;
out((k.*g)-(g-1):k.*g,1:points)=y_c;

% Output graphs to Adobe Illustrator files:

saveas(gcf,[files(k).name],'ai')

clear x y xf xs ys n m ans d iter q qs z x_c y_c u sig t g z windowSize dx ans nbins points
end

% Data need to be converted back to double precision for 'ascii' output

results=double(results);

save(['\\directory\GCA.txt'],'results','-ascii');
```

A. AUTOMATED GAUSSIAN-COMPONENT ANALYSIS: MATLAB CODE

Appendix B

Automated image-based analysis of particle morphology: Matlab code

The following is the Matlab code used to perform the automated particle morphology analysis detailed in Chapter 4. It should be noted that this code is specific only to the images used in this project. Notes are provided for those familiar with Matlab to be able to apply this to any given set of images. It is the intention of the author to make this code more accessible by integrating it into a cross-platform graphical user interface-based application.

```
% PARTICLE MORPHOLOGY ANALYSIS %

% DESIGNED BY SAM ROBERSON %

% VERSION 1.2.8 %

% This script builds on a number of other freely available MATLAB scripts,
% but is primarily indebted to the work of Diepenbroek et al. (1992).

cd 'volume:\directory\directory' % select your directory

files = dir('*.JPG');

% The following files correct for lens distortion.
This is focal depth and height specific.

INPUT_POINTS=dlmread('INPUT_POINTS.txt');
BASE_POINTS=dlmread('BASE_POINTS.txt');
TFORM = cp2tform(INPUT_POINTS,BASE_POINTS,'polynomial',4);

size=6800 % enter number of pixels per metre.
```

B. AUTOMATED IMAGE-BASED ANALYSIS OF PARTICLE MORPHOLOGY: MATLAB CODE

```
% h is a window with a series of progress bars:
% 1 for overall progress and 1 for each sub-process

h = cwaitbar([0 0 0 0], {'Overall Progress','Image Processing','Roundness algorithm',
'Roughness algorithm'},{[.8 .2 .8] , 'y', 'b', 'r'});

% start the outer loop

for k = 1:numel(files)
image=imread(files(k).name);

% image registration process

cwaitbar([2 1/50])

regimg=imtransform(image, TFORM,'XYScale',[0.0147],'XData',[-43,1],'YData',[-29.5,1]);

cwaitbar([2 2/20])

% image segmentation algorithms - these may be manually adjusted depending on the type
% of lithologies used
% See the work of Graham et al. (2004) for more ideas on image segmentation

r=regimg(:,:,1);
b=regimg(:,:,2);
g=regimg(:,:,3);
cwaitbar([2 3/20])
r=imadjust(r);
b=imadjust(b);
cwaitbar([2 4/20])
c=g+r;
c=imadjust(c);
cwaitbar([2 5/20])
c=c-b;
cwaitbar([2 6/20])
c=imadjust(c);
cwaitbar([2 7/20])
c=imadjust(c,[0.3 0.7],[]);
cwaitbar([2 8/20])
t=graythresh(c);
cwaitbar([2 9/20])
c=im2bw(c,t);
cwaitbar([2 10/20])
c=(c-1).^2;
cwaitbar([2 11/20])
se90=strel('line',3,90);
```

```
se0=strel('line',3,0);
cwaitbar([2 12/20])
c=imdilate(c,[se90 se0]);
cwaitbar([2 13/20])
c=imfill(c,'holes');
cwaitbar([2 14/20])
c=bwareaopen(c,300);
cwaitbar([2 15/20])
se = strel('disk',2);
c = imclose(c,se);
cwaitbar([2 16/20])
c=imfill(c,'holes');
cwaitbar([2 17/20])
c=imclearborder(c,4);
cwaitbar([2 18/20])
seD = strel('diamond',1);
c=imerode(c,seD);
cwaitbar([2 19/20])
c = bwareaopen(c,1000);
cwaitbar([2 20/20])
cwaitbar([2 0/20])

[B,L] = bwboundaries(c,'noholes');

stats=regionprops(L,'Centroid','Perimeter','Majoraxislength','Minoraxislength');

% roundness calculation

for j=1:length(stats)
perimeter=B{j};
res=length(perimeter);
perimeter=resizem(perimeter,[1024,2]);
x=perimeter(:,1);
y=perimeter(:,2);
[c,d]=ellipsefit(perimeter);
x=x-d(1,1);
y=y-d(1,2);
[t,r]=cart2pol(x,y);
[Y,a0,a,b]=fftcoeff(r,1,2);
r=r-Y(1:length(r),3);
Y=fft(r,1024);
Y=Y./Y(1);
Y(1)=[];
Y=abs(Y);
f=(1:23);
ck=0.56.*(exp(0.2.*f));
```

```
R(1:23)=Y(1:23);

% adjustment for pixel resolution

R=R-(0.17./res);
R=R.*ck;
R=sum(R(3:23));
R=exp(-3.*R);
roundness(j,1)=R;
cwaitbar([3 j/length(stats)])
end
cwaitbar([3 0])

% roughness and a-,b-,c-axes calculations

for i=1:length(stats)
f=stats(i).Perimeter;

f=f./size;

C=stats(i).Centroid;
L=stats(i).MajorAxisLength;
L=L./6800;
W=stats(i).MinorAxisLength;
W=W./6800;
perimeter=B{i};
perimeter=perimeter./size;
x=perimeter(:,1);
y=perimeter(:,2);
[c,d]=ellipsefit(perimeter);
x=x-d(1,1);
y=y-d(1,2);
[x,y]=interpm(x,y,(length(x)./10240));
x=resizem(x,[1024,1]);
y=resizem(y,[1024,1]);
[t,r]=cart2pol(x,y);
[Y,a0,a,b]=fftcoeff(r,1,2);
r=r-Y(1:1024,3);

s=0.4./f;
q=int16(1024./(f./0.4));

% this extends the length of each particle outline to 4 m for SPD calculation

for v = 1:12
if (s > v) & (s <= v+1)
```

```
r((1024*v)+1:q)=r(1:q-(1024*v));
end

Y=fft(r,800);
Y(1)=[];
P = Y.*conj(Y)/800;
R=sum(P(100:400));
roughness(i,1)=R;
Width(i,1)=W;
Length(i,1)=L;
Centre(i,:)=C;
cwaitbar([4 i/length(stats)])
end;
cwaitbar([4 0])

% data are saved as n x 6 array of N files where n is the number of particles per image
% and N is the number of images in the directory

data(:,1:2)=Centre;   % centre co-ordinates used to cross-reference particles between images
data(:,3)=Length; % length of best-fit ellipse
data(:,4)=Width; % width of best-fit ellipse
data(:,5)=roundness; % P-value
data(:,6)=roughness; % Xi-value

save (['OUTPUT\filename-' files(k).name],'data','-ASCII');

clear data % clears data from memeory for next loop

cwaitbar([1 k/numel(files)])

end
close(h)
```

B. AUTOMATED IMAGE-BASED ANALYSIS OF PARTICLE MORPHOLOGY: MATLAB CODE

References

Allen, C., Kamb, W., Meier, M. and Sharp, R. (1960). Structure of the lower Blue Glacier, Washington, *The Journal of Geology* **68**: 601–625.

Alley, R. (1989). Water-pressure coupling of sliding and bed deformation: II. Velocity-depth profiles, *Journal of Glaciology* **35**(119): 119–129.

Alley, R. (1991). Deforming-bed origin for southern laurentide till sheets?, *Journal of Glaciology* **37**(125): 67–76.

Alley, R., Cuffey, K., Evenson, E., Strasser, J., Lawson, D. and Larson, G. (1997). How glaciers entrain and transport basal sediment: physical constraints, *Quaternary Science Reviews* **16**(9): 1017–1038.

Alley, R., Lawson, D., Evenson, E., Strasser, J. and Larson, G. (1998). Glaciohydraulic supercooling: a freeze-on mechanism to create stratified, debris-rich basal ice: II. Theory, *Journal of Glaciology* **44**(148): 563–569.

Alley, R., Lawson, D., Larson, G., Evenson, E. and Baker, G. (2003). Stabilizing feedbacks in glacier-bed erosion, *Nature* **424**(6950): 758–760.

Alley, R. and MacAyeal, D. (1994). Ice-rafted debris associated with binge/purge oscillations of the Laurentide Ice Sheet, *Paleoceanography* **9**(4): 503–511.

Anderson, R., Hallet, B., Walder, J. and Aubry, B. (1982). Observations in a cavity beneath Grinnell Glacier, *Earth Surface Processes and Landforms* **7**(1): 63–70.

Anderson, R., Molnar, P. and Kessler, M. (2006). Features of glacial valley profiles simply explained, *Journal of Geophysical Research* **111**(F1004).

Andreas, E. (1987). A theory for the scalar roughness and the scalar transfer coefficients over snow and sea ice, *Boundary-Layer Meteorology* **38**(1): 159–184.

Anonymous (1989). Geotechniek : Classificatie van onverharde grondmonsters, NEN 5104, *Technical report*, Nederlands Normalisatie Instituut.

REFERENCES

Arnold, N. S., Rees, W. G., Hodson, A. J. and Kohler, J. (2006). Topographic controls on the surface energy balance of a high arctic valley glacier, *Journal of Geophysical Research-Earth Surface* **111**(F2): F02011.

Atkins, C., Barrett, P. and Hicock, S. (2002). Cold glaciers erode and deposit: Evidence from Allan Hills, Antarctica, *Geology* **30**(7): 659–662.

Bailey, O. (2007). *Temperature of a "Temperate" Alpine Glacier: Glacier de Tsanfleuron, Switzerland.*, PhD thesis, University of Wales, Aberystwyth.

Barrett, P. (1980). The shape of rock particles, a critical review, *Sedimentology* **27**(3): 291–303.

Benn, D. and Ballantyne, C. (1994). Reconstructing the transport history of glacigenic sediments: a new approach based on the co-variance of clast form indices, *Sedimentary Geology* **91**(1-4): 215–227.

Benn, D. I. (1994). Fluted moraine formation and till genesis below a temperate valley glacier: Slettmarkbreen, Jotunheimen, southern Norway, *Sedimentology* **41**(2): 279–292.

Benn, D. I. and Evans, D. J. A. (1998). *Glaciers and glaciation*, John Wiley & Sons, New York.

Benn, D. I. and Gemmell, A. M. D. (2002). Fractal dimensions of diamictic particle-size distributions: Simulations and evaluation, *Bulletin of the Geological Society of America* **114**(5): 528–532.

Benn, D. I., Kirkbride, M. P., Owen, L. A. and Brazier, V. (2003). Glaciated valley landsystems, *in* D. Evans (ed.), *Glacial Landsystems*, Hodder Arnold, London, pp. 372–406.

Bennett, M. R., Hambrey, M. J. and Huddart, D. (1997). Modification of clast shape in high-arctic glacial environments, *Journal of Sedimentary Research* **67**(3): 550–559.

Bennett, M. R., Huddart, D., Hambrey, M. J. and Ghienne, J. F. (1996). Moraine development at the high-arctic valley glacier Pedersenbreen, Svalbard, *Geografiska Annaler* **78A**: 209–222.

Benoist, J. (1979). The spectral power density and shadowing function of glacial microrelief at the decimetre scale, *Journal of Glaciology* **23**(89): 57–66.

Björnsson, H., Gjessing, Y., Hamran, S. E., Hagen, J. O., Liestøl, O., Palsson, F. and Erlingsson, B. (1996). The thermal regime of sub-polar glaciers mapped by multi-frequency radio-echo sounding, *Journal of Glaciology* **42**(140): 23–32.

Blott, S. and Pye, K. (2006). Particle size distribution analysis of sand-sized particles by laser diffraction: an experimental investigation of instrument sensitivity and the effects of particle shape, *Sedimentology* **53**(3): 671–685.

Blott, S. and Pye, K. (2008). Particle shape: a review and new methods of characterization and classification, *Sedimentology* **55**(1): 31–63.

Boulton, G. (1970). On the origin and transport of englacial debris in Svalbard glaciers, *Journal of Glaciology* **9**(56): 213–229.

Boulton, G. (1972). The role of thermal regime in glacial sedimentation: Institute of British Geographers, *Special Publication* **4**: 1–19.

Boulton, G. (1976). The origin of glacially fluted surfaces: observations and theory, *Journal of Glaciology* **17**(76): 287–309.

Boulton, G. S. (1967). The development of a complex supraglacial moraine at the margin of Sorbreen, Ny Friesland, Vestspitsbergen, *Journal of Glaciology* **6**(47): 717–735.

Boulton, G. S. (1978). Boulder shapes and grain-size distributions of debris as indicators of transport paths through a glacier and till genesis, *Sedimentology* **25**(6): 773–799.

Boulton, G. S. and Hindmarsh, R. C. A. (1987). Sediment deformation beneath glaciers: rheology and geological consequences, *Journal of Geophysical Research-Solid Earth* **92**(B9): 9059–9083.

Boulton, G. S., Morris, E. M., Armstrong, A. A. and Thomas, A. (1979). Direct measurement of stress at the base of a glacier, *Journal of Glaciology* **22**(86).

Bowman, E., Soga, K. and Drummond, W. (2001). Particle shape characterisation using fourier descriptor analysis, *Géotechnique* **51**(6): 545–554.

Brandt, O., Langley, K., Kohler, J. and Hamran, S. (2007). Detection of buried ice and sediment layers in permafrost using multi-frequency ground penetrating radar: A case examination on svalbard, *Remote Sensing of Environment* **111**(2-3): 212–227.

Brasington, J., Wheaton, J., Vericat, D. and Hodge, R. (2007). Modelling braided river morphodynamics with terrestrial laser scanning, *Eos Transactions AGU* **88**: 52.

REFERENCES

Bridges, N., Razdan, A., Yin, X., Greeley, R., Ali, S. and Kushunapally, R. (In Press). Quantification of shape and texture for wind abrasion studies: Proof of concept using analog targets, *Geomorphology* .

Carter, R. and Yan, Y. (2003). On-line particle sizing of pulverized and granular fuels using digital imaging techniques, *Measurement Science and Technology* **14**(7): 1099–1109.

Chamberlin, R. (1928). Instrumental work on the nature of glacier motion, *The Journal of Geology* **38**(1): 1–30.

Chandler, D., Hubbard, B., Hubbard, A., Murray, T. and Rippin, D. (2008). Optimising ice flow law parameters using borehole deformation measurements and numerical modelling, *Geophysical Research Letters* **35**(12): L12502.

Chandler, D. M. (2005). *Measuring and modelling glacier sliding*, PhD thesis, University of Wales, Aberystwyth.

Chandler, J., Buffin-Belanger, T., Rice, S., Reid, I. and Graham, D. (2003). The accuracy of a river bed moulding/casting system and the effectiveness of a low-cost digital camera for recording river bed fabric, *The Photogrammetric Record* **18**(103): 209–223.

Chinn, T., McSaveney, M. and McSaveney, E. (1992). *The Mount Cook Rock Avalanche of 14 December 1991*, Institute of Geological and Nuclear Sciences, Wellington.

Christoffersen, P. and Tulaczyk, S. (2003a). Response of subglacial sediments to basal freeze-on, 1, Theory and comparison to observations from beneath the West Antarctic Ice Sheet, *J. Geophys. Res* **108**(222): 10–1029.

Christoffersen, P. and Tulaczyk, S. (2003b). Thermodynamics of basal freeze-on: predicting basal and subglacial signatures of stopped ice streams and interstream ridges, *Annals of Glaciology* **36**: 233–243.

Christoffersen, P., Tulaczyk, S., Carsey, F. and Behar, A. (2006). A quantitative framework for interpretation of basal ice facies formed by ice accretion over subglacial sediment, *Journal of Geophysical Research* **111**: F01017.

Clarke, G. (2005). Subglacial Processes, *Annual Review of Earth and Planetary Sciences* **33**: 247–276.

Cole, D. (2003). A dislocation-based analysis of the creep of granular ice: preliminary experiments and modeling, *Annals of Glaciology* **37**: 18–22.

Cook, S. J., Waller, R. I. and Knight, P. G. (2006). Glaciohydraulic supercooling: the process and its significance, *Progress in Physical Geography* **30**(5): 577.

Cook, S., Knight, P., Waller, R., Robinson, Z. and Adam, W. (2007). The geography of basal ice and its relationship to glaciohydraulic supercooling: Svínafellsjökull, southeast Iceland, *Quaternary Science Reviews* **26**(19-21): 2309–2315.

Cox, E. (1927). A method of assigning numerical and percentage values to the degree of roundness of sand grains, *Journal of Paleontology* **1**(3): 179–183.

Creyts, T. and Clarke, G. (2005). The Conditions Necessary for Glaciohydraulic Supercooling, *American Geophysical Union, Fall Meeting 2005, abstract# C51B-0296*.

Cuffey, K., Clow, G., Alley, R., Stuiver, M., Waddington, E. and Saltus, R. (1995). Large Arctic temperature change at the Wisconsin-Holocene glacial transition, *Science* **270**(5235): 455.

Cuffey, K., Conway, H., Gades, A., Hallet, B., Lorrain, R., Severinghaus, J., Steig, E., Vaughn, B. and White, J. (2000). Entrainment at cold glacier beds, *Geology* **28**(4): 351–354.

Czarnecka, E. and Gillott, J. (1977). A modified fourier method of shape and surface texture analysis of planar sections of particles, *Journal of Testing and Evaluation, American Society for Testing and Materials* **5**(4): 292–298.

Darwin, C. (1842). Notes on the effects produced by the ancient glaciers of Caernarvonshire, and on the boulders transported by floating ice, *Philosophical Magazine Series 3* **21**(137): 180–188.

Darwin, C. (1887). The life and letters of Charles Darwin, *The Autobiography of Charles Darwin* pp. 26–107.

Dash, J., Fu, H. and Wettlaufer, J. (1995). The premelting of ice and its environmental consequences, *Reports on Progress in Physics* **58**: 115–167.

Diepenbroek, M., Bartholoma, A. and Ibbeken, H. (1992). How round is round? a new approach to the topic 'roundness' by fourier grain shape analysis, *Sedimentology* **39**(3): 411–422.

Dowdeswell, J. (1982). Scanning electron micrographs of quartz sand grains from cold environments examined using fourier shape analysis, *Journal of Sedimentary Research* **52**(4): 1315–1323.

REFERENCES

Dowdeswell, J., Hambrey, M. and Wu, R. (1985). A comparison of clast fabric and shape in Late Precambrian and modern glacigenic sediments, *Journal of Sedimentary Petrology* **55**(3): 691–704.

Dowdeswell, J., Ó Cofaigh, C. and Pudsey, C. (2004). Thickness and extent of the subglacial till layer beneath an Antarctic paleo-ice stream, *Geology* **32**(1): 13–16.

Drevin, G. (2000). Using entropy to determine the roundness of rock particles, *Signal Processing Proceedings, 2000. WCCC-ICSP 2000. 5th International Conference on*, Vol. 2.

Drewry, D. (1972). A quantitative assessment of dirt-cone dynamics, *Journal of Glaciology* **11**(63): 431–446.

Echelmeyer, K. and Zhongxiang, W. (1987). Direct observation of basal sliding and deformation of basal drift at sub-freezing temperatures, *Journal of Glaciology* **33**(113): 83–98.

Ehrlich, R., Brown, P., Yarus, J. and Przygocki, R. (1980). The origin of shape frequency distributions and the relationship between size and shape, *Journal of Sedimentary Research* **50**(2): 475–483.

Ehrlich, R. and Weinberg, B. (1970). An exact method for characterization of grain shape, *Journal of Sedimentary Research* **40**(1): 205–212.

Eklund, A. and Hart, J. (1996). Glaciotectonic deformation within a flute from the isfallsglaciaren, sweden, *Journal of Quaternary Science* **11**(4): 299–310.

Ensminger, S. L., Alley, R. B., Evenson, E. B. and Lawson, D. E. (2001). Basal-crevasse-fill origin of laminated debris bands at Matanuska Glacier, Alaska, U.S.A., *Journal of Glaciology* **47**(2): 412–422.

Epifanov, V. (2004). Rupture and dynamic hardness of ice, *Doklady Physics* **49**(2): 86–89.

Essery, R., Rutter, N. and Bayley, O. (2006). Measurement and modelling of energy fluxes over snow, ice and bedrock at Glacier de Tsanfleuron, Switzerland, *American Geophysical Union, Fall Meeting 2006, abstract# C32B-02*.

ETHZ (2008). Glacier de Tsanfleuron: Length variation measurements between 1884 and 2008.
URL: *http://glaciology.ethz.ch/messnetz/download/tsanfleuron.pdf*

Evans, D. J. A. (1989). Apron entrainment at the margins of subpolar glaciers, north west Ellesmere Island, Canadian high arctic., *Journal of Glaciology* **35**(2): 317–324.

Evans, D. J. A. and Rea, B. R. (1999). Geomorphology and sedimentology of surging glaciers: a land-systems approach, *Annals of Glaciology* **28**: 75–82.

Eyles, N. (1979). Facies of supraglacial sedimentation on Icelandic and alpine temperate valley glaciers, *Canadian Journal of Earth Sciences* **16**: 1341–1361.

Eyles, N. and Rogerson, R. (1978a). Sedimentology of medial moraines on Berendon Glacier, British Columbia, Canada; implications for debris transport in a glacierized basin, *Bulletin of the Geological Society of America* **89**(11): 1688–1693.

Eyles, N. and Rogerson, R. J. (1978b). Sedimentology of medial moraines on Berendon Glacier, British Columbia, Canada; implications for debris transport in a glacierized basin, *Bulletin of the Geological Society of America* **89**(11): 1688–1693.

Fairchild, I., Bradby, L., Sharp, M. and Tison, J. (1994). Hydrochemistry of carbonate terrains in alpine glacial settings, *Earth Surface Processes and Landforms* **19**(1).

Finnegan, D., Arcone, S., Bulmer, M. and Anderson, S. (2007). Fine-scale Topographic Analysis of Rock Size Distributions Derived From High-resolution Ground-based Li-DAR, *EOS Transactions American Geophysical Union* **88**(25): 23.

Fischer, U. and Clarke, G. (1994). Ploughing of subglacial sediment, *Journal of Glaciology* **40**(134): 97–106.

Fischer, U. and Hubbard, B. (1999). Subglacial sediment textures: character and evolution at Haut Glacier d'Arolla, Switzerland, *Annals of Glaciology* **28**: 241–246.

Fitzsimons, S. (1997). Entrainment of glaciomarine sediments and formation of thrust-block moraines at the margin of Sorsdale Glacier, East Antarctica, *Earth Surface Processes and Landforms* **22**(2): 175–187.

Fitzsimons, S., McManus, K. and Lorrain, R. (1999). Structure and strength of basal ice and substrate of a dry-based glacier: evidence for substrate deformation at sub-freezing temperatures, *Annals of Glaciology* **28**: 236–240.

Flint, R., Sanders, J. and Rodgers, J. (1960). Diamictite, a substitute term for symmictite, *Geological Society of America Bulletin* **71**(12): 1809–1810.

Folk, R. (1955). Student operator error in determination of roundness, sphericity, and grain size, *Journal of Sedimentary Research* **25**(4): 297–301.

Fowler, A. (1987). Sliding with cavity formation, *Journal of Glaciology* **33**(115): 255–267.

REFERENCES

Frayssines, M. and Hantz, D. (2009). Modelling and back-analysing failures in steep limestone cliffs, *International Journal of Rock Mechanics and Mining Sciences* **46**(7): 1115–1123.

Freeman, H., Kulessa, B. and Hubbard, B. (2005). Ultrasonic velocity logging of cores from Glacier de Tsanfleuron, Switzerland, *Geophysical Research Abstracts*, Vol. 7, p. 05126.

Fuller, S. and Murray, T. (2002). Sedimentological investigations in the forefield of an Icelandic surge-type glacier: implications for the surge mechanism, *Quaternary Science Reviews* **21**(12-13): 1503–1520.

Gale, S. and Hoare, P. (1992). Bulk sampling of coarse clastic sediments for particle-size analysis, *Earth Surface Processes and Landforms* **17**(7): 1729–733.

Gilpin, R. (1979). A model of the "liquid-like" layer between ice and a substrate with applications to wire regelation and particle migration, *Journal of Colloid Interface Science* **68**(2): 235–251.

Gilpin, R. (1980). Wire regelation at low temperatures, *Journal of Colloid Interface Science* **77**(2): 435–448.

Glasser, N. F. and Hambrey, M. J. (2001). Styles of sedimentation beneath svalbard valley glaciers under changing dynamic and thermal regimes, *Journal of the Geological Society* **158**(4): 697–707.

Glasser, N. F., Hambrey, M. J., Crawford, K. R., Bennett, M. R. and Huddart, D. (1998). The structural glaciology of Kongsvegen, Svalbard, and its role in landform genesis, *Journal of Glaciology* **44**(146): 136–148.

Glasser, N. F., Hambrey, M. J., Etienne, J. L., Jansson, P. and Pettersson, R. (2003). The Origin and Significance of Debris-Charged Ridges at the Surface of Storglaciären, Northern Sweden, *Geografiska Annaler* **85A**(2): 127–147.

Goldthwait, R. P. (1951). Development of end moraines in east-central Baffin Island, *Journal of Geology* **59**(6): 567–577.

Goodman, D., King, G., Millar, D. and Robin, G. (1979). Pressure-melting effects in basal ice of temperate glaciers: Laboratory studies and field observations under glacier d'Argentiere, *Journal of Glaciology* **23**(89): 259–271.

Goodsell, B., Hambrey, M. J. and Glasser, N. F. (2002). Formation of band ogives and associated structures at Bas Glacier d'Arolla, Valais, Switzerland, *Journal of Glaciology* **48**(161): 287–300.

Goodsell, B., Hambrey, M. J. and Glasser, N. F. (2005). Debris transport in a temperate valley glacier: Haut Glacier d'Arolla, Valais, Switzerland, *Journal of Glaciology* **51**(172): 139–146.

Gordon, J. E. (1992). The formation of glacial flutes: assessment of models with evidence from Lyngsdalen, North Norway, *Quaternary Science Reviews* **11**: 709–731.

Graham, D., Reid, I. and Rice, S. (2005). Automated sizing of coarse-grained sediments: image-processing procedures, *Mathematical Geology* **37**(1): 1–28.

Gremaud, V., Goldscheider, N., Savoy, L., Favre, G. and Masson, H. (2009). Geological structure, recharge processes and underground drainage of a glacierised karst aquifer system, tsanfleuron-sanetsch, swiss alps, *Hydrogeology Journal* pp. 1–16.

Grust, K. (2004). *The hydrology and dynamics of a glacier overlying a linked-cavity drainage system*, PhD thesis, University of Glasgow.

Gudmundsson, G. H. (1997). Ice deformation at the confluence of two glaciers investigated with conceptual map-plane and flowline models, *Journal of Glaciology* **43**(145): 537–547.

Gurnell, A. and Clark, M. (1987). *Glacio-fluvial sediment transfer: an Alpine perspective*, John Wiley & Sons Inc.

Hagen, J. O. and Liestøl, O. (1990). Long-term glacier mass-balance investigations in svalbard, 1950-88, *Annals of Glaciology* **14**: 102–106.

Hagen, J. O., Liestøl, O., Roland, E. and Jørgensen, T. (1993). *Glacier atlas of Svalbard and Jan Mayen*, Norsk Polarinstitutt Medd., Oslo.

Hagen, J. and Sætrang, A. (1991). Radio-echo soundings of sub-polar glaciers with low-frequency radar, *Polar Research* **9**(1): 99–107.

Haldorsen, S. (1981). Grain-size distribution of subglacial till and its relation to glacial crushing and abrasion, *Boreas* **10**(1): 91–105.

Hallet, B., Hunter, L. and Bogen, J. (1996). Rates of erosion and sediment evacuation by glaciers: A review of field data and their implications, *Global and Planetary Change* **12**(1-4): 213–235.

Hambrey, M. J. (1977). Foliation, minor folds and strain in glacier ice, *Tectonophysics* **39**(1-3): 397–416.

REFERENCES

Hambrey, M. J. (1994). *Glacial Environments*, UBC Press.

Hambrey, M. J., Bennett, M. R., Dowdeswell, J. A., Glasser, N. F. and Huddart, D. (1999). Debris entrainment and transfer in polythermal valley glaciers, *Journal of Glaciology* **45**(149): 69–86.

Hambrey, M. J. and Dowdeswell, J. A. (1994). Flow regime of the Lambert Glacier-Amery Ice Shelf system, Antarctica: structural evidence from Landsat imagery, *Annals of Glaciology* **20**: 401–401.

Hambrey, M. J., Dowdeswell, J. A., Murray, T. and Porter, P. R. (1996). Thrusting and debris entrainment in a surging glacier: Bakaninbreen, Svalbard, *Annals of Glaciology* **22**: 241–248.

Hambrey, M. J. and Ehrmann, W. (2004). Modification of sediment characteristics during glacial transport in high-alpine catchments: Mount Cook area, New Zealand, *Boreas* **33**(4): 300–318.

Hambrey, M. J. and Glasser, N. F. (2003). The role of folding and foliation development in the genesis of medial moraines: examples from Svalbard glaciers, *The Journal of Geology* **111**(4): 471–485.

Hambrey, M. J. and Huddart, D. (1995). Englacial and proglacial glaciotectonic processes at the snout of a thermally complex glacier in Svalbard, *Journal of Quaternary Science* **10**(4): 313–326.

Hambrey, M. J. and Müller, F. (1978). Structures and ice deformation in the White glacier, Axel Heiberg Island, Northwest Territories, Canada, *Journal of Glaciology* **20**(82): 41–66.

Hambrey, M. J., Murray, T., Glasser, N. F., Hubbard, A., Hubbard, B., Stuart, G., Hansen, S. and Kohler, J. (2005). Structure and changing dynamics of a polythermal valley glacier on a centennial timescale: Midre Lovénbreen, Svalbard, *Journal of Geophysical Research* **110**(F1).

Hambrey, M. and Lawson, W. (2000). Structural styles and deformation fields in glaciers: a review, *in* A. Maltman, B. Hubbard and M. Hambrey (eds), *Deformation of Glacial Materials*, Geological Society, pp. 59–83.

Hambrey, M., Milnes, A. and Siegenthaler, H. (1980). Dynamics and structure of Griesgletscher, Switzerland, *Journal of Glaciology* **25**(92): 215–228.

Haneberg, W. (2006). Measurement and visualization of directional rock surface profiles using three-dimensional photogrammetric or laser point clouds, *International Journal of Rock Mechanics and Mining Sciences* .

Harbor, J. (2009). Subglacial water storage and routing through basal crevasses, *Svartisen Subglacial Workshop - 25th-26th March 2009 – Engabreen tunnel, Svartisen, Norway*.

Harris, C. (2005). Climate change, mountain permafrost degradation and geotechnical hazard, *Global Change and Mountain Regions: An Overview of Current Knowledge*, Springer, Netherlands, pp. 215–224.

Harris, T., Tweed, F. and Knudsen, O. (2004). A Polygenetic Landform At Stiga, Oraefajokull, Southern Iceland, *Geografiska Annaler* **86A**(2): 143–154.

Harrison, W. (1972). Temperature of a temperate glacier, *Journal of Glaciology* **11**: 15–29.

Hart, J. (2006). An investigation of subglacial processes at the microscale from Briksdalsbreen, Norway, *Sedimentology* **53**(1): 125–146.

Herbst, P. and Neubauer, F. (2000). The Pasterze glacier, Austria: an analogue of an extensional allochthon, *in* A. Maltman, B. Hubbard and M. Hambrey (eds), *Deformation of Glacial Materials*, Geological Society Publication House, London, pp. 159–170.

Herbst, P., Neubauer, F. and Schopfer, M. (2006). The development of brittle structures in an alpine valley glacier: Pasterzenkees, Austria, 1887-1997, *Journal of Glaciology* **52**(176): 128.

Higgitt, D. and Warburton, J. (1999). Applications of differential gps in upland fluvial geomorphology, *Geomorphology* **29**(1-2): 121–134.

Hildes, D. (2001). *Modelling subglacial erosion and englacial sediment transport of the North American ice sheets*, PhD thesis, The University of British Columbia.

Hindmarsh, R. C. A. (1998). The stability of a viscous till sheet coupled with ice flow, considered at wavelengths less than the ice thickness, *Journal of Glaciology* **44**(147): 285–292.

Hindmarsh, R. C. A. (2000). Sliding over anisotropic beds, *Annals of Glaciology* **30**: 137–145.

Hodson, A. and Ferguson, R. (1999). Fluvial suspended sediment transport from cold and warm-based glaciers in Svalbard, *Earth Surface Processes and Landforms* **24**(11): 957–974.

Hodson, A., Tranter, M. and Vatne, G. (2000). Contemporary rates of chemical denudation and atmospheric co2 sequestration in glacier basins: an arctic perspective, *Earth Surface Processes and Landforms* **25**(13): 1447–1471.

Höglund, R. and Large, P. (2003). *Direct reflex EDM technology for the surveyor and civil engineer*, Trimble Integrated Surveying Group, Westminster, CO.

Holdsworth, G. and Bull, C. (1970). The flow law of cold ice: investigations on Meserve Glacier, Antarctica, *International Association of Scientific Hydrology Publication* **86**: 204–216.

Hooke, R. (1973). Flow near the margin of the Barnes Ice Cap, and the development of ice-cored moraines, *Geological Society of America Bulletin* **84**(12): 3929.

Hooke, R. (1991). Positive feedbacks associated with erosion of glacial cirques and overdeepenings, *Bulletin of the Geological Society of America* **103**(8): 1104–1108.

Hooke, R. L. and Hudleston, P. J. (1978). Origin of foliation in glaciers, *Journal of Glaciology* **20**(83): 285–299.

Hooke, R. L. and Iverson, N. (1995). Grain-size distribution on deforming subglacial tills: the role of grain fracture, *Geology* **23**(1): 57–60.

Hooke, R. and Pohjola, V. (1994). Hydrology of a segment of a glacier situated in an overdeepening, Storglaciären, Sweden, *Journal of Glaciology* **40**(134): 140–148.

Hooyer, T. and Iverson, N. (2000). Clast-fabric development in a shearing granular material: Implications for subglacial till and fault gouge, *Geological Society of America Bulletin* **112**(5): 683.

Hoppe, G. and Schytt, V. (1953). Some observations on fluted moraine surfaces, *Geografiska Annaler* **35**(2): 105–115.
URL: *http://www.jstor.org/stable/520195*

Hubbard, A. (2000). The verification and significance of three approaches to longitudinal stresses in high-resolution models of glacier flow, *Geografiska Annaler* **82**(4): 471–487.

Hubbard, A., Blatter, H., Nienow, P., Mair, D. and Hubbard, B. (1998). Comparison of a three-dimensional model for glacier flow with field data from Haut Glacier d'Arolla, Switzerland, *Journal of Glaciology* **44**(147): 368–378.

Hubbard, A. and Hubbard, B. (2000). The potential contribution of high-resolution glacier flow modelling to structural glaciology, *in* A. Maltman, B. Hubbard and M. Hambrey (eds), *Deformation of Glacial Materials*, Geological Society Pub. House, pp. 135–146.

Hubbard, B. (1991). Freezing-rate effects on the physical characteristics of basal ice formed by net adfreezing, *Journal of Glaciology* **37**(127): 339–347.

Hubbard, B. (2002). Direct measurement of basal motion at a hard-bedded, temperate glacier: Glacier de Tsanfleuron, Switzerland, *Journal of Glaciology* **48**(160): 1–8.

Hubbard, B., Cook, S. and Coulson, H. (2009). Basal ice facies: a review and unifying approach, *Quaternary Science Reviews* **28**(19-20): 1956–1969.

Hubbard, B. and Glasser, N. F. (2005). *Field techniques in glaciology and glacial geomorphology*, Wiley, Chichester.

Hubbard, B., Glasser, N., Hambrey, M. and Etienne, J. (2004). A sedimentological and isotopic study of the origin of supraglacial debris bands: Kongsfjorden, Svalbard, *Journal of Glaciology* **50**(169): 157–170.

Hubbard, B. and Hubbard, A. (1998). Bedrock surface roughness and the distribution of subglacially precipitated carbonate deposits: implications for formation at Glacier de Tsanfleuron, Switzerland, *Earth Surface Processes and Landforms* **23**(3).

Hubbard, B., Hubbard, A., Mader, H., Tison, J. and Duval, P. (2003). Spatial variability in the water content and rheology of temperate glaciers: Glacier de Tsanfleuron, Switzerland, *Annals of Glaciology* **37**: 1–6.

Hubbard, B. and Nienow, P. (1997). Alpine subglacial hydrology, *Quaternary Science Reviews* **16**(9): 939–955.

Hubbard, B., Roberson, S., Samyn, D. and Merton-Lyn, D. (2008). Digital optical televiewing of ice boreholes, *Journal of Glaciology* **54**(188): 823–830.

Hubbard, B. and Sharp, M. (1993). Weertman regelation, multiple refreezing events and the isotopic evolution of the basal ice layer, *Journal of Glaciology* **39**(132): 275–291.

Hubbard, B. and Sharp, M. (1995a). Basal ice facies and their formation in the western Alps, *Arctic and Alpine Research* **27**(4): 301–310.

Hubbard, B., Sharp, M. J., Willis, I. C., Nielsen, M. K. and Smart, C. C. (1995b). Borehole water-level variations and the structure of the subglacial hydrological system of Haut Glacier d'Arolla, Valais, Switzerland, *Journal of Glaciology* **41**(139): 572–583.

Hubbard, B., Siegert, M. and McCarroll, D. (2000). Spectral roughness of glaciated bedrock geomorphic surfaces: Implications for glacier sliding, *Journal of Geophysical Research - Solid Earth* **105**(B9).

Hubbard, B., Tison, J. L., Janssens, L. and Spiro, B. (2000). Ice-core evidence of the thickness and character of clear-facies basal ice: Glacier de Tsanfleuron, Switzerland, *Journal of Glaciology* **46**(152): 140–150.

Huddart, D., Bennett, M., Hambrey, M., Glasser, N. and Crawford, K. (1998). Origin of well-rounded gravels in glacial deposits from Brøggerhalvøya, northwest Spitsbergen: potential problems caused by sediment reworking in the glacial environment, *Polar Research* **17**(1): 61–69.

Hudleston, P. J. (1977). Similar folds, recumbent folds, and gravity tectonics in ice and rocks, *Journal of Geology* **85**: 113–122.

Hudleston, P. J. (1989). The association of folds and veins in shear zones, *Journal of Structural Geology* **11**(8): 949–957.

Hulbe, C. (1955). Mounting technique for grain size and shape measurement, *Journal of Sedimentary Research* **25**(4): 302–303.

Hunter, L., Powell, R. and Lawson, D. (1996). Flux of debris transported by ice at three Alaskan tidewater glaciers, *Journal of Glaciology* **42**(140): 123–135.

Iken, A. (1981). The effect of the subglacial water pressure on the sliding velocity of a glacier in an idealized numerical model, *Journal of Glaciology* **27**(97): 407–421.

Imbrie, J. and Purdy, E. (1962). Classification of modern Bahamian carbonate sediments, *in* W. Ham (ed.), *Classification of carbonate rocks: a symposium*.

Irvine-Fynn, T. D. L., Moorman, B. J., Sjogren, D. and Walter, F. (2005b). Cryological processes implied in Arctic proglacial stream sediment dynamics using principal components analysis and regression, *in* C. Harris and M. J.B. (eds), *Cryospheric Systems: Glaciers and Permafrost*, Geological Society Pub. House, London, pp. 83–98.

Irvine-Fynn, T. D. L., Moorman, B. J., Willis, I. C., Sjogren, D. B., Hodson, A. J., Mumford, P. N., Walter, F. S. A. and Williams, J. L. M. (2005a). Geocryological processes linked to High Arctic proglacial stream suspended sediment dynamics: examples from Bylot Island, Nunavut, and Spitsbergen, Svalbard, *Hydrological Processes* **19**(1): 115–135.

Iverson, N. (2000). Sediment entrainment by a soft-bedded glacier: a model based on regelation into the bed, *Earth Surface Processes and Landforms* **25**(8): 881–893.

Iverson, N., Hooyer, T. and Baker, R. (1998). Ring-shear studies of till deformation: Coulomb-plastic behavior and distributed strain in glacier beds, *Journal of Glaciology* **44**(148): 634–642.

Iverson, N., Hooyer, T. and Hooke, R. (1996). A laboratory study of sediment deformation: stress heteroeneity and grain-size evolution, *Annals of Glaciology* **22**: 167–175.

Iverson, N. and Semmens, D. (1995). Intrusion of ice into porous media by regelation: A mechanism of sediment entrainment by glaciers, *Journal of Geophysical Research-Solid Earth* **100**(B6): 10219–10230.

Jacka, T., Donoghue, S., Li, J., Budd, W. and Anderson, R. (2003). Laboratory studies of the flow rates of debris-laden ice, *Annals of Glaciology* **37**: 108–112.

Jain, S., Singh, P., Saraf, A. and Seth, S. (2003). Estimation of sediment yield for a rain, snow and glacier fed river in the Western Himalayan region, *Water Resources Management* **17**(5): 377–393.

Jansson, P. (1995). Water pressure and basal sliding on Storglaciären, northern Sweden, *Journal of Glaciology* **41**(138): 232–240.

Kamb, B. (1991). Rheological nonlinearity and flow instability in the deforming bed mechanism of ice stream motion, *Journal of Geophysical Research-Solid Earth* **96**(B10).

Kamb, B. and LaChapelle, E. (1964). Direct observation of the mechanism of glacier sliding over bedrock, *Journal of Glaciology* **5**(38): 159–172.

Kamb, B. and LaChapelle, E. (1968). Flow dynamics and structure in a fast-moving icefall, *Transactions of the AGU* **49**: 312.

Kamb, B., Raymond, C., Harrison, W., Engelhardt, H., Echelmeyer, K., Humphrey, N., Brugman, M. and Pfeffer, T. (1985). Glacier surge mechanism: 1982–83 surge of variegated glacier, alaska, *Science* **227**(4686): 469–479.

Kelly, M., Kubik, P., Von Blanckenburg, F. and SchlUchter, C. (2004). Surface exposure dating of the Great Aletsch Glacier Egesen moraine system, western Swiss Alps, using the cosmogenic nuclide 10Be, *Journal of Quaternary Science* **19**(5): 431–441.

Kennedy, S. and Mazzullo, J. (2007). Image analysis method of grain size measurement, *in* J. Syvitski (ed.), *Principles, Methods and Application of Particle Size Analysis*, Cambridge University Press, Cambridge, pp. 76–87.

Khatwa, A., Hart, J. and Payne, A. (1999). Grain textural analysis across a range of glacial facies, *Annals of Glaciology* **28**(1): 111–117.

King, E. C., Smith, A. M., Murray, T. and Stuart, G. W. (2008). Glacier-bed characteristics of midtre Lovenbreen, Svalbard, from high-resolution seismic and radar surveying, *Journal of Glaciology* **54**(184): 145–156.

King, E., Hindmarsh, R. and Stokes, C. (2009). Formation of mega-scale glacial lineations observed beneath a West Antarctic ice stream, *Nature Geoscience* **2**(8): 585–588.

Kirkbride, M. and Spedding, N. (1996). The influence of englacial drainage on sediment-transport pathways and till texture of temperate valley glaciers, *Annals of Glaciology* **22**: 160–166.

Kjaer, K. (1999). Mode of subglacial transport deduced from till properties, Mýrdalsjökull, Iceland, *Sedimentary Geology* **128**(3): 271–292.

Kleman, J. (2007). Subglacial processes and the geomorphological impact of cold-based ice sheets, *Geophysical Research Abstracts* **9**: 06999.

Knight, P. G. (1987). Observation at the Edge of the Greenland Ice Sheet: Boundary Condition Implications of Modellers, *The Physical Basis of Ice Sheet Modeling*, International Association of Hydrological Sciences Press, Institute of Hydrology, Wallingford, Oxfordshire UK., pp. 359–366.

Knight, P. G. (1988). The basal ice and debris sequence at the margin of an equatorial ice cap; El Cotopaxi, Ecuador, *Geografiska Annaler* **70A**(1): 9–13.

Knight, P. G. (1995). Debris structures in basal ice exposed at the margin of the Greenland ice-sheet, *Boreas* **24**(1): 11–12.

Knight, P. G. (1997). The basal ice layer of glaciers and ice sheets, *Quaternary Science Reviews* **16**(9): 975–993.

Knudsen, Ó., Roberts, M., Tweed, F., Russell, A., Lawson, D., Larson, G., Evenson, E. and Björnsson, H. (2001). Five 'supercool' Icelandic glaciers, *Eos Transactions, AGU, 82 (47), Fall Meeting Supplement, 10–14 December 2001, San Francisco*.

Konert, M. and Vandenberghe, J. (1997). Comparison of laser grain size analysis with pipette and sieve analysis: a solution for the underestimation of the clay fraction, *Sedimentology* **44**(3): 523–535.

Kozarski, S. and Szupryczynski, J. (1973). Glacial forms and deposits in the Sidujokull deglaciation area, *Geographia Polonica* **26**: 255–311.

Krautblatter, M. and Dikau, R. (2007). Towards a uniform concept for the comparison and extrapolation of rockwall retreat and rockfall supply, *Geografiska Annaler* **89A**(1): 21–40.

Krumbein, W. (1941). Measurement and geological significance of shape and roundness of sedimentary particles, *Journal of Sedimentary Research* **11**(2): 64–72.

Krumbein, W. and Pettijohn, F. (1938). *Manual of sedimentary petrography*, D. Appleton-Century Company. New York.

Kuenen, P. (1959). Experimental abrasion of pebbles. 2. rolling by current, *Journal of Geology* **64**(1): 336–368.

Kung, H. (2005). Effects of surface roughness on high-temperature oxidation of carbon-fiber-reinforced polyimide composites, *Journal of Composite Materials-Lancaster* **39**(18): 1677.

Lawson, D. (1979). *Sedimentological analysis of the western terminus region of the Matanuska Glacier, Alaska*, CRREL Hanover, New Hampshire.

Lawson, D., Strasser, J., Evenson, E., Alley, R., Larson, G. and Arcone, S. (1998). Glacio-hydraulic supercooling: a freeze-on mechanism to create stratified, debris-rich basal ice: I. Field evidence, *Journal of Glaciology* **44**(148): 547–562.

Lawson, W. (1996). Structural evolution of Variegated Glacier, Alaska, USA, since 1948, *Journal of Glaciology* **42**(141): 261–270.

Lawson, W., Sharp, M. and Hambrey, M. (1994). The structural geology of a surge-type glacier, *Journal of Structural Geology* **16**(10): 1447–1462.

Le Meur, E., Gagliardini, O., Zwinger, T. and Ruokolainen, J. (2004). Glacier flow modelling: a comparison of the Shallow Ice Approximation and the full-Stokes solution, *Comptes Rendus Physique* **5**(7): 709–722.

Lefauconnier, B. and Hagen, J. (1991). Surging and calving glaciers in eastern Svalbard.

REFERENCES

Lewis, W. (1940). Dirt cones on the northern margins of Vatnajökull, Iceland., *Journal of Geomorphology* **3**: 16–26.

Liestøl, O. (1988). The glaciers in the Kongsfjorden area, Spitsbergen, *Norsk Geografisk Tidsskrift* **42**(4): 231–238.

Lliboutry, L. (1968). General theory of subglacial cavitation and sliding of temperature glaciers.

Lliboutry, L. (1975). Law of sliding for glaciers without cavitation, *Annals of Geophysics* **35**: 207–225.

Lliboutry, L. (1993). Internal melting and ice accretion at the bottom of temperate glaciers, *Journal of Glaciology* **39**(131): 50–64.

Lliboutry, L. (2002). Velocities, strain rates, stresses, crevassing and faulting on Glacier de Saint-Sorlin, French Alps, 1957-76, *Journal of Glaciology* **48**(160): 125–141.

MacAyeal, D. (1993). Binge/purge oscillations of the Laurentide ice sheet as a cause of the North Atlantic's Heinrich events, *Paleoceanography* **8**(6): 775–784.

Mahaney, W. (1995). Glacial crushing, weathering and diagenetic histories of quartz grains inferred from scanning electron microscopy, *in* J. Menzies (ed.), *Modern glacial environments - Processes, dynamics and sediments*, Butterworth-Heinemann, Oxford, pp. 487 – 506.

Mahaney, W. (2002). *Atlas of sand grain surface textures and applications*, Oxford University Press, USA.

Mahaney, W., Milner, M., Kalm, V., Dirszowsky, R., Hancock, R. and Beukens, R. (2008). Evidence for a Younger Dryas glacial advance in the Andes of northwestern Venezuela, *Geomorphology* **96**(1-2): 199–211.

Manninen, A. (1997). Surface roughness of baltic sea ice, *Journal of Geophysical Research-Oceans* **102**(C1).

Masotti, D. (1991). Contribution à l'etude scientifique du karst de Tsanfleuron, Valais, *Actes du 9ème Congrés national de SSS*, pp. 173–176.

Mazzullo, J. and Kennedy, S. (1985). Automated measurement of the nominal sectional diameters of individual sedimentary particles: Research method paper, *Journal of Sedimentary Research* **55**(4): 593–595.

McCarroll, D. (1997). A template for calculating rock surface roughness, *Earth Surface Processes and Landforms* **22**(13): 1229–1230.

McCarroll, D. and Ballantyne, C. (2000). The last ice sheet in Snowdonia, *Journal of Quaternary Science* **15**(8): 765–778.

Menzies, J. (1981). Temperatures within subglacial debris; a gap in our knowledge, *Geology* **9**(6): 271–273.

Menzies, J. (2002). *Modern and past glacial environments*, Butterworth-Heinemann.

Mickelson, D. M. and Berkson, J. M. (1974). Till ridges presently forming above and below sea level in Wachusett Inlet, Glacier Bay, Alaska, *Geografiska Annaler* **56A**(1): 111–119.

Milnes, A. and Hambrey, M. (1976). A method for estimating approximate cumulative strains in glacier ice, *Tectonophysics* **43**: T23–27.

Moncrieff, A. (1989). Classification of poorly-sorted sedimentary rocks, *Sedimentary Geology* **65**(1-2): 191–194.

Morris, E. and Morland, L. (1976). A theoretical analysis of the formation of glacial flutes, *Journal of Glaciology* **17**(76): 311–323.

Murray, T., Booth, A. and Rippin, D. (2007). Water-content of glacier-ice: limitations on estimates from velocity analysis of surface ground-penetrating radar surveys, *Journal of Environmental & Engineering Geophysics* **12**(1): 87.

Nakamura, T. and Jones, S. (1970). Softening effect of dissolved hydrogen chloride in ice crystals, *Scripta Metallurgica* **4**(2): 123–126.

Nath, P. and Vaughan, D. (2003). Subsurface crevasse formation in glaciers and ice sheets, *Journal of Geophysical Research* **108**(B1): 2020.

Nesje, A., McCarroll, D. and Dahl, S. (1994). Degree of rock surface weathering as an indicator of ice-sheet thickness along an east-west transect across southern norway, *Journal of Quaternary Science* **9**(4): 337–348.

Nicholson, D. and Nicholson, F. (2000). Physical deterioration of sedimentary rocks subjected to experimental freeze-thaw weathering, *Earth Surface Processes and Landforms* **25**(12): 1295–1307.

REFERENCES

Nickling, W. and Bennett, L. (1984). The shear strength characteristics of frozen coarse granular debris, *Journal of Glaciology* **30**(106): 348–357.

Nye, J. F. (1951). The flow of glaciers and ice-sheets as a problem in plasticity, *Proceedings of the Royal Society of London. Series A, Mathematical and Physical Sciences* **207**(1091): 554–572.

Nye, J. F. (1952). The mechanics of glacier flow, *Journal of Glaciology* **2**(12): 82–93.

Nye, J. F. (1969). A calculation on the sliding of ice over a wavy surface using a Newtonian viscous approximation, *Proceedings of the Royal Society of London. Series A, Mathematical and Physical Sciences* **311**(1506): 445–467.

Nye, J. F. (1970). Glacier sliding without cavitation in a linear viscous approximation, *Proceedings of the Royal Society of London. Series A, Mathematical and Physical Sciences* **1522**(315): 381–403.

Ó Cofaigh, C., Larter, R., Dowdeswell, J., Hillenbrand, C., Pudsey, C., Evans, J. and Morris, P. (2005). Flow of the West Antarctic Ice Sheet on the continental margin of the Bellingshausen Sea at the Last Glacial Maximum, *Journal of Geophysical Research-Solid Earth* **110**(B11): B11103.

Obbard, R., Iliescu, D., Cullen, D., Chang, J. and Baker, I. (2003). SEM/EDS comparison of polar and seasonal temperate ice, *Microscopy research and technique* **62**(1): 49–61.

Orford, J. (1981). Particle form, *Geomorphological Techniques*, Allen and Unwin, London, pp. 86–90.

Ottesen, D. and Dowdeswell, J. (2006). Assemblages of submarine landforms produced by tidewater glaciers in Svalbard, *Journal of Geophysical Research-Earth Surface* **111**(F1): F01016.

Owen, L., Derbyshire, E. and Scott, C. (2003). Contemporary sediment production and transfer in high-altitude glaciers, *Sedimentary Geology* **155**(1-2): 13–36.

Passchier, C. and Trouw, R. (2005). *Microtectonics*, Springer.

Paterson, W. S. B. (2000). *The physics of glaciers*, Butterworth-Heinemann.

Paul, F. and Maisch, M. (2006). Historical glacier fluctuations, *in* P. Knight (ed.), *Glacier science and environmental change*, Blackwell Publishing Ltd., pp. 432–439.

Paul, M. and Evans, H. (1974). Observations of the internal structure and origin of some flutes in glacio-fluvial sediments, Blomstrandbreen, north-west Spitsbergen, *Journal of Glaciology* **13**(69): 393 – 401.

Pearce, J., Pazzaglia, F., Evenson, E., Lawson, D., Alley, R., Germanoski, D. and Denner, J. (2003). Bedload component of glacially discharged sediment: Insights from the Matanuska Glacier, Alaska, *Geology* **31**(1): 7–10.

Perret, S., Stoffel, M. and Kienholz, H. (2006). Spatial and temporal rockfall activity in a forest stand in the Swiss Prealps—a dendrogeomorphological case study, *Geomorphology* **74**(1-4): 219–231.

Philip, J. (1980). Thermal fields during regelation, *Cold Regions Science and Technology* **3**: 193–203.

Powers, M. (1953). A new roundness scale for sedimentary particles, *Journal of Sedimentary Research* **23**(2): 117–119.

Rabinowicz, E. (1995). *Friction and wear of materials*, Wiley, Chichester.

Rea, B. R., Whalley, W. B. and Meneely, J. (2004). Cation and sediment concentrations in basal ice from Oksfjordjokelen, north Norway, *Geografiska Annaler* **86**(1): 91–105.

Rees, W. G. and Arnold, N. S. (2007). Mass balance and dynamics of a valley glacier measured by high-resolution lidar, *Polar Record* **43**(4): 311–319.

Rempel, A., Wettlaufer, J. and Worster, M. (2004). Premelting dynamics in a continuum model of frost heave, *Journal of Fluid Mechanics* **498**: 227–244.

Reynolds, J. (1997). *An introduction to applied and environmental geophysics*, Wiley, Chichester.

Rippin, D., Bamber, J., Siegert, M., Vaughan, D. and Corr, H. (2006). Basal conditions beneath enhanced-flow tributaries of slessor glacier, east antarctica, *Journal of Glaciology* **52**(179): 481–490.

Rippin, D., Willis, I., Arnold, N., Hodson, A. and Brinkhaus, M. (2005). Spatial and temporal variations in surface velocity and basal drag across the tongue of the polythermal glacier midre Lovénbreen, Svalbard, *Journal of Glaciology* **51**(175): 588–600.

REFERENCES

Rippin, D., Willis, I., Arnold, N., Hodson, A., Moore, J., Kohler, J. and Bjornsson, H. (2003). Changes in geometry and subglacial drainage of Midre Lovénbreen, Svalbard, determined from digital elevation models, *Earth Surface Processes and Landforms* **28**(3): 273–298.

Rippin, D., Willis, I. and Kohler, J. (2007). Changes in the thermal regime of the polythermal Midre Lovénbreen, Svalbard, *Geophysical Research Abstracts*, Vol. 9, p. 03737.

Roberson, S. (2008). Structural composition and sediment transfer in a composite cirque glacier: Glacier de St. Sorlin, France, *Earth Surface Processes and Landforms* **33**(13): 1931–1947.

Roberts, M., Russell, A., Tweed, F. and Knudsen, O. (2001). Controls on englacial sediment deposition during the November 1996 jokulhlaup, Skeiđararjokull, Iceland, *Earth Surface Processes and Landforms* **26**(9): 935–952.

Roberts, M., Tweed, F., Russell, A., Knudsen, O., Lawson, D., Larson, G., Evenson, E. and Bjornsson, H. (2002). Glaciohydraulic supercooling in Iceland, *Geology* **30**(5): 439–442.

Robin, G. (1976). Is the basal ice of a temperate glacier at the pressure melting point?, *Journal of Glaciology* **16**(74): 183–196.

Rose, J. (1989). Glacier stress patterns and sediment transfer associated with the formation of superimposed flutes, *Sedimentary geology* **62**(2-4): 151–176.

Rose, K. C. and Hart, J. K. (2008). Subglacial comminution in the deforming bed: Inferences from SEM analysis, *Sedimentary Geology* **203**(1-2): 87–97.

Rosenfeld, M. and Griffiths, J. (1953). An experimental test of visual comparison technique in estimating two dimensional sphericity and roundness of quartz grains, *American Journal of Science* **251**(8): 553.

Röthlisberger, H. (1968). Erosive processes which are likely to accentuate or reduce the bottom relief of valley glaciers, *International Union of Geodesy and Geophysics, International Association of Scientific Hydrology, Commission of Snow and Ice, Publication* **46**: 87–97.

Röthlisberger, H. (1972). Water pressure in intra- and subglacial channels, *Journal of Glaciology* **11**(62): 177–203.

Röthlisberger, H. (1973). Water pressure in subglacial channels, *Symposium on the Hydrology of Glaciers, Cambridge, 7-13 Sept. 1969*, International Association of Scientific Hydrology, p. 97.

Sammis, C., King, G. and Biegel, R. (1987). The kinematics of gouge deformation, *Pure and Applied Geophysics* **125**(5): 777–812.

Sayers, M. and Karamihas, S. (1997). *The little book of profiling*, University of Michigan Transportation Research Institute.

Schafer, A. (1982). The Kontron Videoplan, a new device for determination of grain-size distributions from thin sections, *Neuse Jarbuch für Geologie und Paläontologie Monatschefte* **15**(2): 115–128.

Schneider, G., Perinpanayagam, H., Clegg, M., Zaharias, R., Seabold, D., Keller, J. and Stanford, C. (2003). Implant surface roughness affects osteoblast gene expression, *Journal of Dental Research* **82**(5): 372–376.

Schoof, C. and Clarke, G. (2008). A model for spiral flows in basal ice and the formation of subglacial flutes based on a Reiner-Rivlin rheology for glacial ice, *Journal of Geophysical Research* **113**: B004957.

Schulson, E. (2001). Brittle failure of ice, *Engineering Fracture Mechanics* **68**(17-18): 1839–1887.

Schulson, E. M. (1990). The brittle compressive fracture of ice, *Acta Metallurgica et Materialia* **38**(10): 1963–1976.

Schulson, E. M. (1999). The structure and mechanical behavior of ice, *JOM Journal of the Minerals, Metals and Materials Society* **51**(2): 21–27.

Schwarcz, H. and Exner, K. (1980). The implementation of the concept of fractal dimensions on a semi-automated image analyser, *Powder Technology* **27**(1): 207–213.

Schwarcz, H. and Shane, K. (1969). Measurement of particle shape by fourier analysis, *Sedimentology* **13**(3-4): 213–231.

Schytt, V. (1963). Fluted moraine surfaces, *Journal of Glaciology* **4**(36): 825–827.

Sharp, M. (1982). Modification of clasts in lodgement tills by glacial erosion, *Journal of Glaciology* **28**(2): 475–481.

Sharp, M. (1984). Annual moraine ridges at Skalafellsjökull, south-east Iceland, *Journal of Glaciology* **30**(1): 82–93.

Sharp, M. (1985). "Crevasse-Fill" Ridges: a landform type characteristic of surging glaciers?, *Geografiska Annaler* **67A**(3/4): 213–220.

Sharp, M., Gemmell, J. and Tison, J. (1989). Structure and stability of the former subglacial drainage system of the Glacier de Tsanfleuron, Switzerland, *Earth Surface Processes and Landforms* **14**(2).

Sharp, M. and Gomez, B. (1986). Processes of debris comminution in the glacial environment and implications for quartz sand-grain micromorphology, *Sedimentary Geology* **46**(1-2): 33–47.

Sharp, M., Jouzel, J., Hubbard, B. and Lawson, W. (1994). The character, structure and origin of the basal ice layer of a surge-type glacier, *Journal of Glaciology* **40**(135): 327–340.

Sharp, M., Richards, K., Willis, I., Arnold, N., Nienow, P., Lawson, W. and Tison, J. (1993). Geometry, bed topography and drainage system structure of the Haut Glacier d'Arolla, Switzerland, *Earth Surface Processes and Landforms* **18**(6): 557–571.

Sheridan, M., Wohletz, K. and Dehn, J. (1987). Discrimination of grain-size subpopulations in pyroclastic deposits, *Geology* **15**(4): 367.

Shreve, R. (1984). Glacier sliding at subfreezing temperatures, *Journal of Glaciology* **30**(106): 341–347.

Siegert, M., Taylor, J. and Payne, A. (2005). Spectral roughness of subglacial topography and implications for former ice-sheet dynamics in east antarctica, *Global and Planetary Change* **45**(1-3): 249–263.

Small, R., Beecroft, I. and Stirling, D. (1984). Rates of deposition on lateral moraine embankments, Glacier de Tsidjiore Nouve, Valais, Switzerland, *Journal of Glaciology* **30**(106): 275–281.

Small, R. J. (1987). Englacial and supraglacial sediment: transport and deposition, *in* A. Gurnell and M. Clark (eds), *Glacio-Fluvial Sediment Transfer: An Alpine Perspective*, John Wiley and Sons, New York, pp. 111–145.

Souchez, R. A. (1967). The formation of shear moraines: an example from south Victoria Land, Antarctica, *Journal of Glaciology* **6**(48): 837–843.

Souchez, R. and Lemmens, M. (1985). Subglacial carbonate deposition: an isotopic study of a present-day case, *Palaeogeography, palaeoclimatology, palaeoecology* **51**(1-4): 357–364.

Souchez, R. and Lorrain, R. (1991). *Ice composition and glacier dynamics*, Springer-Verlag.

Souchez, R., Samyn, D., Lorrain, R., Pattyn, F. and Fitzsimons, S. (2004). An isotopic model for basal freeze-on associated with subglacial upward flow of pore water, *Geophysical Research Letters* **31**(2): L02401.

Spillmann, T., Maurer, H., Willenberg, H., Evans, K. F., Heincke, B. and Green, A. G. (2007). Characterization of an unstable rock mass based on borehole logs and diverse borehole radar data, *Journal of Applied Geophysics* **61**(1): 16–38.

Stephen, K. and W.H., L. (1986). A Fortran subroutine to calculate the variables necessary to determine the fractal dimensions of closed forms, *Computers and Geoscience* **12**(5): 705–712.

Stewart, C., Rignot, E., Steffen, K., Cullen, N. and Huff, R. (2004). Basal topography and thinning rates of Petermann Gletscher, northern Greenland, measured by ground-based phase-sensitive radar, *FRISP Report* **15**: 1 – 5.

Stone, D., Clarke, G. and Ellis, R. (1997). Inversion of borehole-response test data for estimation of subglacial hydraulic properties, *Journal of Glaciology* **43**(143): 103–113.

Sugden, D. and John, B. (1976). *Glaciers and landscape: a geomorphological approach*, Edward Arnold.

Swift, D., Nienow, P., Spedding, N. and Hoey, T. (2002). Geomorphic implications of subglacial drainage configuration: rates of basal sediment evacuation controlled by seasonal drainage system evolution, *Sedimentary Geology* **149**(1-3): 5–19.

Swithinbank, C. (1950). The origin of dirt cones on glaciers, *Journal of Glaciology* **1**(8): 461–65.

Syvitski, J. (2007). *Principles, methods and application of particle size analysis*, Cambridge University Press, Cambridge.

Taylor, J., Siegert, M., Payne, A. and Hubbard, B. (2004). Regional-scale bed roughness beneath ice masses: measurement and analysis, *Computers and Geosciences* **30**(8): 899–908.

Thomas, M., Wiltshire, R. and Williams, A. (1995). The use of fourier descriptors in the classification of particle shape, *Sedimentology* **42**(4): 635–645.

Thomas, P. (1991). *Geological maps and sections for civil engineers*, Blackie and Sons Ltd., Glasgow.

Thomson, J. (1860). On crystallization and liquefaction, as influenced by stresses tending to change of form in the crystals, *Proceedings of the Royal Society of London* pp. 472–481.

Tickell, F. (1948). *The Examination of Fragmental Rocks*, Stanford University Press.

Tison, J. L. and Hubbard, B. (2000). Ice crystallographic evolution at a temperate glacier: Glacier de Tsanfleuron, Switzerland, *in* A. Maltman, B. P. Hubbard and M. J. Hambrey (eds), *Deformation of Glacial Materials*, Geological Society London Special Publications, pp. 23–38.

Tison, J. L. and Lorrain, R. D. (1987). A mechanism of basal ice-layer formation involving major ice-fabric changes, *Journal of Glaciology* **33**(113): 47–50.

Tison, J. L., Souchez, R. and Lorrain, R. (1989). On the incorporation of unconsolidated sediments in basal ice: Present-day examples, *Zeitschrift für Geomorphologie Supplementband* **72**: 173–183.

Tison, J., Petit, J., Barnola, J. and Mahaney, W. (1993). Debris entrainment at the ice-bedrock interface in sub-freezing temperature conditions(Terre Adélie, Antarctica), *Journal of Glaciology* **39**(132): 303–315.

Tranter, M., Brown, G., Hodson, A. and Gurnell, A. (1996). Hydrochemistry as an indicator of subglacial drainage system structure: a comparison of alpine and sub-polar environments, *Hydrological Processes* **10**(4): 541–556.

Truffer, M., Echelmeyer, K. and Harrison, W. (2001). Implications of till deformation on glacier dynamics, *Journal of Glaciology* **47**(156): 123–134.

Tulaczyk, S., Kamb, B., Scherer, R. and Engelhardt, H. (1998). Sedimentary processes at the base of a west antarctic ice stream; constraints from textural and compositional properties of subglacial debris, *Journal of Sedimentary Research* **68**(3): 487–496.

Tulaczyk, S., Kamb, W. and Engelhardt, H. (2000). Basal mechanics of ice stream B, West Antarctica 1. Till mechanics, *Journal of Geophysical Research-Solid Earth* **105**(B1): 483–494.

van der Veen, C. J. (1998). Fracture mechanics approach to penetration of bottom crevasses on glaciers, *Cold Regions Science and Technology* **27**(3): 213–223.

van Steijn, H., Boelhouwers, J., Harris, S. and Hetu, B. (2002). Recent research on the nature, origin and climatic relations of blocky and stratified slope deposits, *Progress in Physical Geography* **26**(4): 551–575.

Vincent, C., Le Meur, E., Six, D. and Funk, M. (2005). Solving the paradox of the end of the Little Ice Age in the Alps, *Geophysical Research Letters* **32**(9): L09706.

Vivian, R. and Bocquet, G. (1973). Subglacial cavitation phenomena under the Glacier d'Argentiere, Mont Blanc, France, *J. Glaciol* **12**(66): 439–451.

Wadell, H. (1932). Volume, shape and roundness of rock particles, *Journal of Geology* **30**(5): 377–392.

Wadham, J. L. and Nuttall, A. M. (2002). Multiphase formation of superimposed ice during a mass-balance year at a maritime high-arctic glacier, *Journal of Glaciology* **48**(163): 545–551.

Walder, J. (1986). Hydraulics of subglacial cavities, *Journal of Glaciology* **32**(112): 439–445.

Walder, J. and Fowler, A. (1994). Channelized subglacial drainage over a deformable bed, *Journal of Glaciology* **40**(134): 3–15.

Walder, J. and Hallet, B. (1978). Geometry of former subglacial water channels and cavities, *Journal of Glaciology* **23**: 335–346.

Waller, R. (2001). The influence of basal processes on the dynamic behaviour of cold-based glaciers, *Quaternary International* **86**(1): 117–128.

Waller, R. I., Hart, J. K. and Knight, P. G. (2000). The influence of tectonic deformation on facies variability in stratified debris-rich basal ice, *Quaternary Science Reviews* **19**(8): 775–786.

Warburton, J. and Beecroft, I. (1993). Use of meltwater stream material loads in the estimation of glacial erosion rates, *Zeitschrift fur Geomorphologie* **37**: 19–19.

Weertman, J. (1957). On the sliding of glaciers, *Journal of Glaciology* **3**(21): 33–38.

Weertman, J. (1961). Mechanism for the formation of inner moraines found near the edge of cold ice caps and ice sheets, *Journal of Glaciology* **3**(30): 965–978.

Weiss, J. (2004). Subcritical crack propagation as a mechanism of crevasse formation and iceberg calving, *Journal of Glaciology* **50**(168): 109–115.

Weiss, J. and Schulson, E. M. (1995). The failure of fresh-water granular ice under multiaxial compressive loading, *Acta Metallurgica et Materialia* **43**(6): 2303–2315.

Weiss, J. and Schulson, E. M. (2000). Grain-boundary sliding and crack nucleation in ice, *Philosophical Magazine A* **80**(2): 279–300.

Wentworth, C. (1922). A scale of grade and class terms for clastic sediments, *The Journal of Geology* **30**(5): 377–392.

Whalley, W., Rea, B. and Rainey, M. (2004). Weathering, blockfields, and fracture systems and the implications for long-term landscape formation: Some evidence from Lyngen and Øksfordjøkelen areas in north Norway, *Polar Geography* **28**(2): 93–119.

Whitehouse, D. (1982). The parameter rash: is there a cure?, *Wear* **83**(1): 75–78.

Williams, J. H. and Johnson, C. D. (2004). Acoustic and optical borehole-wall imaging for fractured-rock aquifer studies, *Journal of Applied Geophysics* **55**(1-2): 151–159.

Willis, I., Mair, D., Hubbard, B., Nienow, P., Fischer, U. and Hubbard, A. (2003). Seasonal variations in ice deformation and basal motion across the tongue of Haut Glacier d'Arolla, Switzerland, *Annals of Glaciology* **36**: 157–167.

Wilson, C. and Marmo, B. (1999). The School of Earth Sciences, The University of Melbourne, Australia.
URL: *http://web.earthsci.unimelb.edu.au/wilson/ice1*

Woodward, J., Murray, T. and McCaig, A. (2002). Formation and reorientation of structure in the surge-type glacier Kongsvegen, Svalbard, *Journal of Quaternary Science* **17**(3): 201–209.

Ximenis, L., Calvet, J., Garcia, D., Casas, J. and Sabat, F. (2000). Folding in the Johnsons Glacier, Livingston Island, Antarctica, *in* A. Maltman, B. Hubbard and M. Hambrey (eds), *Deformation of Glacial Materials*, Geological Society Publication House, pp. 147–158.

Young, D., Blankenship, D. and Holt, J. (2007). Subglacial Roughness of the West Antarctic Ice Sheet, *Antarctica: A Keystone in a Changing World–Online Proceedings of the 10 th ISAES X, edited by AK Cooper and CR Raymond et al., USGS Open-File Report* **1047**.

Young, P., Roberts, D., Chiou, H., Rae, W., Chan, H. and Traini, D. (2008). Composite carriers improve the aerosilisation efficiency of drugs for respiratory delivery, *Journal of Aerosol Science* **38**(1): 82–93.